

AFRL-AFOSR-VA-TR-2024-0002

Quantifying nonequilibrium dynamics of stochastic systems with partial information

Bisker, Gili
TEL AVIV UNIVERSITY
55 LEBANON HAIM
TEL AVIV-JAFFA, , 006905904
ISR

10/03/2023
Final Technical Report

DISTRIBUTION A: Distribution approved for public release.

Air Force Research Laboratory
Air Force Office of Scientific Research
Arlington, Virginia 22203
Air Force Materiel Command

REPORT DOCUMENTATION PAGE

PLEASE DO NOT RETURN YOUR FORM TO THE ABOVE ORGANIZATION.

1. REPORT DATE	2. REPORT TYPE	3. DATES COVERED	
20231003	Final	START DATE 20200930	END DATE 20230929

4. TITLE AND SUBTITLE
Quantifying nonequilibrium dynamics of stochastic systems with partial information

5a. CONTRACT NUMBER	5b. GRANT NUMBER	5c. PROGRAM ELEMENT NUMBER
	FA9550-20-1-0426	61102F
5d. PROJECT NUMBER	**5e. TASK NUMBER**	**5f. WORK UNIT NUMBER**

6. AUTHOR(S)
Gili Bisker

7. PERFORMING ORGANIZATION NAME(S) AND ADDRESS(ES)
TEL AVIV UNIVERSITY
55 LEBANON HAIM
TEL AVIV-JAFFA 006905904
ISR

8. PERFORMING ORGANIZATION REPORT NUMBER

9. SPONSORING/MONITORING AGENCY NAME(S) AND ADDRESS(ES)	10. SPONSOR/MONITOR'S ACRONYM(S)	11. SPONSOR/MONITOR'S REPORT NUMBER(S)
Air Force Office of Scientific Research 875 N. Randolph St. Room 3112 Arlington, VA 22203	AFRL/AFOSR RTA2	AFRL-AFOSR-VA-TR-2024-0002

12. DISTRIBUTION/AVAILABILITY STATEMENT
A Distribution Unlimited: PB Public Release

13. SUPPLEMENTARY NOTES

14. ABSTRACT
Far-from-equilibrium processes constantly dissipate energy while converting a free-energy source to another form of energy. Living systems, for example, rely on an orchestra of molecular motors that consume chemical fuel to produce mechanical work. Drawing inspiration from biology, where the underlying nonequilibrium activity gives rise to a plethora of emergent collective phenomena such as adaptation, pattern-formation, prediction, selfreplication, decision-making, computation, etc., we strive to capture their mechanistic essence in order to mimic life-like behavior in synthetic systems. Estimating the amount of the free energy budget lost to dissipation is crucial for a deeper understanding of the underlying nonequilibrium dynamics of driven systems, aiming for general design principles for biomimicking custom-made systems. Although there are theoretical tools for detecting and quantifying nonequilibrium activity and dissipation in the framework of stochastic thermodynamics, these mostly rely on a detailed description of the microscopic dynamics. Hence, there is a growing gap between these analytical calculations and their experimental applicability. The difficulty stems from the limited accessibility to the myriad degrees of freedom of complex systems and the finite measurement resolution, which can mask the footprints of nonequilibrium dynamics such that they appear as passive thermal fluctuations. My goal is to develop a new toolkit for studying nonequilibrium systems with complex network structures and many degrees of freedom. I will advance theoretical tools for estimating the dissipation from partial information based on an approach I have pioneered for detecting time-- irreversibility from asymmetry in waiting time distributions for discrete sets of states. I will use tools of stochastic thermodynamics to derive entropy production bounds for continuous variables and study the effects of coarse-graining using numerical simulations. I will verify the optimal bound based on irreversibility and compare it to other dissipation estimators. Finally, I will demonstrate my approach to a nonlinear reaction-diffusion network model system.

15. SUBJECT TERMS

16. SECURITY CLASSIFICATION OF:			17. LIMITATION OF ABSTRACT	18. NUMBER OF PAGES
a. REPORT	b. ABSTRACT	c. THIS PAGE		
U	U	U	UU	86

19a. NAME OF RESPONSIBLE PERSON	19b. PHONE NUMBER *(Include area code)*
FREDERICK LEVE	696-9730

DISTRIBUTION A: Distribution approved for public release.

DISTRIBUTION A: Distribution approved for public release.

Quantifying nonequilibrium dynamics of stochastic systems with partial information

Principal Investigator: Bisker, Gili
PI Email: bisker@tauex.tau.ac.il
Program Officer: Leve, Frederick
Report Type: Final Report
Reporting Period
Start Date: 10/01/2020
End Date: 9/30/2023
Award Number: FA9550-20-1-0426

Abstract

Far-from-equilibrium processes constantly dissipate energy while converting a free-energy source to another form of energy. Living systems, for example, rely on an orchestra of molecular motors that consume chemical fuel to produce mechanical work. Drawing inspiration from biology, where the underlying nonequilibrium activity gives rise to a plethora of emergent collective phenomena such as adaptation, pattern-formation, prediction, self-replication, decision-making, computation, etc., we strive to capture their mechanistic essence in order to mimic life-like behavior in synthetic systems. Estimating the amount of the free energy budget lost to dissipation is crucial for a deeper understanding of the underlying nonequilibrium dynamics of driven systems, aiming for general design principles for biomimicking custom-made systems. Although there are theoretical tools for detecting and quantifying nonequilibrium activity and dissipation in the framework of stochastic thermodynamics, theses mostly rely on a detailed description of the microscopic dynamics. Hence, there is a growing gap between these analytical calculations and their experimental applicability. The difficulty stems from the limited accessibility to the myriad degrees of freedom of complex systems and the finite measurement resolution, which can mask the footprints of nonequilibrium dynamics such that they appear as passive thermal fluctuations. Our goal is to advance theoretical tools for estimating the entropy production rate (EPR) from partial information based on an approach for detecting time-irreversibility from asymmetry in waiting-time distributions for a discrete set of states.

DISTRIBUTION A: Distribution approved for public release.

Accomplishments

Research Objectives

I will use tools of stochastic thermodynamics to derive the entropy production bound based on the KLD for continuous variables and study the effects of coarse-graining using numerical simulations. I will show that this is the optimal bound based on irreversibility and compare it to other dissipation estimators. Finally, I will demonstrate my approach to a model system of a biochemical reaction network with nonlinear dynamics.
In order to achieve my goal, I will pursue the following aims:

- Specific Aim 1: Derive the novel estimator of the breaking of time-reversal symmetry in the absence of observable currents based on waiting time distributions for systems with continuous variables
- Specific Aim 2: Prove the superiority of the waiting time distribution approach and demonstrate it is the best possible bound on entropy production using irreversibility
- Specific Aim 3: Compare and contrast current state-of-the-art bounds on entropy production and unify all non-invasive measures of nonequilibrium
- Specific Aim 4: Demonstrating optimal strategies for nonequilibrium quantification for a nonlinear biochemical reaction network model system

Accomplishments

Here, we list our main accomplishments, which will be detailed in the technical section at the end of the report:

- We estimate a lower bound on the total entropy production rate (EPR) for a system with a single observed variable following Langevin dynamics, coarse-grained into discrete states. As a model system, we use hair-cell bundle oscillations driven by molecular motors, such that the bundle tip position is observed, but the positions of the motors are hidden. We invoke the underlying broken time-reversal symmetry embedded in waiting time distributions of the partially observed system to calculate a lower bound on the total EPR [**Phys. Chem. Chem. Phys., 2022, 24, 24021**]
- We calculate partial EPR values of Markov chains driven by external forces from different notions of partial information. We calculate partial EPR from state-based coarse-graining, namely decimation and two lumping protocols with different constraints, either preserving transition flux, or the occupancy number correlation function. Finally, we compare these partial EPR values with the EPR inferred from the observed cycle affinity. Our results can further be extended to other networks and various external driving forces [**J. Phys. D: Appl. Phys. 56 (2023) 254001**]
- We consider different levels of observed statistics from different coarse-graining (CG) approaches for continuous-time Markov chain (CTMC), and infer the EPR from the observed data using the KLD estimator, the Plug-in estimator, and the RNEEP estimator, when applicable. These estimators do not require prior knowledge of the systems and only use

the observed statistics to infer and quantify time-irreversibility. First, we use the sequence of observed microstates and coarse-grained macrostates and the transitions between them. Then, we include information about transitions between the hidden microstates within the coarse-grained macrostates (intra-transitions). Finally, we reformulate the trajectory data of observed states and transitions and intra-transitions within macrostates by labeling the coarse-grained macrostates according to the number of times they are visited before jumping into an observed state. We apply the CG approaches to two model systems, namely, a 4-state system in which two of the states are coarse-grained into a single hidden state and the discrete Flashing Ratchet with time-varying potential, whose values cannot be observed. We provide a unifying comparison between the estimators on the different CG schemes and show how additional information is exploited for inferring tighter lower bounds on the total EPR [**arXiv preprint arXiv:2212.13487**].

- We propose a new inference approach for a tight lower bound on the total EPR given partial information based on an optimization scheme that uses the observed transitions and waiting times statistics. We introduce hierarchical bounds relying on the first- and second-order transitions and the moments of the observed waiting time distributions and apply our approach to two generic systems of a hidden network and a molecular motor with lumped states. Finally, we show that a lower bound on the total EPR can be obtained even when assuming a simpler network topology of the full system [**arXiv preprint arXiv:2212.01783**].

Dissemination

The main results were published or submitted to arXiv are currently under review:

Aishani Ghosal, Gili Bisker, "Inferring entropy production rate from partially observed Langevin dynamics under coarse-graining", https://doi.org/10.48550/arXiv.2205.14688

1. Inferring entropy production rate from partially observed Langevin dynamics systems under coarse-graining
   Aishani Ghosal and **Gili Bisker**
   Physical Chemistry Chemical Physics, 24, 24021-24031 (2022)
2. Nonequilibrium self-assembly of multiple stored targets in a dimer-based system
   Adi Ben-Ari, Liron Ben-Ari, and **Gili Bisker**
   The Journal of Chemical Physics, 155(23), 234113 (2021)
3. Entropy production rates for different notions of partial information
   Aishani Ghosal and **Gili Bisker**
   Journal of Physics D: Applied Physics 56, 254001 (2023)
4. Nonequilibrium Self Assembly Time Forecasting by the Stochastic Landscape Method
   Michael Faran and **Gili Bisker**
   The Journal of Physical Chemistry B (2023)
5. Universal bounds on entropy production inferred from observed statistics
   Eden Nitzan, Aishani Ghosal, **Gili Bisker**
   arXiv:2212.01783 (2022)

6. Utilizing time-series measurements for entropy production estimation in partially observed systems
   Uri Kapustin, Aishani Ghosal, and **Gili Bisker**
   arXiv:2212.13487 (2022)

Invited talks at conferences and scientific meetings:

1. AFOSR Dynamical Systems and Control Theory Program, Air Force Office of Scientific Research, Arlington VA, USA — Sep 2023
2. Workshop on Signatures of Nonequilibrium Fluctuations in Life, The International Centre for Theoretical Physics (ICTP), Strada Costiera, Trieste, Italy — May 2023
3. Dynamical Systems and Control Theory Meeting, Niceville, Florida, USA — August 2022
4. Physics of Living Systems, Department of Physics, Massachusetts Institute of Technology (MIT), Cambridge, MA, USA — July 2022
5. The 3rd Workshop on Stochastic Thermodynamics (WOST III), Tokyo, Japan — May 2022
6. Non-Markovian dynamics far from equilibrium Meeting, Active and Soft Matter session, International Centre for Theoretical Physics (ICTP), Trieste, Italy — May 2022
7. Stochastic Thermodynamics: Junior Women's Caucus (Virtual) — April 2022
8. Physics of Life Seminar Series, Imperial College, London, UK — Nov 2021
9. 2021 Dynamical Systems and Control Theory Program Review, Air Force Office of Scientific Research, University of Florida Research Engineering & Education Facility (UF REEF), Shalimar, FL, USA — Sep 2021
10. The Israel Physical Society (IPS) Annual Meeting, Soft-matter Nonlinear Biological and Statistical Physics — Feb 2021
11. TAU-Potsdam joint workshop on biophysics, soft matter and nanomaterials — Nov 2020
12. Physics Department Colloquium, Ben-Gurion University — Nov 2020
13. Statistical physics seminar series, University of Maryland, College Park, USA — Nov 2020
14. "Nonequilibrium Features of Life", Department of Chemical Physics, School of Chemistry, Tel Aviv University — Oct 2020

DISTRIBUTION A: Distribution approved for public release.

Impacts

Development of the principal discipline(s) of the project

- In a recent study [New J. Phys., 2021, 23, 1–16], Roldan *et al.* transformed the forward and backward time series data of an observed variable of a continuous hair bundle system into two independent and identically distributed time series using a whitening approximation to estimate the KLD from two univariate distributions. They first calculated the EPR bound using only the observed degree of freedom, *i.e.*, the tip position of the hair bundle. The EPR estimate calculated with only one observed degree of freedom was typically three orders of magnitude smaller than the total EPR. We quantify the irreversibility using a non-invasive method to provide a lower bound on the total EPR in a partially observed model system with continuous variables following oscillatory dynamics, where one of its observables is coarse-grained into a few discrete states. We simulate an oscillating hair-bundle model in which the bundle's tip position is experimentally observed, whereas the position of the molecular motor is hidden. The coarse-grained process follows second-order *semi-Markov* statistics in the *reduced state space* (tip position variable space). In this model, the affinity entropy production contribution vanishes; therefore, the irreversibility information can only be accessed from the asymmetries of the waiting time distributions of the forward and the reversed transitions. After the decimation, we exploit the underlying broken time-reversal symmetry stemming from the difference in the PDFs of the waiting times for the upward and the corresponding downward transitions among different coarse-grained states, to calculate the EPR bound, EPR_{WTD}, by applying the KLD estimator. We show that the ratio of the means of the dwell time PDFs of the forward and reverse trajectories, termed the mean dwell-time asymmetry factor, can qualitatively detect the broken time-reversal symmetry, and its variation with the number of coarse-grained states is studied. The lower bound on the EPR was estimated using the underlying broken time-reversal symmetry induced by the active force for a system with Langevin dynamics and zero net currents along the reduced variable space. This approach can be applied to a system following Langevin dynamics with an arbitrary number of observed and hidden states carrying a net flux that vanishes on the observed state-space to quantify the deviation from thermal equilibrium manifested in the irreversibility of the observed degrees of freedom.
- We study different notions of partial information in driven systems and the corresponding mean EPR values associated with them. The predicted EPR values are then compared with the true mean EPR (TM), which is calculated considering all the edges of the network topology, where tighter lower bounds on the TM EPR are considered better. The SCGF, which is calculated for coarse-graining by decimation and redistribution of the steady-state probabilities and transition rates, produces the total mean EPR (TM), as expected. For the other coarse-graining approaches, systems are considered to follow approximated Markovian dynamics, and the resulting modified/coarse-grained transition rate matrices are used to calculate the mean EPRs for different methods (AM, L, HS). For certain topologies, we find that as we decrease the hidden state connectivity, the AM approaches the total mean EPR (topologies I, II, and III) since the contribution to the EPR from the loss cycles carrying transition flux decreases. By comparing the mean EPR values calculated from the

state-based coarse-graining methods, namely, lumping (L, HS) and coarse-graining by decimation (SCGF, AM), where one is assumed to know the network topology, with the mean EPR inferred from partial information of only the observed states and the transitions between them (IPEP), we find that the effect of the partial information reflected on the inferred EPR for state-based coarse-graining depends on the network topology. Our study can be extended to larger systems with more than two hidden microstates or having a hidden cycle current, etc.

- We have compared time-irreversibility-based EPR estimators for different coarse-graining schemes, focusing on KLD-based estimators, with (KLD) and without (Plug-in and RNEEP) WTD statistics, using two coarse-graining approaches. We have confirmed that the semi-coarse-graining framework, which includes intra-transitions data, yields tighter EPR bounds compared to the full-coarse-graining framework, as it exploits more information on time-irreversibility. In addition, we have proposed a novel approach for reformulating semi-CG trajectories, previously used for the Plug-in and RNEEP estimators, for applying the KLD estimator. Using the Transformed semi-CG approach and the KLD estimator, we could distill time-irreversibility encoded in the intra-transitions within hidden microstates to achieve the tightest lower bound on the total EPR among the estimators we tested. Moreover, comparing the EPR bounds obtained from the full-CG and the semi-CG statistics provides a direct quantification of the time-irreversibility in the intra-transitions captured by each estimator. The proposed transformation and EPR estimators can be applied to other discrete-state continuous-time systems to provide a lower bound on the total EPR when only partial information is available.
- We presented a new estimator for the entropy production rate, which gave a tight bound by formulating an optimization problem using both transitions and waiting times statistics. Such data is readily available in different experimental settings, for example, tracking a bead attached to a rotating bacterial flagellum, or cortical granules embedded in the actomyosin cortex of an oocyte. Our estimator can be applied to any system with a known topology, and it significantly surpasses previous estimators, as demonstrated for the two studied systems, the fully connected hidden network and the molecular motor. The variables for the optimization problem can be inferred from the observed statistics, where longer trajectories result in more accurate estimation and enable a smaller constraint tolerance value. Finally, for both systems, our approach can provide a lower bound on the total EPR for more complex systems, assuming a simpler underlying topology of the hidden states. Our approach is based on an optimization problem formulated using the observed statistics of a partially accessible system, utilizing information on the underlying topology in order to provide a tight lower bound on the total EPR. The estimator can be used as a benchmark for comparing the performance of other estimators that rely on coarse-grained or partial information about the system.

Other disciplines:

Your work has broad applicability beyond physics and could influence fields like biology, data science, and engineering. For instance, the biological applications of your work could be extended to understanding the thermodynamics of cellular processes, while the computational

DISTRIBUTION A: Distribution approved for public release.

aspects could be used in machine learning algorithms for estimating system states from partial observations. The model we used in our calculations is a generic model with coupled degrees of freedom, where only a subset of the variables can be observed with a finite resolution. Hence, our approach is of general interest to many researchers studying nonequilibrium systems, being alive or not, with numerous degrees of freedom.

Impact on the development of human resources

This project has offered numerous opportunities for young researchers to work in a multidisciplinary setting, learning to apply rigorous physical theories to complex real-world problems. It has engaged undergraduate and graduate students and postdocs, fostering a new generation of thinkers who are well-versed in tackling interdisciplinary challenges.

The project gave the opportunity to Dr. Aishani Ghosal and Dr. Shubhadeep Nag to conduct their postdoctoral research in my group at Tel Aviv University. They have been exposed to cutting-edge research in Israel and participated, as well as presented, in scientific meetings. Dr. Ghosal also had the opportunity to mentor graduate students in my group, which is extremely important for her scientific development as an independent researcher.

Moreover, I have mentored graduate students: Michael Faran, Uri Kapustin, and Eden Nitzan, and undergraduate students: Liron Ben-Ari, Adi Ben-Ari, and Itamar Magar.

Impact on teaching and educational experiences

The theoretical and computational tools developed through this research have been integrated into a new graduate-level course I have developed, “Stochastic Thermodynamics in Biology”, which is closely related to the methodologies and approaches used in this project.

Impact on Physical, Institutional, and Information Resources

The research has made optimal use of computational facilities in our faculty and may lead to the need for more specialized computing infrastructure for more detailed simulations. Institutionally, this research strengthens the profile of your organization as a leader in theoretical and applied physics. The published papers and preprints serve as information resources that advance the scientific community’s understanding of nonequilibrium systems.

Impact on society beyond science and technology:

I took part in an outreach activity, describing the main questions of the field. Specifically, I was the host of an “Excellence in Science Program” visit of middle-school female students to my lab at Tel Aviv University.

Generally, by mimicking life-like behavior in synthetic systems, the research has the potential to impact fields such as medicine, robotics, and environmental science. For example, a more detailed understanding of molecular motors could pave the way for innovative medical treatments. Likewise, better models of nonequilibrium systems could lead to more efficient energy-conversion technologies.

DISTRIBUTION A: Distribution approved for public release.

Changes

Changes in approach
In our work, we decided to work with an oscillating hair-bundle model in which the bundle's tip position is experimentally observed, whereas the position of the molecular motor is hidden. In this model, the affinity entropy production contribution vanishes; therefore, the irreversibility information can only be accessed from the asymmetries of the waiting time distributions of the forward and the reversed transitions. This model was chosen instead of the nonlinear biochemical reaction network model, originally proposed in Specific Aim 4. The main reason is that the hair-bundle system has received a lot of attention recently, see New J. Phys., 2021, 23, 1–16 and references within, and was also studied experimentally. Therefore, we decided to apply our approach to this system for a larger impact and an opportunity to contribute to an experimentally relevant system.
Further, our idea to provide a tight bound on the total EPR by formulating an optimization problem based on the statistics of both transitions and waiting times was completely novel, and it was developed during the course of the work, addressing the challenge of finding an optimal bound that suppresses other approaches.

Problems or delays
Nothing to report.

Expenditure Impacts
Overall, our financial status remains within the anticipated parameters, and we do not foresee any issues in meeting our objectives within the planned budget.

Significant changes in the use or care of human subjects, vertebrate animals and/or biohazards
Our research does not involve human subjects, vertebrate animals, or biohazards. Therefore, there have been no changes, deviations, or unexpected outcomes in this area that would require institutional or agency approvals.

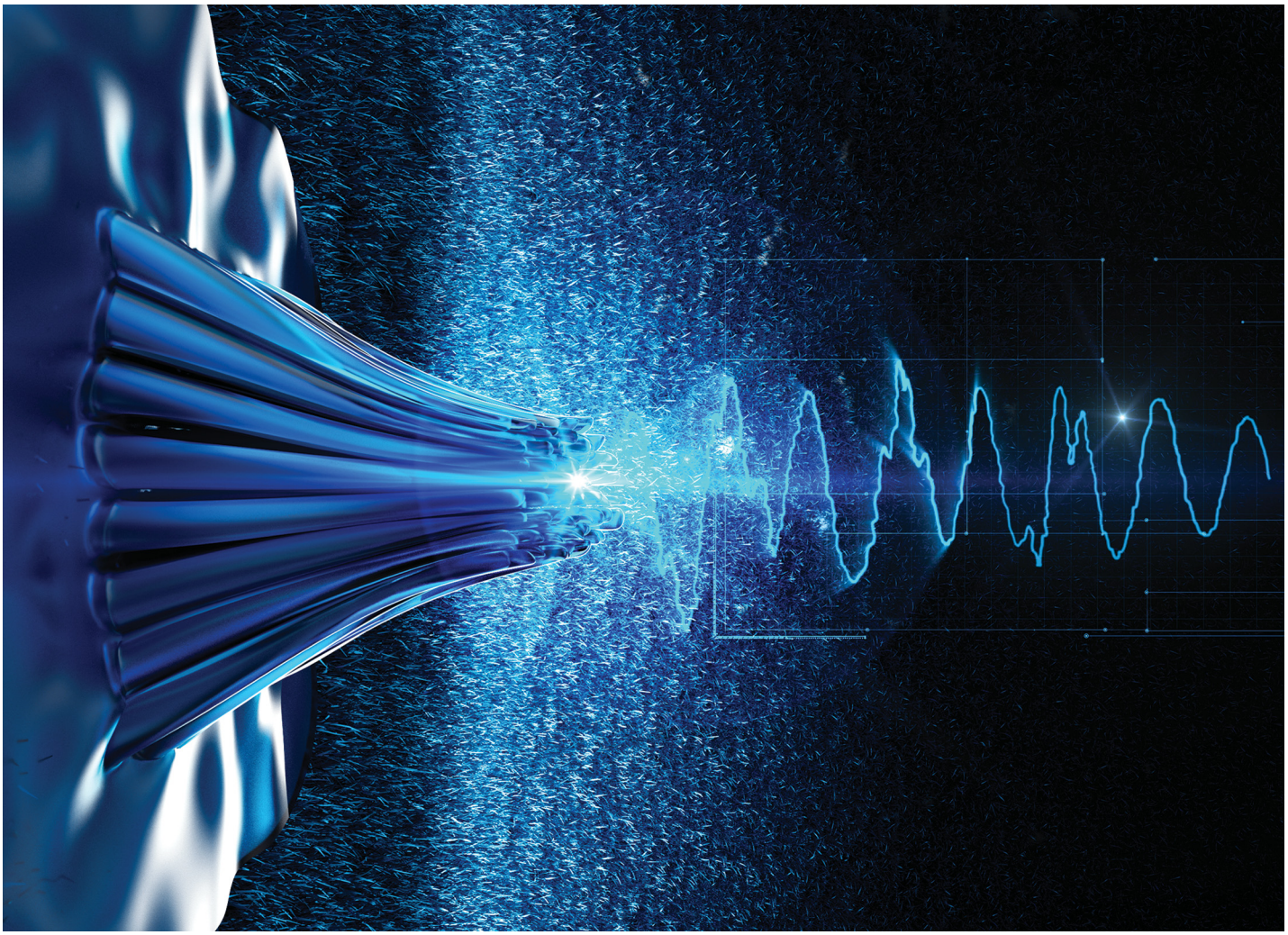
Changes to the primary place of performance from that originally proposed
There has been no change in the primary location of performance. All research activities continue to be conducted as originally planned at Tel Aviv University.

DISTRIBUTION A: Distribution approved for public release.

Technical Updates

The results of the work funded by this project were published or submitted to arXiv, currently under review.
We are including the publications and preprints as technical updates.

DISTRIBUTION A: Distribution approved for public release.



Showcasing research from the group of Prof. Gili Bisker at Tel Aviv University, Israel.

Inferring entropy production rate from partially observed Langevin dynamics under coarse-graining

We estimate a lower bound on the total entropy production rate (EPR) for a system with a single observed variable following Langevin dynamics, coarse-grained into discrete states. As a model system, we use hair-cell bundle oscillations, driven by molecular motors, such that the bundle tip position is observed, but the positions of the motors are hidden. We invoke the underlying broken time-reversal symmetry embedded in waiting time distributions of the partially observed system to calculate a lower bound on the total EPR.

As featured in:



See Aishani Ghosal and Gili Bisker, *Phys. Chem. Chem. Phys.*, 2022, **24**, 24021.

ROYAL SOCIETY OF CHEMISTRY

rsc.li/pccp

Registered charity number: 207890

DISTRIBUTION A: Distribution approved for public release.

PCCP

PAPER

Check for updates

Cite this: *Phys. Chem. Chem. Phys.*, 2022, **24**, 24021

Inferring entropy production rate from partially observed Langevin dynamics under coarse-graining†

Aishani Ghosal[a] and Gili Bisker*[abcd]

Received 6th July 2022,
Accepted 25th August 2022

DOI: 10.1039/d2cp03064k

rsc.li/pccp

The entropy production rate (EPR) measures time-irreversibility in systems operating far from equilibrium. The challenge in estimating the EPR for a continuous variable system is the finite spatiotemporal resolution and the limited accessibility to all of the nonequilibrium degrees of freedom. Here, we estimate the irreversibility in partially observed systems following oscillatory dynamics governed by coupled overdamped Langevin equations. We coarse-grain an observed variable of a nonequilibrium driven system into a few discrete states and estimate a lower bound on the total EPR. As a model system, we use hair-cell bundle oscillations driven by molecular motors, such that the bundle tip position is observed, but the positions of the motors are hidden. In the observed variable space, the underlying driven process exhibits second-order semi-Markov statistics. The waiting time distributions (WTD), associated with transitions among the coarse-grained states, are non-exponential and convey the information on the broken time-reversal symmetry. By invoking the underlying time-irreversibility, we calculate a lower bound on the total EPR from the Kullback–Leibler divergence (KLD) between WTD. We show that the mean dwell-time asymmetry factor – the ratio between the mean dwell-times along the forward direction and the backward direction, can qualitatively measure the degree of broken time reversal symmetry and increases with finer spatial resolution. Finally, we apply our methodology to a continuous-time discrete Markov chain model, coarse-grained into a linear system exhibiting second-order semi-Markovian statistics, and demonstrate the estimation of a lower bound on the total EPR from irreversibility manifested only in the WTD.

1 Introduction

Irreversible processes in living systems lead to the production of entropy, which is a measure of energy dissipation and a signature of the arrow of time.[1–5] Quantifying the entropy production can shed light on the underlying nonequilibrium dynamics and provide insights into the thermodynamic burden of biological processes.[6–8] There are primarily two methods to infer that a system is out-of-equilibrium: (i) invasive methods,[9–12] and (ii) non-invasive[13–16] methods. In invasive methods, the system's response to a perturbation is measured following an external manipulation, and the violation of the fluctuation–dissipation theorem (FDT)[9,17–22] confirms the nonequilibrium nature of the underlying process. On the other hand, non-invasive methods do not require a direct perturbation to a system, and can detect the nonequilibrium nature of the process from various system properties, such as broken time-reversal symmetry,[23,24] presence of net probability current of observables,[7,13,16,25–29] or asymmetric probability density function (PDF) of the timing of maximal observable values.[30]

One can estimate the EPR for discrete[31] and continuous systems[32–34] given that all out-of-equilibrium system variables are accessible; otherwise, the EPR estimation becomes challenging,[35–39] and the best estimate would be a lower bound on the total EPR value. Several studies focused on the fluctuations of the EPR calculated from partial information.[40–48] The mathematical relations that bound the EPR using the fluctuations of time asymmetric and generic variables are known as the thermodynamic uncertainty relation (TUR)[49–54] and kinetic uncertainty relation (KUR),[55] respectively. These relations have also been generalized for semi-Markov processes.[56,57] Recently, a unified relation considering both thermodynamic and kinetic quantities has been proposed.[58–60] For systems with partial information,

[a] *Department of Biomedical Engineering, Tel Aviv University, Tel Aviv 6997801, Israel. E-mail: bisker@tauex.tau.ac.il*
[b] *Center for Physics and Chemistry of Living Systems, Tel-Aviv University, Tel Aviv 6997801, Israel*
[c] *Center for Nanoscience and Nanotechnology, Tel-Aviv University, Tel Aviv 6997801, Israel*
[d] *Center for Light-Matter Interaction, Tel-Aviv University, Tel Aviv 6997801, Israel*

† Electronic supplementary information (ESI) available. See DOI: https://doi.org/10.1039/d2cp03064k

DISTRIBUTION A: Distribution approved for public release.

estimators like the passive partial entropy production[47,61,62] and the informed partial entropy production[61–64] are helpful to get a dissipation bound; however, these fail to provide a tight bound on the total EPR for vanishing net current. These average partial entropy production estimators satisfy fluctuations theorems, and as such, they can be derived as a Kullback–Leibler divergence between the forward trajectory and the backward trajectory under auxiliary dynamics.[61]

The k-variable irreversibility measure is defined as, $\sigma_k \equiv k_B \lim_{t\to\infty} \frac{1}{t} D[P(\Gamma^k \parallel \tilde{\Gamma}^k)]$, where k_B is the Boltzmann constant, $D[p\|q]$ denotes the Kullback–Leibler divergence (KLD)[65,66] between two probability distributions p and q, defined by $D[p \parallel q] = \int \mathrm{d}x p(x) \log(p(x)/q(x))$ and calculated on the positive support.[66] It is a measure of distinguishability[67] between two probability distributions, being non-negative in general and zero for identical distributions. Γ^k denotes the forward path of k nonequilibrium variables for a time duration t, whereas $\tilde{\Gamma}^k$ denotes the corresponding backward path. Owing to the chain-rule of the relative entropy,[68] the more nonequilibrium variables (larger k) included in the path probability measure, the better the KLD bound is, *i.e.*, $0 \le \sigma_1 \le \cdots \le \sigma_k \le \sigma_{k+1} \le \cdots \le \sigma_{\mathrm{tot}}$, where σ_{tot} is the total EPR calculated by the KLD between the forward and reverse trajectories with all the nonequilibrium degrees of freedom.[69,70] Obtaining a tight bound for a continuous variable system using the KLD estimator is challenging since some of the nonequilibrium variables may be inaccessible and sampling the distribution of paths becomes difficult.

In a recent study,[71] Roldan *et al.* transformed the forward and backward time series data of an observed variable of a continuous hair bundle system into two independent and identically distributed time series using a whitening approximation to estimate the KLD from two univariate distributions. They first calculated the EPR bound using only the observed degree of freedom, *i.e.*, the tip position of the hair bundle. Moreover, they used the finite time thermodynamic uncertainty relation to obtain a lower bound on the total EPR using two observables, the tip position and the transduction current, and found a better lower bound on the EPR compared to the one calculated using only one variable, as expected. The EPR estimate calculated with only one observed degree of freedom was typically three orders of magnitude smaller than the total EPR. However, using two observables and the TUR, their measure was three orders of magnitude better than their single-variable result for the oscillatory regime and few fold smaller than the total EPR, but in the quiescent regime, the result was three orders of magnitude smaller than the total EPR.

An estimator based on the KLD between waiting time distributions of the time forward and the time backward transitions between discrete states was shown to provide a lower bound on the total EPR,[64] given that the time-reversal operator does not lead to kinetic hysteresis.[72–75] Applied to a second-order semi-Markov process, this KLD estimator of the EPR breaks into two contributions,[64] the affinity EPR, $\mathrm{EPR}_{\mathrm{aff}}$, which accounts for the net flux and affinity or the thermodynamic force,[68,70] and the waiting-time-distribution (WTD) EPR, $\mathrm{EPR}_{\mathrm{WTD}}$, which accounts for the broken time-reversal symmetry in the waiting time distributions.[64] For second-order semi-Markov processes, which naturally emerge when "lumping" adjacent states,[64,76] the $\mathrm{EPR}_{\mathrm{WTD}}$ can provide a lower bound on the total EPR, even when the system does not have any net current observed and $\mathrm{EPR}_{\mathrm{aff}} = 0$. Describing processes by transitions instead of states,[77] the KLD estimator for the EPR was further applied to waiting times in between observed transitions.[75,78]

Skinner *et al.* presented new estimators to obtain the lower bound on the entropy production rates using optimization techniques.[79,80] They found an estimator given observables characterizing one-step transitions and two successive transitions, whereas in another publication the authors proposed an estimator given the observed waiting time distributions.[80]

There are several studies on the effect of coarse-graining (CG) on the EPR estimation[81–94] specifically discussing whether the CG procedure preserves the EPR fluctuations or not. In a recent study, using a Markovian model of a driven molecular motor, Hartich *et al.* compared different coarse-graining schemes, "milestoning" and "lumping", and found that the "milestoning" method can restore Markovian dynamics in the case of time-scale separation and preserves local detailed balance.[76,86]

The quantitative effect of the coarse-graining on the EPR was estimated in an experimental system of steady-state trajectories of a microtubule length using an optimization procedure of a two-step estimator, where it was demonstrated that increasing the spatial and temporal resolution while coarse-graining leads to an improved EPR bound.[79] Moreover, a recent study by Tan *et al.*[95] has found that the time-irreversibility varies non-monotonically with the lag time, *i.e.*, the time intervals between the position measurements, which determines the dissipation timescale.[95]

Here, we quantify the irreversibility using a non-invasive method to provide a lower bound on the total EPR in a partially observed model system with continuous variables following oscillatory dynamics, where one of its observables is coarse-grained into a few discrete states. We simulate an oscillating hair-bundle model in which the bundle's tip position is experimentally observed, whereas the position of the molecular motor is hidden. The coarse-grained process follows second-order semi-Markov statistics in the reduced state space (tip position variable space). In this model, the affinity entropy production contribution vanishes; therefore, the irreversibility information can only be accessed from the asymmetries of the waiting time distributions of the forward and the reversed transitions. After the decimation, we exploit the underlying broken time-reversal symmetry stemming from the difference in the PDFs of the waiting times for the upward and the corresponding downward transitions among different coarse-grained states, to calculate the EPR bound, $\mathrm{EPR}_{\mathrm{WTD}}$, by applying the KLD estimator. We show that the ratio of the means of the dwell time PDFs of the forward and reverse trajectories, termed the mean dwell-time asymmetry factor, can qualitatively detect the broken time reversal symmetry, and its variation with the number of coarse-grained states is studied. We further calculate

 This journal is © the Owner Societies 2022

DISTRIBUTION A: Distribution approved for public release.

the ratio between the EPR_{WTD} and the total EPR as a function of the number of coarse-grained states to evaluate the tightness of the lower bound, and find that with finer resolution (larger number of coarse-grained states), the EPR_{WTD} provides a better lower bound on the dissipation rate.

The paper is organized as follows. First, we introduce the model system and outline the calculation of the total EPR. Then, we describe our coarse-graining procedure, second-order semi-Markovian dynamics of the coarse-grained system, different contributions to the EPR, and mean dwell-time asymmetry factor in the next section. Subsequently, the effect of coarse-graining on the broken time-reversal symmetry, the EPR estimate, and the tightness of the lower bound as a function of the number of coarse-grained states are discussed. Finally, we summarize and provide a future outlook.

2 Model system

We estimate the entropy production rate in a partially observed system described by a Langevin equation. To do so, we consider a model which captures the experimental observation of spontaneous oscillations of mechanosensory hair bundles of auditory hair cells.[71,96–100] These oscillations help to amplify the sound stimuli in the ear of vertebrates, and provide sensitivity and frequency selectivity. Moreover, these oscillations are known as ''active'' oscillations, and they are distinct from ''passive'' oscillations that are obtained by blocking the corresponding transduction ion channels.[71] The activity originates from various molecular motors, which cannot be experimentally accessed. However, another degree of freedom coupled to the activity of the molecular motors – the tip position of the hair bundle (X_1) is experimentally observed. Due to the presence of activity, the system is out-of-equilibrium, and its dynamics is governed both by a conservative force $V(X_1,X_2)$, where X_2 represents the position of the center of mass of the molecular motors, and a non-conservative driving force, $F_{act}(X_1,X_2)$. The system can be described by the following coupled stochastic differential equations.[71,96–98]

$$\lambda_1 \dot{X}_1 = -\frac{\partial V(X_1,X_2)}{\partial X_1} + \sqrt{2k_B T \lambda_1}\xi_1 \quad (1)$$

$$\lambda_2 \dot{X}_2 = -\frac{\partial V(X_1,X_2)}{\partial X_2} - F_{act}(X_1,X_2) + \sqrt{2k_B T_{eff} \lambda_2}\xi_2 \quad (2)$$

where λ_1 and λ_2 are the friction coefficients of the hair bundle tip and the molecular motor, respectively, T and T_{eff} are the environment temperature and the effective temperature characterizing the motor fluctuations, respectively, with ratio $T_{eff}/T > 1$. ξ_1 and ξ_2 are two independent white noise terms with zero-mean and correlation $\langle \xi_i(t)\xi_j(t')\rangle = \delta_{ij}\delta(t-t')$, and k_B is the Boltzmann constant. The functional form of the conservative force, $V(X_1,X_2)$, which is proportional to the difference between the positions of the coupled variables,[96–98] is:

$$V(X_1,X_2) = \frac{k_{gs}\Delta X^2 + k_{sp}X_1^2}{2} - Nk_B T \ln\left[e^{\left(\frac{k_{gs}D\Delta X}{Nk_B T}\right)} + A\right] \quad (3)$$

where k_{gs} and k_{sp} are the stiffness coefficients, $\Delta X = X_1 - X_2$ is the separation between the position of the hair bundle and the molecular motors, D is the gating swing, and N is the number of transduction channels. $A = \exp[(\Delta G + (k_{gs}D^2)/2N)/(k_B T)]$, and ΔG is the energy difference between the open and closed states of the ion channel. The active non-conservative force exerted by the molecular motors is defined by $F_{act}(X_1,X_2) = F_{max}(1 - SP_0(X_1,X_2))$. The probability of the transduction channel being open is $P_0(X_1,X_2)$, and is defined by $P_0(X_1,X_2) = 1/[1 + A\exp(-k_{gs}D\Delta X/Nk_B T)]$. The non-conservative force depends on the maximum motor force acting on the system (F_{max}), and the calcium-mediated feedback strength (S). The main sources of the non-equilibrium drive come from the ratio T_{eff}/T being greater than unity, and the maximal force (F_{max}) exerted by the molecular motors. This model[71,96–98] was shown to agree well with experimental results.

First, we numerically solve the coupled differential equations (eqn (1) and (2)) for a fixed ratio between the effective temperature and the temperature of the environment ($T_{eff}/T = 1.5$), and different values of S (0.5, 1, 1.5) and F_{max} (70 pN, 80 pN, 90 pN) to obtain simulated trajectories of the hair bundle tip position and the motor position (see Fig. 1 for details on all the parameters used). Although there is clearly a directional current in the X_1–X_2 plane (Fig. 1a) manifesting the nonequilibrium nature of the process, its signature is not obviously present in the trajectories of X_1 or X_2 as a function of time, which oscillate

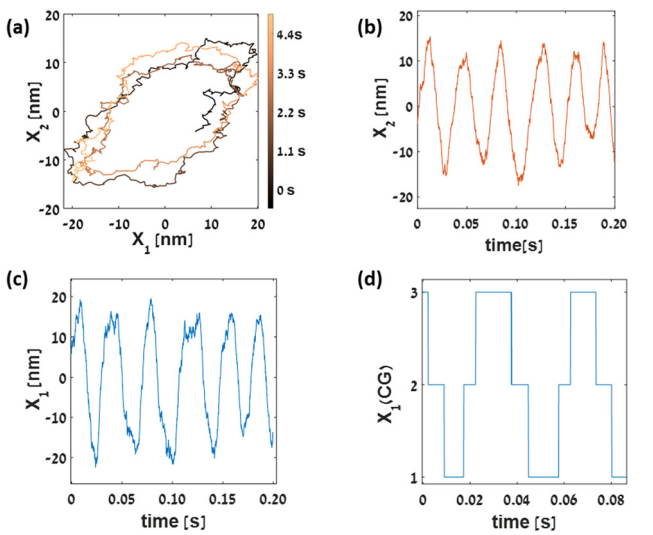


Fig. 1 Simulated trajectories of the observed (X_1, the tip position of the hair bundle) and the hidden (X_2, the position of the molecular motors) variables and the coarse-grained trajectory of the observed variable after spatial coarse-graining (a) the trajectories in the X_1–X_2 plane for fixed values of driving parameters: (F_{max} = 70 pN, S = 1, T_{eff}/T = 1.5). The color of the curve represents time going from dark to bright (b) $X_2 = X_2 - \langle X_2\rangle$, as a function of time for fixed values of driving (F_{max} = 70 pN, S = 1, T_{eff}/T = 1.5). (c) $X_1 = X_1 - \langle X_1\rangle$, as a function of time for the same values of driving parameters, which does not show any sign of net flux, (d) the coarse-grained trajectory for 3 CG states at above mentioned parameter values. All the quantities plotted are calculated for the following additional parameter values: λ_1 = 2.8 pN ms nm^{-1}, λ_2 = 10 pN ms nm^{-1}, k_{gs} = 0.75 pN nm^{-1}, k_{sp} = 0.6 pN nm^{-1}, D = 61 nm, $k_B T$ = 4 pN nm, $\Delta G = 10k_B T$.

DISTRIBUTION A: Distribution approved for public release.

around their respective mean values (as shown in Fig. 1b and c) for a particular set of the driving parameter values, and ESI,† Fig. S1 for additional realizations with different parameters).

As the system is driven out-of-equilibrium by the non-conservative force and the effective temperature, there is a positive dissipation rate. The total entropy production rate can be calculated from the forces and their conjugated currents:[71,101]

$$\mathrm{EPR}_{\mathrm{tot}} = -\langle \dot{Q}_1 \rangle \left(\frac{1}{T} - \frac{1}{T_{\mathrm{eff}}} \right) + \frac{\langle \dot{W}_{\mathrm{act}} \rangle}{T_{\mathrm{eff}}} \tag{4}$$

where $\langle \cdots \rangle$ represents the steady state average. The steady state rate of the dissipated heat to the reservoir at temperature T is $\langle \dot{Q}_1 \rangle = \langle (\partial V/\partial X_1) \circ \dot{X}_1 \rangle$, with $\circ$ being the Stratonovich product, and $\langle \dot{W}_{\mathrm{act}} \rangle = -\langle F_{\mathrm{act}} \circ \dot{X}_2 \rangle$ is the rate of work done by the active force.

3 Coarse-graining, lower bound on the total entropy production rate, and the mean dwell-time asymmetry factor

We used two approaches for spatial coarse-graining to discretize the continuous variable space (the trajectories of the tip position of the hair bundle, X_1) into discrete states: (i) dividing the continuous variable space equally into N (N = 3, 4, 5, 6, 7) coarse-grained states with the ratios 1 : 1 : 1, 1 : 1 : 1 : 1, 1 : 1 : 1 : 1 : 1, 1 : 1 : 1 : 1 : 1 : 1, and 1 : 1 : 1 : 1 : 1 : 1 : 1, respectively. This type of equal coarse-graining is only possible for a smooth trajectory for a particular choice of the driving parameter values (Fig. S1, ESI,† *e.g.* $F_{\max}$ = 70 pN, S = 1, and $F_{\max}$ = 80 pN, S = 1), (ii) diving the continuous variable space into unequal division, where N (N = 3, 4, 5, 6, 7) coarse-grained states correspond to dividing the trajectory with the ratios $1:1:1$, $1:\frac{1}{2}:\frac{1}{2}:1$, $1:\frac{1}{3}:\frac{1}{3}:\frac{1}{3}:1$, $1:\frac{1}{4}:\frac{1}{4}:\frac{1}{4}:\frac{1}{4}:1$, and $1:\frac{1}{5}:\frac{1}{5}:\frac{1}{5}:\frac{1}{5}:\frac{1}{5}:1$, respectively, as shown schematically in Fig. S2 of the ESI.† This type of coarse-graining is better suited to track the irregular oscillations of the tip of the hair cell bundle for driving parameter values $F_{\max}$ = 90 pN, S = 1, and $F_{\max}$ = 80 pN, S = 1.5, *etc.* (see ESI,† Fig. S1).

We have two layers of coarse-graining: (I) one of the dynamical variables describing the system is decimated (in our example, the tip position of the hair bundle is observed, but the positions of the molecular motor are hidden) (II) we further coarse-grained the observed variable into a few discrete states.

Our system is coarse-grained such that the topology of the coarse-grained system is linear, without any cycles. The probability for a transition between the neighbouring states is non-zero, but the transition probability from one boundary state to the other boundary state is zero, and *vice versa*. For example, in a 3 coarse-grained system (N = 3, 1 : 1 : 1 spatial division), the probabilities of jumping from macro-state 2 to state 3 or 1 are both non-zero, whereas given the system is in state 1, the probability of finding it in state 3 in the next jump is zero, and *vice versa*. The waiting time distribution of the dwell time at state 2 depends, however, on the state visited before, whether it was state 3 or state 1, rendering the process a second order Markov process. Thus, we consider states composed of the current state, i, and previous state, j, *i.e.*, $[i,j]$ when applying the KLD estimator. Similarly, the approach can be generalized to higher order semi-Markov processes.

Estimating dissipation is non-trivial in the absence of the observable currents or flows, but as dissipated systems exhibit broken time-reversal symmetry, time irreversibility can be exploited to infer the out-of-equilibrium nature of the underlying process from the time series.[64] Martínez *et al.* developed an estimator based on the waiting time distributions containing information about irreversibility in hidden states even in the absence of visible transitions among the observed states. They applied the technique[64] for a partially hidden network where a subset of states are hidden, and a molecular motor system where the internal states are unresolved. In both cases, their estimator is able to predict a non-zero bound on the entropy production rate at the stalling driving force (the driving parameter value at which the current between the observed states vanishes).

To estimate the lower bound of the irreversibility, we use the KLD estimator,[101,102] which relies on the broken time-reversal symmetry of the underlying waiting-time distributions.[64] Due to the presence of coupled hidden degrees of freedom, the jump process in the observed variable space becomes a second-order[64] semi-Markov. The jump probability depends on the previous state, the time since the last jump, and the final state. The last two conditions make the system direction-time dependent,[91] which means that the joint distribution of times and transitions ($\psi_{nn'}(t)$) cannot be written as a product of the probability distribution for a transition ($\Phi_{nn'}$) and the probability distribution of the time t the system waits at the initial state n ($\psi_n(t)$). As proved earlier,[64] the KLD estimator of the EPR for a second-order semi-Markov process consists of two contributions: the affinity EPR ($\mathrm{EPR}_{\mathrm{aff}}$) and the waiting-time-distribution EPR ($\mathrm{EPR}_{\mathrm{WTD}}$). $\mathrm{EPR}_{\mathrm{aff}}$ accounts for the net current and the thermodynamic force of the system. It is sometimes called the "equivalent dissipation".[91] A non-Markovian system and its memoryless counterpart – a system with the same network topology generating a Markovian sequence of states – have the same expression, but, the rate constants are replaced with the effective rate constants for the non-Markovian system. The affinity EPR is written as

$$\mathrm{EPR}_{\mathrm{aff}} = \frac{1}{\tau} \sum_{ijk} p(ijk) \ln \frac{p([ij] \to [jk])}{p([kj] \to [ji])} \tag{5}$$

where $p(ijk) = R_{[ij]} p([ij] \to [jk])$ is the probability to observe the sequence $i \to j \to k$. $R_{[ij]}$ denotes the normalized occupancy probability at the CG state j given the previous CG state was i. The numerator and the denominator of the argument of the logarithmic function are of the form $p([ij] \to [jk])$, which denotes the probability that the system makes a transition from a CG state j to a CG state k, given that the previous CG state was i. τ is the mean step duration given by $\tau = \sum_{ij} R_{[i,j]} \tau_{[i,j]}$, where $\tau_{[i,j]}$ is the mean time the system spends at a CG state j,

 This journal is © the Owner Societies 2022

DISTRIBUTION A: Distribution approved for public release.

given that the previous CG state was i. The sum is performed over all CG states (i,j, and k). For the active hair bundle system, there is no contribution to the EPR from the affinity EPR, since the coarse-grained system is a linear chain of states.

The other component of the KLD estimator comes from the broken time-reversal symmetry in the waiting-time distributions, and is obtained using the following equation:

$$\mathrm{EPR}_{\mathrm{WTD}} = \frac{1}{\tau}\sum_{ijk} p(ijk) D[\Psi(t|ijk) \parallel \Psi(t|kji)] \qquad (6)$$

where $\Psi(t|ijk)$ denotes the probability density function of the time t the system spends at a CG state j before jumping to another CG state k, given that the previous CG state was i, *i.e.*, for $i \to j \to k$ transition. The WTD estimator, $\mathrm{EPR}_{\mathrm{WTD}}$, or the "memory dissipation",[91] is the additional contribution that only exists for non-Markovian systems in contrast to their memoryless Markovian counterpart. It was shown that a semi-Markov process results in non-exponential waiting time distributions,[103] which is related to memory.[91]

Since there is no net current in the observed variable space, the position of the hair-bundle tip, X_1, we use the KLD estimator[64] to calculate a lower bound on the total EPR. In order to apply this estimator, which was developed for discrete states, to a continuous variable system, we coarse-grain the observed variable into a few discrete states (a realization of 3 CG states is shown in Fig. 1d), from which the lower bound is estimated by $\mathrm{EPR}_{\mathrm{WTD}}$, and study how the bound varies as a function of the number of coarse-grained states.

In order to demonstrate that a lower bound on the total EPR can be inferred from the WTD asymmetry in a system with second-order Markov process statistics with a linear topology having zero net current, we use a simple 6-state (i = 1, 2, 3 and i' = 1′, 2′, 3′, where states i and i' are indistinguishable) continuous-time Markov chain (CTMC) model coarse-grained into a 3-state linear continuous-time second-order semi-Markov system (observed states 1″, 2″, 3″) as shown in Fig. 2a. The net current in the 6-state model mimics the net current in the X_1–X_2 plane of the active hair bundle model Fig. 1a, whereas the coarse-grained 3-state system resembles the coarse-grained, observed hair-bundle position, X_1. We simulated trajectories using the Gillespie algorithm[104] for 10^8 steps, where after the decimation, we were left with approximately 10^6 jumps. Fig. 2b shows the difference in the distribution of the times the system waits at state 2″ for an upward transition (1″ → 2″ → 3″) and the corresponding downward transition (3″ → 2″ → 1″). The non-exponential distribution originates from the non-Markovian statistics of the coarse-grained trajectory, whereas the difference between the distributions of the upward and downward waiting times originates from the nonequilibrium nature of the process.[64] Therefore, we can measure the irreversibility from the Kullback–Leibler divergence between the waiting time probability density functions $\mathrm{EPR}_{\mathrm{WTD}}$, for the coarse-grained system with zero $\mathrm{EPR}_{\mathrm{aff}}$ to provide a lower bound on the total EPR.

For example, the waiting time distributions for the hair bundle system at equilibrium ($F_{\max}$ = 0 pN, T = T_{eff}) and at nonequilibrium conditions driven according to eqn (1) and (2) are shown in Fig. 3a and b, respectively. The distinguishability between the two WTD in the latter case (b), results in a positive KLD, which bounds the total EPR. The estimation of the $\mathrm{EPR}_{\mathrm{WTD}}$ improves with increasing the number of simulation steps (Fig. 3c) as evident from the decreasing error and the plateauing of the estimation value for the active hair bundle model governed by eqn (1) and (2).[64]

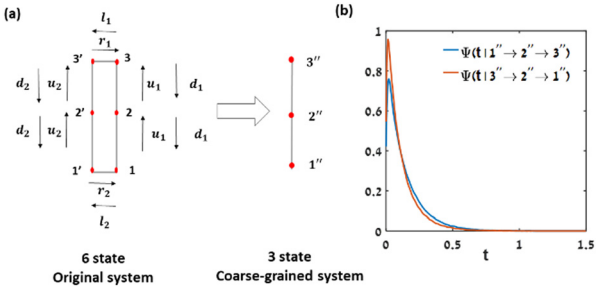


Fig. 2 The $X_1 - X_2$ trajectory of the hair bundle system coarse-grained into a linear topology in X_1 state space after decimation of the X_2 states with zero net flux motivates to use KLD estimator of the waiting times (t [s]): (a) The circles with the lines represents a 6 state system, which after decimation is reduced to a linear 3 state system, (b) non-zero contribution from the Kullback–Leibler divergence of the waiting time distributions: the distribution of the waiting times (t [s]) the system waits at CG state 2″ for an (1″ → 2″ → 3″) upward transition (blue solid line) and (3″ → 2″ → 1″) the downward transition (red solid line) for the following parameter values: u_1 = 10, u_2 = 3, d_1 = 2, d_2 = 4, r_1 = 3, r_2 = 3, l_1 = 1, l_2 = 1.

The unimodal nature of the waiting time distributions also refers to the underlying network topology. If a network has internal cycles, the densities could exhibit multimodal behaviour.[75] For a second-order semi-Markov process, the waiting time distributions are direction-time dependent. Thus, the mean dwell-times that the system spends at a particular state for the forward and the reverse transitions are not necessarily identical, and a deviation of their ratio from one provides information regarding the irreversible nature of the process.[80] We calculate the mean dwell-time asymmetry factor (MDAF), *i.e.*, the ratio between the means of the dwell time distributions ($\langle\tau_{k\to j\to i}\rangle$ or $\langle\tau_{kji}\rangle$) of times spent at

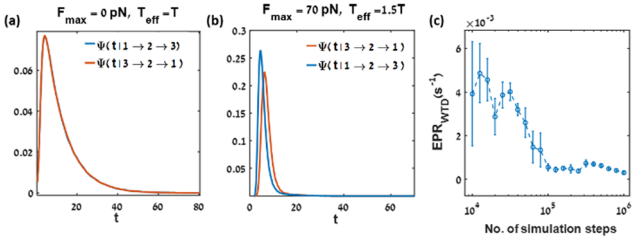


Fig. 3 Entropy production rate estimation from the Kullback–Leibler divergence between the waiting time distributions for 3 equally spaced coarse-grained states of the active hair bundle's tip position: probability density functions of the time (t [s]) that the system stays at state 2 for an upward transition (blue solid line), and for a downward transition (red solid line) for two different parameter values: (a) $F_{\max}$ = 0 pN, T_{eff} = T, and S = 1.5, (b) $F_{\max}$ = 70 pN, T_{eff} = 1.5 T, and S = 1.5, (c) $\mathrm{EPR}_{\mathrm{WTD}}$ as a function of length of the simulation for $F_{\max}$ = 70 pN, T_{eff}/T = 1.5, and S = 1.5. The error bar at each point describes the standard error of the mean.

DISTRIBUTION A: Distribution approved for public release.

a CG state j before transitioning to i, given that it arrived from k, $k \to j \to i$, to the mean time the system spends at a CG state j for a $i \to j \to k$ transition, ($\langle \tau_{i\to j\to k} \rangle$ or $\langle \tau_{ijk} \rangle$). The ratio between the mean times the system spends at a particular state before transitioning to another state and the mean times along the opposite direction ($\langle \tau_{kji} \rangle / \langle \tau_{ijk} \rangle$) being not equal to unity indicates a broken time-reversal symmetry in the system. To obtain the total MDAF for a system with N coarse-grained states, we average the individual MDAF of different transitions among the N coarse-grained states. Therefore, the total MDAF equals $N^{-1} \sum \langle \tau_{kji} \rangle / \langle \tau_{ijk} \rangle$. The ratios stemming from the transitions among different coarse-grained states are plotted in the ESI† (Fig. S3).

In the following, we calculate the contribution of the $\mathrm{EPR_{WTD}}$ from eqn (6), and the effect of coarse-graining on the EPR and the MDAF, or the time-reversal symmetry breaking.

4 Effect of coarse-graining on the entropy production rate estimation and mean dwell-time asymmetry factor

We exploit the time-reversal symmetry breaking in the coarse-grained system to estimate the EPR. Since the affinity EPR vanishes, the signature of the irreversibility can only be tracked from the KLD between waiting time distributions, $\mathrm{EPR_{WTD}}$.

First, The EPR estimate ($\mathrm{EPR_{WTD}}$) values are calculated using eqn (6) by coarse-graining the X_1 variable into N CG states (where N = 3, 4, 5, 6, 7) by equal partitioning of the state space, and plotted as a function of N (Fig. 4a), for $F_{\max}$ = 70 pN, S = 1, and T_{eff}/T = 1.5. The lower bound on the EPR estimate is improved with increasing resolution. The maximal value of $\mathrm{EPR_{WTD}}/\mathrm{EPR_{tot}}$ = 0.0013 at 7 coarse-grained states. Moreover, the MDAF is plotted as a function of the number of the coarse-grained states (Fig. 4b).

Next, we calculate the $\mathrm{EPR_{WTD}}$ for several driving parameter values ($F_{\max}$ = 70 pN, $F_{\max}$ = 80 pN, $F_{\max}$ = 90 pN, and S = 0.5, 1, 1.5) and for unequal spatial spacing of the coarse-grained states (N = 3, 4, 5, 6, 7). Both the estimate of the EPR (Fig. 5a) and the mean dwell-time asymmetry factor (Fig. 5b) increase with increasing spatial resolution. Indeed, the EPR estimate is correlated with the MDAF (Fig. 5c), which is related to the non-Markovian nature of the process and the memory involved.[105]

As we mentioned, $\mathrm{EPR_{WTD}}$ was calculated for equal (Fig. 4) and unequal (Fig. 5) partitioning of the observed trajectory. For certain driving parameter values at which the trajectories are not that smooth or regular. In that case, the equal partition of the trajectory space of the observed variable would lack enough statistics for the boundary states in the time series. Therefore, we consider unequal spatial partitioning of the trajectory.

To assess the tightness of the bound, we compare the ratio between $\mathrm{EPR_{WTD}}$ estimates and the total EPR ($\mathrm{EPR_{tot}}$) calculated for different driving parameter values, $F_{\max}$ = 70 pN, 80 pN, 90 pN, S = 0.5, 1, 1.5, and for different coarse-graining levels (Fig. 6), and find that the tightest bounds is obtained for 7 CG states (N = 7), where the $\mathrm{EPR_{WTD}}$ values are between 1 to 2 orders of magnitude smaller than the total EPR (Fig. 6). The tightness of the bounds for unequal partitioning for 7 CG states are given in Table S1 of ESI.†

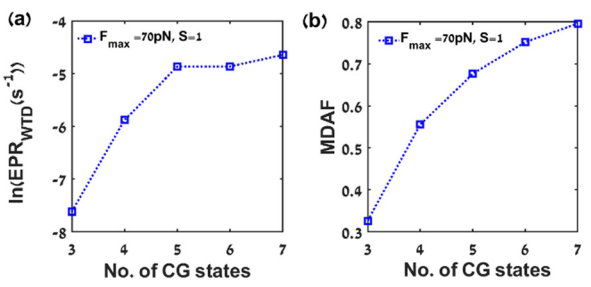


Fig. 4 Entropy production rate estimation and the mean dwell-time asymmetry factor (MDAF) for equal spacing coarse-graining of X_1 trajectory: (a) $\mathrm{EPR_{WTD}}$ ($\mathrm{s^{-1}}$) (WTD estimate of the EPR) as a function of the number of CG states with equal spacing for parameter values $F_{\max}$ = 70 pN, S = 1, and T_{eff}/T = 1.5 (b) MDAF (mean dwell-time asymmetry factor) as a function of the number of CG states. The other parameter values are the same as mentioned in Fig. 1. The lines are drawn to as a guide to the eye. The total EPR for this set of parameter values is 7.3312 $\mathrm{s^{-1}}$.

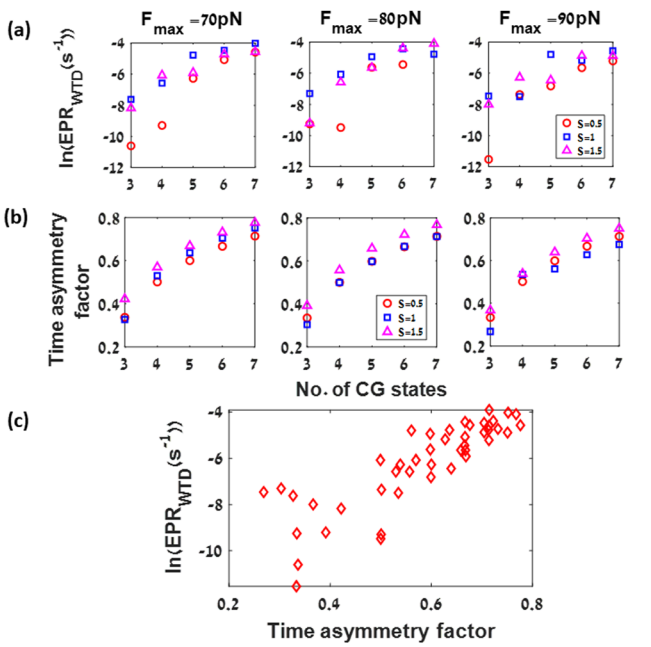


Fig. 5 Effect of coarse-graining on the $\mathrm{EPR_{WTD}}$ ($\mathrm{s^{-1}}$) and the mean dwell-time asymmetry factor (MDAF): (a) $\mathrm{EPR_{WTD}}$ ($\mathrm{s^{-1}}$) as a function of number of CG states (3 CG: 1 : 1 : 1, 4 CG: 1 : 1/2 : 1/2 : 1, 5 CG: 1 : 1/3 : 1/3 : 1/3 : 1, 6CG: 1 : 1/4 : 1/4 : 1/4 : 1/4 : 1, and 7CG: 1 : 1/5 : 1/5 : 1/5 : 1/5 : 1/5 : 1) for different parameter values, (left) $F_{\max}$ = 70 pN for S = 0.5, 1, 1.5, (middle) $F_{\max}$ = 80 pN for S = 0.5, 1, 1.5, and (right) $F_{\max}$ = 90 pN, S = 0.5, 1, 1.5. (b) The MDAF as a function of number of CG states for different parameter values: (left) $F_{\max}$ = 70 pN, S = 0.5, 1, 1.5; (middle) $F_{\max}$ = 80 pN, S = 0.5, 1, 1.5; (right) $F_{\max}$ = 90 pN, S = 0.5, 1, 1.5. In both panels: red circle symbols correspond to S = 0.5, blue square symbols correspond to S = 1, and magenta triangle symbols correspond to S = 1.5. (c) The values of $\mathrm{EPR_{WTD}}$ as a function of the MDAF for all transitions and all parameter values as mentioned earlier. The other parameter values used in these figures are mentioned in Fig. 1.

This journal is © the Owner Societies 2022
DISTRIBUTION A: Distribution approved for public release.

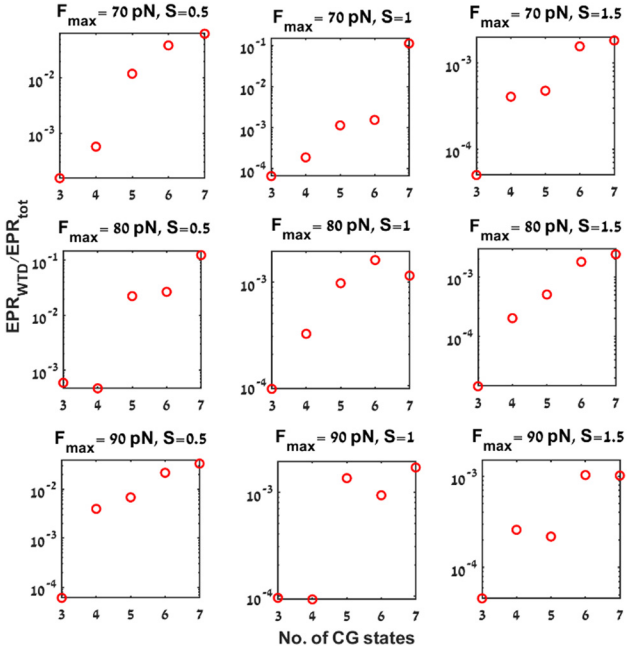


Fig. 6 Tightness of the EPR bound (EPR_{WTD}) as a function of number of CG states: ratio between the EPR estimates from the waiting time distribution (EPR_{WTD} (s^{-1})) and the total entropy production rate (EPR_{tot} (s^{-1})) for different parameter values. The coarse-graining corresponds to unequal divisions of the X_1 state space. The parameter values are F_{max} = 70 pN, S = 0.5, 1, 1.5 (upper row), F_{max} = 80 pN, S = 0.5, 1, 1.5 (middle row), F_{max} = 90 pN, S = 0.5, 1, 1.5 (lower row). The other parameter values used in this figure are as mentioned in Fig. 1.

5 Discussion

Most of the previous studies on partially observed systems were performed on Markov chains where some nodes are observed, and the rest are either traced out or lumped together into a hidden state. These processes are performed with the constraints of preserving different quantities (depending on the applied coarse-graining method) like the transition flux among the observed states[93] or preserving the mean value and fluctuations of the entropy production rate at stationary state[87] before and after the coarse-graining. In this paper, we have discussed a different partially observed system where one of the coupled variables following the Langevin dynamics is observed experimentally, and the other is hidden. In addition, we have two layers of coarse-graining, where we preserve the equilibrium density of a particular state before and after the coarse-graining, but due to the linear topology, it cannot support current; therefore, it loses the net current of the original system. We have shown the benefit of using the waiting time distributions in estimating the dissipation rate using the hair bundle cell oscillations as an example. If the edge current vanishes in the observed states, the waiting time distributions may capture the broken time-reversal symmetry in the case of driven systems, depending on the network topology. We infer the irreversibility of the dynamics by coarse-graining the observed system variable into a few discrete states and applying the KLD estimator.[64] The coarse-grained linear system considered in our study is not Markovian, but rather a second-order semi-Markov system, and the breaking of time-reversal symmetry is manifested in the KLD between the non-exponential waiting time distributions of the forward and the reversed transitions among different coarse-grained states.[64] We show that instead of using the full probability distributions, the first cumulants of the dwell time distributions (easier to obtain in experimental scenarios), already provide predictions for the broken time-reversal symmetry and the dissipation rates. This quantity is much easier to quantify, both experimentally and theoretically, serving as a straightforward footprint for time-irreversibility. We further study the mean dwell time asymmetry factor variation with the number of the coarse-grained states.

Berezhkovskii *et al.*[105–108] discussed the case of low-resolution experimental observables in nonequilibrium systems, where the non-Markovian dynamics breaks time-reversal symmetry manifested in differences in the forward and backward waiting times. As suggested by several studies,[105–108] the time asymmetry in the active hair bundle system arises when the following two conditions hold: (i) the reduced variable system follows non-Markovian statistics, and (ii) the system is out-of-equilibrium. Using a 6-state CTMC model which is coarse-grained into a linear 3-state system (Fig. 2), (mimicking the hair cell bundle system with one degree of freedom is decimated), we demonstrate that the resulting waiting time distributions calculated by the Gillespie algorithm[104] show characteristics of second-order semi-Markov statistics, and break time-reversal symmetry under nonequilibrium driving, and thus KLD estimator would be the good choice for the estimation of the EPR. The 6-state network decimated into 3 states mimics the coarse-graining of the X_1 trajectory into 3 coarse-grained states (Fig. 1d), in which a fundamental cycle is lost, and the contribution of the EPR_{aff} vanishes. Indeed, we infer a lower bound on the total EPR, which can be calculated from the KLD between the distributions.

We calculate EPR estimates (EPR_{WTD}) of the continuous-space model system, an oscillating hair cell bundle, after coarse-graining the observed X_1 trajectory to equal (Fig. 4a) and unequal (Fig. 5a) spatial divisions. Comparing the results for a particular set of parameter values, F_{max} = 70 pN, S = 1, and T_{eff}/T = 1.5, for which the trajectory is rather smooth and regular (see ESI,† Fig. S1). For the equal and unequal coarse-graining, the lower bounds on the total EPR (*i.e.*, EPR_{WTD}/EPR_{tot}) are 0.0013, and 0.0024, respectively at parameter values F_{max} = 70 pN, S = 1, and T_{eff}/T = 1.5.

The tightness of the lower bounds on the total EPR, *i.e.*, EPR_{WTD}/EPR_{tot}, is found to be 0.0013 for equal spatial division (Fig. 4a) for N = 7 CG state at parameter value F_{max} = 70 pN, S = 1, and T_{eff}/T = 1.5. Whereas, for unequal spatial division (Fig. 6), EPR_{WTD}/EPR_{tot} equals to 0.1244 for N = 7 coarse-grained states at F_{max} = 80 pN, S = 0.5, T_{eff}/T = 1.5, respectively. The similar values of the EPR_{WTD}/EPR_{tot} ratio results from the smooth nature of the X_1 trajectory at the chosen parameter set (as can be seen from Fig. 1c) in contrast to the other parameter values (ESI,† Fig. S1). Equal spatial division for N = 5, 6, 7 coarse-grained states becomes challenging for parameter values that lead to very rugged trajectories due to the lack of statistics for the boundary states.

DISTRIBUTION A: Distribution approved for public release.

The inferred time-irreversibility and the EPR_{WTD} estimate increase with finer spatial resolution, *i.e.*, larger number of CG states. Testing a wide range of parameter values, the EPR_{WTD} is smaller by 1 to 2 orders of magnitude compared to the total ERP for the largest spatial resolution ($N = 7$) considered and unequal spacing of the observed X_1 trajectory, where the tightest bound, $EPR_{WTD}/EPR_{tot} \sim 0.1244$, is obtained for $F_{max} = 80$ pN, $S = 0.5$, and $T_{eff}/T = 1.5$. All the ratios (EPR_{WTD}/EPR_{tot}) for 7 coarse-grained states are listed in Table S1 in the ESI.†

6 Conclusions

In summary, the hair bundle system was used as a model to study the effect of coarse-graining on the lower bound on the total entropy production rate, and the mean dwell-time asymmetry factor. The lower bound on the EPR was estimated using the underlying broken time reversal symmetry induced by the active force for a system with Langevin dynamics and zero net current along the reduced variable space. This approach can be applied to a system following Langevin dynamics with an arbitrary number of observed and hidden states carrying a net flux which vanishes on the observed state-space to quantify the deviation from thermal equilibrium manifested in the irreversibility of the observed degrees of freedom.

Author contributions

A. G. and G. B. designed research, performed research, analysed data, and wrote the paper.

Conflicts of interest

There are no conflicts to declare.

Acknowledgements

G. Bisker acknowledges the Zuckerman STEM Leadership Program, and the Tel Aviv University Center for AI and Data Science (TAD). A. Ghosal acknowledges the support of the Pikovsky Valazzi scholarship. This work was supported by the ERC NanoNonEq 101039127, the Air Force Office of Scientific Research (AFOSR) under award number FA9550-20-1-0426, and by the Army Research Office (ARO) under grant number W911NF-21-1-0101. The views and conclusions contained in this document are those of the authors and should not be interpreted as representing the official policies, either expressed or implied, of the Army Research Office or the U.S. Government.

Notes and references

1 C. Jarzynski, Equalities and Inequalities: Irreversibility and the Second Law of Thermodynamics at the Nanoscale, *Annu. Rev. Condens. Matter Phys.*, 2011, **2**, 329–351.
2 U. Seifert, Stochastic thermodynamics, fluctuation theorems and molecular machines, *Rep. Prog. Phys.*, 2012, **75**, 126001.
3 U. Lucia, G. Grisolia and A. L. Kuzemsky, Time, irreversibility and entropy production in nonequilibrium systems, *Entropy*, 2020, **22**, 1–12.
4 J. M. R. Parrondo, C. Van Den Broeck and R. Kawai, Entropy production and the arrow of time, *New J. Phys.*, 2009, **11**, 073008.
5 A. Gomez-Marin, J. M. R. Parrondo and C. Van Den Broeck, The 'footprints' of irreversibility, *EPL*, 2008, **82**(5), 50002.
6 C. W. Lynn, E. J. Cornblath, L. Papadopoulos, M. A. Bertolero and D. S. Bassett, Broken detailed balance and entropy production in the human brain, *Proc. Natl. Acad. Sci. U. S. A.*, 2021, **118**, e2109889118.
7 F. S. Gnesotto, F. Mura, J. Gladrow and C. P. Broedersz, Broken detailed balance and non-equilibrium dynamics in living systems: a review, *Rep. Prog. Phys.*, 2018, **81**, 066601.
8 G. Lan, P. Sartori, S. Neumann, V. Sourjik and Y. Tu, The energy-speed-accuracy trade-off in sensory adaptation, *Nat. Phys.*, 2012, **8**, 422–428.
9 J. Prost, J.-F. F. Joanny and J. M. R. R. Parrondo, Generalized fluctuation–dissipation theorem for steady-state systems, *Phys. Rev. Lett.*, 2009, **103**, 1–4.
10 F. Ritort, Nonequilibrium fluctuations in small systems: from physics to biology, *Adv. Chem. Phys.*, 2008, **137**, 31–123.
11 D. Mizuno, C. Tardin, C. F. Schmidt and F. C. MacKintosh, Nonequilibrium mechanics of active cytoskeletal networks, *Science*, 2007, **315**, 370–373.
12 M. Manosas and F. Ritort, Thermodynamic and kinetic aspects of RNA pulling experiments, *Biophys. J.*, 2005, **88**, 3224–3242.
13 C. Battle, C. P. Broedersz, N. Fakhri, V. F. Geyer, J. Howard, C. F. Schmidt and F. C. MacKintosh, Broken detailed balance at mesoscopic scales in active biological systems, *Science*, 2016, **352**, 604–607.
14 S. Muy, A. Kundu and D. Lacoste, Non-invasive estimation of dissipation from non-equilibrium fluctuations in chemical reactions, *J. Chem. Phys.*, 2013, **139**, 124109.
15 B. Lander, J. Mehl, V. Blickle, C. Bechinger and U. Seifert, Noninvasive measurement of dissipation in colloidal systems, *Phys. Rev. E: Stat., Nonlinear, Soft Matter Phys.*, 2012, **86**, 1–4.
16 R. K. P. Zia and B. Schmittmann, Probability currents as principal characteristics in the statistical mechanics of non-equilibrium steady states, *J. Stat. Mech.: Theory Exp.*, 2007, P07012.
17 É. Fodor, W. W. Ahmed, M. Almonacid, M. Bussonnier, N. S. Gov, M. H. Verlhac, T. Betz, P. Visco and F. Van Wijland, Nonequilibrium dissipation in living oocytes, *EPL*, 2016, **116**(3), 30008.
18 É. Fodor, C. Nardini, M. E. Cates, J. Tailleur, P. Visco and F. Van Wijland, How Far from Equilibrium Is Active Matter?, *Phys. Rev. Lett.*, 2016, **117**, 1–6.
19 D. Loi, S. Mossa and L. F. Cugliandolo, Effective temperature of active complex matter, *Soft Matter*, 2011, **7**, 3726–3729.
20 P. Martin, A. J. Hudspeth and F. Jülicher, Comparison of a hair bundle's spontaneous oscillations with its response to mechanical stimulation reveals the underlying active process, *Proc. Natl. Acad. Sci. U. S. A.*, 2001, **98**, 14380–14385.

 This journal is © the Owner Societies 2022

DISTRIBUTION A: Distribution approved for public release.

21 L. F. Cugliandolo, J. Kurchan and L. Peliti, Energy flow, partial equilibration, and effective temperatures in systems with slow dynamics, *Phys. Rev. E: Stat. Phys., Plasmas, Fluids, Relat. Interdiscip. Top.*, 1997, **55**, 3898–3914.

22 N. Shiraishi, Time-symmetric current and its fluctuation response relation around nonequilibrium stalling stationary state, *Phys. Rev. Lett.*, 2022, **129**, 020602.

23 D. Andrieux, P. Gaspard, S. Ciliberto, N. Garnier, S. Joubaud and A. Petrosyan, Entropy production and time asymmetry in nonequilibrium fluctuations, *Phys. Rev. Lett.*, 2007, **98**, 98–101.

24 C. Maes and K. Netočný, Time-Reversal and Entropy, *J. Stat. Phys.*, 2003, **110**, 269–310.

25 Q. Liu and J. Wang, Quantifying the flux as the driving force for nonequilibrium dynamics and thermodynamics in non-Michaelis-Menten enzyme kinetics, *Proc. Natl. Acad. Sci. U. S. A.*, 2020, **117**, 923–930.

26 J. Li, J. M. Horowitz, T. R. Gingrich and N. Fakhri, Quantifying dissipation using fluctuating currents, *Nat. Commun.*, 2019, **10**, 1666.

27 T. R. Gingrich, G. M. Rotskoff and J. M. Horowitz, Inferring dissipation from current fluctuations, *J. Phys. A: Math. Theor.*, 2017, **50**, aa672f.

28 A. Ghanta, J. C. Neu and S. Teitsworth, Fluctuation loops in noise-driven linear dynamical systems, *Phys. Rev. E*, 2017, **95**, 1–9.

29 H. Qian, Vector field formalism and analysis for a class of thermal ratchets, *Phys. Rev. Lett.*, 1998, **81**, 3063–3066.

30 F. Mori, S. N. Majumdar and G. G. Schehr, Distribution of the time of the maximum for stationary processes, *EPL*, 2021, **135**, 30003.

31 L. Cocconi, R. Garcia-Millan, Z. Zhen, B. Buturca and G. Pruessner, Entropy production in exactly solvable systems, *Entropy*, 2020, **22**, 1–33.

32 T. Tomé and M. J. De Oliveira, Entropy production in irreversible systems described by a Fokker-Planck equation, *Phys. Rev. E: Stat., Nonlinear, Soft Matter Phys.*, 2010, **82**, 1–10.

33 T. Tomé, Entropy production in nonequilibrium systems described by a Fokker-Planck equation, *Braz. J. Phys.*, 2006, **36**, 1285–1289.

34 U. Seifert, Entropy production along a stochastic trajectory and an integral fluctuation theorem, *Phys. Rev. Lett.*, 2005, **95**, 1–4.

35 M. Barrio, A. Leier and T. T. Marquez-Lago, Reduction of chemical reaction networks through delay distributions, *J. Chem. Phys.*, 2013, **138**, 104114.

36 T. Jia and R. V. Kulkarni, Intrinsic noise in stochastic models of gene expression with molecular memory and bursting, *Phys. Rev. Lett.*, 2011, **106**, 1–4.

37 J. M. Pedraza and J. Paulsson, Effects of molecular memory and bursting on fluctuations in gene expression, *Science*, 2008, **319**, 339–343.

38 A. Basu and D. Chowdhury, Traffic of interacting ribosomes: effects of single-machine mechanochemistry on protein synthesis, *Phys. Rev. E: Stat., Nonlinear, Soft Matter Phys.*, 2007, **75**, 1–11.

39 K. Nishinari, Y. Okada, A. Schadschneider and D. Chowdhury, Intracellular transport of single-headed molecular motors KIF1A, *Phys. Rev. Lett.*, 2005, **95**, 1–4.

40 J. Ehrich, Tightest bound on hidden entropy production from partially observed dynamics, *J. Stat. Mech.: Theory Exp.*, 2021, 083214.

41 S. K. Manikandan, D. Gupta and S. Krishnamurthy, Inferring Entropy Production from Short Experiments, *Phys. Rev. Lett.*, 2020, **124**, 120603.

42 D. K. Kim, Y. Bae, S. Lee and H. Jeong, Learning Entropy Production via Neural Networks, *Phys. Rev. Lett.*, 2020, **125**, 140604.

43 M. Uhl, P. Pietzonka and U. Seifert, Fluctuations of apparent entropy production in networks with hidden slow degrees of freedom, *J. Stat. Mech.: Theory Exp.*, 2018, 023203.

44 M. Kahlen and J. Ehrich, Hidden slow degrees of freedom and fluctuation theorems: an analytically solvable model, *J. Stat. Mech.: Theory Exp.*, 2018, 063204.

45 R. Rao and M. Esposito, Detailed fluctuation theorems: a unifying perspective, *Entropy*, 2018, **20**, 8–11.

46 M. Polettini and M. Esposito, Effective Thermodynamics for a Marginal Observer, *Phys. Rev. Lett.*, 2017, **119**, 1–5.

47 N. Shiraishi and T. Sagawa, Fluctuation theorem for partially masked nonequilibrium dynamics, *Phys. Rev. E: Stat., Nonlinear, Soft Matter Phys.*, 2015, **91**, 3–8.

48 S. Rahav and C. Jarzynski, Fluctuation relations and coarse-graining, *J. Stat. Mech.: Theory Exp.*, 2007, **2007**, P09012.

49 N. Shiraishi, Optimal thermodynamic uncertainty relation in Markov jump processes, *J. Stat. Phys.*, 2021, **185**(19), 1–5.

50 J. M. Horowitz and T. R. Gingrich, Thermodynamic uncertainty relations constrain non-equilibrium fluctuations, *Nat. Phys.*, 2020, **16**, 15–20.

51 G. Falasco, M. Esposito and J. C. Delvenne, Unifying thermodynamic uncertainty relations, *New J. Phys.*, 2020, 053046.

52 T. R. Gingrich, J. M. Horowitz, N. Perunov and J. L. England, Dissipation Bounds All Steady-State Current Fluctuations, *Phys. Rev. Lett.*, 2016, **116**, 1–5.

53 A. C. Barato and U. Seifert, Thermodynamic Uncertainty Relation for Biomolecular Processes, *Phys. Rev. Lett.*, 2015, **114**, 158101.

54 T. Koyuk and U. Seifert, Thermodynamic Uncertainty Relation for Time-Dependent Driving, *Phys. Rev. Lett.*, 2020, **125**, 260604.

55 I. Di Terlizzi, M. Baiesi, I. Di Terlizzi and M. Baiesi, Kinetic uncertainty relation, *J. Phys. A: Math. Theor.*, 2018, **52**, 02LT03.

56 B. Ertel, J. van der Meer and U. Seifert, Operationally Accessible Uncertainty Relations for Thermodynamically Consistent Semi-Markov Processes, *Phys. Rev. E*, 2022, **105**, 044113.

57 T. Van Vu and Y. Hasegawa, Generalized uncertainty relations for semi-Markov processes, *J. Phys.: Conf. Ser.*, 2020, **1593**, 012006.

58 V. T. Vo, T. Van Vu and Y. Hasegawa, arXiv, 2022, preprint, arXiv:2203.11501v2 [cond-mat.stat-mech], DOI: **10.48550/arXiv.2203.11501**.

DISTRIBUTION A: Distribution approved for public release.

59 A. Pal, S. Reuveni and S. Rahav, Thermodynamic uncertainty relation for first-passage times on Markov chains, *Phys. Rev. Res.*, 2021, **3**, 1–6.

60 A. Pal, S. Reuveni and S. Rahav, Thermodynamic uncertainty relation for systems with unidirectional transitions, *Phys. Rev. Res.*, 2021, **3**, 13273.

61 G. Bisker, M. Polettini, T. R. Gingrich and J. M. Horowitz, Hierarchical bounds on entropy production inferred from partial information, *J. Stat. Mech.: Theory Exp.*, 2017, **2017**, aa8c0d.

62 D. Hartich, A. C. Barato and U. Seifert, Stochastic thermodynamics of bipartite systems: transfer entropy inequalities and a Maxwell's demon interpretation, *J. Stat. Mech.: Theory Exp.*, 2014, P02016.

63 M. Polettini and M. Esposito, Effective Fluctuation and Response Theory, *J. Stat. Phys.*, 2019, **176**, 94–168.

64 I. A. Martínez, G. Bisker, J. M. Horowitz and J. M. R. R. Parrondo, Inferring broken detailed balance in the absence of observable currents, *Nat. Commun.*, 2019, **10**, 1–10.

65 G. R. Terrell and D. W. Scott, Variable Kernel Density, *Ann. Stat.*, 1992, **20**, 1236–1265URL: **http://www.jstor.org/stable/2242011**.

66 Z. I. Botev, J. F. Grotowski and D. P. Kroese, Kernel density estimation via diffusion, *Ann. Stat.*, 2010, **38**, 2916–2957.

67 T. M. Cover and J. A. Thomas, *Elements of Information Theory*, 2005.

68 É. Roldán and J. M. R. Parrondo, Entropy production and Kullback–Leibler divergence between stationary trajectories of discrete systems, *Phys. Rev. E: Stat., Nonlinear, Soft Matter Phys.*, 2012, **85**, 1–12.

69 R. Kawai, J. M. R. Parrondo and C. Van Den Broeck, Dissipation: the phase-space perspective, *Phys. Rev. Lett.*, 2007, **98**, 1–4.

70 I. Roldán and J. M. R. Parrondo, Estimating dissipation from single stationary trajectories, *Phys. Rev. Lett.*, 2010, **105**, 1–4.

71 É. Roldán, J. Barral, P. Martin, J. M. R. Parrondo and F. Jülicher, Quantifying entropy production in active fluctuations of the hair-cell bundle from time irreversibility and uncertainty relations, *New J. Phys.*, 2021, **23**, 1–16.

72 D. Hartich and A. Godec, Emergent memory and kinetic hysteresis in strongly driven networks, *Phys. Rev. X*, 2021, **11**, 041047.

73 D. Hartich and A. Godec, arXiv, 2022, preprint, arXiv:2112.08978v3, DOI: **10.48550/arxiv.2112.08978**.

74 G. Bisker, I. A. Martinez, J. M. Horowitz and J. M. Parrondo, arXiv, 2022, preprint, arXiv:2202.02064v1, DOI: **10.48550/arxiv.2202.02064**.

75 J. van der Meer, B. Ertel and U. Seifert, Thermodynamic inference in partially accessible Markov networks: a unifying perspective from transition-based waiting time distributions, *Phys. Rev. X*, 2022, **12**, 031025.

76 D. Hartich and A. Godec, arXiv, 2021, preprint, arXiv:2111.14734v2 [cond-mat.stat-mech], DOI: **10.48550/arXiv.2111.14734**.

77 P. E. Harunari, A. Garilli and M. Polettini, arXiv, 2022, preprint, arXiv:2205.05060v1 [cond-mat.stat-mech], DOI: **10.48550/arXiv.2205.05060**.

78 P. E. Harunari, A. Dutta, M. Polettini and É. Roldán, arXiv, 2022, preprint, arXiv:2203.07427v2 [cond-mat.stat-mech], DOI: **10.48550/arXiv.2203.07427**.

79 D. J. Skinner and J. Dunkel, Improved bounds on entropy production in living systems, *Proc. Natl. Acad. Sci. U. S. A.*, 2021, **118**(18), e2024300118.

80 D. J. Skinner and J. Dunkel, Estimating entropy production from waiting time distributions, *Phys. Rev. Lett.*, 2021, **127**, 198101.

81 D. M. Busiello, D. Gupta and A. Maritan, Coarse-grained entropy production with multiple reservoirs: unraveling the role of time scales and detailed balance in biology-inspired systems, *Phys. Rev. Res.*, 2020, **2**, 43257.

82 D. M. Busiello, J. Hidalgo and A. Maritan, Entropy production for coarse-grained dynamics, *New J. Phys.*, 2019, **21**, 073004.

83 S. Bo and A. Celani, Entropy Production in Stochastic Systems with Fast and Slow Time-Scales, *J. Stat. Phys.*, 2014, **154**, 1325–1351.

84 S. Bo and A. Celani, Multiple-scale stochastic processes: decimation, averaging and beyond, *Phys. Rep.*, 2017, **670**, 1–59.

85 M. Esposito, Stochastic thermodynamics under coarse graining, *Phys. Rev. E: Stat., Nonlinear, Soft Matter Phys.*, 2012, **85**, 1–11.

86 K. Kawaguchi and Y. Nakayama, Fluctuation theorem for hidden entropy production, *Phys. Rev. E: Stat., Nonlinear, Soft Matter Phys.*, 2013, **88**, 1–5.

87 G. Teza and A. L. Stella, Exact Coarse Graining Preserves Entropy Production out of Equilibrium, *Phys. Rev. Lett.*, 2020, **125**, 110601.

88 A. Gomez-Marin, J. M. R. Parrondo and C. Van Den Broeck, Lower bounds on dissipation upon coarse graining, *Phys. Rev. E: Stat., Nonlinear, Soft Matter Phys.*, 2008, **78**, 1–11.

89 P. Bilotto, L. Caprini and A. Vulpiani, Excess and loss of entropy production for different levels of coarse graining, *Phys. Rev. E*, 2021, **104**, 1–8.

90 J. il Sohn, An example of temporal coarse-graining of entropy production, *Eur. Phys. J. B*, 2015, **88**, 1–5.

91 X. Yang, Y. Chen, T. Zhou and J. Zhang, Exploring dissipative sources of non-Markovian biochemical reaction systems, *Phys. Rev. E*, 2021, **103**, 052411.

92 S. Pigolotti and A. Vulpiani, Coarse graining of master equations with fast and slow states, *J. Chem. Phys.*, 2008, **128**, 154114.

93 D. Seiferth, P. Sollich and S. Klumpp, Coarse graining of biochemical systems described by discrete stochastic dynamics, *Phys. Rev. E*, 2020, **102**, 1–17.

94 A. Celani, S. Bo, R. Eichhorn and E. Aurell, Anomalous thermodynamics at the microscale, *Phys. Rev. Lett.*, 2012, **109**, 1–4.

95 T. H. Tan, G. A. Watson, Y.-C. Chao, J. Li, T. R. Gingrich, J. M. Horowitz and N. Fakhri, arXiv, 2021, preprint, arXiv:2107.05701v1 [physics.bio-ph], DOI: **10.48550/arXiv.2107.05701**.

 This journal is © the Owner Societies 2022

DISTRIBUTION A: Distribution approved for public release.

96 J. Barral, F. Jülicher and P. Martin, Friction from Transduction Channels' Gating Affects Spontaneous Hair-Bundle Oscillations, *Biophys. J.*, 2018, **114**, 425–436.
97 V. Bormuth, J. Barral, J. F. Joanny, F. Jülicher and P. Martin, Transduction channels' gating can control friction on vibrating hair-cell bundles in the ear, *Proc. Natl. Acad. Sci. U. S. A.*, 2014, **111**, 7185–7190.
98 J. Y. Tinevez, F. Jülicher and P. Martin, Unifying the various incarnations of active hair-bundle motility by the vertebrate hair cell, *Biophys. J.*, 2007, **93**, 4053–4067.
99 P. Martin, D. Bozovic, Y. Choe and A. J. Hudspeth, Spontaneous oscillation by hair bundles of the bullfrog's sacculus, *J. Neurosci.*, 2003, **23**, 4533–4548.
100 B. Nadrowski, P. Martin and F. Jülicher, Active hair-bundle motility harnesses noise to operate near an optimum of mechanosensitivity, *Proc. Natl. Acad. Sci. U. S. A.*, 2004, **101**, 12195–12200.
101 L. Dabelow, S. Bo and R. Eichhorn, Irreversibility in Active Matter Systems: Fluctuation Theorem and Mutual Information, *Phys. Rev. X*, 2019, **9**, 21009.
102 B. Gaveau, L. Granger, M. Moreau and L. S. Schulman, Relative entropy, interaction energy and the nature of dissipation, *Entropy*, 2014, **16**, 3173–3206.
103 Y. Tu, The nonequilibrium mechanism for ultrasensitivity in a biological switch: sensing by Maxwell's demons, *Proc. Natl. Acad. Sci. U. S. A.*, 2008, **105**, 11737–11741.
104 C. Xiaodong, Exact stochastic simulation of coupled chemical reactions with delays, *J. Chem. Phys.*, 2007, **126**, 2340–2361.
105 J. Shin, J. Shin, A. M. Berezhkovskii, A. B. Kolomeisky, A. B. Kolomeisky, A. B. Kolomeisky and A. B. Kolomeisky, Biased Random Walk in Crowded Environment: Breaking Uphill/Downhill Symmetry of Transition Times, *J. Phys. Chem. Lett.*, 2020, **11**, 4530–4535.
106 A. M. Berezhkovskii and D. E. Makarov, On the forward/backward symmetry of transition path time distributions in nonequilibrium systems, *J. Chem. Phys.*, 2019, **151**, 065102.
107 J. Shin, A. M. Berezhkovskii and A. B. Kolomeisky, Crowding breaks the forward/backward symmetry of transition times in biased random walks, *J. Chem. Phys.*, 2021, **154**, 204104.
108 A. M. Berezhkovskii, G. Hummer and S. M. Bezrukov, Identity of distributions of direct uphill and downhill translocation times for particles traversing membrane channels, *Phys. Rev. Lett.*, 2006, **97**, 1–4.

DISTRIBUTION A: Distribution approved for public release.

Electronic Supplementary Material (ESI) for Physical Chemistry Chemical Physics.
This journal is © the Owner Societies 2022

Supplementary Information

Inferring Entropy Production Rate from partially observed Langevin dynamics under Coarse-Graining

Aishani Ghosal[a] and Gili Bisker[*,a,b,c,d]

[a] Department of Biomedical Engineering, Tel Aviv University, Tel Aviv 6997801, Israel

[b] Center for Physics and Chemistry of Living Systems, Tel-Aviv University, Tel Aviv 6997801, Israel

[c] Center for Nanoscience and Nanotechnology, Tel-Aviv University, Tel Aviv 6997801, Israel

[d] Center for Light-Matter Interaction, Tel-Aviv University, Tel Aviv 6997801, Israel

*Corresponding author: Gili Bisker
Email: bisker@tauex.tau.ac.il

Supplementary Information Text

Simulated trajectories. We simulated Eq. 1 and Eq. 2 for the trajectories of the tip position of the hair bundle (X_1) – the observed variable. The trajectories for different values of the driving parameters (F_{max}, S, and keeping $T_{max} = 1.5\,T$) are plotted in *Figure S1*. These trajectories are later used to calculate the EPR bounds $(\mathrm{EPR}_{\mathrm{WTD}})$ on the total EPR $(\mathrm{EPR}_{\mathrm{tot}})$ and the mean dwell- time asymmetry factor (MDAF) as described in the main manuscript.

Coarse-graining method. We coarse-grain the trajectories of the observed variable (X_1) into 3, 4, 5, 6, and 7 discrete states by spatially dividing the X_1 state space to segments with ratios 1:1:1, $1{:}\frac{1}{2}{:}\frac{1}{2}{:}1$, $1{:}\frac{1}{3}{:}\frac{1}{3}{:}\frac{1}{3}{:}1$, $1{:}\frac{1}{4}{:}\frac{1}{4}{:}\frac{1}{4}{:}\frac{1}{4}{:}1$, $1{:}\frac{1}{5}{:}\frac{1}{5}{:}\frac{1}{5}{:}\frac{1}{5}{:}\frac{1}{5}{:}1$ respectively (as shown in *Figure S2* for *N*=3, 4, 5, 6). The parameters used for the calculations in *Figure S2* are: $F_{max} = 70\ pN$, $T_{eff} = 1.5T$, and $S = 1$. This coarse-graining is used for the results presented in Figure 5 and Figure 6 in the main manuscript.

Mean dwell-time asymmetry factor (MDAF). We calculate the total mean dwell-time asymmetry factor using $\boldsymbol{N}^{-1}\sum\langle\boldsymbol{\tau_{kji}}\rangle/\langle\boldsymbol{\tau_{ijk}}\rangle$, where $\boldsymbol{N}$ is the total number of coarse-grained states. The values of $(\langle\boldsymbol{\tau_{kji}}\rangle/\langle\boldsymbol{\tau_{ijk}}\rangle)$ from transitions among different coarse-grained states are plotted in *Figure S3.*

Tightness of the bounds for different parameters: We calculate the tightness of the bounds for unequal coarse-graining (as shown in *Figure S2*) for 7 coarse-grained states (*N*=7) at different driving parameter values, as shown in Table 1.

Method The steady state averages in Eq. 4 of the form $\langle F \circ \frac{dX}{dt}\rangle = \lim_{t\to\infty}\frac{1}{t}\int_0^t dt' F(t') \circ dx\,(t')$ were calculated using $\langle F \circ \frac{dX}{dt}\rangle \cong \frac{1}{t_{tot}}\sum_{i=1}^{n}\left(\frac{F(t_i)+F(t_{i-1})}{2}\right)\left(X(t_i) - X(t_{i-1})\right)$, where $t_i = i\Delta t$, and $n = t_{tot}/\Delta t$. We have used $\Delta t = 0.1\ ms$ and the calculation was performed for a trajectory of length $t_{tot} = 100\ s$.

DISTRIBUTION A: Distribution approved for public release.

Figure S1

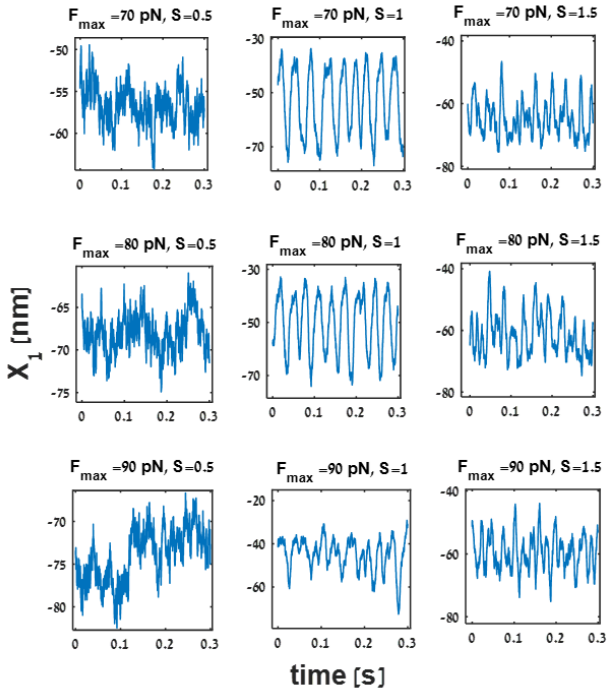


Figure S1. The trajectories of the position of the tip of the hair bundle $(\boldsymbol{X_1})$ *as calculated by solving the coupled differential equations, Eq. 1 and Eq. 2 in the main text for different values of the parameter choices as a function of time. The driving parameter values are written in the subtitles with* $\boldsymbol{T_{eff} = 1.5\,T}$*. All other parameter values are the same as mentioned in Figure 1 in the main text.*

DISTRIBUTION A: Distribution approved for public release.

Figure S2.

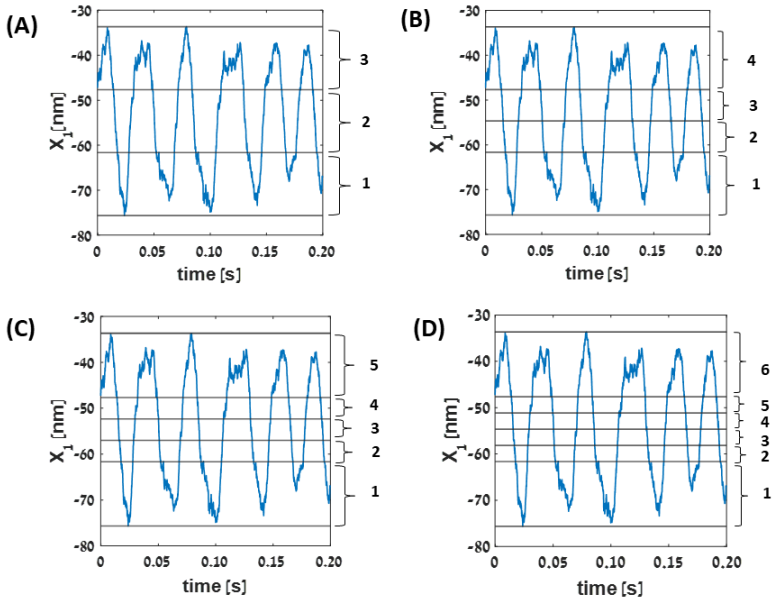


Figure S2. Coarse-graining of the hair bundle tip position $(\boldsymbol{X_1})$ *for parameter values* $\boldsymbol{F_{max} = 70\ pN}$, $\boldsymbol{S = 1}$, $\boldsymbol{T_{eff} = 1.5\ T}$ *. The index numbers on the right side of each panel indicate the number of the coarse-grained states: (A) 3 CG states (1:1:1 division), (B) 4 CG states (*$\boldsymbol{1:\frac{1}{2}:\frac{1}{2}:1}$ *division) (C) 5 CG states (*$\boldsymbol{1:\frac{1}{3}:\frac{1}{3}:\frac{1}{3}:1}$ *division) and (D) 6 CG states (*$\boldsymbol{1:\frac{1}{4}:\frac{1}{4}:\frac{1}{4}:\frac{1}{4}:1}$ *division). Panels (B), (C), and (D) show coarse-graining with unequal division of the* $\boldsymbol{X_1}$ *trajectory as mentioned in the main manuscript. The top and bottom borders are determined by the extremum values of the* $\boldsymbol{X_1}$ *parameter.*

DISTRIBUTION A: Distribution approved for public release.

Figure S3.

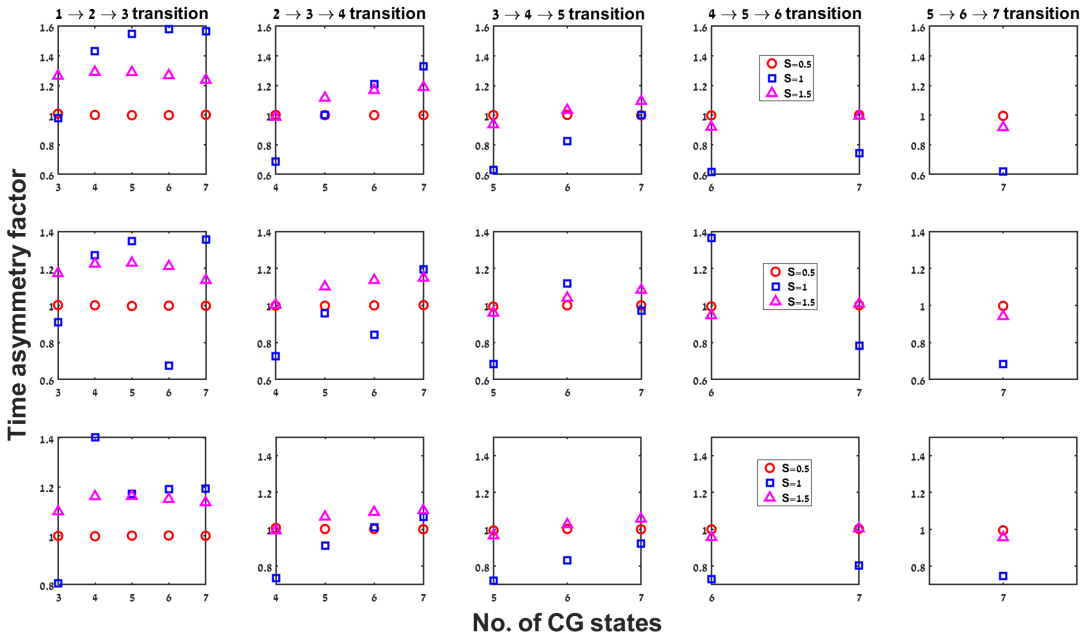


Figure S3. The mean dwell-time asymmetry factors (MDAF, $\langle \boldsymbol{\tau_{kji}} \rangle / \langle \boldsymbol{\tau_{ijk}} \rangle$) as a function of the number of coarse-grained states for different transitions (shown in the subtitles) between the coarse-grained states for different parameter values: $\boldsymbol{F_{max}} = \mathbf{70}\,\boldsymbol{pN}$ (upper panel), *$\boldsymbol{F_{max}} = \mathbf{80}\,\boldsymbol{pN}$* (middle panel), *$\boldsymbol{F_{max}} = \mathbf{90}\,\boldsymbol{pN}$* (lower panel), *$\boldsymbol{S} = \mathbf{0.5}$* (red open circles), *$\boldsymbol{S} = \mathbf{1}$* (blue open square), *$\boldsymbol{S} = \mathbf{1.5}$* (magenta open triangle)), and *$\boldsymbol{T_{eff}} = \mathbf{1.5}\,\boldsymbol{T}$. All other parameter values are the same as mentioned in Figure 1 in the main text.*

DISTRIBUTION A: Distribution approved for public release.

Table 1

The tightness of the bounds for unequal coarse-graining for 7 coarse-grained states at different driving parameter values

Driving parameter values	$\mathbf{EPR_{WTD}/EPR_{tot}}$
$F_{max} = 70\ pN, S = 0.5, T_{eff}/T = 1.5$	0.0666
$F_{max} = 70\ pN, S = 1, T_{eff}/T = 1.5$	0.0024
$F_{max} = 70\ pN, S = 1.5, T_{eff}/T = 1.5$	0.0018
$F_{max} = 80\ pN, S = 0.5, T_{eff}/T = 1.5$	0.1244
$F_{max} = 80\ pN, S = 1, T_{eff}/T = 1.5$	0.0012
$F_{max} = 80\ pN, S = 1.5, T_{eff}/T = 1.5$	0.0024
$F_{max} = 90\ pN, S = 0.5, T_{eff}/T = 1.5$	0.0335
$F_{max} = 90\ pN, S = 1, T_{eff}/T = 1.5$	0.0017
$F_{max} = 90\ pN, S = 1.5, T_{eff}/T = 1.5$	0.0010

DISTRIBUTION A: Distribution approved for public release.

Journal of Physics D: Applied Physics

PAPER • OPEN ACCESS

Entropy production rates for different notions of partial information

To cite this article: Aishani Ghosal and Gili Bisker 2023 *J. Phys. D: Appl. Phys.* **56** 254001

View the article online for updates and enhancements.

You may also like

- Determination of thermal conductivity of eutectic Al-Cu compounds utilizing experiments, molecular dynamics simulations and machine learning
Alireza Nazarahari, A. Fromm, HÜSEYN CAN ÖZDEMR et al.
- Birotor hydrodynamic microswimmers: From single to collective behaviour
Marisol Ripoll and Joscha Mecke
- Stacking order and driving forces in the layered charge density wave phase of 1T-MX2 (M = Nb, Ta and X = S, Se)
Wenjun Zhang and Jiansheng Wu

This content was downloaded from IP address 132.66.11.215 on 13/04/2023 at 21:06

DISTRIBUTION A: Distribution approved for public release.

OPEN ACCESS
IOP Publishing
Journal of Physics D: Applied Physics
J. Phys. D: Appl. Phys. **56** (2023) 254001 (10pp)
https://doi.org/10.1088/1361-6463/acc957

Entropy production rates for different notions of partial information

Aishani Ghosal[1] **and Gili Bisker**[1,2,3,4,*]

[1] Department of Biomedical Engineering, Tel Aviv University, Tel Aviv 6997801, Israel
[2] Center for Physics and Chemistry of Living Systems, Tel Aviv University, Tel Aviv 6997801, Israel
[3] Center for Nanoscience and Nanotechnology, Tel Aviv University, Tel Aviv 6997801, Israel
[4] Center for Light-Matter Interaction, Tel Aviv University, Tel Aviv 6997801, Israel

E-mail: bisker@tauex.tau.ac.il

Received 3 November 2022, revised 14 March 2023
Accepted for publication 31 March 2023
Published 13 April 2023

Abstract

Experimentally monitoring the dynamics of a physical system, one cannot possibly resolve all the microstates or all the transitions between them. Theoretically, these partially observed systems are modeled by considering only the observed states and transitions while the rest are hidden, by merging microstates into a single mesostate, or by decimating unobserved states. The deviation of a system from thermal equilibrium can be characterized by a non-zero value of the entropy production rate (EPR). Based on the partially observed information of the states or transitions, one can only infer a lower bound on the total EPR. Previous studies focused on several approaches to optimize the lower bounds on the EPR, fluctuation theorems associated with the apparent EPR, information regarding the network topology inferred from partial information, etc. Here, we calculate partial EPR values of Markov chains driven by external forces from different notions of partial information. We calculate partial EPR from state-based coarse-graining, namely decimation and two lumping protocols with different constraints, either preserving transition flux, or the occupancy number correlation function. Finally, we compare these partial EPR values with the EPR inferred from the observed cycle affinity. Our results can further be extended to other networks and various external driving forces.

Keywords: stochastic thermodynamics, nonequilibrium, entropy production rate, coarse-graining, lumping, decimation

(Some figures may appear in colour only in the online journal)

1. Introduction

Entropy production (EP) is a thermodynamic quantity intimately tied to the irreversibility of a nonequilibrium process [1, 2]. The EP sets fundamental bounds on the efficiency of physical systems like heat engines [2] and biological processes [3–6], and provides insight into the thermodynamics of nonequilibrium systems [7]. Estimating the total EP along a trajectory requires access to the entropy change of the system and the amount of heat dissipated to the surrounding reservoirs during the process [2, 8]. A major challenge in EP inference is the large number of out-of-equilibrium degrees of freedom, many of which are not accessible to an external observer and cannot be directly resolved [9, 10]. Nevertheless, a lower bound on the total EP can be obtained, for example, based on the fluctuations of an observed thermodynamic flux, like transition currents [11–14] or first passage times of the current [15–17], by the thermodynamic uncertainty relations. In essence, one can only estimate a lower bound on the total EP

* Author to whom any correspondence should be addressed.

Original content from this work may be used under the terms of the Creative Commons Attribution 4.0 licence. Any further distribution of this work must maintain attribution to the author(s) and the title of the work, journal citation and DOI.

© 2023 The Author(s). Published by IOP Publishing Ltd

DISTRIBUTION A: Distribution approved for public release.

for a partially observed system. The observations can be, due to the finite spatiotemporal resolution, a subset of the 'states' [18–23] or a subset of the 'transitions' [24, 25] between the different states.

Theoretically, the effective, coarse-grained dynamics of various chemical and biological processes which occur over a wide range of timescales can be written in terms of the slow timescale processes while taking into account the action of the fast ones [26, 27]. A coarse-grained system, however, might appear to be time-reversible despite underlying nonequilibrium dynamics in hidden cycles [26, 27]. Still, eliminating fast degrees of freedom does not necessarily alter the apparent EP if the cycle carrying the probability current is not removed in the decimation process [28]. Coarse-graining of this kind was first studied using a Markovian master equation, and the coarse-grained EP was shown to satisfy a Fluctuation theorem [29]. In other scenarios, the entropy production rate (EPR) estimation for a coarse-grained system can exactly produce the total EPR. For example, by decimating states [30] while considering the inclusion of self-loops, the EPR obtained from a Markovianized master equation for the underlying non-Markov process estimates the actual EPR. Moreover, proper coarse-graining in the cycle space [31], or reducing bridge-states [32], can also preserve the mean EPR. Finally, observing a single transition in a unicycle network is sufficient to recover the total EPR [18, 24, 25].

EPR estimators for partially accessible systems have been studied widely, and several approaches have been proposed, including the passive partial entropy production (PPEP) and informed partial entropy production (IPEP) [18–23, 33], which provide a lower bound on the total EPR. For the case of the PPEP estimation, the observer has access only to a few microstates and the transitions between them. In contrast, in the IPEP estimation, the observer relies on the observed dynamics and the affinity of the observed cycles. Both the PPEP and the IPEP fail at stalling conditions, e.g. in the absence of a net current along the accessible link. However, the Kullback-Leibler divergence (KLD) estimator based on the asymmetry of the waiting time distributions (WTDs) can provide a tighter lower bound in the absence of the net flux along the observed link for second-order Markov processes [19, 24, 34, 35]. Recently, EPR estimators have been proposed based on observed transitions rather than observed states [24, 25]. The lower bound on the total EPR was estimated based on observing two successive repeated transitions along the same direction and the waiting times between the transitions or the 'inter-transition time' [24, 25]. The topology information of the network can also be deduced using this method from a single observed link for a unicyclic network or multiple observed links for a general Markov network [25]. The transition-based estimators equal the informed partial EPR for a unicyclic network [18, 25] and a general Markov network without hidden cycles.

Several attempts have been made to find a tighter bound on the total EPR. One approach suggests fitting the observed dynamics of a discrete-time Markov chain to an underlying Markov model that produces the observed statistics of the coarse-grained system [36]. When the number of hidden states is known, this fitting method can provide a tight bound on the total EPR. Moreover, two recently developed estimators are based on an optimization process of searching over possible underlying Markov models that obey the observed statistics of mass transfer between the mesostates [37] and the WTDs for the time forward and time-reversed transitions [38]. A novel approach for utilizing waiting time information by reformulation of the observed statistics of intra-transitions within macrostates was demonstrated to yield an improved lower bound on the EPR [39]. Further, a hierarchy of EPR estimators has been recently proposed, by optimizing over systems with the same observed mass rates and the same moments of the WTDs between coarse-grained states [40].

In general, there are two notions of partial information. In the first notion, the observer can distinguish between the observed and the hidden part of the system, where no information about the network topology is available for the hidden subsystem. Here, the sum of the partial EP of the observed and the hidden subsystems equals the total EP [18]. The other notion involves coarse-graining [28, 29, 32, 41–48], performed by lumping, i.e. merging several states into a single compound state [49, 50], or decimating [30] states. In decimation, the probability densities of the decimated states equal zero and are redistributed between the probability densities of the surviving states [51]. Similarly, in lumping [49, 50], the steady-state probabilities of the merged states sum up, whereas the rest of the states are not affected. In addition, one lumping protocol preserves the transition fluxes between the states, except for the states undergoing lumping [49]. However, another specific procedure for lumping conserves the time-dependent occupation number correlation function after the coarse-graining [50]. The accountability of the internal dissipation of the state undergoing coarse-graining is not guaranteed and depends on the coarse-graining procedure. Generally, coarse-graining is one method by which partially observed systems are often modeled. Further details on the different coarse-graining methods are discussed in the upcoming sections.

Here, we study how the above notions of partial information affect the partial EPR values obtained from partially observed systems. We start with the evolution equation for the EP of a driven system governed by a Master Equation, introduce lumping and decimation procedures on the system states, and obtain the partial EPR from an approximated Master (AM) equation. We further compare EPR values obtained from different coarse-graining approaches for different network topologies with the total mean EPR values.

The paper is organized as follows. First, we briefly review the EPR obtained from partially observed systems with observed and hidden substates in section 2. Next, we discuss the EPR inferred following the various coarse-graining methods. Section 3 shows the calculation of the total mean EPR from the evolution of the EP for a Markov chain and the evaluation of the partial mean EPR from the non-Markovian coarse-grained system following AM equation. Section 4 discusses the decimation method and the mean EPRs (scaled

DISTRIBUTION A: Distribution approved for public release.

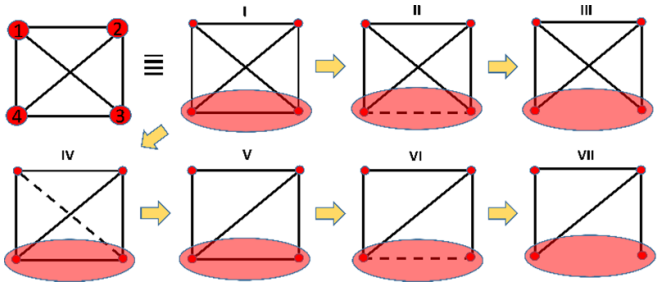


Figure 1. Different network topologies in which states 1 and 2 are observed, and states 3 and 4 are indistinguishable, and collectively called 'hidden state' (shaded with red color). The weights of the 3–4 link and 1–3 link are denoted by ν and μ, respectively. The networks are denoted by these two parameters (I) $\mu=1,\nu=1$; (II) $\mu=1,\nu=0.2$; (III) $\mu=1,\nu=0$; (IV) $\mu=0.05,\nu=1$; (V) $\mu=0,\nu=1$; (VI) $\mu=0,\nu=0.05$; (VII) $\mu=0,\nu=0$. The other transition rates are: $\bar{w}_{12}=2\ \mathrm{s}^{-1}$,$\bar{w}_{21}=3\ \mathrm{s}^{-1}$, $w_{14}=1\ \mathrm{s}^{-1}$, $w_{41}=8\ \mathrm{s}^{-1}$, $w_{24}=35\ \mathrm{s}^{-1}$, $w_{42}=0.2\ \mathrm{s}^{-1}$, $w_{23}=2\ \mathrm{s}^{-1}$, $w_{32}=50\ \mathrm{s}^{-1}$, $w_{13}=13\,\mu\mathrm{s}^{-1}$, $w_{31}=20\,\mu\mathrm{s}^{-1}$, $w_{34}=0.7\ \nu\mathrm{s}^{-1}$, $w_{43}=75\ \nu\mathrm{s}^{-1}$.

cumulant generating function (SCGF) and AM) obtained from their respective AM equations. In section 5, we describe two different lumping coarse-graining methods and calculate the corresponding mean EPRs. We discuss our results in section 6, and, finally, conclude our findings in section 7.

1.1. Partial EPRs

We consider a continuous-time Markov chain over a finite number of discrete states. The generator of the Markov jump-process, or the transition rate matrix, is defined by a matrix $\boldsymbol{W}$. The non-diagonal elements ($w_{ji}=[\boldsymbol{W}]_{j\neq i}$) of the matrix refer to transition rates between different states i and j, where w_{ji} is non-zero only if w_{ij} is non-zero. The diagonal elements ($w_{ii}=[\boldsymbol{W}]_{i=j}$) represent exit rates ($\lambda_i=-w_{ii}=\sum_{j\neq i}w_{ji}$) from a particular state i. The evolution of the state probabilities is governed by a Master Equation $d_t\boldsymbol{P}(t)=\boldsymbol{W}\boldsymbol{P}(t)$, where d_t denotes the time derivative, and $\boldsymbol{P}(t)=(P_1(t),P_2(t),\ldots)^{\mathrm{T}}$ denotes the probability vector to find the system in the respective states at time t. The system reaches a steady state at the long-time limit, denoted by the state probabilities vector $\boldsymbol{\pi}$, which can be obtained from solving $\boldsymbol{W}\boldsymbol{\pi}=0$. The distributions at steady state can also be obtained directly from the transition rates using the matrix-tree theorem [23, 52]. The stationary current between states i and j is defined by $J^{\pi}_{ji}=w_{ji}\pi_i-w_{ij}\pi_j$.

We start with simple yet non-trivial networks of continuous-time Markov chains (figure 1) [18, 53] to calculate the mean partial EPR for partially observed dynamics. In our model, we chose a system with 4 microstates, in which states 1 and 2 are observed, whereas states 3 and 4 cannot be distinguished, and are masked into a coarse-grained hidden state, H, as shown in the shaded area of figure 1. In practical scenarios, one can only observe a few transitions among states, and only a subset of the states. In PPEP, the observer only has access to an observed link between two microstates and the transition rates w_{12},w_{21} between them

At a long time limit, the PPEP reaches its steady-state rate [18, 21–23], given by

$$\sigma^{\mathrm{PPEP}}=J^{\pi}_{12}\log\left[w_{12}\pi_2/w_{21}\pi_1\right] \tag{1}$$

where log is the natural logarithm in base e.

On the other hand, for the IPEP [18, 21–23], in addition to the cycle affinity of the observed link, one has access to the steady state probability densities of both of the observed states at stalling conditions. For calculating the IPEP, we additionally assume that the observer can tune the rates over the observed link and use the system's steady state probabilities when the new rates are applied to infer information about the hidden states. The observer can tune the transition rates according to $w_{12}(F)=\bar{w}_{12}e^{\beta\tilde{F}L}=\bar{w}_{12}e^{F}$ and, with driving force $\tilde{F}$ of dimension $\beta^{-1}L^{-1}$ and F dimensionless. L is the characteristic length scale, and β is the inverse temperature. To calculate the IPEP, the system is tuned to stalling conditions, in which the current over the observed link vanishes at $F=F_{\mathrm{stall}}$, and the resulting steady-state probability densities of the two observed states are π^{st}_1, and π^{st}_2, respectively. At a long-time limit, the IPEP rate is given by [18, 23]:

$$\sigma^{\mathrm{IPEP}}=J^{\pi}_{12}\log\left[w_{12}\pi^{st}_2/w_{21}\pi^{st}_1\right]. \tag{2}$$

The stalling distribution can be calculated by solving $\boldsymbol{W}^{st}\boldsymbol{\pi}^{st}=0$, where the modified generator $\boldsymbol{W}^{st}$ is obtained by setting the rates over the observed link (1–2 link) as zero in the original Markov rate matrix $\boldsymbol{W}$, i.e. $w_{12}=w_{21}=0$ and adjusting the exit rates accordingly (see [18, 21–23] for full derivation). The value of the stalling force can then be calculated according to $F_{\mathrm{stall}}=\left(w_{12}\pi^{\mathrm{st}}_2/w_{21}\pi^{\mathrm{st}}_1\right)/2$.

Due to added information about the hidden states through the stall force, IPEP provides a better bound to the total EPR compared to the PPEP [18], and therefore we only compare to IPEP in the following. In this manuscript, we assume to have access only to the state information, without having knowledge regarding the fluctuations of the thermodynamic flux, first passage time associated with the thermodynamic flux, and waiting time information.

1.2. EPR estimation from master equation

We consider a trajectory γ with a sequence of N states $\{i_0,\ldots,i_N\}$ and the corresponding waiting times $\{t_0,\ldots,t_n\}$ for a total observation time T, $\sum_i t_i=T$, given by $\gamma=\{(i_0,t_0),\ldots,(i_N,t_N)\}$. The probability of observing such a trajectory is given by

$$P[\gamma]=e^{-t_N\lambda_{i_N}}\prod_{n=0}^{N-1}\left[w_{i_{n+1},i_n}e^{-t_n\lambda_{i_n}}\right]\pi_{i_0}. \tag{3}$$

Similarly, one can define the probability $\tilde{P}[\tilde{\gamma}]$ for the time-reversed trajectory $\tilde{\gamma}=\{(i_N,t_N),\ldots,(i_0,t_0)\}$, and express the total EP along the trajectory, Δ using their ratio [18]:

$$\begin{aligned}\Delta&=\log\left(\frac{P[\gamma]}{\tilde{P}[\tilde{\gamma}]}\right)=\log\frac{\pi_{i_0}}{\pi_{i_N}}+\sum\nolimits_{n=0}^{N-1}\log\left(\frac{w_{i_{n+1},i_n}}{w_{i_n,i_{n+1}}}\right)\\&=\log\frac{\pi_{i_0}}{\pi_{i_N}}+\sum\nolimits_{i<j}\phi_{ij}\log\frac{w_{ij}}{w_{ji}}\end{aligned} \tag{4}$$

DISTRIBUTION A: Distribution approved for public release.

where ϕ_{ij} is the net number of transitions from state j to state i.

The EPR can be calculated from the evolution of the EP governed by the Master equation. Following Teza and Stella [30], we denote the probability $P_i(S,t)$ that the system is at state i at time t, and have produced entropy S from all possible trajectories up to that time. Since each transition between a pair of states i and j adds up $\log(w_{ji}/w_{ij})$ to the total EP, we can write Master Equations for all the state probabilities $P_i(S,t)$ having EP S at time t:

$$d_t P_i(S,t) = -\lambda_i P_i(S,t) + \sum\nolimits_{j\neq i} w_{ij} P_j(S - \log w_{ij}/w_{ji}, t) \quad (5)$$

where λ_i is the exit or the escape rate from a particular state i. Let us denote $G_i(\Lambda,t) = \sum_S e^{\Lambda S} P_i(S,t)$, where $G_i(\Lambda,t)$ is the discrete Laplace transform of $P_i(S,t)$ with respect to the entropy S. We reformulate equation (5) as:

$$d_t G_i(\Lambda,t) = -\lambda_i G_i(\Lambda,t) + \sum\nolimits_{j\neq i} w_{ij} e^{\Lambda \log(w_{ij}/w_{ji})} G_j(\Lambda,t). \quad (6)$$

Equation (6) can be cast in matrix form as $d_t G(\Lambda,t) = \tilde{W} G(\Lambda,t)$, with $G(\Lambda,t)$ being a column vector with $G_i(\Lambda,t)$ as its ith entry, and $\tilde{W}$ the tilted transition matrix [30, 54]:

$$\left[\tilde{W}\right]_{ji} = \begin{cases} w_{ji} e^{\Lambda \log(w_{ji}/w_{ij})}, & i \neq j \\ -\lambda_i, & i = j \end{cases} \quad (7)$$

The dominant eigenvalue (Ω^{TM}) of the tilted transition matrix, $\tilde{W}$, is the SCGF of the EP. The mean EPR can be calculated from [30, 54, 55]:

$$\sigma^{\mathrm{TM}} = \partial_\Lambda \Omega^{\mathrm{TM}}(\Lambda)|_{\Lambda\to 0}. \quad (8)$$

TM refers to 'Total mean' (figure 2) as all the states' dynamics have been considered during its calculation.

In the next sections, we discuss EP obtained from the decimation and the lumping coarse-graining methods. In each of the methods, we find a Markovianized rate matrix ($\boldsymbol{U}$) associated with the coarse-grained system dynamics, modelled by an AM equation of the form $d_t \boldsymbol{Q}(t) = \boldsymbol{U}\boldsymbol{Q}(t)$, where $\boldsymbol{Q}$ is the column vector of probability densities of the coarse-grained states at time t.

1.3. Coarse graining via decimation

Decimation involves removing some states and redistributing their population density among the rest of the states. In this section, we consider *decimating* one of the states, say state d from equation (5), and evaluate the mean EPR from the decimated system. To do so, we perform the following four steps [30, 51].

We start with the following Master equation in terms of the probability of the EP:

$$d_t P_i(S,t) = \left[-\lambda_i P_i(S,t) + \sum\nolimits_{k\neq i} w_{ik} P_k\left(S - \frac{w_{ik}}{w_{ki}}, t\right)\right] \quad (9)$$

where λ_i is the exit rate from state i, w_{ik} is the transition rates between different states k and i, and $P_i(S,t)$ is the probability of being in state i and having EP S at time t.

The terms are the same as mentioned in section 3. First, we Fourier transform equation (9) using $\widetilde{P}_i(S,\omega) = \int dt\, e^{-i\omega t} P_i(S,t)$, where i includes all the states. Second, we substitute $\widetilde{P}_d(S,\omega)$ in the Fourier transformed equations, where $\widetilde{P}_d(S,\omega)$ is given by

$$\widetilde{P}_d(S,\omega) = \left(\frac{1}{\lambda_d + i\omega}\right) \sum\nolimits_{k\neq d} w_{dk} \widetilde{P}_k\left(S - \frac{w_{dk}}{w_{kd}}, \omega\right). \quad (10)$$

Substituting $\widetilde{P}_d(S,\omega)$ in the Fourier transformed equations, we obtain the following:

$$\begin{aligned}(\lambda_i + i\omega)\tilde{P}_i(S,\omega) &= \sum\nolimits_{k\neq d} w_{ik} \tilde{P}_k\left(S - \frac{w_{ik}}{w_{ki}}, \omega\right) + \left(\frac{w_{id} w_{di}}{\lambda_d + i\omega}\right) \tilde{P}_i(S,\omega) \\ &\quad + \left(\frac{w_{id}}{\lambda_d + i\omega}\right) \sum\nolimits_{k\neq d} w_{dk} \tilde{P}_k\left(S - \frac{w_{dk} w_{id}}{w_{kd} w_{di}}, \omega\right). \quad (11)\end{aligned}$$

Multiplying both sides by $(\lambda_d + i\omega)$, we get

$$\begin{aligned}(\lambda_d + i\omega)(\lambda_i + i\omega)\widetilde{P}_i(S,\omega) &= (\lambda_d + i\omega) \sum\nolimits_{k\neq d} w_{ik} \widetilde{P}_k\left(S - \frac{w_{ik}}{w_{ki}}, \omega\right) + w_{id} w_{di} \widetilde{P}_i(S,\omega) \\ &\quad + w_{id} \sum_{\substack{k\neq d \\ k\neq i}} w_{dk} \tilde{P}_k\left(S - \frac{w_{dk} w_{id}}{w_{kd} w_{di}}, \omega\right). \quad (12)\end{aligned}$$

Third, we perform the inverse Fourier transform on $\widetilde{P}_i(S,\omega)$, and we obtain second-order differential equations. However, we only retain the first-order terms in t, i.e. $\mathcal{O}(t)$ therefore considering a *Markovianized approximation* [51]. In order to get the same mean EPR as the mean total EPR (TM) after coarse-graining at steady-state, we use an approximation following [51] for the proportionality relation between states i and j at steady state $\partial_t P_i \to (\pi_i/\pi_j)\partial_t P_j$.

After the decimation of state d (i.e. redistributing $P_d(S,t)$ among other states), the remaining states have renormalized probabilities that sum up to 1. If state d is decimated, then the probability of being in the decimated state d in the *coarse-grained system* equals zero, $P_d^{\mathrm{CG}} = 0$.However, the occupation probabilities of the rest of the states $i \neq d$are affected by the transition probability ($\varpi_{id} = w_{id}/\sum_k w_{kd} = w_{id}/\lambda_d$) from the decimated state d to state i in order to preserve the population density. Thus, in the fourth and the last step, the probabilities are renormalized according to $P_i^{\mathrm{CG}} = P_i + \varpi_{id} P_d = P_i + P_d w_{id}/\lambda_d$, where P_i^{CG} is the probability of the coarse-grained state i, P_i is the probability before the coarse-graining, and ϖ_{id} is the transition probability from state d to state i. The transition probability is given by the ratio of the transition rate from state d to state i (w_{id}) to the total exit rate from state d (λ_d), i.e. $\varpi_{id} = P_d w_{id}/\lambda_d$.

Using $P_i^{\mathrm{CG}} \sim P_i(1 + \pi_d w_{id}/\lambda_d \pi_i)$ as an approximation [51], and consider this relation to hold throughout the evolution, we find the relation between the probabilities

DISTRIBUTION A: Distribution approved for public release.

of a state before and after the decimation. From, $P_i^{\mathrm{CG}} \sim P_i\left(1+\pi_d w_{id}/\lambda_d \pi_i\right)$ we get

$$P_i = \frac{P_i^{\mathrm{CG}}}{\gamma_i}, \; i \neq d \tag{13}$$

where $\gamma_i = 1 + \frac{w_{id}\pi_d}{\lambda_d \pi_i}$, and $\lambda_d = \sum_{j\neq d} w_{jd}$.

The equation in terms of the probability distribution function for the EP of the coarse-grained state is written by

$$\begin{aligned} d_t P_i^{\mathrm{CG}}(S,t) = N_i^{-1}\Bigg[& -\left(\lambda_i\lambda_d - w_{id}w_{di}\right) P_i^{\mathrm{CG}}(S,t) \\ & + \sum\nolimits_{k\neq i,d} \frac{\gamma_i}{\gamma_k}\left(\lambda_d w_{ik} P_k^{\mathrm{CG}}\left(S - \frac{w_{ik}}{w_{ki}}, t\right)\right. \\ & \left. + w_{id}w_{dk} P_k^{\mathrm{CG}}\left(S - \frac{w_{id}w_{dk}}{w_{di}w_{kd}}, t\right)\right)\Bigg] \end{aligned} \tag{14}$$

where $N_i = \left(\lambda_i + \lambda_d - \sum_{j\neq i,d} w_{ij}a_{ji}\right)$ and $a_{ij} = (\pi_i/\pi_j)$.

We now write the equations for the transformed variable associated with the coarse-grained states,$G_i^{\mathrm{CG}}(\Lambda,t) = \sum_s e^{\Lambda S} P_i^{\mathrm{CG}}(S,t)$, as follows:

$$\begin{aligned} d_t G_i^{\mathrm{CG}}(\Lambda,t) = N_i^{-1}\Bigg[& -\left(\lambda_i\lambda_d - w_{id}w_{di}\right) G_i^{\mathrm{CG}}(\Lambda,t) \\ & + \sum\nolimits_{k\neq i,d} \frac{\gamma_i}{\gamma_k}\left(\lambda_d w_{ik} e^{\Lambda log\left(\frac{w_{ik}}{w_{ki}}\right)}\right. \\ & \left. + w_{id}w_{dk} e^{\Lambda log\left(\frac{w_{id}w_{dk}}{w_{di}w_{kd}}\right)}\right) G_k^{\mathrm{CG}}(\Lambda,t)\Bigg]. \end{aligned} \tag{15}$$

We want to emphasize that G_i^{CG} is also a function of the transition rates w_{ji}, but for the sake of simplicity, we show the explicit dependencies only on Λ and t. In matrix notation, equation (15) can be written as

$$d_t G_i^{\mathrm{CG}}(\Lambda,t) = \Gamma^{\mathrm{SCGF}} G_i^{\mathrm{CG}}(\Lambda,t) \tag{16}$$

with the matrix elements of Γ^{SCGF} being

$$\begin{aligned} & \left[\Gamma^{\mathrm{SCGF}}\right]_{ji} \\ & = \begin{cases} N_i^{-1}\sum_{k\neq i,d}\frac{\gamma_i}{\gamma_k}\left(\lambda_d w_{ik} e^{\Lambda log\left(\frac{w_{ik}}{w_{ki}}\right)} + w_{id}w_{dk} e^{\Lambda \log\left(\frac{w_{id}w_{dk}}{w_{di}w_{kd}}\right)}\right), & i \neq j \\ N_i^{-1}\left[\left(-\lambda_i\lambda_d + w_{id}w_{di}\right)\right], & i = j \end{cases}. \end{aligned} \tag{17}$$

We calculate the mean EPR from the scaled cumulant generating function, $\Omega^{\mathrm{SCGF}}(\Lambda)$, which is the dominant eigenvalue of the 3×3 tilted transition matrix $\left(\Gamma^{\mathrm{SCGF}}\right)$. The mean EPR (σ^{SCGF}) is calculated in the following way

$$\sigma^{\mathrm{SCGF}} = \partial_\Lambda \Omega^{\mathrm{SCGF}}(\Lambda)\,|_{\Lambda\to 0}. \tag{18}$$

We refer to this mean EPR as SCGF (figure 2) as this quantity is calculated from the scaled cumulant generating function of the EP.

As mentioned earlier at the end of section 3, we consider the coarse-grained system dynamics to follow an AM equation with effective transition rates, derived from equation (14). We write the approximated equation governed by the probability density of the coarse-grained system to be in the coarse-grained state i (where $i = i\backslash\{d\}$) at time t as the following,

$$\begin{aligned} d_t P_i^{\mathrm{CG,approx}}(t) = N_i^{-1}\Bigg[& -\left(\lambda_i\lambda_d - w_{id}w_{di}\right) P_i^{\mathrm{CG,approx}}(t) \\ & + \sum\nolimits_{k\neq i,d}\frac{\gamma_i}{\gamma_k}\left(\lambda_d w_{ik} + w_{id}w_{dk}\right) P_k^{\mathrm{CG,approx}}(t)\Bigg]. \end{aligned} \tag{19}$$

In terms of the probability distribution of the EP, $P_i^{\mathrm{CG,approx}}(S,t)$, we obtain similar equation as equation (14), which we can rewrite in terms of the generating function, $G_i^{\mathrm{approx}}(\Lambda,t) = \sum_S e^{\Lambda S} P_i^{\mathrm{CG,approx}}(S,t)$,

$$\begin{aligned} d_t G_i^{\mathrm{approx}}(\Lambda,t) = N_i^{-1}\Bigg[& -\left(\lambda_i\lambda_d - w_{id}w_{di}\right) G_i^{\mathrm{approx}}(\Lambda,t) \\ & + \sum\nolimits_{k\neq i,d}\frac{\gamma_i}{\gamma_k}\left(\lambda_d w_{ik} + w_{id}w_{dk}\right) G_k^{\mathrm{CG,approx}}(\Lambda,t)\Bigg]. \end{aligned} \tag{20}$$

In matrix notation which reads as $d_t G_i^{\mathrm{approx}} = \Gamma^{\mathrm{AM}} G_i^{\mathrm{approx}}$, where AM stands for EP obtained from the AM equation. As previously, a tilted matrix, Γ^{AM}, is used to calculate the mean EPR

$$\left[\Gamma^{AM}\right]_{ji} = \begin{cases} N_i^{-1}\sum_{k\neq i,d}\frac{\gamma_i}{\gamma_k}\left(\lambda_d w_{ik} + w_{id}w_{dk}\right), & i \neq j \\ N_i^{-1}\left(-\lambda_i\lambda_d + w_{id}w_{di}\right), & i = j \end{cases}. \tag{21}$$

We obtain the mean EPR from the dominant eigenvalue of the above matrix, $\Omega^{AM}(\Lambda)$:

$$\sigma^{\mathrm{AM}} = \partial_\Lambda \Omega^{\mathrm{AM}}(\Lambda)\,|_{\Lambda\to 0}. \tag{22}$$

The mean EPR calculated using this value is shown as AM in figure 2.

1.4. Coarse graining via lumping

A different strategy of coarse-graining is lumping several microstates into a single mesostate H. Our goal is to find a rate matrix by the lumping method [49] where the coarse-grained system dynamics follow an AM equation. The probabilities of the merged states, $i \in H$, are summed up, while the steady states probabilities of the rest of the states remain unchanged,

$$P_k^{\mathrm{CG}} = \begin{cases} \sum_{i\in H} P_i & k = H \\ P_k & k \notin H \end{cases}. \tag{23}$$

In this scenario, the coarse-grained transition rates are modified to conserve the steady-state probabilities and the transition flux among all the states except for the flux between the merged states, so the coarse-grained system is expected to have similar steady-state properties as the original system [49]. As the affinity is not preserved in this method, the EPR of the

DISTRIBUTION A: Distribution approved for public release.

coarse-grained system is changed. The modified rates for the AM equation are as follows [49]:

$$\begin{aligned} w_{mk}^{CG} &= w_{mk}, \quad m,k \notin H, \\ w_{mk}^{CG} &= \sum_{\substack{m \in H, \\ k \notin H}} w_{mk} \\ w_{km}^{CG} &= \left(w_{km}P_m + w_{kn}P_n\right)/\left(P_m + P_n\right), k \notin H, m,n \in H \end{aligned} \quad (24)$$

These transition rates are proven to minimize the KLD of the trajectories and can be used for lumping any two states even without a timescale separation [49]. The diagonal terms of the coarse-grained transition matrix are $w_{kk}^{CG} = -\sum_{k \neq l} w_{kl}^{CG}$. We calculate the mean EPR from the following tilted transition matrix

$$[\Xi]_{ji} = \begin{cases} w_{ji}^{CG} e^{\Lambda \log\left[w_{ji}^{CG}/w_{ij}^{CG}\right]}, i \neq j \\ -\sum_{j \neq i} w_{ji}^{CG}, \qquad i = j \end{cases}. \quad (25)$$

The mean EPR is obtained from the dominant eigenvalue of the matrix, $\Omega^{\mathrm{L}}(\Lambda)$.

$$\sigma^{\mathrm{L}} = \partial_\lambda \Omega^{\mathrm{L}}(\Lambda)\,|_{\Lambda \to 0} \quad (26)$$

where the mean EPR from this matrix is referred to in figure 2 as L (lumping with preserving steady-state properties).

Hummer and Szabo [50] developed another procedure for defining a transition rate matrix for a coarse-grained system. Their method ensures that the time-dependent occupancy number correlation functions in the coarse-grained system are equal to the ones of the original system. The same reduced matrix (rate matrix for the coarse-grained system) can be obtained from the projection operator technique. In the approximated Markovian limit, the reduced transition rate matrix was calculated analytically [50]. This coarse-graining procedure of merging or lumping microstates into a single merged state was suggested to be used for optimal aggregation and applied to Markov chains, random walk models, models with discrete states and discrete time, and with continuous states and discrete time. This coarse-graining method works well at intermediate timescale. The autocorrelation function between coarse-grained states I and J at time t is defined by $\langle \theta_I(t)\,\theta_J(0)\rangle$, where $\theta_I(t)$ equals 1 when the system is at state I. The autocorrelation function of the coarse-grained system and the full system are related by $\langle \theta_I(t)\,\theta_J(0)\rangle = \sum_{\substack{i \in I, \\ j \in J}} \langle \theta_i(t)\,\theta_j(0)\rangle$. At the Markovian limit, the reduced matrix $\boldsymbol{R}$ is given by [50]:

$$\boldsymbol{R} = \boldsymbol{P}_{\mathrm{eq}} 1_N{}^{\mathrm{T}} - \boldsymbol{D}_N \left(\boldsymbol{A}^{\mathrm{T}} \left(\boldsymbol{p}_{\mathrm{eq}} 1_n{}^{\mathrm{T}} - \boldsymbol{K}\right)^{-1} \boldsymbol{D}_n \boldsymbol{A}\right)^{-1} \quad (27)$$

where the initial rate matrix $\boldsymbol{K}$ is of order n-by-n (being the number of microstates), and the reduced matrix $\boldsymbol{R}$ is of the order of N-by-N (N is the number of coarse-grained states after merging). The normalized equilibrium probability density for the merged state I is given by $\boldsymbol{P}_{\mathrm{eq}}$, and the matrix obeys $\boldsymbol{R}\boldsymbol{P}_{\mathrm{eq}} = 0$, where $\boldsymbol{P}_{\mathrm{eq}}$ is a column vector with entries $P_{\mathrm{eq}}(I)$. The elements with the suffix N (n) refer to the merged states (constituent microstates). $\boldsymbol{D}_N$ and $\boldsymbol{D}_n$ are the diagonal matrices with the equilibrium distributions as diagonal elements. 1_N is the unit matrix of dimension N-by-N. $\boldsymbol{A}$ is the adjacency matrix of dimension n-by-N, defined as $A_{iI} = 1$ for $i \in I$. The adjacency matrix ($\boldsymbol{A}$) was introduced to map the coarse-grained system onto the full system via matrix notation. Note that the expression in equation (27) for the coarse-grained system is a reduced form of the full system transition rate matrix $\boldsymbol{K}$. The reduced matrix can have negative off-diagonal elements [50], and therefore, it is not a 'true' transition rate matrix. We calculate the mean EPR from the tilted transition matrix $\widehat{\boldsymbol{R}}$, and call it HS.

$$\left[\widehat{\boldsymbol{R}}\right]_{ji} = \begin{cases} [\boldsymbol{R}]_{ji} e^{\Lambda \log\left[[\boldsymbol{R}]_{ji}/[\boldsymbol{R}]_{ij}\right]}, i \neq j \\ -\sum_{j \neq i} [\boldsymbol{R}]_{ji} \qquad i = j \end{cases} \quad (28)$$

where $[\boldsymbol{R}]_{ji}$ is the ji^{th} element of the transition matrix $\boldsymbol{R}$. HS is calculated from the dominant eigenvalue of the matrix, $\Omega^{\mathrm{HS}}(\Lambda)$,

$$\sigma^{\mathrm{HS}} = \partial_\Lambda \Omega^{\mathrm{HS}}(\Lambda)\,|_{\Lambda \to 0}. \quad (29)$$

We compare the mean EPR values obtained from the lumping and decimation coarse-graining methods, with the informed partial EP for the networks shown in figure 2. The results are presented and discussed in the next section.

2. Results and discussion

In this section, we compare EPR obtained from different methods like SCGF, AM (AM equation), L (coarse-graining method where the transition flux among all states except the merged states and the steady state probabilities are preserved), IPEP (considering parameter dependent transition rates between the observed states), HS (considering the time dependent occupation number correlation function to be preserved) with TM (true mean value of the EPR considering all the edges). The closer the mean EPR values predicted from different coarse-graining methods to the TM, the better is the prediction. In all the methods mentioned above, we consider the coarse-grained system dynamics to follow AM equations. Therefore, the error of the approximation is expected to be smaller if there is a timescale separation (except for the lumping). Except for SCGF, all other state-based coarse-graining methods (AM, L, HS) are calculated from tilted matrices based on the corresponding modified rate matrices, given by equations (21), (25), and (27), respectively. We calculate the mean EPRs from different state-based coarse-graining methods like lumping and decimation and compare them with the mean EPR obtained from partial information of only the observed link, i.e. IPEP (equation (2)). For partially observed systems, we always get lower bounds on the total EPR. Therefore, the higher the bound, the better it is, as it provides a tighter estimation of the total EPR.

We plot TM, SCGF, AM, L, and IPEP as a function of dimensionless driving forces ($F = \beta \tilde{F} L$) for different network topologies, as shown in figure 1. All the parameter values are

DISTRIBUTION A: Distribution approved for public release.

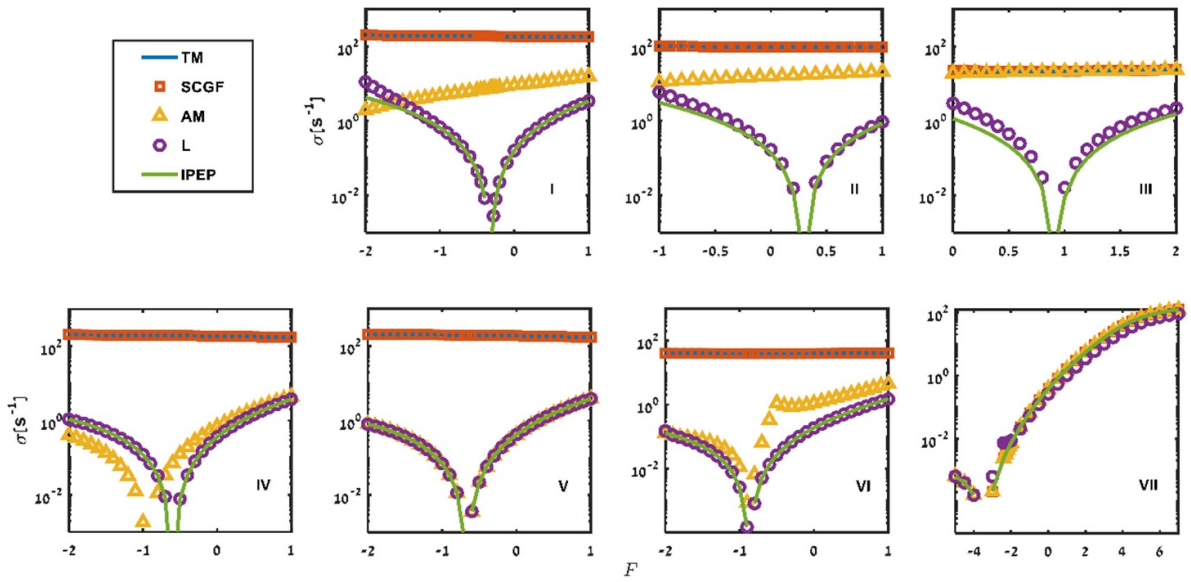


Figure 2. Mean EPR estimation from the total mean (TM) or σ^{TM}, scaled cumulant generating function (SCGF or σ^{SCGF}), from approximated master equation (AM or σ^{AM}), lumping by preserving the transition flux and steady-state probabilities (L or σ^{L}), informed partial entropy production (IPEP or σ^{IPEP}) for different network topologies. The parameter values for each subplot (network topology, I–VII) are the same as mentioned in figure 1. The ranges of the x-axes were chosen to include the stall force and to show the behavior of the estimators around and away from it.

given in the caption of figure 1, and the subplots of figure 2 correspond to the same network topologies as in figure 1.

In figure 2, we present TM, SCGF, AM, L, and IPEP correspond to σ^{TM}, σ^{SCGF}, σ^{AM}, σ^{L}, and σ^{IPEP} as calculated using equations (8), (18), (22), (26), and (2), respectively. TM provides the mean EPR for fully observed systems, so the closer the EPR bounds to the TM, the better the estimators. The mean EPR obtained from the scaled cumulant generating function of the EP (σ^{SCGF} or SCGF) by decimating one of the states (applying all the constraints mentioned before equation (13)) always estimates the total mean EPR (σ^{TM} or TM), as expected. In other words, the decimation procedure is constructed in a manner that it reproduces the mean EPR at steady states. As the EPR's are calculated at the steady state, the EPR from the scaled cumulant generating function exactly produces the TM. In the following, we compare the AM, L, HS, and IPEP with the total mean EPR values (TM) for all the network topologies.

The EPR calculated from the AM Equation (σ^{AM} or AM) provides a lower bound on the total mean EPR (σ^{TM} or TM), since after decimation, the coarse-grained system is not Markovian, and therefore, the AM cannot capture the total EP. When the hidden substates are disconnected (network topology III and VII in figure 1), we do not lose any cycles carrying transition currents in the coarse-graining, so the AM provides values closer to the total mean EPR (σ^{TM}). We note that for topology VII (figure 1), the observed information is sufficient for precisely inferring the total EP, since the observed cycle is the only entropy-producing fundamental cycle in the network, and the AM equals the total EPR (TM). In that case, the IPEP also equals the total EPR, as expected [18].

We further compare the mean EPR from a state-based coarse-graining (L), i.e. lumping by conserving the steady-state probabilities and the transition fluxes between all states except the merged states, with the IPEP. Since it is difficult to compare based on the subplots in figure 2, we plot $\left|\sigma^{\mathrm{IPEP}}-\sigma^{\mathrm{L}}\right|/\sigma^{\mathrm{IPEP}}$ in figure 3, as a function of the driving force F in semi-log plots. From figure 3(a), we find the difference between L and IPEP is larger for network topology III compared to I, near their corresponding stall forces (labeled with dash-dotted lines). For network topology V (figure 3(b)), with connected hidden states, the difference between σ^{L} and σ^{IPEP} is less than 0.1% for the range of F values tested around the stall force, whereas for network topology VII, with disconnected hidden states, the difference $\left|\sigma^{\mathrm{IPEP}}-\sigma^{\mathrm{L}}\right|/\sigma^{\mathrm{IPEP}}$ is approximately two orders of magnitude larger compared to topology V, near the corresponding stall force. IPEP accounts for the hidden states transition information via a single rate, which is missing if the hidden states are disconnected, and therefore, the difference between the L and IPEP increases.

IPEP is calculated from the observed cycle affinity, whereas L is based on preserving the steady state properties of the system, e.g. the probabilities and the transition fluxes. So, it is difficult to compare the trade-offs between the input information provided and its output (mean EPR estimation). We find that for connected hidden substates (network topology I and V), the difference between L and IPEP is smaller compared to disconnected hidden substates (network topology III and VII) at their respective stall forces.

In figure 4, we compare the EPR obtained from the two lumping methods described in section 5, namely, L, where the steady-state probabilities and the transition flux between the observed states are preserved, and HS, where the auto-correlation function of the population for the coarse-grained states is the same as the full system. Both methods consider the coarse-grained system to follow approximated Markovian dynamics, and therefore, the error in the approximation

DISTRIBUTION A: Distribution approved for public release.

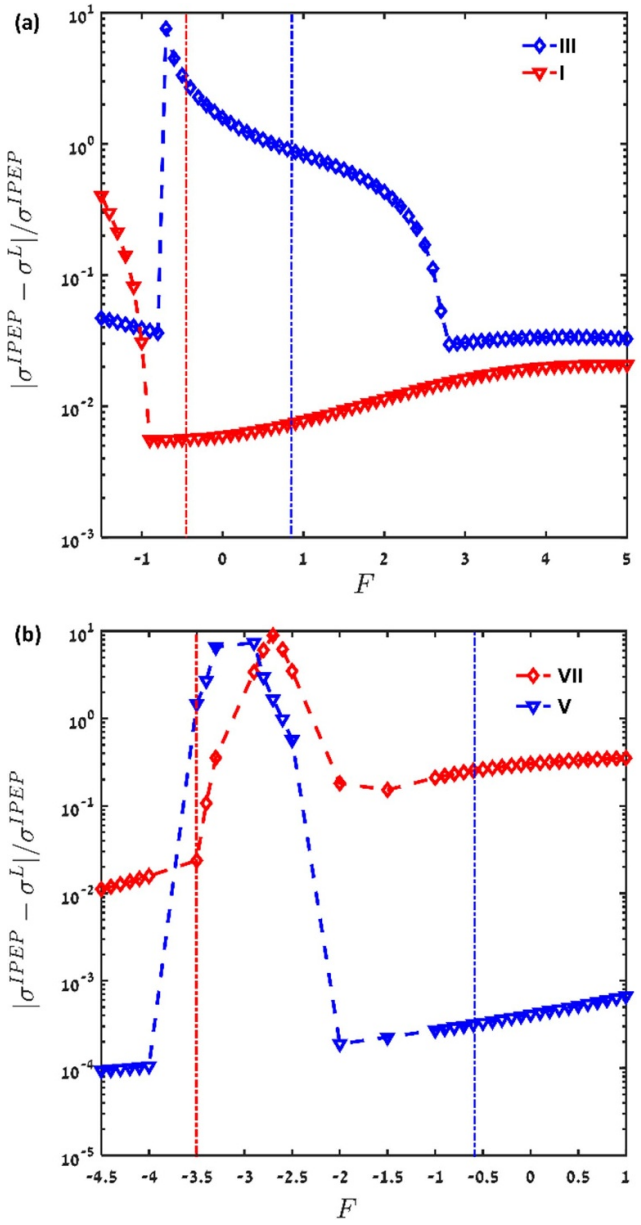


Figure 3. Comparison of σ^{IPEP} and σ^{L} as a function of the dimensionless driving force (F) for different network topologies: weight of the connectivity of the hidden substates and in between state 1 and state 3 are given by ν and μ, respectively. The parameters used have the same values as mentioned in figure 1. (a) Red downward triangles and blue diamonds refer to network topology I and III, respectively. (b) Blue downward triangles and red diamonds refer to network topologies V and VII, respectively. The lines are drawn to guide the eye. The stalling forces are labeled by dash-dotted lines for each topology.

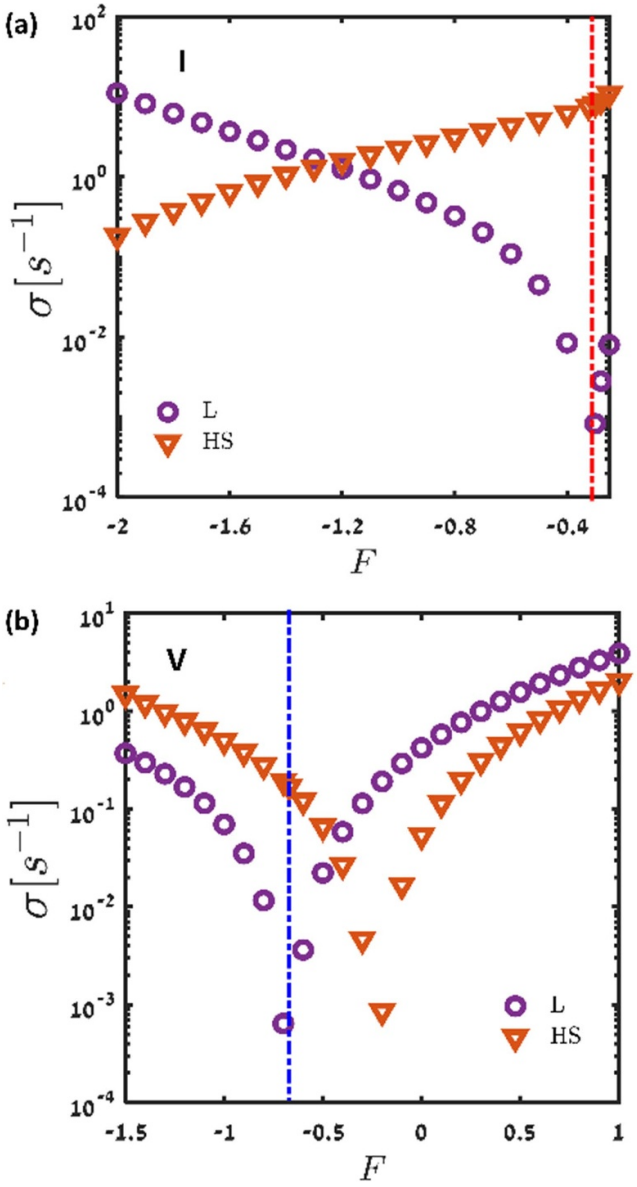


Figure 4. Comparison between two lumping methods (L and HS) for (a) network topology I and (b) network topology V. The parameter values are the same as given in figure 1. The red downward triangles denote the HS method, and the purple circles refer to the L method. The stalling forces are labeled with dashed-dotted (a) red line for topology I, and (b) blue line for topology V.

varies depending on the timescale separation. The coarse-grained transition rates in equation (24) are based on minimizing the KLD between the trajectories, whereas the reduced matrix in equation (25) is constructed to maximize the relaxation time of the reduced matrix so that the coarse-grained system would have the same characteristic time as the full system.

For both network topologies I (figure 4(a)) and V (figure 4(b)), L dominates over HS for certain driving parameter values (F), whereas for other driving parameter values, HS dominates over L. At stalling force, HS results in larger EPR values compared to L. The non-diagonal elements of the reduced matrix of topology I (equation (27)) become negative above a certain driving force ($F > -0.25$) [50], and therefore we are unable to calculate HS beyond this value (figure 4(a)). As the HS coarse-graining approximation's accuracy depends on the timescale separation between the states undergoing merging

DISTRIBUTION A: Distribution approved for public release.

and in between the merged states, EPR prediction using this coarse-graining method also depends on the intrinsic timescale difference. However, the method predicting L can be used without a timescale separation. Therefore, the performance of the estimators for the two coarse-graining approaches depends on the system at hand. The optimal Markov matrix, R (equation (27)), was calculated based on the assumption that there are no disconnected microstates, according to HS [50]. Therefore, we only compare the results among the two lumping methods for network topology I (figure 4(a)) and topology V (figure 4(b)) of figure 1.

3. Conclusion

This paper studies different notions of partial information in driven systems and the corresponding mean EPR values associated with them. The predicted EPR values are then compared with the true mean EPR (TM) which is calculated considering all the edges of the network topology, where tighter lower bounds on the TM EPR are considered better. The SCGF, which is calculated for coarse-graining by decimation and redistribution of the steady-state probabilities and transition rates, produces the total mean EPR (TM), as expected. For the other coarse-graining approaches, systems are considered to follow approximated Markovian dynamics, and the resulting modified/coarse-grained transition rate matrices are used to calculate the mean EPRs for different methods (AM, L, HS). For certain topologies, we find that as we decrease the hidden state connectivity, the AM approaches the total mean EPR (topologies I, II, and III) since the contribution to the EPR from the loss cycles carrying transition flux decreases. By comparing the mean EPR values calculated from the state-based coarse-graining methods, namely, lumping (L, HS) and coarse-graining by decimation (SCGF, AM), where one is assumed to know the network topology, with the mean EPR inferred from partial information of only the observed states and the transitions between them (IPEP), we find that the effect of the partial information reflected on the inferred EPR for state-based coarse-graining depends on the network topology. Further, IPEP provides similar entropic information as one would obtain by L, a state-based coarse-graining (lumping with preserving the steady-state properties), where the difference between is bigger for disconnected hidden substates (topologies III and VII), compared to the networks with connected hidden substates (topologies I and III) at their corresponding stall force. Hidden state information inferred by the IPEP is lost for disconnected hidden substates, and due to this missing information, the difference between L and IPEP increases with decreasing connectivity between the hidden substates. The difference between the HS and L varies as a function of the stalling force, and the timescale difference plays a role in it. HS is sensitive towards the timescale separation in between the merged states and between two merged states, whereas L does not depend on the timescale separation. Our study can be extended to larger systems with more than two hidden microstates, or having a hidden cycle current, etc.

Data availability statement

All data that support the findings of this study are included within the article (and any supplementary files).

Acknowledgments

G Bisker acknowledges the Zuckerman STEM Leadership Program, and the Tel Aviv University Center for AI and Data Science (TAD). A Ghosal acknowledges the support of the Pikovsky Valazzi scholarship. This work was supported by the ERC NanoNonEq 101039127, the Air Force Office of Scientific Research (AFOSR) under Award Number FA9550-20-1-0426, and by the Army Research Office (ARO) under Grant No. W911NF-21-1-0101. The views and conclusions contained in this document are those of the authors and should not be interpreted as representing the official policies, either expressed or implied, of the Army Research Office or the U.S. Government. A Ghosal acknowledges helpful discussion with Dr Gianluca Teza.

ORCID iD

Gili Bisker https://orcid.org/0000-0003-2592-7956

References

[1] Den Broeck C V and Esposito M 2015 Ensemble and trajectory thermodynamics: a brief introduction *Physica* A **418** 6–16
[2] Seifert U 2012 Stochastic thermodynamics, fluctuation theorems and molecular machines *Rep. Prog. Phys.* **75** 126001
[3] Bo S, Del Giudice M and Celani A 2015 Thermodynamic limits to information harvesting by sensory systems *J. Stat. Mech. Theory Exp.* **2015** P01014
[4] Saadat N P, Nies T, Rousset Y and Ebenhö O 2020 Thermodynamic limits and optimality of microbial growth *Entropy* **22** 1–19
[5] Fang X and Wang J 2020 Nonequilibrium thermodynamics in cell biology: extending equilibrium formalism to cover living systems *Annu. Rev. Biophys.* **49** 227–46
[6] Sartori P and Pigolotti S 2015 Thermodynamics of error correction *Phys. Rev.* X **5** 1–9
[7] Gnesotto F S, Mura F, Gladrow J and Broedersz C P 2018 Broken detailed balance and non-equilibrium dynamics in living systems: a review *Rep. Prog. Phys.* **81** 066601
[8] Sekimoto K 2010 *Stochastic Energetics* (*Lecture Notes in Physics* vol 53) (Springer) (Accessed 1 January 1764)
[9] Chiang K H, Chou C W, Lee C L, Lai P Y and Chen Y F 2016 Fluctuations of entropy production in partially masked electric circuits *Europhys. Lett.* **113** 30001
[10] Mehl J, Lander B, Bechinger C, Blickle V and Seifert U 2012 Role of hidden slow degrees of freedom in the fluctuation theorem *Phys. Rev. Lett.* **108** 1–5
[11] Seifert U 2019 From stochastic thermodynamics to thermodynamic inference *Annu. Rev. Condens. Matter Phys.* **10** 171–92
[12] Horowitz J M and Gingrich T R 2020 Thermodynamic uncertainty relations constrain non-equilibrium fluctuations *Nat. Phys.* **16** 15–20

DISTRIBUTION A: Distribution approved for public release.

[13] Li J, Horowitz J M, Gingrich T R and Fakhri N 2019 Quantifying dissipation using fluctuating currents *Nat. Commun.* **10** 1666
[14] Gingrich T R, Horowitz J M, Perunov N and England J L 2016 Dissipation bounds all steady-state current fluctuations *Phys. Rev. Lett.* **116** 1–5
[15] Gingrich T R and Horowitz J M 2017 Fundamental bounds on first passage time fluctuations for currents *Phys. Rev. Lett.* **119** 1–6
[16] Wampler T and Barato A C 2021 Skewness and kurtosis in stochastic thermodynamics *J. Phys.* A **55** 014002
[17] Pal A, Reuveni S and Rahav S 2021 Thermodynamic uncertainty relation for first-passage times on Markov chains *Phys. Rev. Res.* **3** 1–6
[18] Bisker G, Polettini M, Gingrich T R and Horowitz J M 2017 Hierarchical bounds on entropy production inferred from partial information *J. Stat. Mech. Theory Exp.* **2017** aa8c0d
[19] Martínez I A, Bisker G, Horowitz J M and Parrondo J M R R 2019 Inferring broken detailed balance in the absence of observable currents *Nat. Commun.* **10** 1–10
[20] Ghosal A and Bisker G 2022 Inferring entropy production rate from partially observed Langevin dynamics under coarse-graining *Phys. Chem. Chem. Phys.* **24** 24021–31
[21] Shiraishi N, Ito S, Kawaguchi K and Sagawa T 2015 Role of measurement-feedback separation in autonomous Maxwell's demons *New J. Phys.* **17** 045012
[22] Shiraishi N and Sagawa T 2015 Fluctuation theorem for partially masked nonequilibrium dynamics *Phys. Rev.* E **91** 3–8
[23] Polettini M and Esposito M 2017 Effective thermodynamics for a marginal observer *Phys. Rev. Lett.* **119** 1–5
[24] Harunari P E, Dutta A, Polettini M and Roldán É 2022 What to learn from few visible transitions' statistics? *Phys. Rev.* X **12** 1–22
[25] van der Meer J, Ertel B and Seifert U 2022 Thermodynamic inference in partially accessible Markov networks: a unifying perspective from transition-based waiting time distributions *Phys. Rev.* X **12**
[26] Bo S and Celani A 2017 Multiple-scale stochastic processes: decimation, averaging and beyond *Phys. Rep.* **670** 1–59
[27] Bo S and Celani A 2014 Entropy production in stochastic systems with fast and slow time-scales *J. Stat. Phys.* **154** 1325–51
[28] Puglisi A, Pigolotti S, Rondoni L and Vulpiani A 2010 Entropy production and coarse graining in Markov processes *J. Stat. Mech. Theory Exp.* **2010** P05015
[29] Rahav S and Jarzynski C 2007 Fluctuation relations and coarse-graining *J. Stat. Mech. Theory Exp.* **2007** P09012
[30] Teza G and Stella A L 2020 Exact coarse graining preserves entropy production out of equilibrium *Phys. Rev. Lett.* **125** 110601
[31] Knoch F and Speck T 2015 Cycle representatives for the coarse-graining of systems driven into a non-equilibrium steady state *New J. Phys.* **17** 115004
[32] Altaner B and Vollmer J 2012 Fluctuation-preserving coarse graining for biochemical systems *Phys. Rev. Lett.* **108** 1–5
[33] Polettini M and Esposito M 2019 Effective fluctuation and response theory *J. Stat. Phys.* **176** 94–168
[34] Bisker G, Martinez I A, Horowitz J M and Parrondo J M 2022 Comment on inferring broken detailed balance in the absence of observable currents (arXiv:2202.02064)
[35] Hartich D and Godec A 2021 Comment on inferring broken detailed balance in the absence of observable currents (arXiv:2112.08978)
[36] Ehrich J 2021 Tightest bound on hidden entropy production from partially observed dynamics *J. Stat. Mech. Theory Exp.* **2021** 083214
[37] Skinner D J and Dunkel J 2021 Improved bounds on entropy production in living systems *Proc. Natl Acad. Sci. USA* **118**
[38] Skinner D J and Dunkel J 2021 Estimating entropy production from waiting time distributions *Phys. Rev. Lett.* **127** 198101
[39] Kapustin U, Ghosal A and Bisker G 2022 Utilizing time-series measurements for entropy production estimation in partially observed systems (arXiv:2212.13487)
[40] Nitzan E, Ghosal A and Bisker G 2022 Universal bounds on entropy production inferred from observed statistics (arXiv:2212.01783)
[41] Kawaguchi K and Nakayama Y 2013 Fluctuation theorem for hidden entropy production *Phys. Rev.* E **88** 1–5
[42] Zimmermann E and Seifert U 2015 Effective rates from thermodynamically consistent coarse-graining of models for molecular motors with probe particles *Phys. Rev.* E **91** 1–16
[43] Esposito M 2012 Stochastic thermodynamics under coarse graining *Phys. Rev.* E **85** 1–11
[44] Borrelli M, Koski J V, Maniscalco S and Pekola J P 2015 Fluctuation relations for driven coupled classical two-level systems with incomplete measurements *Phys. Rev.* E **91** 1–8
[45] Esposito M and Parrondo J M R 2015 Stochastic thermodynamics of hidden pumps *Phys. Rev.* E **91** 1–7
[46] Horowitz J and Jarzynski C 2009 Illustrative example of the relationship between dissipation and relative entropy *Phys. Rev.* E **79** 1–7
[47] Gomez-Marin A, Parrondo J M R and Van Den Broeck C 2008 Lower bounds on dissipation upon coarse graining *Phys. Rev.* E **78** 1–11
[48] Kawai R, Parrondo J M R and Van Den Broeck C 2007 Dissipation: the phase-space perspective *Phys. Rev. Lett* **98** 1–4
[49] Seiferth D, Sollich P and Klumpp S 2020 Coarse graining of biochemical systems described by discrete stochastic dynamics *Phys. Rev.* E **102** 1–17
[50] Hummer G and Szabo A 2015 Optimal dimensionality reduction of multistate kinetic and Markov-state models *J. Phys. Chem.* B **119** 9029–37
[51] Teza G Out of equilibrium dynamics: from an entropy of the growth to the growth of the entropy production *PhD Thesis* (Padova: Universit̀adegliStudidi Padova)
[52] Dutta A, Schütz G M and Chowdhury D 2020 Stochastic thermodynamics and modes of operation of a ribosome: a network theoretic perspective *Phys. Rev.* E **101** 1–28
[53] Ertel B, van der Meer J and Seifert U 2021 Operationally accessible uncertainty relations for thermodynamically consistent semi-Markov processes *Phys. Rev.* E **105** 1–19
[54] Di Terlizzi I and Baiesi M 2018 Kinetic uncertainty relation *J. Phys. A: Math. Theor.* **52** 02LT03
[55] Ghosal A 2021 Statistics of reaction flux and dynamical activity associated with a diffusion-influenced ligand-binding reaction *J. Phys. Chem.* B **125** 1760–7

DISTRIBUTION A: Distribution approved for public release.

The Journal of Chemical Physics

Nonequilibrium self-assembly of multiple stored targets in a dimer-based system

Cite as: J. Chem. Phys. **155**, 234113 (2021); https://doi.org/10.1063/5.0069161
Submitted: 29 August 2021 • Accepted: 29 November 2021 • Published Online: 20 December 2021

Adi Ben-Ari, Liron Ben-Ari and Gili Bisker

View Online Export Citation CrossMark

ARTICLES YOU MAY BE INTERESTED IN

Modeling of biomolecular machines in non-equilibrium steady states
The Journal of Chemical Physics **155**, 230901 (2021); https://doi.org/10.1063/5.0070922

Gated reactions in discrete time and space
The Journal of Chemical Physics **155**, 234112 (2021); https://doi.org/10.1063/5.0072393

Fast quasi-centroid molecular dynamics
The Journal of Chemical Physics **155**, 231101 (2021); https://doi.org/10.1063/5.0076704

Lock-in Amplifiers up to 600 MHz
Zurich Instruments
Watch



© 2021 Author(s).

DISTRIBUTION A: Distribution approved for public release.

The Journal of Chemical Physics ARTICLE scitation.org/journal/jcp

Nonequilibrium self-assembly of multiple stored targets in a dimer-based system

Cite as: J. Chem. Phys. 155, 234113 (2021); doi: 10.1063/5.0069161
Submitted: 29 August 2021 • Accepted: 29 November 2021 •
Published Online: 20 December 2021

View Online Export Citation CrossMark

Adi Ben-Ari,[1] Liron Ben-Ari,[1] and Gili Bisker[2,3,a)]

AFFILIATIONS

[1] Faculty of Engineering, School of Electrical Engineering, Tel Aviv University, Tel Aviv 6997801, Israel
[2] Faculty of Engineering, Department of Biomedical Engineering, Tel Aviv University, Tel Aviv 6997801, Israel
[3] Center for Physics and Chemistry of Living Systems, Center for Nanoscience and Nanotechnology, Center for Light Matter Interaction, Tel Aviv University, Tel Aviv 6997801, Israel

[a)] **Author to whom correspondence should be addressed:** bisker@tauex.tau.ac.il

ABSTRACT

Nonequilibrium self-assembly can be found in various biological processes where chemical potential gradients are exploited to steer the system to a desired organized structure with a particular function. Microtubules, for example, are composed of two globular protein subunits, α-tubulin and β-tubulin, which bind together to form polar dimers that self-assemble a hollow cylinder structure in a process driven by GTPase activity. Inspired by this process, we define a generic self-assembly lattice model containing particles of two subunits, which is driven out-of-equilibrium by a dimer-favoring local driving force. Using Monte Carlo simulations, we characterize the ability of this system to restore pre-encoded target structures as a function of the initial seed size, interaction energy, chemical potential, number of target structures, and strength of the nonequilibrium drive. We demonstrate some intriguing consequences of the drive, such as a smaller critical seed and an improved target assembly stability, compared to the equilibrium scenario. Our results can expand the theoretical basis of nonequilibrium self-assembly and provide deeper understanding of how nonequilibrium driving can overcome equilibrium constraints.

Published under an exclusive license by AIP Publishing. https://doi.org/10.1063/5.0069161

I. INTRODUCTION

Self-assembly processes play a major role in every living system. Biology has given us numerous examples of many-body self-assembly, including the assembly of the ribosome,[1] protein folding,[2] virus capsids,[3] the nuclear pore complex,[4] and actin filaments.[5] Another key example, which is involved in various cellular functions, is microtubules—the most rigid form of cytoskeletal elements, built from 13 parallel filaments forming a tube. These filaments, called *protofilaments*, are chains of dimers, where each dimer is composed of α-tubulin and β-tubulin protein subunits.[6]

The astonishing examples of self-assembly nature has accomplished, encourage us to gain deeper understanding of such emergent organization in complex many-body systems. Analyzing generic model systems performing self-assembly can provide insights into biological processes, such as the assembly of protein complexes,[7] or possible universal aspects of genotype–phenotype maps.[8] Practically, such minimal models may provide ways for creating desirable molecular structures in practice, e.g., coating particles with certain patches for assembling rings, pyramids, or tetrahedra.[9] In addition, simulation of a relatively simplified model of the self-assembly of DNA origami can be performed to study various thermodynamical aspects of different origami designs.[10]

Minimal models have also been used in the investigation of active matter: nonequilibrium locally driven multicomponent systems, in which interacting particles perform collective directed motion.[11–14] Simulating a minimal model describing such collectively moving particles has shown a phase transition between a disordered and collective movement, estimated its critical exponents, and led to an insight into the applicability of the theoretical framework of critical phenomena to such a nonequilibrium process.[15] A different schematic model was used to obtain hydrodynamic equations for density and velocity fields of the particles, which are consistent with previous phenomenological results.[16]

Consequently, extensive research has been performed regarding self-assembly systems and their ability to restore multiple target structures as a function of temperature,[17] interaction topology,[18] interaction strength,[7,19–21] cooperativity,[22] chemical potential,[7,19,20] or the concentrations of components.[19,20,23]

Published under an exclusive license by AIP Publishing

DISTRIBUTION A: Distribution approved for public release.

In many cases, biological processes occur far-from-equilibrium, rendering the principle of free-energy minimization irrelevant. Such processes, for example, govern the dynamic instability of microtubules.[24] The tubulin dimers forming the microtubules bind guanosine-5′-triphosphate (GTP), where the β-tubulins hydrolyze GTP to guanosine 5′-diphosphate (GDP), destabilizing the assembly. Since the binding of more dimers to the protofilament catalyzes the GTP hydrolysis, the structure becomes less stable up to a *catastrophe*, where the microtubule falls apart and begins to shrink. In turn, the disassembled free dimers return to the GTP-state, promoting assembly and the *rescue* of the microtubule.[6] This is a nonequilibrium process fueled by the chemical potential difference between GTP and GDP in the cell cytosol and the GTPase activity of the β-tubulins in the protofilament.

Many studies have demonstrated experimentally nonequilibrium self-assembly driven by external forces. For example, the driving may be done by chemical fuel,[25] light,[26] or fluid flow.[27,28] Moreover, experiments have demonstrated the assembly of crystals in rotating magnetic fields,[29] GTP-driven assembly of microtubules,[30] and pH or temperature triggered self-assembly of dynamic covalent surfactants.[31]

From the theoretical perspective, several studies have focused on nonequilibrium self-assembly.[32] A toy lattice model with a local nonequilibrium driving force has shown improvements in both stability and assembly speed compared to the equilibrium dynamics.[33] Other systems, driven out-of-equilibrium by a global chemical potential driving force, were found to obey a set of thermodynamic bounds.[34] In addition, nonequilibrium driving by time-oscillatory inter-particle potentials was shown to result in nontrivial dissipative structures,[35] and a simple protocol of time-dependent interactions was shown to improve self-assembly in a model colloidal system.[36]

Inspired by the structure of microtubules, we present a generic toy model of a system having two-subunits coupled to heat and particle baths, which assembles pre-encoded target structures, driven out-of-equilibrium by a local driving force, which favors dimer formation. We analyze the properties of such a system for different interaction energies, chemical potential values, number of encoded targets, seed sizes, and nonequilibrium driving strengths and show several improvements in the ability of the system to restore pre-encoded target structures, including faster assembly, and a smaller critical seed. We also discuss the limitation of the proposed nonequilibrium drive, which is a higher rate of undesired targets assembly.

II. MODEL PROPERTIES

Our model consists of N species of particles: $\{i = 1, 2, \ldots, N\}$, where we assume that N is even and a square number. The species are divided into two groups: The first $N/2$ species are called *α-subunits* and the rest are called *β-subunits*. A particle of species i is denoted as s_i. The particles are placed on a 2D square lattice consisting of N_0 sites (N_0 is a square number), where each site can be either occupied by a single particle or empty. Each particle can interact with up to z other particles (nearest neighbors, denoted as n.n.), where the directionality of the bond of s_i with s_j is defined as $\delta = 1, 2, \ldots, z$. The system operates in the grand-canonical ensemble, with temperature T, and all species share the same chemical potential μ. In each simulation, there are m target structures, each one consists of M particles, where we choose $N_0 = 4M$. Throughout the simulations in this work, we used $N_0 = 400$, which is also the maximal number of particles that can be simultaneously present along the realization.

For our simulations, we take $M = N$ and $z = 4$, which means that $\delta = 1, 2, 3, 4$ stands for the directions *up, right, down*, and *left*, respectively. For simplicity, we take $k_B T \equiv 1$. This means that we measure E and μ in units of $k_B T$; thus, changing the temperature is equivalent to multiplying E and μ by a constant, while μ/E remains constant. We also note that the proposed model is described in the grand-canonical ensemble, namely, the lattice is coupled to both a particle-bath and a heat-bath, with which it can exchange particles and heat. Therefore, the chemical potential of each species is related to the concentration of this species in the particle-bath.

A. Target structures

We define a *target chain* as a row or a column of $\sqrt{M}$ particles of different species, where no two adjacent particles are of the same subunit. For example, for $M = N = 16$, a possible target chain is shown in Fig. 1(a).

Each target structure is a $\sqrt{M} \times \sqrt{M}$ square, made of $\sqrt{M}$ parallel target chains, where each chain contains different particles. An example of a possible target structure, for the same set of $\{M, N\}$ values, is shown in Fig. 1(b).

B. Energy

In this model, all particle species have zero internal energy. The interaction energy between two adjacent particles s_i, s_j where the directionality of s_j with respect to s_i is δ is given by

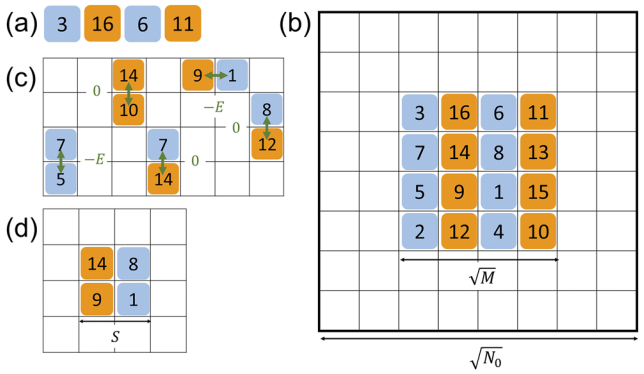


FIG. 1. Lattice model for $M = N = 16$. The blue squares represent α-subunits, the orange squares represent β-subunits, and the numbers represent the different species. (a) A possible target chain. (b) A possible target structure, containing the target chain from (a). The bold line represents the lattice borders. (c) Examples for interaction energies between pairs of particles, assuming that the target structure from (b) is the only one encoded. The interaction energy is non-zero only if the two particles are in the same configuration as in a certain target structure, including the same directionality. (d) A seed of the target structure from (b), which is the initial state of the lattice in our simulations.

Published under an exclusive license by AIP Publishing

DISTRIBUTION A: Distribution approved for public release.

$$U_{ij}^{\delta} = \begin{cases} -E, & s_i, s_j \text{ are n.n. with bond directionality } \delta \\ & \text{with respect to } s_i \text{ in any target,} \\ 0 & \text{otherwise.} \end{cases} \quad (1)$$

Examples for interaction energies between pairs of particles are depicted in Fig. 1(c).

C. Simulations

We run Monte Carlo (MC) simulations with the Metropolis algorithm.[37] In each simulation, the initial state of the lattice is the $S \times S$ central region of one of the target structures. This central part is a *seed* of length S, and the respective target structure is denoted as the *seeded* or *desired* target. An example for a seed is shown in Fig. 1(d). In each step, one of the N_0 sites of the lattice is chosen randomly. Then, a species from the set $\{0, 1, 2, \ldots, N\}$ is chosen randomly, where "0" stands for "unoccupied."

At equilibrium, the site accepts the new species with probability p_{eq},

$$p_{eq} = \min\left(1, e^{-\frac{\Delta U}{k_B T}}\right), \quad (2)$$

where ΔU is the difference in energy U between the proposed state and the current state, and U is defined as

$$U = \sum U_{ij}^{\delta} + \mu N_{oc}, \quad (3)$$

where N_{oc} is the current number of occupied sites and the summation is over all pairs of nearest neighbor particles s_i, s_j on the lattice.

Now that we have established the model properties at equilibrium, a nonequilibrium local driving force is added.

D. Driving force

The local driving force is included through a modulation of the acceptance probability of a Monte Carlo step,[33] p_{eq}. The essence of the proposed drive is increasing the acceptance probability of steps which promote the assembly of chains and thus breaking detailed balance. Formally, the driving force encourages the formation of the following structure: two neighbors of a particle along the same axis are of the same subunit, which is the opposite to the particle between them, namely, α–β–α or β–α–β triplets. We define such a structure as an *intermittent subunit triplet*. The new acceptance probability is

$$p_{neq} = \min\left(1, e^{-\frac{\Delta U - D}{k_B T}}\right), \quad (4)$$

where $D = \Delta\lambda$ if the proposed step completes an intermittent subunit triplet, $D = -\Delta\lambda$ if the proposed step destroys an existing intermittent subunit triplet, and otherwise $D = 0$. $\Delta\lambda$ is, therefore, the drive strength.

Whenever multiple triplets are affected by a proposed step, the value of D is determined by a majority voting of D values from all triplets involved, where tie means $D = 0$. Formally, we take $D = \Delta\lambda \times \text{sign}(\sum_i D_i)$, summing over all triplets affected by the proposed move. We note that such a definition accounts for a case where the mechanism creating the local driving force reaches a saturation value when the number of intermittent subunit triplets following a certain move is larger than the current number of intermittent subunit triplets by 1. This way, the saturation effect is realized with reasonable probability, and a driving force with a saturating nature is being modeled. Further elaboration can be found in the supplementary material, Sec. S1. Examples for several scenarios and their respective D values are shown in Fig. 2, along with an example for a cycle breaking detailed balance.

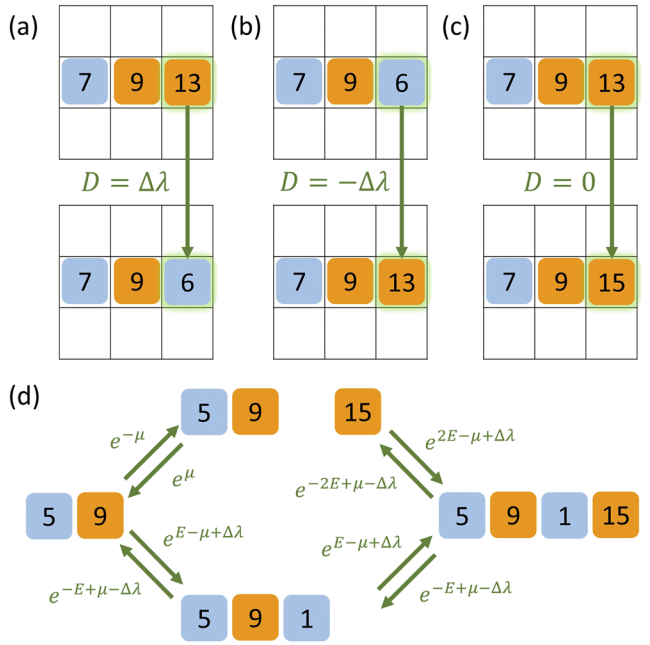


FIG. 2. Local driving force. (a)–(c) Examples of situations yielding different D values. The initial state is presented on top, and the proposed step at the bottom. (a) The initial state does not include an intermittent subunit triplet, and the proposed step does; thus, $D = \Delta\lambda$. (b) The initial state includes an intermittent subunit triplet, and the proposed step does not; thus, $D = -\Delta\lambda$. (c) Neither the initial state nor the proposed one includes an intermittent subunit triplet; thus, $D = 0$. (d) Example of a cycle breaking detailed balance. The acceptance probabilities of the moves appear near the corresponding arrows. The probability of moving from the leftmost state to the rightmost state depends on the path taken: the probability for the upper path is $p_u = \exp\{2E - 2\mu + \Delta\lambda\}$, while for the lower path $p_l = \exp\{2E - 2\mu + 2\Delta\lambda\}$, meaning $\ln(p_u/p_l) \neq 0$, i.e., broken detailed balance. Here, we assumed that the target structure from Fig. 1(b) is the only one encoded.

III. QUANTIFYING ASSEMBLY

In order to quantitatively characterize the assembly of a target structure, given a set of pre-defined parameters such as μ, E, S, and m, we use the following measures:

- *Final distance* (d_f): distance from the desired target structure, averaged over the last 5% of the simulation steps (5000 lattice sweeps for typical simulations, where one lattice sweep equals N_0 Monte Carlo steps), where the *distance* (d) is defined as the difference between M and the number of particles that are in their designated location according to the target structure.
- *First assembly time* (T_{fa}): time, measured in Monte Carlo steps, until the system first assembles a structure close to the desired target structure, within a distance determined by the

Published under an exclusive license by AIP Publishing

DISTRIBUTION A: Distribution approved for public release.

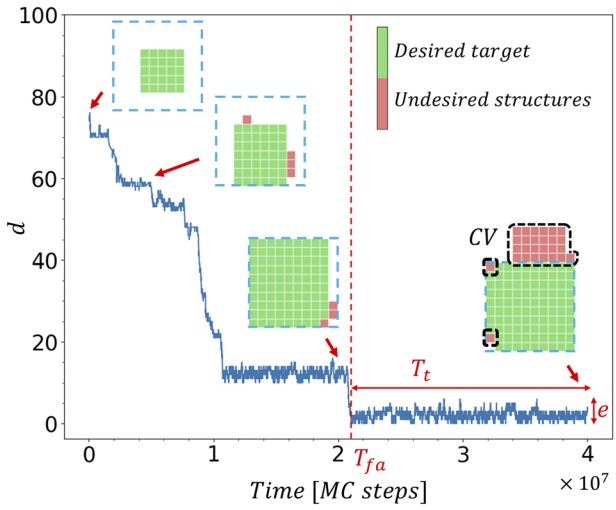


FIG. 3. Distance from the desired target structure as a function of time, measured in Monte Carlo steps. Highlighted on the plot, T_{fa} is the time until first assembly, T_t is the time spent in the desired target structure, and e is the fluctuation deviation. The images show the state of the lattice at certain timepoints. Structures that belong to the desired target structure are marked in green, and other, undesired, structures are marked in red. The boundaries of the target structure are marked in blue (for more elaboration on the coloring scheme, see the supplementary material, Sec. S2). The chimeric structures, whose size is the chimeric value, are also highlighted. This example dataset was taken from a simulation of 10^5 lattice sweeps, with parameters $\{m = 6, M = 100, N_0 = 400, E = 9, \mu/E = 1.78, S = 5,$ and $\Delta\lambda = 1.5\}$.

average root mean square (rms) fluctuations around the target. The motivation for the definition of this *fluctuation deviation* and its derivation can be found in the supplementary material, Sec. S3.

- *Time spent in target* (T_t): the total time the system is within the rms fluctuation distance around the target.
- *Chimeric value* (CV): the number of particles in the biggest structure, which do not belong to the desired target. The chimeric value is averaged over all the simulation steps. This parameter quantifies the size of chimeric structures bound to the growing seed, where lower CV means a more selective assembly of the desired target.
- *Characteristic growth time* (T_g): time until the system first assembles a structure of size M. Note that it does not necessarily have to be the target structure, but rather any structure of size M. This parameter quantifies the inverse of the aggregate growth rate.

An example for a distance-over-time plot is presented in Fig. 3, where some of the above measures are denoted. We note that Fig. 3 shows the distance from the desired target and thus only partly reveals the simulation dynamics after assembling this target ($T > T_{fa}$). More elaboration on post-assembly dynamics can be found in the supplementary material, Sec. S4.

IV. FINE TUNING OF THE SYSTEM

We start by exploring the $\{\mu, E\}$ parameter space, where E is the binding energy and μ is the chemical potential of all of the species, to find the phase space regime in which the system can retrieve the stored target structures.

Qualitatively, too low chemical potential results in a high rate of particles entering the lattice, whether they fit the desired target structure or not. Conversely, too high chemical potential results in a high rate of particles leaving the lattice, hindering the formation of large structures. Similarly, if the binding energy is too weak, there is no significant energetic preference to the target structure compared to a random organization of the particles, whereas too high binding energy leads to kinetic traps along the assembly.[33]

Roughly, the optimal region in phase space can be narrowed down by simple calculations. Let us denote the microstate s_t, in which the lattice solely contains a target structure of M particles, and define $l \equiv \sqrt{M}$. For s_t, there are l^2 particles on the lattice with $2l(l-1)$ strong bonds. Therefore, according to Eq. (3), the total energy U of the microstate s_t is given by $U_t = -2l(l-1)E + l^2\mu$. The total energy U of a microstate s_e corresponding to an empty lattice is 0. In order to achieve assembly, we first choose parameters such that the equilibrium probability of the system being at the microstate s_t is larger than the probability of an empty lattice, s_e. Since the equilibrium probability of a certain microstate is proportional to its Boltzmann factor e^{-U}, we get $U_t < 0$, which gives

$$\frac{\mu}{E} < 2\,\frac{l-1}{l}. \tag{5}$$

Substituting the value $l = 10$, which is used later in the simulations, we get $\mu/E < 1.8$.

For estimating optimal values for the binding energy E, we seek for a condition that differentiates between desired and undesired MC moves and ensures that the undesired ones are accepted with small enough probability during each simulation step. The condition we choose states that removal of the seed's least bounded particle is more likely to be rejected than accepted. Given a square-shape seed, the most loosely bound particles are the ones in its corners. The probability of accepting an undesired step that removes a corner particle is given by $p_r = \exp\{-2E + \mu\}$. In order for this unwanted move to have a better than an even chance to be rejected, we set $p_r < 1/2$. This inequality, together with Eq. (5), determine E as follows:

$$E > \frac{l}{2}\ln(2). \tag{6}$$

Full derivation of Eq. (6) can be found in the supplementary material, Sec. S5. Substituting the value of $l = 10$, condition $E > 5\ln(2) \approx 3.47$ is obtained.

As for the driving force value $\Delta\lambda$, we use the following observation: At equilibrium, the undesired step with the highest acceptance probability that is still smaller than unity is the removal of a particle while breaking two strong bonds (e.g., removing a corner particle from the seed). Its corresponding acceptance probability is $p_r = \exp\{-2E + \mu\}$. While applying an encouraging driving force ($D = \Delta\lambda$) in this situation is impossible, choosing $e^{\Delta\lambda}p_r < 1$ ensures that the driving force would not be able to make any undesired step, a one which is accepted with probability 1. Namely, we set

$$\Delta\lambda < 2E - \mu. \tag{7}$$

To test the above statements and find the optimal region in phase space for the assembly, we ran the simulations and calculated

Published under an exclusive license by AIP Publishing

DISTRIBUTION A: Distribution approved for public release.

the final distance of the system from the desired target structure, with $N = M = 100$, $m = 6$ targets, a seed length of $S = 7$, and a lattice size of $N_0 = 400$. The energy E was varied in the range $[5, 12]$ and the ratio μ/E was varied in the range $[1.2, 2]$, which roughly correspond to the estimated optimal region in parameter space, and the system was examined both at equilibrium, $\Delta\lambda = 0$, and out-of-equilibrium, taking $\Delta\lambda = 1$.

These simulations yielded a set of $(\mu/E, E, d_f)$ points, for both the equilibrium and nonequilibrium cases, which can be presented as a heat-map of the d_f values as a function of μ/E and E values, shown in Figs. 4(a) and 4(b) following a Gaussian interpolation[38] (see the supplementary material, Sec. S6). The interpolation was applied in order to improve the resolution of the obtained heat-map.

From these results, we recognize three regimes in $(\mu/E, E)$ space [Figs. 4(a) and 4(b)]. In order to inspect these regimes more carefully, the state of the lattice by the end of the simulation was captured, at both equilibrium and nonequilibrium conditions, for two regions in $(\mu/E, E)$ space—at the left boundary of regime III [Figs. 4(c) and 4(d)] and at the right boundary of regime III [Figs. 4(e) and 4(f)].

In regime I, the system partly assembles the desired target structure as the distance values are larger than twice the fluctuation deviation, in agreement with the qualitative prediction of a μ value too low. In regime II, the initial seed dissolves and all the particles leave the lattice, as reflected in a distance value close to $M = 100$. Such a distance does not necessarily indicate an empty lattice, but here, the final lattice state was examined and indeed found to be empty. This scenario is in agreement with both the qualitative and quantitative estimations since in the equilibrium heat-map, this regime is bounded by $\mu/E \gtrsim 1.8$. In regime III, defined as the region where the distance from the target is lower than two fluctuation deviations, a compromise between the limitations of the two other regimes is found. Hence, it is considered as the optimal regime in parameter space for the self-assembly and will be used for later simulations.

These regimes I, II, and III are found in both equilibrium and nonequilibrium conditions, where in the nonequilibrium case, regime II is smaller and regime III remains approximately the same size. This is a positive effect of the driving force as the initial seed does not dissolve for a wider range of $\{\mu, E\}$ parameters.

This behavior may be explained by a closer inspection of the influence of the driving force on the lattice growth and the lattice shrinkage. The driving force may or may not encourage a move of a particle entering an empty site but would never discourage it as such a move may or may not form a new intermittent subunit triplet but cannot destroy one. In a similar manner, the driving force would never encourage a move where a particle is removed from the lattice since such a move would never increase the total number of intermittent subunit triplets and may discourage it (when a removal of a particle results in a destruction of an intermittent subunit triplet). Consequently, for high μ/E, where lattice shrinkage is preferred over growth, the drive cannot encourage shrinkage and may possibly discourage it. This way, the driving force restrains the extensive shrinkage, which characterizes this region in $(\mu/E, E)$ space, as can be seen in Figs. 4(c) and 4(d). This effect enables the system to assemble the target structure for higher μ/E values, which is seen on the heat-maps as regime II becomes smaller and regime III stretches to higher μ/E values. Conversely, for low μ/E, where

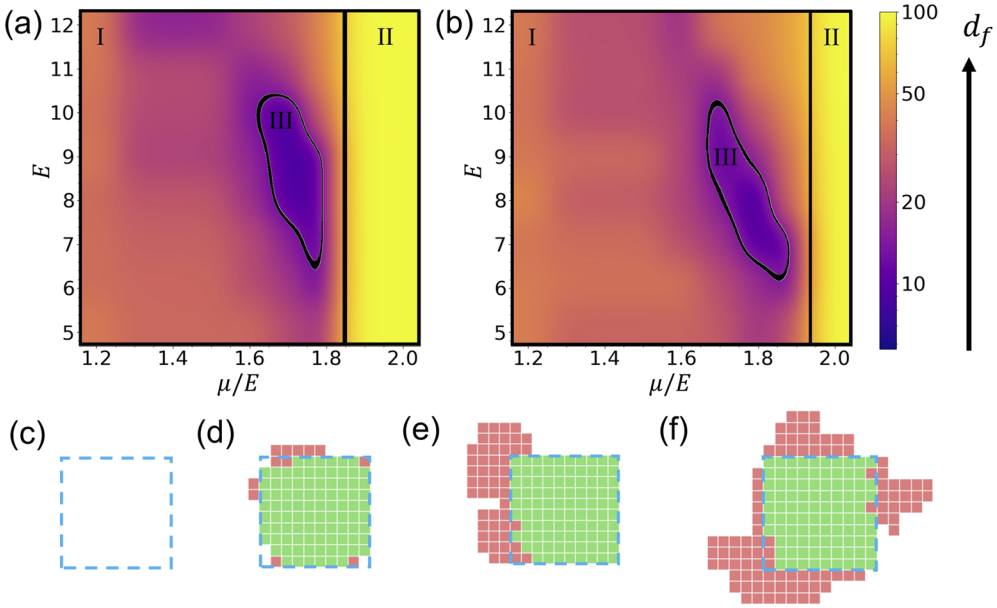


FIG. 4. (a) and (b) Final distance from the seeded target as a function of μ/E and E at equilibrium ($\Delta\lambda = 0$) (a) and nonequilibrium ($\Delta\lambda = 1$) (b), following Gaussian interpolation. Colors represent final distances in a logarithmic scale. Each data point is averaged over ten realizations (see the supplementary material, Sec. S6). [(c)–(f)] The state of the lattice by the end of the simulation on the boundaries of nonequilibrium regime III, colored as described in Fig. 3. (c) Right boundary (namely, μ/E and E values, which correspond to the right boundary of nonequilibrium regime III) at equilibrium: $E = 7$, $\mu/E = 1.9, \Delta\lambda = 0$. (d) Right boundary out-of-equilibrium: $E = 7$, $\mu/E = 1.9, \Delta\lambda = 1$. (e) Left boundary at equilibrium: $E = 8$, $\mu/E = 1.7, \Delta\lambda = 0$. (f) Left boundary out-of-equilibrium: $E = 8$, $\mu/E = 1.7, \Delta\lambda = 1$.

Published under an exclusive license by AIP Publishing

DISTRIBUTION A: Distribution approved for public release.

lattice growth is preferred over shrinkage, the drive cannot discourage growth but may encourage unwanted growth (e.g., insertion of a particle to a site where it forms an intermittent subunit triplet but does not correspond to the desired target structure). Thus, the driving force further fuels the extensive growth of undesired structures, which characterizes this region in $(\mu/E, E)$ space, as shown in Figs. 4(e) and 4(f). This effect allows for successful nonequilibrium assembly only for higher μ/E values. The two effects mentioned above make nonequilibrium assembly possible for higher μ/E values compared to the equilibrium case, while preventing it for lower μ/E values, resulting in regime III being shifted to the right while retaining its size in the driven scenario presented in Fig. 4(b).

V. NUMBER OF PRE-ENCODED TARGET STRUCTURES

In order to challenge the capacity of the system at equilibrium and nonequilibrium conditions, we ran the simulations with an increasing number of targets and characterized the time spent in target, T_t, and the first assembly time, T_{fa} (Fig. 5). Specifically, we ran simulations with 10^5 lattice sweeps (4×10^7 MC steps), with the parameter set $\{m = 2, 3, \ldots, 9,\ N = M = 100,\ N_0 = 400,\ E = 8,\ \mu/E = 1.78,\ S = 5,\ \Delta\lambda \in [0, 1.7]\}$ chosen from the optimal range within regime III.

For $m > 6$, the system does not assemble the desired target structure with or without the driving force, as evident from the values of $T_t = 0$ [Fig. 5(a)] and $T_{fa} > T_{tot}$ [Fig. 5(b)], indicating a storage capacity of $m_{\max} = 6$ for the parameters chosen.

The trends of T_t and T_{fa} as a function of the number of encoded targets, showing optimal behavior for intermediate m values, can be rationalized through a trade-off between the probability of forming chimeric structures and the mobility of the system. For low m values, the number of structures which can form with considerable probability (i.e., parts of target structures) is low, resulting in slow dynamics of the system and slower assembly [Fig. 5(b)]. This, in turn, limits the time the system can spend near the target structure [Fig. 5(a)]. Since the desired result is specifically assembling the seeded target structure, the number of desired structures (e.g., desired pairs and triplets) remains constant as m is varied. However, for larger m, there is an increasing number of possible structures which are energetically favorable, yet do not belong to the desired target, i.e., chimeric structures, resulting in kinetic traps, which lead to lower assembly quality. When the rate of the formation of chimeric structures is too high, the desired structure cannot be assembled during the simulation.

Although the driving force does not increase storage capacity, as $m_{\max} = 6$ also for nonequilibrium conditions, it does contribute to the quality of the assembly for $m \leq 6$ pre-encoded target structures, which become both more stable (higher T_t) and assembled faster (lower T_{fa}), as seen from Figs. 5(a) and 5(b), respectively.

Next, we chose $m = 3$ to study the effect of the drive on the system. Compared to the equilibrium case, $\Delta\lambda = 0$, nonequilibrium driving both increases the target stability and accelerates the assembly, as evident from the higher values of the time spent in the desired target structure T_t [Fig. 5(c)] and the lower values of the first

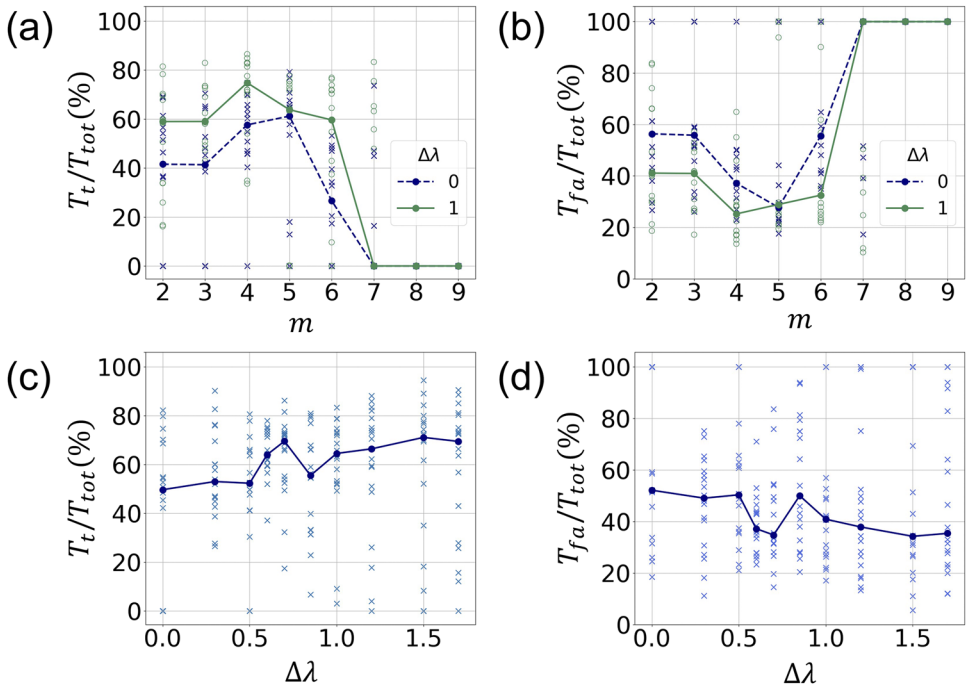


FIG. 5. Time spent in the target and first assembly time, normalized by the total number of MC steps. (a) Time spent in the target as a function of the number of target structures. (b) First assembly time as a function of the number of target structures. (c) Time spent in the target as a function of driving force for $m = 3$. (d) First assembly time as a function of driving force for $m = 3$. Each marker, "X" or "○" symbol, represents a result from one realization, and each point represents the median of 14 simulations for (a) and (b) or 18 simulations for (c) and (d).

Published under an exclusive license by AIP Publishing

DISTRIBUTION A: Distribution approved for public release.

assembly time T_{fa} [Fig. 5(d)], respectively. However, both T_t and T_{fa} do not vary monotonically by increasing the drive $\Delta\lambda$. Specifically, there exists a value of drive that optimizes both the stability and the assembly speed, $\Delta\lambda = 0.7$, for the given simulation parameter set. This non-monotonic behavior is a consequence of a nonequilibrium trade-off, which is discussed in Sec. VII.

VI. SUB-CRITICAL SEED

Based on nucleation theory, Murugan *et al.*[19] calculated the size of a "critical seed" $S_c \times S_c$ for equilibrium self-assembly, below which the system dissolves,

$$S_c = \frac{1}{2 - \frac{\mu}{E}}. \tag{8}$$

In order to test this constraint for the nonequilibrium system, we ran simulations with various seed sizes and found the final distance of the system from the desired target structure (Fig. 6). The simulations were run for 10^5 lattice sweeps (4×10^7 MC steps), with the parameter set $\{m = 6, N = M = 100, N_0 = 400, E = 9, \mu/E = 1.78, S = 2, 3, \ldots, 9, \Delta\lambda \in [0, 1.7]\}$. Similar to the previous set of simulations, the values of E and μ/E were chosen from the optimal range within regime III. Substituting the values of $\mu/E = 1.78$, in Eq. (8), we get $S_c = 4.54$.

At equilibrium, the final distance from the target is close to 100, the target size, for $S \leq 4$, meaning that the initial seed is dissolved. For $S \geq 5$, however, assembly is achieved, in agreement with the theoretical prediction of the critical seed size. In contrast, when the system is driven away from equilibrium, the equilibrium critical seed constraint no longer holds, and the system assembles the seeded target structure for sub-critical seed lengths as well. We again notice an optimal value of the drive $\Delta\lambda = 1.2$, which yields the minimal distance from the target. Again, the existence of an optimal drive value stems from a nonequilibrium trade-off, which is treated in Sec. VII.

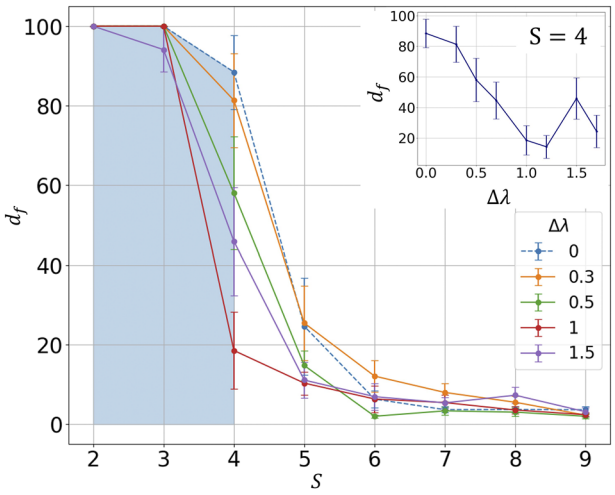


FIG. 6. Final distance from the desired target structure as a function of seed length. The blue area is the sub-critical seed region. The inset shows the final distance for the maximal equilibrium sub-critical seed, $S = 4 < S_c$, as a function of the drive value. Each point is the average value over ten simulations, with the error bars representing the statistical error.

For the sake of completeness, we briefly discuss the situation in which no seed is introduced ($S = 0$), and the initial state is an empty lattice. In an empty lattice, a move of a particle entering the lattice is accepted with probability of $p_{init} = e^{-\mu}$. In order for such a move to happen with a reasonable probability of, for instance, 1%, we should set $\mu \lesssim 4.7$. In such a case, Fig. 4(a) shows that assembly is unlikely to happen. Namely, for μ values low enough, a structure would form (since p_{init} is large enough and the rate of particles entering the lattice is high), but its distance from a target structure would be high, and for higher μ values, no structure would form. We note that the local driving force does not influence p_{init}, as no triplet exists nor can be formed in the initial state, so high-μ scenario stays the same also for the nonequilibrium case. For low μ values, the lattice grows rapidly, so driving the system would only increase the error, as explained in Sec. IV. Therefore, the drive does not change the above equilibrium conclusion.

VII. A NONEQUILIBRIUM TRADE-OFF

Our results show a non-monotonic behavior of the time spent in the target T_t, the first assembly time T_{fa}, and the final distance d_f as a function of the drive. As the drive value increased, the assembly was first accelerated, the targets became more stable, and the assembled structure was closer to the target structure, up to a certain drive value, above which there was a decrease in assembly speed and target stability and an increase in the distance from the target.

In order to unveil the reason behind this phenomenon, we ran simulations for 10^5 lattice sweeps (4×10^7 MC steps), with a similar parameter set $\{m = 6, N = M = 100, N_0 = 400, E = 7, \mu/E = 1.78, \Delta\lambda \in [0, 1.9]\}$, and examined the characteristic growth time T_g and chimeric value CV (Fig. 7). The system was challenged with a high number of pre-encoded targets, $m = 6$, increasing the possibility of forming chimeric structures and thus yielding more valuable information about CV.

Indeed, the aggregate growth process is accelerated when increasing the drive, up to certain drive value, $\Delta\lambda = 1.4$, above which

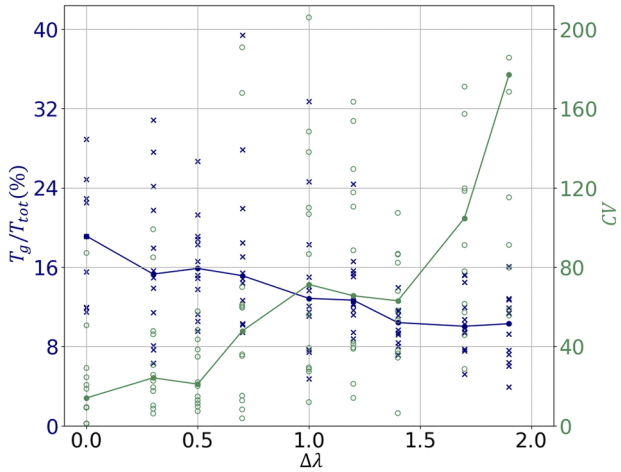


FIG. 7. Two quality parameters for varied drive intensity, $\Delta\lambda$: characteristic growth time, normalized by the total number of MC steps (blue) and chimeric value (green). Each "x" or "o" symbol represents one simulation, and each point represents the median of 12 simulations.

Published under an exclusive license by AIP Publishing

DISTRIBUTION A: Distribution approved for public release.

the growth rate does not improve anymore. However, the chimeric value is higher for increasing drive values, meaning that in addition to the assembly of the desired target, other chimeras are being assembled as well.

We thus recognize a trade-off between the accelerated assembly and the reduced chimeric value. On the one hand, a stronger drive increases the formation rate of chain-like structures necessary for building the target, thereby accelerating the assembly process. On the other hand, too strong of a drive encourages chain-like structures, which are not necessarily of the seeded target, to bind to the growing seed, reflected in the chimeric value. This trade-off governs the non-monotonic behavior of the time spent in the target, the first assembly time, and the final distance from the desired target as a function of the drive, as shown in Figs. 5 and 6.

VIII. DISCUSSION

In this work, we have described a toy model for a dimer-based self-assembly system. We examined its ability to assemble pre-encoded target structures at both equilibrium and nonequilibrium regimes. The nonequilibrium drive used in this work increased the acceptance probability of chain-forming moves while decreasing the probability of chain-destroying ones.

Initial exploration of the parameter space yielded three different regimes corresponding to a partial assembly of the seeded target (regime I), dissolution of the seed (regime II), and a successful assembly of the desired target (regime III) as a function of the binding energy E and the ratio between the chemical potential and the binding energy μ/E.

Next, we tested the effect of the nonequilibrium local drive on the assembly quality measured by the time spent in the target, which corresponds to target stability, and the first assembly time, which corresponds to the speed of assembly, and demonstrated an improved assembly compared to the equilibrium case. This improvement, however, does not increase monotonically for larger drive values but rather shows an optimal behavior for intermediate values. The underlying mechanism behind this phenomenon is an inherent nonequilibrium trade-off between the assembly speed and the exclusiveness of the assembled structure, where too fast of an assembly is accompanied by chimeras.[19] This is an example of a concept present in various biological systems, where increased dissipation, or irreversibility, does not necessarily improve life-supporting properties.[39]

Perhaps the most striking property of the local drive shown in this work is its ability to promote target assembly in the sub-critical seed region, overcoming the equilibrium constraint. This unveils the power of such nonequilibrium driving force, allowing the system to assemble a target structure in a region in parameter space, which is inaccessible at equilibrium.

This decrease in the critical seed size explains the increase in the rate of chimeric structures compared to the equilibrium scenario. Small seeds of undesired targets are constantly forming, and due to the small critical seed, they grow and create larger chimeras.

While we were inspired by general aspects of the microtubule structure, our model is a generic toy model, aimed at describing a wide range of dimer-based physical systems. For this reason, it is essential to understand the range of systems for which our results and conclusions are applicable. In the following paragraphs, we will examine the compatibility of the proposed model to real-life systems.

For instance, the concept of programming inter-particle interactions in order to make some structures local minima in the free-energy landscape is analogous to DNA origami, where different DNA strands are chosen such that a certain folding of the scaffold strand is achieved through relaxation of the strands mixture toward equilibrium.[40] Furthermore, our proposed interaction energy landscape, having sharp local minima for certain structures and none for others, can be found in the modeling of the process of protein binding to DNA. In this process, a protein slides along the DNA, searching for its target site, where it binds the DNA. The interaction energy between the protein and the DNA is spatially (sequence) dependent, and it was shown that an adequate model for such energy landscape involves the protein experiencing, for most of the time, a Gaussian energy-sequence landscape with relatively small variance.[41,42] This follows the same logic of the interaction-energy matrix of our proposed model, accounting for a $-E$ interaction energy between pairs of particles from a certain target structure and no interaction otherwise. In addition, dependence of certain assembly probabilities on their chain structure, which appears in our model driving force, exists in microtubules. In microtubules, a dimer at the end of the filament is more likely to move into a specific, confrontationally different, state when another dimer binds the end of the microtubule. This confrontational change, involving hydrolysis of GTP to GDP in the dimer, promotes disassembly of the microtubule, as part of the nonequilibrium process we discussed in Sec. I.[6]

However, there are certain aspects of the proposed model that limit the range of real-life systems for which our findings may be applicable.

First, the model we proposed is a lattice model. Generally speaking, such a model is a powerful tool, which can capture much of the behaviors of a compatible off-lattice model for patchy particles.[43,44] When comparing a model of a driven fluid, similar to the one suggested here, with its continuous off-lattice counterpart, it has been shown that while both experience an order–disorder phase transition, several aspects, such as the critical exponent or critical temperature, vary non-trivially.[45] This much richer phase diagram for an off-lattice model shown by Díez-Minguito *et al.* may imply that while the existence of the critical seed and its relative change compared to the non-driven case are likely to be consistent with an off-lattice model, specific values such as the critical seed length should be taken with extra caution.

Second, while our model includes moves of insertion or deletion of a particle to or from a certain lattice site, it does not allow for the movement of a cluster. This might seem incomplete in light of several studies that describe assembly as a process in which smaller clusters of subunits from a target structure (fragments) are formed and interact[46] and show that assembly of certain structures may follow a mechanism where pairs of multimers hybridize with one another, leading to the creation of larger bonding networks and to extensive bonding of the subunits.[47] However, the dynamics of the general set of systems described by our model, determined by the external parameters μ, E, are slightly different. For low μ values, the rate of particles entering the lattice is high, hindering the retrieval of the desired target structure. Therefore, the μ value must be high enough, resulting in a large critical seed size [according to Eq. (8)].

Published under an exclusive license by AIP Publishing

DISTRIBUTION A: Distribution approved for public release.

As stated by Jacobs *et al.*,[46] the existence of a large critical seed size implies that newly formed small fragments are more likely to dissolve rather than keep growing, and thus, substantial fragments cannot form in empty lattice sites. Therefore, the only stable structure in the system is the growing initial seed. This kind of dynamics, where new structures only bind to the initial seed rather than creating new nucleation seeds, is demonstrated in the images of the system states in Fig. 3. Consequently, if we allowed particles or clusters to move to neighboring sites as part of the simulation dynamics, this would only result in the main cluster (the grown initial seed) moving back and forth along the lattice, not changing the assembly quality parameters.

There are a few other simplifying assumptions in our model: the first is the zero-interaction energy we chose for undesigned interactions. Nevertheless, we have demonstrated that such interaction energy can serve as a model for finite, low enough, weak interaction energies (see the supplementary material, Sec. S7). The second assumption has to do with the fixed finite size of the lattice that was simulated. However, we have shown that different lattice sizes have minimal effect on the behaviors of the model (see the supplementary material, Sec. S8). The third assumption is the lack of rotational moves in the simulation. Still, adding rotations would only make the assembly times longer, leaving the nature of the dynamics unchanged (see the supplementary material, Sec. S9).

Further studies may be done, examining this dimer-based system in an off-lattice model and achieving a better quantitative estimation of the critical values obtained in this work. Future works may also verify the universality of our conclusions to general n-mer systems or to larger more complicated dimer-based systems.

Our findings provide insights into dimer-based biomolecular systems operating far-from-equilibrium, which can be used for designing adaptive materials.[48] The sub-critical seed operation demonstrated in this work may be exploited for compressing information or associative memory models[20] as the smaller seed can be expanded to the whole target structure by applying the local drive.

IX. METHODS

Monte Carlo simulations and image interpolation for the heat-maps were run using a Python code, including the libraries NumPy,[49] Matplotlib,[50] and SciPy.[51]

SUPPLEMENTARY MATERIAL

See the supplementary material for detailed information on the simulation dynamics, justifications for assumptions, and data analysis methods, as referenced in the main text.

ACKNOWLEDGMENTS

Gili Bisker acknowledges the support from the Zuckerman STEM Leadership Program; the Israel Science Foundation (Grant No. 456/18); the Ministry of Science, Technology, and Space, Israel (Grant No. 3-17426); and the Tel Aviv University Center for AI and Data Science (TAD). Adi Ben-Ari and Liron Ben-Ari acknowledge the support from the Excellence Program of the Faculty of Engineering at Tel Aviv University.

This work was supported by the Air Force Office of Scientific Research (AFOSR) under Award No. FA9550-20-1-0426. Research was sponsored by the Army Research Office (ARO) and was accomplished under Grant No. W911NF-21-1-0101. The views and conclusions contained in this document are those of the authors and should not be interpreted as representing the official policies, either expressed or implied, of the Army Research Office or the U.S. Government. The U.S. Government is authorized to reproduce and distribute reprints for Government purposes notwithstanding any copyright notation herein.

AUTHOR DECLARATIONS

Conflict of Interest

The authors have no conflicts to disclose.

Author Contributions

A.B. and L.B. equally contributed to this work.

DATA AVAILABILITY

The data that support the findings of this study are available from the corresponding author upon reasonable request.

REFERENCES

[1] S. A. Woodson, "RNA folding pathways and the self-assembly of ribosomes," Acc. Chem. Res. **44**, 1312–1319 (2011).
[2] J. A. Pelesko, in *Self Assembly: The Science of Things that Put Themselves Together*, 1st ed. (Chapman and Hall; CRC, 2007), Chap. 3.
[3] K. Das, L. Gabrielli, and L. J. Prins, "Chemically fueled self-assembly in biology and chemistry," Angew. Chem., Int. Ed. **60**, 20120 (2021).
[4] E. Grossman, O. Medalia, and M. Zwerger, "Functional architecture of the nuclear pore complex," Annu. Rev. Biophys. **41**, 557–584 (2012).
[5] G. C. L. Wong, J. X. Tang, A. Lin, Y. Li, P. A. Janmey, and C. R. Safinya, "Hierarchical self-assembly of F-actin and cationic lipid complexes: Stacked three-layer tubule networks," Science **288**, 2035–2039 (2000).
[6] H. Hess and J. L. Ross, "Non-equilibrium assembly of microtubules: From molecules to autonomous chemical robots," Chem. Soc. Rev. **46**, 5570–5587 (2017).
[7] P. Sartori and S. Leibler, "Lessons from equilibrium statistical physics regarding the assembly of protein complexes," Proc. Natl. Acad. Sci. U. S. A. **117**, 114–120 (2020).
[8] S. F. Greenbury, I. G. Johnston, A. A. Louis, and S. E. Ahnert, "A tractable genotype–phenotype map modelling the self-assembly of protein quaternary structure," J. R. Soc., Interface **11**, 20140249 (2014).
[9] Z. Zhang and S. C. Glotzer, "Self-assembly of patchy particles," Nano Lett. **4**, 1407–1413 (2004).
[10] A. Cumberworth, A. Reinhardt, and D. Frenkel, "Lattice models and Monte Carlo methods for simulating DNA origami self-assembly," J. Chem. Phys. **149**, 234905 (2018).
[11] É. Fodor and M. Cristina Marchetti, "The statistical physics of active matter: From self-catalytic colloids to living cells," Physica A **504**, 106–120 (2018).
[12] S. Ramaswamy, "The mechanics and statistics of active matter," Annu. Rev. Condens. Matter Phys. **1**, 323–345 (2010).
[13] M. C. Marchetti, J. F. Joanny, S. Ramaswamy, T. B. Liverpool, J. Prost, M. Rao, and R. A. Simha, "Hydrodynamics of soft active matter," Rev. Mod. Phys. **85**, 1143–1189 (2013).
[14] C. Bechinger, R. Di Leonardo, H. Löwen, C. Reichhardt, G. Volpe, and G. Volpe, "Active particles in complex and crowded environments," Rev. Mod. Phys. **88**, 045006 (2016).
[15] T. Vicsek, A. Czirók, E. Ben-Jacob, I. Cohen, and O. Shochet, "Novel type of phase transition in a system of self-driven particles," Phys. Rev. Lett. **75**, 1226–1229 (1995).

Published under an exclusive license by AIP Publishing

DISTRIBUTION A: Distribution approved for public release.

[16]E. Bertin, M. Droz, and G. Grégoire, "Boltzmann and hydrodynamic description for self-propelled particles," Phys. Rev. E **74**, 022101 (2006).
[17]J. Madge and M. A. Miller, "Design strategies for self-assembly of discrete targets," J. Chem. Phys. **143**, 044905 (2015).
[18]J. Madge, D. Bourne, and M. A. Miller, "Controlling fragment competition on pathways to addressable self-assembly," J. Phys. Chem. B **122**, 9815–9825 (2018).
[19]A. Murugan, Z. Zeravcic, M. P. Brenner, and S. Leibler, "Multifarious assembly mixtures: Systems allowing retrieval of diverse stored structures," Proc. Natl. Acad. Sci. U. S. A. **112**, 54–59 (2015).
[20]W. Zhong, D. J. Schwab, and A. Murugan, "Associative pattern recognition through macro-molecular self-assembly," J. Stat. Phys. **167**, 806–826 (2017).
[21]Z. Zeravcic, V. N. Manoharan, and M. P. Brenner, "*Colloquium*: Toward living matter with colloidal particles," Rev. Mod. Phys. **89**, 031001 (2017).
[22]J. D. Halverson and A. V. Tkachenko, "Sequential programmable self-assembly: Role of cooperative interactions," J. Chem. Phys. **144**, 094903 (2016).
[23]A. Murugan, J. Zou, and M. P. Brenner, "Undesired usage and the robust self-assembly of heterogeneous structures," Nat. Commun. **6**, 6203 (2015).
[24]T. Mitchison and M. Kirschner, "Dynamic instability of microtubule growth," Nature **312**, 237–242 (1984).
[25]J. Boekhoven, A. M. Brizard, K. N. K. Kowlgi, G. J. M. Koper, R. Eelkema, and J. H. van Esch, "Dissipative self-assembly of a molecular gelator by using a chemical fuel," Angew. Chem., Int. Ed. **49**, 4825–4828 (2010).
[26]M. Weißenfels, J. Gemen, and R. Klajn, "Dissipative self-assembly: Fueling with chemicals versus light," Chem **7**, 23–37 (2021).
[27]G. Makey, S. Galioglu, R. Ghaffari, E. D. Engin, G. Yıldırım, Ö. Yavuz, O. Bektaş, Ü. S. Nizam, Ö. Akbulut, Ö. Şahin, K. Güngör, D. Dede, H. V. Demir, F. Ö. Ilday, and S. Ilday, "Universality of dissipative self-assembly from quantum dots to human cells," Nat. Phys. **16**, 795–801 (2020).
[28]G. Bisker, "Dissipate your way to self-assembly," Nat. Phys. **16**, 707–708 (2020).
[29]A. C. H. Coughlan, I. Torres-Díaz, J. Zhang, and M. A. Bevan, "Non-equilibrium steady-state colloidal assembly dynamics," J. Chem. Phys. **150**, 204902 (2019).
[30]C. Papaseit, N. Pochon, and J. Tabony, "Microtubule self-organization is gravity-dependent," Proc. Natl. Acad. Sci. U. S. A. **97**, 8364–8368 (2000).
[31]C. B. Minkenberg, L. Florusse, R. Eelkema, G. J. M. Koper, and J. H. van Esch, "Triggered self-assembly of simple dynamic covalent surfactants," J. Am. Chem. Soc. **131**, 11274–11275 (2009).
[32]S. Whitelam and R. L. Jack, "The statistical mechanics of dynamic pathways to self-assembly," Annu. Rev. Phys. Chem. **66**, 143–163 (2015).
[33]G. Bisker and J. L. England, "Nonequilibrium associative retrieval of multiple stored self-assembly targets," Proc. Natl. Acad. Sci. U. S. A. **115**, E10531–E10538 (2018).
[34]M. Nguyen and S. Vaikuntanathan, "Design principles for nonequilibrium self-assembly," Proc. Natl. Acad. Sci. U. S. A. **113**, 14231–14236 (2016).
[35]M. Tagliazucchi, E. A. Weiss, and I. Szleifer, "Dissipative self-assembly of particles interacting through time-oscillatory potentials," Proc. Natl. Acad. Sci. U. S. A. **111**, 9751–9756 (2014).
[36]C. J. Fullerton and R. L. Jack, "Optimising self-assembly through time-dependent interactions," J. Chem. Phys. **145**, 244505 (2016).
[37]M. E. J. Newman and G. Barkema, *Monte Carlo Methods in Statistical Physics* (Clarendon, 1999).
[38]C.-W. Kok and T. Wing-Shan, in *Digital Image Interpolation in Matlab*, 1st ed. (Wiley; IEEE Press, 2019), Chap. 2, p. 42.
[39]M. Baiesi and C. Maes, "Life efficiency does not always increase with the dissipation rate," J. Phys. Commun. **2**, 045017 (2018).
[40]E. S. Andersen, "Biomolecular self-assembly: DNA origami rewired," Nat. Nanotechnol. **10**, 733–734 (2015).
[41]A. Tafvizi, L. A. Mirny, and A. M. van Oijen, "Dancing on DNA: Kinetic aspects of search processes on DNA," ChemPhysChem **12**, 1481–1489 (2011).
[42]M. Slutsky and L. A. Mirny, "Kinetics of protein-DNA interaction: Facilitated target location in sequence-dependent potential," Biophys. J. **87**, 4021–4035 (2004).
[43]N. G. Almarza and E. G. Noya, "Phase transitions of a lattice model for patchy particles with tetrahedral symmetry," Mol. Phys. **109**, 65–74 (2011).
[44]A. Reinhardt and D. Frenkel, "DNA brick self-assembly with an off-lattice potential," Soft Matter **12**, 6253–6260 (2016).
[45]M. Díez-Minguito, J. Marro, and P. L. Garrido, "On the similarities and differences between lattice and off–lattice models of driven fluids," Eur. Phys. J.: Spec. Top. **143**, 269–272 (2007).
[46]W. M. Jacobs, A. Reinhardt, and D. Frenkel, "Rational design of self-assembly pathways for complex multicomponent structures," Proc. Natl. Acad. Sci. U. S. A. **112**, 6313–6318 (2015).
[47]M. Sajfutdinow, W. M. Jacobs, A. Reinhardt, C. Schneider, and D. M. Smith, "Direct observation and rational design of nucleation behavior in addressable self-assembly," Proc. Natl. Acad. Sci. U. S. A. **115**, E5877–E5886 (2018).
[48]M. Fialkowski, K. J. M. Bishop, R. Klajn, S. K. Smoukov, C. J. Campbell, and B. A. Grzybowski, "Principles and implementations of dissipative (dynamic) self-assembly," J. Phys. Chem. B **110**, 2482–2496 (2006).
[49]C. R. Harris, K. J. Millman, S. J. van der Walt, R. Gommers, P. Virtanen, D. Cournapeau, E. Wieser, J. Taylor, S. Berg, N. J. Smith, R. Kern, M. Picus, S. Hoyer, M. H. van Kerkwijk, M. Brett, A. Haldane, J. F. del Río, M. Wiebe, P. Peterson, P. Gérard-Marchant, K. Sheppard, T. Reddy, W. Weckesser, H. Abbasi, C. Gohlke, and T. E. Oliphant, "Array programming with NumPy," Nature **585**, 357–362 (2020).
[50]J. D. Hunter, "Matplotlib: A 2D graphics environment," Comput. Sci. Eng. **9**, 90–95 (2007).
[51]P. Virtanen, R. Gommers, T. E. Oliphant, M. Haberland, T. Reddy, D. Cournapeau, E. Burovski, P. Peterson, W. Weckesser, J. Bright, S. J. van der Walt, M. Brett, J. Wilson, K. J. Millman, N. Mayorov, A. R. J. Nelson, E. Jones, R. Kern, E. Larson, C. J. Carey, İ. Polat, Y. Feng, E. W. Moore, J. VanderPlas, D. Laxalde, J. Perktold, R. Cimrman, I. Henriksen, E. A. Quintero, C. R. Harris, A. M. Archibald, A. H. Ribeiro, F. Pedregosa, P. van Mulbregt *et al.*, "SciPy 1.0: Fundamental algorithms for scientific computing in python," Nat. Methods **17**, 261–272 (2020).

Published under an exclusive license by AIP Publishing

DISTRIBUTION A: Distribution approved for public release.

THE JOURNAL OF PHYSICAL CHEMISTRY B
A JOURNAL OF THE AMERICAN CHEMICAL SOCIETY

pubs.acs.org/JPCB

Article

Nonequilibrium Self-Assembly Time Forecasting by the Stochastic Landscape Method

Published as part of The Journal of Physical Chemistry virtual special issue "Early-Career and Emerging Researchers in Physical Chemistry Volume 2".

Michael Faran and Gili Bisker*

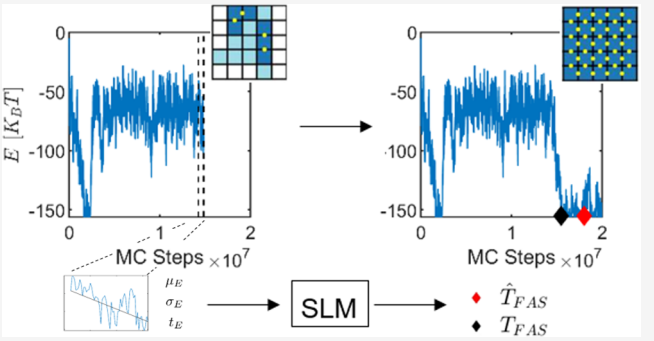
Cite This: https://doi.org/10.1021/acs.jpcb.3c01376

Read Online

ACCESS | Metrics & More | Article Recommendations | Supporting Information

Downloaded via TEL AVIV UNIV on July 5, 2023 at 05:55:32 (UTC).
See https://pubs.acs.org/sharingguidelines for options on how to legitimately share published articles.

ABSTRACT: Many biological systems rely on the ability to self-assemble target structures from different molecular building blocks using nonequilibrium drives, stemming, for example, from chemical potential gradients. The complex interactions between the different components give rise to a rugged energy landscape with a plethora of local minima on the dynamic pathway to the target assembly. Exploring a toy physical model of multicomponents nonequilibrium self-assembly, we demonstrate that a segmented description of the system dynamics can be used to provide predictions of the first assembly times. We show that for a wide range of values of the nonequilibrium drive, a log-normal distribution emerges for the first assembly time statistics. Based on data segmentation by a Bayesian estimator of abrupt changes (BEAST), we further present a general data-based algorithmic scheme, namely, the stochastic landscape method (SLM), for assembly time predictions. We demonstrate that this scheme can be implemented for the first assembly time forecast during a nonequilibrium self-assembly process, with improved prediction power compared to a naïve guess based on the mean remaining time to the first assembly. Our results can be used to establish a general quantitative framework for nonequilibrium systems and to improve control protocols of nonequilibrium self-assembly processes.



INTRODUCTION

Self-assembly is a process in which some form of overall order arises from local interactions between constituents of an initially disordered system. This key phenomenon arises in many physical, chemical, and biological systems.[1−8] Specifically, living systems, at the molecular level, ubiquitously present an ability to self-assemble a variety of different structures emerging from a common set of building blocks.[9−12] It is considered a fundamental process in intra-cellular activity, manifested, for instance, in molecular chaperones that actively participate in protein folding,[9,13,14] the protein components of chromatin regulating gene expression,[15−17] the spindle-assembly checkpoint in mitosis of eukaryotes,[18] and the protofilaments that form microtubules.[19,20] From a physical perspective, the aforementioned building-blocks diversity gives rise to a highly complex energy landscape, with many local minima corresponding to meta-stable states and kinetic traps, which may slow down the self-assembly process.[20−24] To overcome this challenge, living systems utilize nonequilibrium driving, for example, by harvesting a chemical fuel to accelerate the self-healing of an "off-target" state into a desired target assembly.[19,25−27] The advantages of a nonequilibrium drive have been demonstrated in experiments,[28−32] simulations,[20,23,24,33,34] and theoretical models.[35−37] Examples include using KOH and 1,3-propanesultone as chemical fuels for self-healing in supramolecular chiral G-quadruplex hydrogels,[38] using guanosine triphosphate (GTP) hydrolysis for self-healing the growing phase of microtubules,[39,40] and the use of chemical fuel for kinetic proofreading[41,42] in enzymes-substrates reactions,[43] damaged DNA discrimination,[44] and antigen discrimination,[45] where preferred reaction pathways are executed using an active mechanism. Moreover, nonequilibrium self-assembly can be conceptualized as taking part in decision-making and molecular computation.[46−49]

Biomimicking the benefits of nonequilibrium drive has attracted great technological interest,[25] with numerous demonstrations such as artificial light-harvesting systems,[50]

Received: February 28, 2023
Revised: June 12, 2023

© XXXX The Authors. Published by American Chemical Society

DISTRIBUTION A: Distribution approved for public release.

natural viral capsids,[50,51] target-specific delivery of drugs and genes,[52,53] formation of supramolecular hydrogels,[25,54−56] colloidal diamond photonic crystals,[57] and more.[10,11,21,58−60] Realizing a nonequilibrium self-assembly system would further benefit from control protocols that could assist in navigating the system to the desired target while monitoring its state over time.[23,33,34,61−67] Nevertheless, experimental realizations of these protocols are challenging and require quantitative, coarse-grained observables of the self-assembly process.[37,62,68] The time to the first self-assembly can be viewed from the perspective of a mean-first passage time problem,[69−72] where control protocols generally aim to reduce the assembly time. Previous works have examined this analogy to study first self-assembly times.[73−78]

Inspired by deterministic dynamical systems inference[79−81] and correspondence between dissipation and structure,[82−88] a quantitative inference of self-assembly is desired for predicting its outcome and optimizing the process using external control. The Bayesian Estimator of Abrupt change, Seasonality, and Trend (BEAST) algorithm[89] is a general framework for detecting trends and abrupt changes in any time series data and providing change occurrence probability at any time point.[90] This algorithm was originally utilized to detect human and natural disturbances based on the time series Landsat imagery.[91] BEAST combines several models to decompose time series data, improving change-point detection accuracy with robust performance.[90]

Here, we lay the foundation for inference and prediction in nonequilibrium self-assembly processes. Using Monte Carlo (MC) simulations[20,21,68,92] of a toy physical model,[24] we realize a system of distinguishable interacting particles, where self-assembly targets are encoded through specific interactions between the monomers, such that the assembled structures are global energy minima of the simulated system. In analogy to different conformations adopted by proteins, each particle can adopt different internal states, which govern its interaction with other particles. A local, self-healing drive is included through the propensity of a particle to adopt the same internal state as its neighbors.[24] We study the effect of the self-healing drive on the distribution of the time to the first assembly and show that it can be fitted by a log-normal distribution whose median and standard deviation decrease with increasing drive value. In order to provide a prediction for the time to the first assembly, we introduce a novel approach, termed the stochastic landscape method (SLM), which relies on the BEAST algorithm. We apply BEAST time series segmentation on the total energy of the system along the trajectories to extract the slow time-scale variation of the system from the segments. Then, this information is encoded in a map that relates the system's slowly varying statistical moments and the remaining time to the first self-assembly event. We demonstrate the potential of the SLM approach to provide predictions for our model system for different drive values and show how the statistical moments of a transient segmented observable, such as the energy, can be utilized to predict nonequilibrium self-assembly times. Our method can be generalized to other nonequilibrium self-assembly systems and be used as a baseline for control protocol design.

SELF-ASSEMBLY MODEL

Our model[24] consists of N distinguishable particles that can self-assemble M_T target structures. Each particle is represented by its labeled number $i = 1, \cdots, N$ and internal state $s_i = 1, \cdots, M_T$. The particles roam around a $L \times L$ square lattice (Figure 1A), translate to unoccupied adjacent tiles, change their internal state, and interact with neighboring particles (Figure 1B). Each tile can be either unoccupied or solely occupied by a single particle. A target structure of the self-assembly process is a unique spatial arrangement of the particle positions, given all of the particles adopt a specific internal state (Figure 1C). We assume that each internal state of the particles corresponds to a specific target, encoded by favored interactions between neighboring particles according to the target. These encoded targets are thus global minima in the energy landscape of the model. This model is motivated by molecular architectures, in which self-assembled structures rely on the specific conformation of the building blocks.[9,14,19,21]

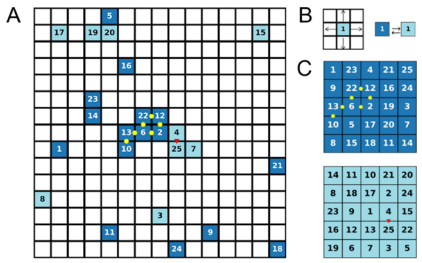


Figure 1. Model system Illustration. (A) Example of a lattice of size $L = 15$, occupied by $N = 25$ particles with $M_T = 2$ possible states identified by either a bright teal color or deep blue. The particles are distinguishable, denoted by numbers from 1 to 25. The red triangles and the yellow circles between some of the nearest-neighbor particle pairs denote a bond between two adjacent particles according to one of the encoded targets. (B) In each iteration, a physical move on the lattice (left) is attempted, followed by an internal state switch (right). The trial moves are accepted with a probability that depends on the energy difference and external drive, as described in the main text. (C) Two target structures in which all of the particles are in one of the two possible internal states. Each one has a unique spatial configuration of the N particles.

When two particles, i and j, occupy adjacent lattice sites, they experience nearest-neighbor (n.n.) interaction, $J(s_i, s_j)$, which depends on their internal states and the encoded targets. A particle pair i, j is defined as a neighboring pair if they are n.n. in one of the stored targets (Figure 1C). When two adjacent particles i, j on the lattice are a neighboring pair according to target m, and both share the internal state $s_i = s_j = m$, they experience a strong attraction, J_s. If the pair i, j is not a neighboring one, the particles experience a weak interaction J_w. Otherwise, if the particles are a neighboring pair according to target m, but only one of them has the appropriate internal state, $s_i = m$, $s_j \neq m$, then the interaction strength is $\frac{1}{2}(J_w + J_s)$, and if none of them is at the internal state m, then the interaction strength is J_w. Mathematically, the interaction energy between particles i and j can be written as

$$J(s_i, s_j) = J_w + \sum_{m=1}^{M_T} I_{i,j}^m \left(\frac{J_s - J_w}{2}\right)(\delta_{m,s_i} + \delta_{m,s_j}) \quad (1)$$

where δ_{m,s_i} is the Kronecker delta and $I_{i,j}^m$ is a matrix representing the stored target, $I_{i,j}^m = 1$ if the particles i and j are nearest neighbors according to target m, and zero otherwise.

The total energy of the system, E, is calculated by

https://doi.org/10.1021/acs.jpcb.3c01376
J. Phys. Chem. B XXXX, XXX, XXX−XXX
DISTRIBUTION A: Distribution approved for public release.

$$E = \sum_{i=1}^{N} \sum_{j=1}^{N} J(s_i, s_j) B(i, j) \quad (2)$$

where $B(i, j)$ is the board nearest neighbors matrix, $B(i, j) = 1$ if particles i and j are nearest neighbors on the lattice according to the current state of the simulation, and zero otherwise.

The dynamics are simulated using a single-particle Monte Carlo Metropolis algorithm.[93] Initially, the N particles are placed randomly on the lattice with $s_i = 1$ for $i = 1, \cdots, N$. In each iteration, a particle is randomly chosen and attempts to translate to an adjacent tile, either up, down, right, or left (Figure 1B), with periodic boundary conditions. If the destination tile is occupied, the move is rejected. Otherwise, the total energy difference ΔE between the post- and pretranslation configurations is calculated, and the probability p to accept the suggested move is given by[93]

$$p = \min(1, e^{-\Delta E}) \quad (3)$$

The energy in eq 3 and generally throughout this paper is given in units of $K_B T$ (Table 1).

Table 1. Simulation Parameters

parameter	notation	value
number of particles	N	25
grid size	L	15
number of targets	M_T	2
strong energy	J_s	$-4\ K_B T$
weak energy	J_w	$-1\ K_B T$
external driving	$\Delta\mu$	$[0.6, 0.8, 1.0, \cdots, 2.8]\ K_B T$
simulation time cap	T	5×10^7

After each attempted physical move, a particle is chosen at random again, along with a new random internal state, different from its current one (Figure 1B). Under equilibrium conditions, the energy difference is calculated, and the internal state switch is accepted with probability, according to eq 3.

When a self-healing drive is introduced, a particle is more likely to adopt the internal state of its neighbors and less likely to change its internal state if it is similar to its neighbors. Specifically, if the chosen particle for an internal state switch has two or more n.n. with the same internal state, the acceptance probability of an attempted move to switch its internal state to that of its neighbors increases by $\Delta\mu$. Moreover, if initially, the internal state of the chosen particle is the same as two or more of its n.n., the acceptance probability of an attempted move to switch its internal state to a different one decreases by $\Delta\mu$. Therefore, the acceptance probability q of an internal state switch under external driving is given by[24]

$$q = \min(1, e^{-\Delta E \pm \Delta\mu}) \quad (4)$$

where the + or − signs in the argument of the exponent are chosen according to the rule defined above, depending on whether the state switch is favored or not. These modified dynamics break detailed balance.[93]

The values of the parameters of the simulations, summarized in Table 1, were chosen based on an initial analysis of the system performance at equilibrium and the available computational resources (see Model Analysis Section in the Supporting Information). We note that the single-particle Monte Carlo simulation may not fully capture all quantitative features of realistic dynamics since collective clusters diffusion is suppressed;[94,95] however, it can still provide insights into the process of self-assembly.[96−99]

RESULTS AND DISCUSSION

MC Simulations. We begin by analyzing the self-assembly process under equilibrium conditions, $\Delta\mu = 0$, quantified by the time to the first assembly, T_{FAS}, starting from random initial conditions, and the total time spent at the target state, T_{target}, when starting in one of the stored targets, as a proxy for target stability (see Model Analysis Section in the Supporting Information). In agreement with previous findings,[24] we find a fundamental trade-off in equilibrium self-assembly, where target stability can come at the cost of the assembly speed (Figure S1). We, therefore, set to explore the self-assembly performance under an external drive.

We simulated the system using the parameters listed in Table 1, with 1000 realizations for each value of the drive (See Numerical Implementation Section in the Supporting Information). During the trajectory of 5×10^7 MC steps, we record the total energy E of the system, the total entropy production, ΔS, and the distance to the two targets, d (Figures 2A and S2). ΔS is calculated by summing up the log ratio of the probability of an accepted move and the probability of its reverse.[85,100] The distance to target m, namely, d_m, is calculated for each target separately by comparing the particles' current adjacency matrix and the adjacency matrix of the two targets (see Distance from Target Calculation Section in the Supporting Information). Whenever $d_m = 0$ or $E = -160$ $K_B T$ (the global minimum energy value of the system), the corresponding target m is assembled. Snapshots of the particle positions and internal states along a single trajectory can be seen in Figure 2B−E and Movies S1, S2, and S3.

We observe that a successful assembly of a target structure is accompanied by a sharp change in the slope of the total entropy production ΔS (Figure 2C). While the system remains close to the assembled target, manifested in small values of d_m, the entropy production rate decreases, which can be attributed to decreased fluctuations due to the emergence of a stable order in the system. Moreover, the trajectory includes segments of energy and distance fluctuations around values that do not correspond to one of the assembled targets, which we attribute to kinetic traps giving rise to meta-stable states in the dynamics.

First Self-Assembly Time Statistics. During a realization in which an assembly occurs, we record the first self-assembly time (in MC steps), T_{FAS}. Histograms of the T_{FAS} for several values of the drive can be seen in Figure 3A, where we used unequal binning to capture the underlying distribution of the data. For values below the median of the data, we chose equal binning in the log scale, whereas for values above the median, we used the standard Scott's rule for binning.[101] Finally, all of the realizations in which an assembly did not occur were captured in a single bin corresponding to the total number of MC steps of the simulation.

The data were fitted by a Kernel density estimator (KDE) with a positive support[102] and a log-normal distribution (Figure 3B). As the drive value increases, the fit of the log-normal distribution better captures the data. We note that for low values of the drive, the probability of not observing a successful assembly during the realization increases, so the simulation results cannot provide the full distribution of T_{FAS}.

Owing to the simulations in which there is no assembly, the mean time to the first self-assembly would be an under-

https://doi.org/10.1021/acs.jpcb.3c01376
J. Phys. Chem. B XXXX, XXX, XXX−XXX
DISTRIBUTION A: Distribution approved for public release.

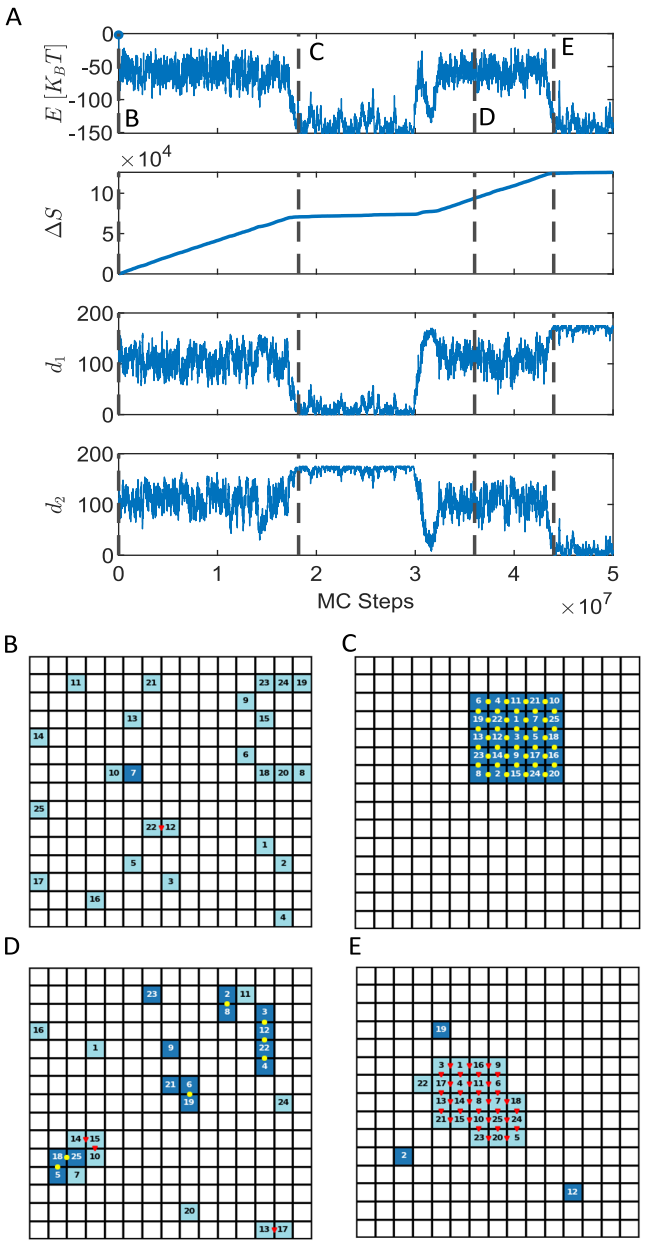


Figure 2. Simulation trajectories. (A) Energy E, total entropy production ΔS, and the distance from the two stored targets, d_1 and d_2, are plotted as a function of the MC steps. The vertical dashed lines indicate selected time points along the realization, corresponding to (B) initial conditions, (C) the first self-assembly event of target 1, (D) a potential kinetic trap characterized by energy fluctuations around a value higher than the global minima, and (E) approaching the successful self-assembly of target 2. The corresponding lattice states are plotted.

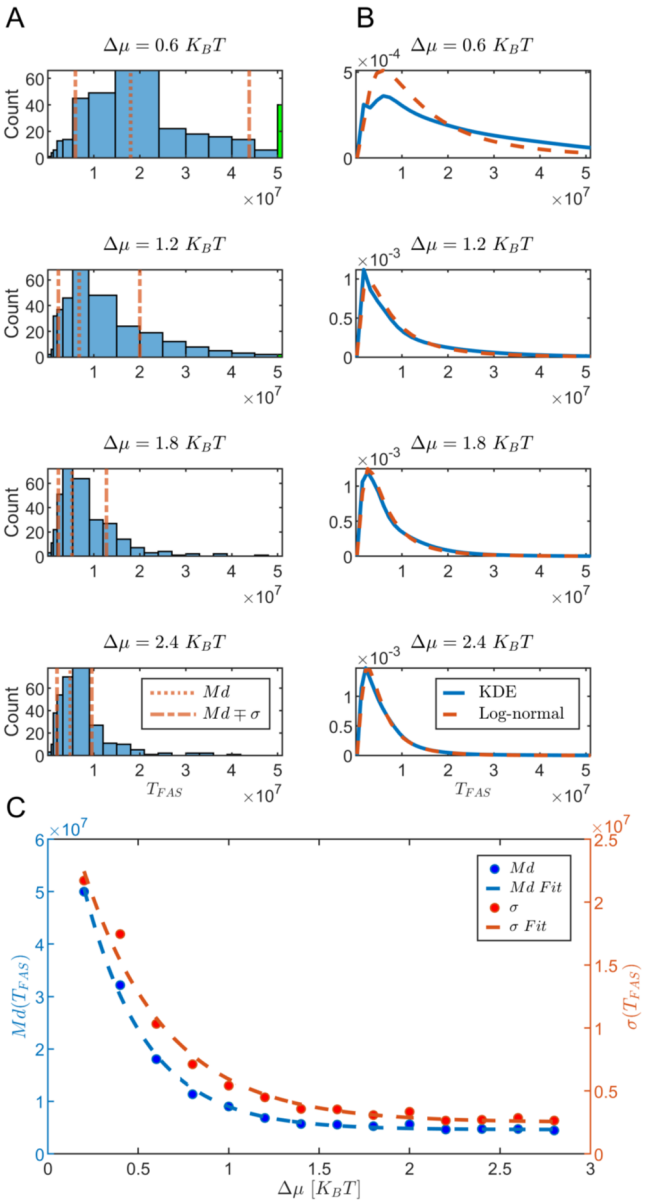


Figure 3. Simulation result statistics. (A) Simulation realizations histograms of the time to the first assembly for nonequilibrium drives, $\Delta\mu$ = 0.6, 1.2, 1.8, and 2.4 K_BT. The dotted vertical lines are the median values, Md, of the histogram, and the dashed lines are the 16th and 84th percentiles of the data, respectively, corresponding to the standard deviation, σ. The green bins stand for the realizations in which no assembly occurred. (B) Fit for the simulations realization histograms with a kernel density estimator (KDE, blue) and a log-normal distribution (dashed orange). (C) Median Md (blue), and the standard deviation σ (red) of the time to the first assembly histograms as a function of the drive value, $\Delta\mu$, with an exponential fit, $Ae^{-b\Delta\mu} + C$ (dashed curves).

estimation of the true value. Therefore, we focus on the median value, Md (dotted orange line in Figure 3A). In addition, we label one standard deviation, σ, above and below the median in the log scale, corresponding to the 16th and 84th percentiles (dashed orange lines in Figure 3A). Histograms and distributions of T_{FAS} for equilibrium and for additional drive values appear in Figure S3 (see Additional MC Simulation Results Section in the Supporting Information).

Both the median, Md, and the standard deviation, σ, decrease with increasing the drive down to a finite positive value (Figure 3C). The trend could be captured by an exponential decay, and the data were fitted using $Ae^{-b\Delta\mu} + C$. The fit parameters are listed in Tables S1 and S2. The finite positive value of the median of T_{FAS} for large drive values stems from the minimal time required for the diffusion of the particles. The system must explore its phase space, seeking one of the global minima, where all of the particles are in their desired locations according to one of the encoded targets.

Remaining Time to the First Assembly. The remaining time to the first assembly, t_r, measured in MC steps, is defined

https://doi.org/10.1021/acs.jpcb.3c01376
J. Phys. Chem. B XXXX, XXX, XXX−XXX

DISTRIBUTION A: Distribution approved for public release.

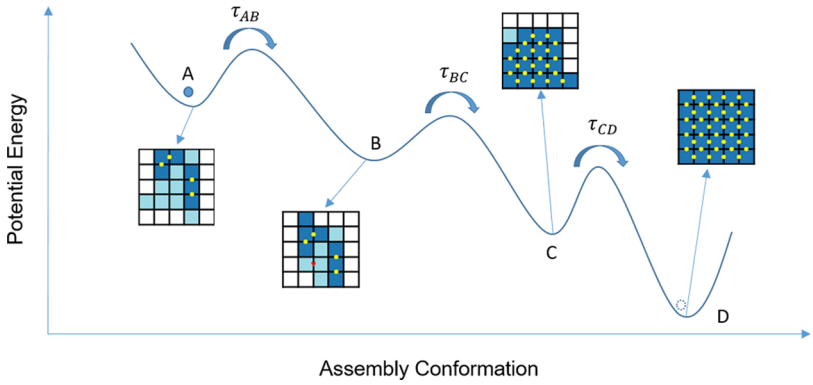


Figure 4. Self-assembly and Kramer's escape rate illustration. The self-assembly process has a rugged energy landscape, and the system needs to cross multiple barriers between local minima (A−C) on the path to the target structure (D). Each barrier is associated with a typical escape rate, so the time to the first assembly can be approximated by the sum of the dwell times in the local minima, $T_{FAS} \approx \tau_{AB} + \tau_{BC} + \tau_{CD}$, in this case.

as the difference between the time to the first assembly, T_{FAS}, for the trajectory at hand, and the observation time, t, i.e., $t_r = T_{FAS} - t$, where $0 \leq t \leq T_{FAS}$. Given the log-normal distribution of T_{FAS}, we examined the distribution of t_r, keeping in mind that $t_r = T_{FAS}$ at $t = 0$. Indeed, we find that the t_r distribution can be approximated as a log-normal distribution as well (Figure S4), so its logarithm is fully characterized by the first two moments (see Remaining Time to First Assembly Statistics Section in the Supporting Information). Therefore, the mean and error of the prediction of $\log(t_r)$ provide an assessment of the predictive power of our approach. As a result, we aim to provide predictions $\hat{Y}$ for the remaining time to the first assembly in log scale $Y = \log(t_r)$.

For the prediction, we rely on a segmented and down-sampled trajectory observable, *e.g.*, the energy, E. Without additional analysis, a naïve guess $\ddot{Y}$ for Y would be the mean value regardless of the statistical characterization of the observable. Here, we seek to utilize the statistical moments of the energy, E, to improve the prediction power of the remaining time to the first assembly, t_r.

Stochastic Landscape Method. The Stochastic Landscape Method (SLM) is an empirical approach for improving the forecast of the remaining time to the first self-assembly along a realization, using the information of the simulated macro-parameters. The key idea is to segment the trajectory data using the BEAST algorithm (see The BEAST Algorithm Details Section in the Supporting Information) and exploit the statistical information of the observable in each segment to predict the remaining time until a self-assembly event, better than the naïve guess based on the mean value of t_r. The SLM can be considered as a supervised machine learning algorithm, as it uses input and output pairs to provide a prediction for unseen data,[103] where the input data are the statistical information of the trajectory segments, and the output is the remaining time to the first assembly. In the following section, we explain the physical intuition behind the choice of the input data, which can also grant the SLM virtue of interpretability.

Motivation. We seek to divide the trajectory of an observable into temporal segments. Here, we chose the energy of the system as the parameter to segment. In our system, the combinatorial interplay of the interaction between the different particles results in a rugged energy landscape due to the kinetic traps in numerous local minima. An example of the simulation dynamics can be seen in the Movies S1−S3, where the trajectory can be considered as "jumping" between kinetic traps.

Along the trajectory, the energy of the system fluctuates with characteristic mean and standard deviation values at each of the meta-stable kinetic traps. When jumping to another kinetic trap, the temporal behavior of the energy changes to new mean and standard deviation values. Occasionally, the system spends time in transition states between two kinetic traps, where the energy value shows a nonzero trend while drifting to lower energy values or, rarely,[104] to higher energy values. Therefore, we assume that each segment can be associated with a different "macrostate" in the complex rugged energy landscape of the system,[105−109] such that the statistics within each segment is a characterization of the position on the energy landscape. We thus describe each segment by its statistical features:[110] the mean, standard deviation, and the mean trend of the segment,[89] which are referred to as the "stochastic coordinates," and we assume they are drawn from a different probability distribution in the different segments.[109]

We now refer to the remaining time to self-assembly prediction. Although not every segment is necessarily meta-stable, the time spent in meta-stable states significantly contributes to the time to the first assembly T_{FAS}, as indicated by the concept of "low rattling."[48] According to Kramer's escape rate theory,[111] the average transition time between two meta-stable states in the energy landscape is determined by the barrier height, the energies of the two states, and the corresponding fluctuations. Inspired by Kramer's idea, we expect that the time to the first assembly T_{FAS} is correlated to the sum of the transition times τ_k between meta-stable states visited along the system path to assembly, so $T_{FAS} \approx \sum_k \tau_k$. (see Figure 4). Following this meta-stability picture, we hypothesize that the information inferred by the stochastic coordinates is valuable for t_r prediction. Furthermore, if the system is found in a transition segment with a negative trend of the energy value, we anticipate the system is moving closer to its global minima, which is one of the target structures. Therefore, we expect the stochastic coordinates to carry valuable information for t_r prediction.

BEAST Algorithm. The SLM relies on an automated division of a trajectory observable into segments with different statistics. The BEAST algorithm was chosen for this purpose due to its versatile utilization and robustness.[89] Moreover, it does not require specifying the number of anticipated statistical change points in the data, but rather, only a maximal number

https://doi.org/10.1021/acs.jpcb.3c01376
J. Phys. Chem. B XXXX, XXX, XXX−XXX

DISTRIBUTION A: Distribution approved for public release.

of change points is needed. BEAST assesses the probability of the number of statistical changes in the data and, by default, chooses the median number of this distribution.

The BEAST algorithm assumes a given time series is constructed from intervals of varying duration, each with Gaussian noise. The underlying unknown model is characterized by a set of model parameters, such as the periods of the seasonal signals, the number of seasonal and trend change points and their timings, the parameters of a linear trend and harmonic model of seasonality, and the magnitude of the Gaussian noise of each segment. BEAST aims to find the model parameters that would yield the time series statistics based on Bayesian inference by maximizing the posterior probability distribution, which is the product of a likelihood and the prior distribution of the model parameters, according to Bayes' theorem. Since the posterior distribution is analytically intractable, the algorithm uses a Monte Carlo Markov Chain for sampling this distribution, to be used for the posterior inference.[89,112,113]

While BEAST can detect both trend changes and seasonal change points, here we focus on segmenting the data only according to trend changes, as there is no reason for seasonality in our case. Moreover, a minimum duration for each segment or a maximal number of change points can be defined in order to coarse-grain short-lived states. In our case, the minimum duration was set to one percent of the total simulation time (see SLM Implementation on Nonequilibrium Self-Assembly Section in the Supporting Information).

An example of the segmentation of an energy trajectory according to the BEAST algorithm can be seen in Figure 5A. Zooming into several segments, we can see that the BEAST algorithm captures significant changes in the signal statistics (Figure 5B). More examples of segmented energy trajectories are presented in Figure S5.

SLM Flowchart. The SLM is an end-to-end algorithm developed for this work in order to infer the emerging complex dynamics of nonequilibrium self-assembly, specifically predicting the statistics of the remaining time to the first assembly, t_r. Nevertheless, it is a general framework that can be modified and applied to other complex stochastic systems. The general step-by-step flowchart of the SLM is depicted in Figure 6, where the specific technical and detailed implementation of the method on the nonequilibrium self-assembly process can be found in the Supporting Information.

As a first step, the input of the SLM is a set of macroparameter trajectories realized with the same parameters from random initial conditions, where a larger number of trajectories improves the statistics. Second, due to computation limitations, the trajectories are down-sampled to effectively limit the minimum duration of each segment. This step depends on the task in question and is generally optional. Third, we use the BEAST algorithm to segment the data with specified conditions (See Figures 5 and S5), i.e., a minimum duration of a segment is one percent of the total simulation time in our case. Fourth, the segments before the first self-assembly, Ω_{FAS}, are collected, as we aim to provide a prediction for the remaining time to the first assembly. This step is also optional and depends on the question at hand. Then, the stochastic coordinates (mean, standard deviation, and the mean trend) are calculated for the chosen segments, Ω_{FAS}, and each segment is labeled with the logarithm of its corresponding remaining time to the first assembly, $Y = \log(t_r)$, based on the log-normal distribution of t_r. The stochastic coordinates are

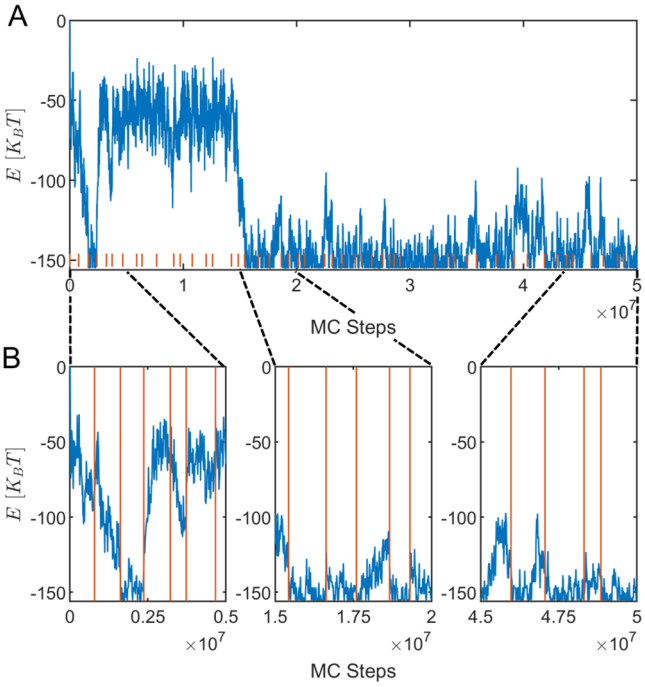


Figure 5. BEAST Segmentation. (A) Energy E of the system as a function of the MC steps for a realization of the system under nonequilibrium drive. The parameters are listed in Table 1, with $\Delta\mu$ = 1. The minimum value of the energy corresponds to a successful target assembly. The vertical orange lines indicate the change points in the statistics detected by the BEAST algorithm with a minimal segment−duration constraint of one percent of the total simulation time. Each segment between two change points is considered a "macrostate." (B) Zoom-in on three different windows of the trajectory. Vertical orange lines mark the corresponding change points.

normalized by subtracting their respective mean values and dividing them by their standard deviation, where the normalization is done for all of the segments in Ω_{FAS} together. A principal component analysis (PCA) is applied to the stochastic coordinates, and the first two principal components are chosen for the following steps.

Fifth, the segments Ω_{FAS} are randomly distributed between three sets: the training set, Ω_T, the cross-validation set, Ω_{CV}, and the test set Ω_{test}. Sixth, the stochastic landscape is constructed from Ω_T following the stochastic coordinate results in the set, by a 2-D triangulation and data smoothing of the $Y = \log(t_r)$ values as a function of the two principal components (see Fig. S6 for a visualization). Seventh, we use the stochastic landscape for generating a $Y = \log(t_r)$ prediction for the cross-validation (CV) set Ω_{CV}, which is referred to as the primary predictor $\hat{Y}_p(\Omega_{CV})$. The fifth to seventh steps are repeated $K = 10$ times to get K different $\hat{Y}_p$ primary predictors, and the bias between each of the predictors $\hat{Y}_p$ and their true values Y is calculated for the segments in the CV set (Fig. S7). Eighth, we construct the stochastic landscape one last time for all of the data in the training and cross-validations sets, $\Omega_{CV} \cup \Omega_T$, and subtract the calculated bias, resulting in a biased corrected predictor $\hat{Y}_{BC}$. Finally, $\hat{Y}_{BC}$ provides a prediction on the test, and the output of the procedure is $\boldsymbol{y} = \hat{Y}_{BC}(\Omega_{test})$.

SLM Performance Evaluation. We quantify the performance of the SLM in three ways: (1) the correlation between the true value, Y, and the predicted values, $\hat{Y}_{BC}$, (2) the mean error of the predicted values $\hat{Y}_{BC}$ compared to a naive guess based on

https://doi.org/10.1021/acs.jpcb.3c01376
J. Phys. Chem. B XXXX, XXX, XXX−XXX

DISTRIBUTION A: Distribution approved for public release.

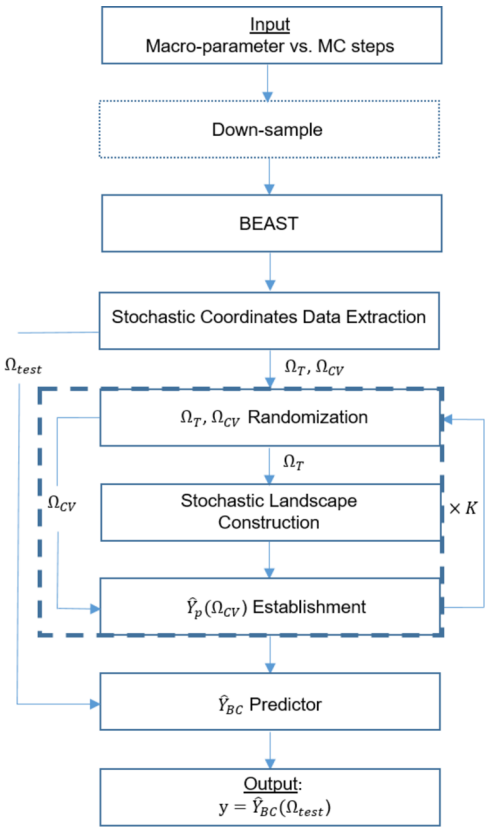


Figure 6. Flowchart of the SLM prediction process. The different steps are described in the text. The dotted rectangle is an optional step, and the dashed frame represents the repeated steps for cross-validation bias correction.

the mean value $\hat{Y}_M$ of the remaining time to the first assembly in a log scale, and (3) the Kullback–Leibler Divergence (KLD) between the $\Delta\hat{Y}_{BC}$ distribution and the data distribution ΔY_{test}, which is compared to the KLD between the $\Delta\hat{Y}_M$ distribution and ΔY_{test}, all defined below.

The mean predictor $\hat{Y}_M$ is the mean of the $\log(t_r)$ values for all of the segments in the set $\Omega_{CV} \cup \Omega_T$. This is the naïve guess if no other information is available. We expect the SLM predictor $\hat{Y}_{BC}$ to perform better than the mean predictor $\hat{Y}_M$, manifested in a smaller prediction error. To define the data distribution ΔY_{test}, we first bin the data according to the values of $\hat{Y}_{BC}$. For each bin, we get a distribution of the true values, i.e.,, the remaining time to the first assembly for the test set in a log scale, Y_{test}, subtracted from their mean, $\Delta Y_{test} = \langle Y_{test} \rangle - Y_{test}$. Similarly, we define the distributions $\Delta\hat{Y}_M = \hat{Y}_M - Y_{test}$ and $\Delta\hat{Y}_{BC} = \hat{Y}_{BC} - Y_{test}$ for each bin. We also calculate the relative weight of each bin by the ratio of the number of data points in the bin to the total number of data points in Y_{test}. The distributions of $\Delta\hat{Y}_{BC}$ and $\Delta\hat{Y}_{test}$ are evaluated by the kernel density estimation (KDE)[102] (see the distributions for $\Delta\mu$ = 1.6 in Figure S8 in the Supporting Information). Then, we compare the KLD between $\Delta\hat{Y}_{BC}$ and $\Delta\hat{Y}_{test}$, to the KLD between $\Delta\hat{Y}_M$ and $\Delta\hat{Y}_{test}$, for each bin, and perform a weighted average according to the weight of the bins to yield KLD_{BC} and KLD_M, respectively. The KLD between two probability distributions, $f_1(x)$ and $f_2(x)$ is[114]

$$\mathrm{KLD}(f_1 \| f_2) = \int_{-\infty}^{\infty} f_1(x) \log\left(\frac{f_1(x)}{f_2(x)}\right) dx \quad (5)$$

As the KLD is a measure of the difference between two probability distributions, smaller KLD values indicate a better estimator of the true values. These evaluations were applied to the simulation data with the parameters listed in Table 1, and they are presented along with the prediction results in the next section.

Self-Assembly Remaining Time Predictions. The results of our test set prediction before and after the bias correction, $\hat{Y}_p$ and $\hat{Y}_{BC}$, for the remaining time to the first assembly, are presented in Figure 7A for the drive $\Delta\mu$ = 1.6 K_BT, and in Figures S9A, S10A, and S11A, for drive values $\Delta\mu$ = 1, 2.2, and 2.8 K_BT, respectively. The figures present sample-wise scatter plots of the remaining time to the first assembly for the test set, Y_{test}, *vs* the predicted values, $\hat{Y}_{BC}$. The Pearson correlation coefficient between Y_{test} and the $\hat{Y}_{BC}$ was found to be in the range between R = 0.34 and R = 0.52 ($p < 0.01$) for all of the drive values (see Table 2).

To assess the performance of our estimator $\hat{Y}_{BC}$, we bin the data of Y_{test} *vs* $\hat{Y}_{BC}$, according to the values of $\hat{Y}_{BC}$, with a bin width of 0.5 in the log scale, and represent the statistics of Y_{test} for each bin in box plots in Figures 7B, S9B, S10B, and S11B, for the various drive values tested. The data are compared to a linear line with a unit slope ($y = Y_{test}$), which represents the results of a perfect predictor. For low drive values (Figures 7B and S9B), the predictor agrees well with the true values, whereas for high drive values (Figures S10B and S11B), the predictor agrees well mostly for intermediate values of $\hat{Y}_{BC}$, probably due to insufficient statistics for high and low values of $\hat{Y}_{BC}$.

To compare the mean error of the predicted values $\hat{Y}_{BC}$ with the mean value of $\hat{Y}_M$, the absolute values of error distributions for each bin, $\Delta\hat{Y}_{BC}$ and $\Delta\hat{Y}_M$, are depicted in box plots in Figures 7C, S9C, S10C, and S11C for the different drive values. The relative number of data points in each bin appears as a colored circle above the corresponding boxes. Indeed, the results of the SLM outperform the naive mean predictor manifested in the smaller absolute mean values of $\Delta\hat{Y}_{BC}$ compared to $\Delta\hat{Y}_M$. As excepted, the prediction is more accurate for shorter remaining times, following the intuition that when the system is closer to the global minimum, it may be easier to predict its future behavior. Close to the assembled state, when there is a relatively large assembled seed, the system is more likely to assemble the target rather than disassemble to the individual components owing to the energy barrier. For all simulated drive values, we found that $KLD_{BC} < KLD_M$ (Table 2), indicating the advantage of $\hat{Y}_{BC}$ compared to $\hat{Y}_M$.

In order to validate the robustness of the SLM approach, we performed a sensitivity analysis by changing the simulation parameters, one factor at a time.[115] Specifically, the number of particles was increased to N = 36 while keeping the number of stored targets M_T = 2, whereas, in another set of simulations, the number of stored targets was varied between M_T = 1, 3, 4 while keeping the initial choice of the number of particles N = 25. The rest of the simulation parameters were chosen according to the values in Table 1. We simulated the system with 1000 realizations for each drive value and activated the SLM (Figure 6), considering only drive values for which more than 60% of the trajectories contained at least one assembly event for the prediction, and calculated the corresponding Pearson correlation coefficients. Moreover, we compared the KLD_M with the KLD_{BC} results to ensure the SLM provided

https://doi.org/10.1021/acs.jpcb.3c01376
J. Phys. Chem. B XXXX, XXX, XXX−XXX

DISTRIBUTION A: Distribution approved for public release.

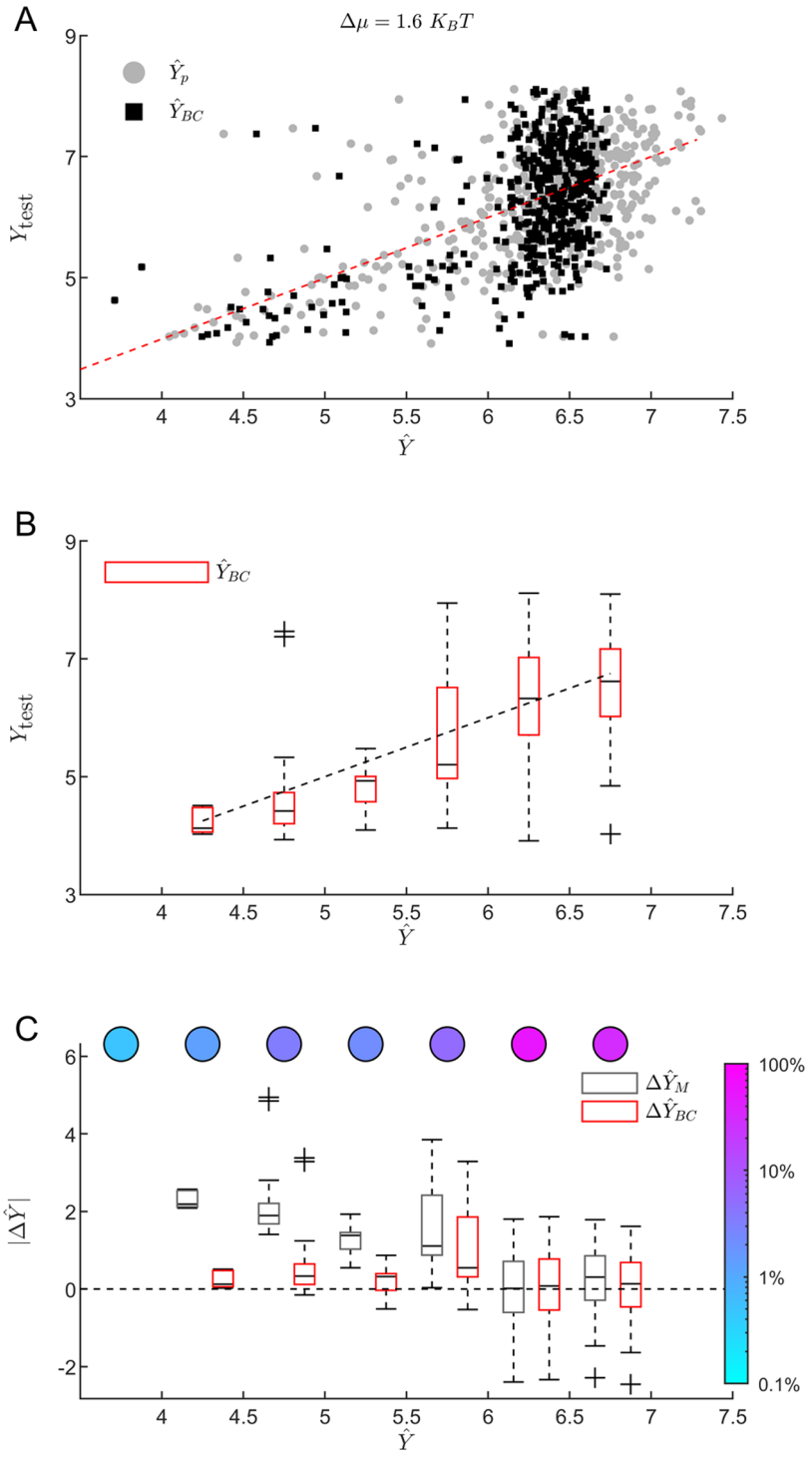


Figure 7. Results of the SLM prediction for the remaining time to the first assembly for the test set, for $\Delta\mu$ = 1.6 K_BT. (A) Y_{test} results are shown *vs* their predicted values $\hat{Y}$, before the bias correction ($\hat{Y}_p$, gray circles) and after the bias correction ($\hat{Y}_{BC}$, black squares). The red line shows the linear regression of the data. (B) Box plot of the Y_{test} *vs* the calculated $\hat{Y}_{BC}$, where the data are binned according to the $\hat{Y}_{BC}$ values (see main text).The box plot whiskers represent the standard interquartile range (IQR), and outliers are defined to be above 1.5 IQR (plus markers). The dashed unit slope, linear line ($y = Y_{\text{test}}$) represents the results of a perfect predictor. (C) Absolute values of $\Delta\hat{Y}_M$ (black) and $\Delta\hat{Y}_{BC}$ (red) *vs* the respective predictor value $\hat{Y}$ for each bin. The dashed black line at $\Delta\hat{Y} = 0$ represents a perfect predictor with zero error. The color bar indicates the relative weight of the data for each bin, calculated from the relative number of data points. Bins with weights less than 1% are omitted.

predictive information (see Sensitivity Analysis in the Supporting Information).

For both the variation in the number of particles (Figure S13 and Table S3) and the number of stored targets (Figures S14–S16 and Tables S4–S6), we found that $R > 0.25$ for all of the simulated system configurations, indicating the correlation between the true and predicted values of the SLM. Furthermore, for all 39 simulated system configurations, with the exception of 3 cases, we found that $\text{KLD}_{BC} < \text{KLD}_M$, demonstrating the improved prediction of the SLM compared

https://doi.org/10.1021/acs.jpcb.3c01376
J. Phys. Chem. B XXXX, XXX, XXX−XXX

DISTRIBUTION A: Distribution approved for public release.

Table 2. Performance Evaluation of the SLM

$\Delta\mu$	R	KLD_M	KLD_{BC}
0.6	0.34	0.27	0.07
0.8	0.4	0.7	0.07
1.0	0.52	1.02	0.06
1.2	0.4	0.64	0.12
1.4	0.43	0.77	0.07
1.6	0.5	1.36	0.18
1.8	0.52	1.29	0.32
2.0	0.37	0.26	0.03
2.2	0.5	0.37	0.11
2.4	0.39	0.73	0.2
2.6	0.35	0.24	0.05
2.8	0.43	0.14	0.03

to the naïve guess of the median value of the remaining time to the first self-assembly. These results further support the predictive power and robustness of the SLM approach.

CONCLUSIONS

This work quantitatively explores nonequilibrium driving in self-assembly processes. We have used a toy model of interacting distinguishable particles that can assemble target structures, which are global energy minima of the system. We found that the time to the first assembly had a log-normal distribution for most drives simulated, whose median and standard deviation decreased exponentially with increasing the drive value. Moreover, we have established a novel data-driven general framework, the stochastic landscape method (SLM), for inferring the stochastic dynamics and providing predictions. Here, we used the SLM to provide a prediction for the remaining time to the first assembly, given the statistics of a down-sampled observable. We further showed that the SLM holds predictive power for different parameter values of the system, demonstrating its robustness.

Our method was theoretically inspired by the prevalence of Kramer's escape rate in nonequilibrium biological systems,[116] and the concept of "low rattling,"[48] stating that a system tends to find regions in phase space in which fluctuations are small, making it less likely for it to escape. Another inspiration was drawn from dynamical systems theory, where systems are studied from a top-down perspective.[80,81] Our approach utilizes a statistics-based segmentation algorithm[89] for constructing the phase space of the system[79] from a trajectory observable,[80,81] in order to provide predictions. We have shown that using different measures of prediction evaluation, the SLM yields better results compared to the trivial guess for the remaining time to self-assembly, where the prediction is more accurate for shorter times since the system is closer to the global minimum.

Although predictability is challenging for stochastic systems,[117,118] the resulting correlation values between the measured and predicted values of the remaining time to the first assembly manifest a predictive power of the SLM. Inevitably, in some cases, the SLM prediction is limited, as can be seen in Figure 7, for larger times. For example, if the system is randomly initiated, the t_r prediction can only be the initial broad distribution of T_{FAS} presented in Figure 3.

The SLM is a novel approach to study nonequilibrium stochastic dynamics with a rugged energy landscape, based on observing the statistical moments of an observable for a short duration. Based on the measured mean, standard deviation, and average trend of the observable, the SLM attributes a particular macrostate to the system, from which it can provide a prediction for the remaining time to the first assembly.

Future work will focus on finding stochastic differential equations[119,120] for the segments representation of the system, assessing the prediction limit of the system, adding predictions based on segmented trajectories, examining the time complexity of the system for larger assemblies,[121] utilizing the framework for real-time drive control protocols of the self-assembly process, allowing collective motions of clusters, using, for example, "virtual-move" Monte Carlo algorithms,[94,96] and applying similar approaches of the SLM to other nonequilibrium systems, relying on its general predictive power. We envision that the SLM would promote a deeper understanding of biophysical nonequilibrium processes and advance the experimental realizations of synthetic self-assembly systems.

ASSOCIATED CONTENT

Supporting Information

The Supporting Information is available free of charge at https://pubs.acs.org/doi/10.1021/acs.jpcb.3c01376.

Simulation realization for equilibrium $\Delta\mu = 0$ K_BT (Movie S1) (AVI)

Simulation realization for $\Delta\mu = 1K_BT$ (Movie S2) (AVI)

Simulation realization for $\Delta\mu = 2K_BT$ (Movie S3) (AVI)

Model analysis; numerical implementation; distance from the target calculation; additional MC simulation results; The BEAST algorithm details; remaining time to fist assembly statistics; SLM implementation on nonequilibrium self-assembly; sensitivity analysis; and simulation equilibrium properties (Figure S1); macroparameters trajectories for the drives of $\Delta\mu = 0$, 1, and 2 K_BT (Figure S2); additional simulation results statistics (Figure S3); simulation results of the remaining time to the first assembly statistics (Figure S4); typical energy trajectories *vs* time for the default simulation parameters and the results of BEAST segmentation (Figure S5); the stochastic landscape results for the primary predictor (Figure S6); the bias correction scheme (Figure S7); the probability density functions of the bin-wise errors for $\Delta\mu = 1.6$ K_BT (Figure S8); results of the SLM prediction values for $\Delta\mu = 1$ K_BT (Figure S9); results of the SLM prediction values for $\Delta\mu = 2.2$ K_BT (Figure S10); results of the SLM prediction values for $\Delta\mu = 2.8$ K_BT (Figure S11); results of the SLM prediction values for $\Delta\mu = 2.6$ K_BT (Figure S12); results of the SLM prediction values for $\Delta\mu = 2.6$ K_BT for $N = 36$ particles (Figure S13); results of the SLM prediction values for $\Delta\mu = 2.6$ K_BT for $M_T = 1$ stored targets (Figure S14); results of the SLM prediction values for $\Delta\mu = 2.6$ K_BT for $M_T = 3$ stored targets (Figure S15); results of the SLM prediction values for $\Delta\mu = 2.6$ K_BT for $M_T = 4$ stored targets (Figure S16); median fit parameters for $T_{fas}(\Delta\mu)$ (Table S1); STD fit parameters for $T_{fas}(\Delta\mu)$ (Table S2); performance evaluation of the SLM for $M_T = 2$ and $N = 36$ (Table S3); performance evaluation of the SLM for $M_T = 1$ and $N = 25$ (Table S4); performance evaluation of the SLM for $M_T = 3$ and $N = 25$ (Table S5); performance evaluation of the SLM for $M_T = 4$ and N = 25 (Table S6) (PDF)

https://doi.org/10.1021/acs.jpcb.3c01376
J. Phys. Chem. B XXXX, XXX, XXX−XXX

DISTRIBUTION A: Distribution approved for public release.

AUTHOR INFORMATION

Corresponding Author

Gili Bisker − *Department of Biomedical Engineering, Faculty of Engineering, Tel Aviv University, Tel Aviv 69978, Israel; The Center for Physics and Chemistry of Living Systems, The Center for Nanoscience and Nanotechnology, and The Center for Light-Matter Interaction, Tel Aviv University, Tel Aviv 6997801, Israel;* orcid.org/0000-0003-2592-7956; Email: bisker@tauex.tau.ac.il

Author

Michael Faran − *Department of Biomedical Engineering, Faculty of Engineering, Tel Aviv University, Tel Aviv 69978, Israel*

Complete contact information is available at: https://pubs.acs.org/10.1021/acs.jpcb.3c01376

Notes

The authors declare no competing financial interest.

ACKNOWLEDGMENTS

G.B. acknowledges the Zuckerman STEM Leadership Program and the Tel Aviv University Center for AI and Data Science (TAD). The authors acknowledge Noam Raviv and Ohad Nir for their contribution to the first version of the code. This work was supported by the ERC NanoNonEq 101039127, the Air Force Office of Scientific Research (AFOSR) under award number FA9550-20-1-0426, and by the Army Research Office (ARO) under Grant Number W911NF-21-1-0101. The views and conclusions contained in this document are those of the authors and should not be interpreted as representing the official policies, either expressed or implied, of the Army Research Office or the U.S. Government.

REFERENCES

(1) Iyer, A. S.; Paul, K. Self-assembly: a review of scope and applications. *IET Nanobiotechnol.* **2015**, *9*, 122−135.
(2) Bisker, G. Dissipate your way to self-assembly. *Nat. Phys.* **2020**, *16*, 707−708.
(3) Makey, G.; Galioglu, S.; Ghaffari, R.; Engin, E. D.; Yıldırım, G.; Yavuz, Ö.; Bektaş, O.; Nizam, ÜS.; Akbulut, Ö.; Şahin, Ö.; et al. Universality of dissipative self-assembly from quantum dots to human cells. *Nat. Phys.* **2020**, *16*, 795−801.
(4) Li, T.; Lu, X.-M.; Zhang, M.-R.; Hu, K.; Li, Z. Peptide-based nanomaterials: Self-assembly, properties and applications. *Bioact. Mater.* **2022**, *11*, 268−282.
(5) Amadi, E. V.; Venkataraman, A.; Papadopoulos, C. Nanoscale self-assembly: concepts, applications and challenges. *Nanotechnology* **2022**, *33*, No. 132001.
(6) Sang, Y.; Liu, M. Hierarchical self-assembly into chiral nanostructures. *Chem. Sci.* **2022**, *13*, 633−656.
(7) Chagri, S.; Ng, D. Y.; Weil, T. Designing bioresponsive nanomaterials for intracellular self-assembly. *Nat. Rev. Chem.* **2022**, *6*, 320−338.
(8) Schwarcz, D.; Burov, S. Self-assembly of two-dimensional, amorphous materials on a liquid substrate. *Phys. Rev. E* **2022**, *105*, No. L022601.
(9) Glover, J. R.; Lindquist, S. Hsp104, Hsp70, and Hsp40: A novel chaperone system that rescues previously aggregated proteins. *Cell* **1998**, *94*, 73−82.
(10) Sartori, P.; Leibler, S. Lessons from equilibrium statistical physics regarding the assembly of protein complexes. *Proc. Natl. Acad. Sci. U.S.A.* **2020**, *117*, 114−120.
(11) Jacobs, W. M. Self-assembly of biomolecular condensates with shared components. *Phys. Rev. Lett.* **2021**, *126*, No. 258101.
(12) Dergham, M.; Lin, S.; Geng, J. Supramolecular Self-Assembly in Living Cells. *Angew. Chem., Int. Ed.* **2022**, *61*, No. e202114267.
(13) Bukau, B.; Horwich, A. L. The Hsp70 and Hsp60 chaperone machines. *Cell* **1998**, *92*, 351−366.
(14) Tyedmers, J.; Mogk, A.; Bukau, B. Cellular strategies for controlling protein aggregation. *Nat. Rev. Mol. Cell Biol.* **2010**, *11*, 777−788.
(15) Bártová, E.; Krejčí, J.; Harničarová, A.; Galiová, G.; Kozubek, S. Histone modifications and nuclear architecture: a review. *J. Histochem. Cytochem.* **2008**, *56*, 711−721.
(16) Cedar, H.; Bergman, Y. Linking DNA methylation and histone modification: Patterns and paradigms. *Nat. Rev. Genet.* **2009**, *10*, 295−304.
(17) Karlić, R.; Chung, H.-R.; Lasserre, J.; Vlahoviček, K.; Vingron, M. Histone modification levels are predictive for gene expression. *Proc. Natl. Acad. Sci. U.S.A.* **2010**, *107*, 2926−2931.
(18) Musacchio, A.; Salmon, E. D. The spindle-assembly checkpoint in space and time. *Nat. Rev. Mol. Cell Biol.* **2007**, *8*, 379−393.
(19) Hess, H.; Ross, J. L. Non-equilibrium assembly of microtubules: from molecules to autonomous chemical robots. *Chem. Soc. Rev.* **2017**, *46*, 5570−5587.
(20) Ben-Ari, A.; Ben-Ari, L.; Bisker, G. Nonequilibrium self-assembly of multiple stored targets in a dimer-based system. *J. Chem. Phys.* **2021**, *155*, No. 234113.
(21) Murugan, A.; Zeravcic, Z.; Brenner, M. P.; Leibler, S. Multifarious assembly mixtures: Systems allowing retrieval of diverse stored structures. *Proc. Natl. Acad. Sci. U.S.A.* **2015**, *112*, 54−59.
(22) Murugan, A.; Zou, J.; Brenner, M. P. Undesired usage and the robust self-assembly of heterogeneous structures. *Nat. Commun.* **2015**, *6*, No. 6203.
(23) Trubiano, A.; Hagan, M. F. Optimization of non-equilibrium self-assembly protocols using Markov state models. *J. Chem. Phys.* **2022**, *157*, No. 244901.
(24) Bisker, G.; England, J. L. Nonequilibrium associative retrieval of multiple stored self-assembly targets. *Proc. Natl. Acad. Sci. U.S.A.* **2018**, *115*, E10531−E10538.
(25) Arango-Restrepo, A.; Barragán, D.; Rubi, J. Self-assembling outside equilibrium: emergence of structures mediated by dissipation. *Phys. Chem. Chem. Phys.* **2019**, *21*, 17475−17493.
(26) Das, K.; Gabrielli, L.; Prins, L. J. Chemically fueled self-assembly in biology and chemistry. *Angew. Chem., Int. Ed.* **2021**, *60*, 20120−20143.
(27) Trubiano, A.; Holmes-Cerfon, M. Thermodynamic stability versus kinetic accessibility: Pareto fronts for programmable self-assembly. *Soft Matter* **2021**, *17*, 6797−6807.
(28) Papaseit, C.; Pochon, N.; Tabony, J. Microtubule self-organization is gravity-dependent. *Proc. Natl. Acad. Sci. U.S.A.* **2000**, *97*, 8364−8368.
(29) Williams, R. J.; Smith, A. M.; Collins, R.; Hodson, N.; Das, A. K.; Ulijn, R. V. Enzyme-assisted self-assembly under thermodynamic control. *Nat. Nanotechnol.* **2009**, *4*, 19−24.
(30) Datta, S.; Bhattacharya, S. Multifarious facets of sugar-derived molecular gels: Molecular features, mechanisms of self-assembly and emerging applications. *Chem. Soc. Rev.* **2015**, *44*, 5596−5637.
(31) Huang, S.; Yu, H.; Li, Q. Supramolecular chirality transfer toward chiral aggregation: Asymmetric hierarchical self-assembly. *Adv. Sci.* **2021**, *8*, No. 2002132.
(32) Nizam, Ü. S.; Makey, G.; Barbier, M.; Kahraman, S. S.; Demir, E.; Shafigh, E. E.; Galioglu, S.; Vahabli, D.; Hüsnügil, S.; Güneş, M. H.; et al. Dynamic evolution of hyperuniformity in a driven dissipative colloidal system. *J. Phys.: Condens. Matter* **2021**, *33*, No. 304002.
(33) Bupathy, A.; Frenkel, D.; Sastry, S. Temperature protocols to guide selective self-assembly of competing structures. *Proc. Natl. Acad. Sci. U.S.A.* **2022**, *119*, No. e2119315119.
(34) Osat, S.; Golestanian, R. Non-reciprocal multifarious self-organization. *Nat. Nanotechnol.* **2023**, *18*, 79−85.
(35) Soto, R.; Golestanian, R. Self-assembly of catalytically active colloidal molecules: tailoring activity through surface chemistry. *Phys. Rev. Lett.* **2014**, *112*, No. 068301.

DISTRIBUTION A: Distribution approved for public release.

(36) Nguyen, M.; Vaikuntanathan, S. Design principles for nonequilibrium self-assembly. *Proc. Natl. Acad. Sci. U.S.A.* **2016**, *113*, 14231−14236.
(37) Nguyen, M.; Vaikuntanathan, S. A mean field thermodynamic framework for time dependent self-assembly and pattern formation. 2021, arXiv:2110.02382. arXiv.org e-Printarchive. https://arxiv.org/abs/2110.02382. (accessed July 05, 2023).
(38) Xie, X.-Q.; Zhang, Y.; Liang, Y.; Wang, M.; Cui, Y.; Li, J.; Liu, C.-S. Programmable Transient Supramolecular Chiral G-quadruplex Hydrogels by a Chemically Fueled Non-equilibrium Self-Assembly Strategy. *Angew. Chem.* **2022**, *134*, No. e202114471.
(39) Mitchison, T.; Kirschner, M. Dynamic instability of microtubule growth. *Nature* **1984**, *312*, 237−242.
(40) Aumeier, C.; Schaedel, L.; Gaillard, J.; John, K.; Blanchoin, L.; Théry, M. Self-repair promotes microtubule rescue. *Nat. Cell Biol.* **2016**, *18*, 1054−1064.
(41) Hopfield, J. J. Kinetic proofreading: A new mechanism for reducing errors in biosynthetic processes requiring high specificity. *Proc. Natl. Acad. Sci. U.S.A.* **1974**, *71*, 4135−4139.
(42) Ninio, J. Kinetic amplification of enzyme discrimination. *Biochimie* **1975**, *57*, 587−595.
(43) Hopfield, J. J.; Yamane, T.; Yue, V.; Coutts, S. Direct experimental evidence for kinetic proofreading in amino acylation of tRNAIle. *Proc. Natl. Acad. Sci. U.S.A.* **1976**, *73*, 1164−1168.
(44) Reardon, J. T.; Sancar, A. Thermodynamic cooperativity and kinetic proofreading in DNA damage recognition and repair. *Cell Cycle* **2004**, *3*, 139−142.
(45) McKeithan, T. W. Kinetic proofreading in T-cell receptor signal transduction. *Proc. Natl. Acad. Sci. U.S.A.* **1995**, *92*, 5042−5046.
(46) Adleman, L. M. Molecular computation of solutions to combinatorial problems. *Science* **1994**, *266*, 1021−1024.
(47) Stern, M.; Murugan, A. Learning without neurons in physical systems. 2022, arXiv:2206.05831. arXiv.org e-Printarchive. https://arxiv.org/abs/2206.05831. (accessed July 05, 2023).
(48) England, J. L. Self-organized computation in the far-from-equilibrium cell. *Biophys. Rev.* **2022**, *3*, No. 041303. (accessed July 05, 2023).
(49) Evans, C. G.; O'Brien, J.; Winfree, E.; Murugan, A. Pattern recognition in the nucleation kinetics of non-equilibrium self-assembly. 2022, arXiv:2207.06399. arXiv.org e-Printarchive https://arxiv.org/abs/2207.06399. (accessed July 05, 2023).
(50) Sun, H.; Luo, Q.; Hou, C.; Liu, J. Nanostructures based on protein self-assembly: From hierarchical construction to bioinspired materials. *Nano Today* **2017**, *14*, 16−41.
(51) Zhou, K.; Zhou, Y.; Pan, V.; Wang, Q.; Ke, Y. Programming dynamic assembly of viral proteins with DNA origami. *J. Am. Chem. Soc.* **2020**, *142*, 5929−5932.
(52) Horcajada, P.; Chalati, T.; Serre, C.; Gillet, B.; Sebrie, C.; Baati, T.; Eubank, J. F.; Heurtaux, D.; Clayette, P.; Kreuz, C.; et al. Porous metal-organic-framework nanoscale carriers as a potential platform for drug delivery and imaging. *Nat. Mater.* **2010**, *9*, 172−178.
(53) Wang, A. Z.; Langer, R.; Farokhzad, O. C. Nanoparticle delivery of cancer drugs. *Annu. Rev. Med.* **2012**, *63*, 185−198.
(54) Yang, Z.; Xu, K.; Guo, Z.; Guo, Z.; Xu, B. Intracellular enzymatic formation of nanofibers results in hydrogelation and regulated cell death. *Adv. Mater.* **2007**, *19*, 3152−3156.
(55) Okesola, B. O.; Redondo-Gómez, C.; Mata, A. *Self-Assembling Biomaterials*; Elsevier, 2018; pp 371−397.
(56) Xu, T.; Cai, Y.; Zhong, X.; Zhang, L.; Zheng, D.; Gao, Z.; Pan, X.; Wang, F.; Chen, M. ea. *β*-Galactosidase instructed supramolecular hydrogelation for selective identification and removal of senescent cells. *Chem. Commun.* **2019**, *55*, 7175−7178.
(57) Rovigatti, L.; Russo, J.; Romano, F.; Matthies, M.; Kroc, L.; Šulc, P. A simple solution to the problem of self-assembling cubic diamond crystals. *Nanoscale* **2022**, *14*, 14268−14275.
(58) Boles, M. A.; Engel, M.; Talapin, D. V. Self-assembly of colloidal nanocrystals: From intricate structures to functional materials. *Chem. Rev.* **2016**, *116*, 11220−11289.
(59) Liu, W.; Halverson, J.; Tian, Y.; Tkachenko, A. V.; Gang, O. Self-organized architectures from assorted DNA-framed nanoparticles. *Nat. Chem.* **2016**, *8*, 867−873.
(60) Bohlin, J.; Turberfield, A. J.; Louis, A. A.; Sulc, P. Designing the self-assembly of arbitrary shapes using minimal complexity building blocks. *ACS Nano* **2023**, *17*, 5387−5398.
(61) Rotskoff, G. M. The Statistical Dynamics of Nonequilibrium Control. Ph.D. thesis; The University of California, 2017.
(62) Nguyen, M.; Qiu, Y.; Vaikuntanathan, S. Organization and self-assembly away from equilibrium: Toward thermodynamic design principles. *Annu. Rev. Condens. Matter Phys.* **2021**, *12*, 273−290.
(63) Fujimoto, Y.; Ito, S. Game-theoretical approach to minimum entropy productions in information thermodynamics. 2021, arXiv:2112.14035. arXiv.org e-Printarchive. https://arxiv.org/abs/2112.14035. (accessed July 05, 2023).
(64) Engel, M. C.; Smith, J. A.; Brenner, M. P. Optimal Control of Nonequilibrium Systemsthrough Automatic Differentiation. 2022, arXiv:2201.00098. arXiv.org e-Printarchive https://arxiv.org/abs/2201.00098. (accessed July 05, 2023).
(65) Whitelam, S.; Schmit, J. D. Low-dissipation self-assembly protocols of active sticky particles. *J. Cryst. Growth* **2022**, *600*, No. 126912.
(66) Becchi, M.; Capelli, R.; Perego, C.; Pavan, G. M.; Micheletti, C. Density-tunable pathway complexity in a minimalistic self-assembly model. *Soft Matter* **2022**, *18*, 8106−8116.
(67) Blaber, S.; Sivak, D. A. Optimal control in stochastic thermodynamics. *J. Phys. Commun.* **2023**, *7*, No. 033001.
(68) D'Orsogna, M.; Lakatos, G.; Chou, T. Stochastic self-assembly of incommensurate clusters. *J. Chem. Phys.* **2012**, *136*, No. 084110.
(69) Szabo, A.; Schulten, K.; Schulten, Z. First passage time approach to diffusion controlled reactions. *J. Chem. Phys.* **1980**, *72*, 4350−4357.
(70) Siegert, A. J. F. On the first passage time probability problem. *Phys. Rev.* **1951**, *81*, 617−623.
(71) Redner, S. *A Guide to First-Passage Processes*; Cambridge University Press: Cambridge, U.K., 2001.
(72) Chou, T.; D'Orsogna, M. R. *First-Passage Phenomena and their Applications*; World Scientific, 2014; pp 306−345.
(73) Yvinec, R.; D'Orsogna, M. R.; Chou, T. First passage times in homogeneous nucleation and self-assembly. *J. Chem. Phys.* **2012**, *137*, No. 244107.
(74) Liao, X.; Purohit, P. K. Self-assembly on a lipid membrane viewed as a first passage time problem. *J. Mech. Phys. Solids* **2020**, *135*, No. 103787.
(75) Misra, N.; Schwartz, R. Efficient stochastic sampling of first-passage times with applications to self-assembly simulations. *J. Chem. Phys.* **2008**, *129*, No. 204109.
(76) Bebon, R.; Schwarz, U. S. First-passage times in complex energy landscapes: a case study with nonmuscle myosin II assembly. *New J. Phys.* **2022**, *24*, No. 063034.
(77) Yvinec, R.; Bernard, S.; Hingant, E.; Pujo-Menjouet, L. First passage times in homogeneous nucleation: Dependence on the total number of particles. *J. Chem. Phys.* **2016**, *144*, No. 034106.
(78) Polizzi, N. F.; Therien, M. J.; Beratan, D. N. Mean first-passage times in Biology. *Isr. J. Chem* **2016**, *56*, 816−824.
(79) Nolte, D. D. The tangled tale of phase space. *Phys. Today* **2010**, *63*, 33−38.
(80) Eckmann, J.-P.; Kamphorst, S. O.; Ruelle, D.; et al. Recurrence plots of dynamical systems. *World Sci. Ser. Nonlinear Sci., Ser. B* **1995**, *16*, 441−446.
(81) Vega, I.; Schütte, C.; Conrad, T. O. Finding metastable states in real-world time series with recurrence networks. *Phys. A* **2016**, *445*, 1−17.
(82) Tretiakov, K. V.; Szleifer, I.; Grzybowski, B. A. The rate of energy dissipation determines probabilities of non-equilibrium assemblies. *Angew. Chem.* **2013**, *125*, 10494−10498.
(83) Grzybowski, B. A.; Fitzner, K.; Paczesny, J.; Granick, S. From dynamic self-assembly to networked chemical systems. *Chem. Soc. Rev.* **2017**, *46*, 5647−5678.

https://doi.org/10.1021/acs.jpcb.3c01376
J. Phys. Chem. B XXXX, XXX, XXX−XXX

DISTRIBUTION A: Distribution approved for public release.

(84) Tociu, L. R. Structure, Fluctuations and Transport in Active Matter Systems: Insights from Stochastic Thermodynamics and Machine Learning. Ph.D. thesis, The University of Chicago, 2022.
(85) Van den Broeck, C.; Esposito, M. Ensemble and trajectory thermodynamics: A brief introduction. *Phys. A* **2015**, *418*, 6−16.
(86) Seifert, U. Stochastic thermodynamics, fluctuation theorems and molecular machines. *Rep. Prog. Phys.* **2012**, *75*, No. 126001.
(87) Shohat, D.; Lahini, Y. Dissipation Indicates Memory Formation in Driven Disordered Systems. *Phys. Rev. Lett.* **2023**, *130*, No. 048202. (accessed July 05, 2023).
(88) Shohat, D.; Hexner, D.; Lahini, Y. Memory from coupled instabilities in unfolded crumpled sheets. *Proc. Natl. Acad. Sci. U.S.A.* **2022**, *119*, No. e2200028119.
(89) Zhao, K.; Wulder, M. A.; Hu, T.; Bright, R.; Wu, Q.; Qin, H.; Li, Y.; Toman, E.; Mallick, B.; Zhang, X.; Brown, M. Detecting change-point, trend, and seasonality in satellite time series data to track abrupt changes and nonlinear dynamics: A Bayesian ensemble algorithm. *Remote Sen. Environ.* **2019**, *232*, No. 111181.
(90) Hu, T.; Toman, E. M.; Chen, G.; Shao, G.; Zhou, Y.; Li, Y.; Zhao, K.; Feng, Y. Mapping fine-scale human disturbances in a working landscape with Landsat time series on Google Earth Engine. *ISPRS J. Photogramm. Remote Sens.* **2021**, *176*, 250−261.
(91) Short, N. M. *The Landsat Tutorial Workbook: Basics of Satellite Remote Sensing*; National Aeronautics and Space Administration, Scientific and Technical Information Branch: Hampton, Virginia, U.S.A., 1982; Vol. *1078*.
(92) Klamser, J. U.; Dauchot, O.; Tailleur, J. Kinetic monte carlo algorithms for active matter systems. *Phys. Rev. Lett.* **2021**, *127*, No. 150602.
(93) Newman, M. E.; Barkema, G. T. *Monte Carlo Methods in Statistical Physics*; Clarendon Press: Oxford, U.K., 1999.
(94) Whitelam, S.; Geissler, P. L. Avoiding unphysical kinetic traps in Monte Carlo simulations of strongly attractive particles. *J. Chem. Phys.* **2007**, *127*, No. 154101.
(95) Whitelam, S.; Feng, E. H.; Hagan, M. F.; Geissler, P. L. The role of collective motion in examples of coarsening and self-assembly. *Soft Matter* **2009**, *5*, 1251−1262.
(96) Whitelam, S.; Jack, R. L. The Statistical Mechanics of Dynamic Pathways to Self-Assembly. *Annu. Rev. Phys. Chem.* **2015**, *66*, 143−163.
(97) Zhang, Z.; Keys, A. S.; Chen, T.; Glotzer, S. C. Self-assembly of patchy particles into diamond structures through molecular mimicry. *Langmuir* **2005**, *21*, 11547−11551.
(98) Hagan, M. F.; Chandler, D. Dynamic pathways for viral capsid assembly. *Biophys. J.* **2006**, *91*, 42−54.
(99) Wilber, A. W.; Doye, J. P.; Louis, A. A.; Noya, E. G.; Miller, M. A.; Wong, P. Reversible self-assembly of patchy particles into monodisperse icosahedral clusters. *J. Chem. Phys.* **2007**, *127*, No. 08B618.
(100) Bisker, G.; Polettini, M.; Gingrich, T. R.; Horowitz, J. M. Hierarchical bounds on entropy production inferred from partial information. *J. Stat. Mech.: Theory Exp.* **2017**, *2017*, No. 093210.
(101) Knuth, K. H. Optimal Data-Based Binning for Histograms. 2006, arXiv:physics/0605197. arXiv.org e-Printarchive. https://arxiv.org/abs/physics/0605197. (accessed July 05, 2023).
(102) Bowman, A. W.; Azzalini, A. *Applied Smoothing Techniques for Data Analysis: the Kernel Approach with S-Plus Illustrations*; Oxford University Press: Oxford, U.K., 1997; Vol. *18*.
(103) Mahesh, B. Machine learning algorithms-a review. *Int. J. Sci. Res.* **2020**, *9*, 381−386.
(104) Derrida, B. Non-equilibrium steady states: fluctuations and large deviations of the density and of the current. *J. Stat. Mech.: Theory Exp.* **2007**, *2007*, No. P07023.
(105) Piscitelli, A.; Ciamarra, M. P. Escape rate and diffusion of a stochastically Driven particle. *Sci. Rep.* **2017**, *7*, No. 41442.
(106) Fan, H.-F.; Liu, Z.-N.; Chow, S.-Y.; Lu, Y.-H.; Li, H. Histone chaperone-mediated nucleosome assembly process. *PLoS One* **2015**, *10*, No. e0115007.
(107) Rondin, L.; Gieseler, J.; Ricci, F.; Quidant, R.; Dellago, C.; Novotny, L. Direct measurement of Kramers turnover with a levitated nanoparticle. *Nat. Nanotechnol.* **2017**, *12*, 1130−1133.
(108) Chen, N.-K.; Liu, Y.-T.; Wang, X.-P.; Li, X.-B. Nucleation dynamics of phase-change memory materials: Atomic motion and property evolution. *Phys. Status Solidi RRL* **2021**, *15*, No. 2000441.
(109) Milanesi, L.; Waltho, J. P.; Hunter, C. A.; Shaw, D. J.; Beddard, G. S.; Reid, G. D.; Dev, S.; Volk, M. Measurement of energy landscape roughness of folded and unfolded proteins. *Proc. Natl. Acad. Sci. U.S.A.* **2012**, *109*, 19563−19568.
(110) Casella, G.; Berger, R. L. *Statistical Inference*; Cengage Learning: Massachusetts, Boston, U.S.A, 2021.
(111) Hänggi, P.; Talkner, P.; Borkovec, M. Reaction-rate theory: fifty years after Kramers. *Rev. Mod. Phys.* **1990**, *62*, 251−341.
(112) Xu, Y.; Yu, L.; Li, W.; Ciais, P.; Cheng, Y.; Gong, P. Annual oil palm plantation maps in Malaysia and Indonesia from 2001 to 2016. *Earth Syst. Sci. Data* **2020**, *12*, 847−867.
(113) Yang, X.; Tian, S.; You, W.; Jiang, Z. Reconstruction of continuous GRACE/GRACE-FO terrestrial water storage anomalies based on time series decomposition. *J. Hydrol.* **2021**, *603*, No. 127018.
(114) Csiszár, I. I-divergence geometry of probability distributions and minimization problems. *Ann. Probab.* **1975**, 146−158.
(115) Morio, J. Global and local sensitivity analysis methods for a physical system. *Eur. J. Phys.* **2011**, *32*, 1577−1583.
(116) Wang, J. Landscape and flux theory of non-equilibrium dynamical systems with application to biology. *Adv. Phys.* **2015**, *64*, 1−137.
(117) Marsland, R.; England, J. Limits of predictions in thermodynamic systems: a review. *Rep. Prog. Phys.* **2017**, *81*, No. 016601.
(118) Xu, T.; He, J.; Li, Y. Predictability exponent of stochastic dynamical systems. 2022, arXiv:2205.06006. arXiv.org e-Printarchive. https://arxiv.org/abs/2205.06006. (accessed July 05, 2023).
(119) Brouste, A.; Fukasawa, M.; Hino, H.; Iacus, S.; Kamatani, K.; Koike, Y.; Masuda, H.; Nomura, R.; Ogihara, T.; Shimuzu, Y.; et al. The yuima project: A computational framework for simulation and inference of stochastic differential equations. *J. Stat. Software* **2014**, *57*, 1−51.
(120) Prigogine, I.; Lefever, R.; Turner, J. S.; Turner, J. Stochastic theory of metastable states and nucleation. *Phys. Lett.* **1975**, *51*, 317−319.
(121) Gartner, F. M.; Graf, I. R.; Frey, E. The time complexity of self-assembly. *Proc. Natl. Acad. Sci. U.S.A.* **2022**, *119*, No. e2116373119.

https://doi.org/10.1021/acs.jpcb.3c01376
J. Phys. Chem. B XXXX, XXX, XXX−XXX

DISTRIBUTION A: Distribution approved for public release.

Utilizing time-series measurements for entropy production estimation in partially observed systems

Uri Kapustin,[1] Aishani Ghosal,[2] and Gili Bisker[2, 3, 4, 5, *]

[1] School of Electrical Engineering, Faculty of Engineering, Tel Aviv University, Tel Aviv 6997801, Israel
[2] Department of Biomedical Engineering, Faculty of Engineering, Tel Aviv University, Tel Aviv 6997801, Israel
[3] The Center for Physics and Chemistry of Living Systems, Tel Aviv University, Tel Aviv 6997801, Israel
[4] The Center for Nanoscience and Nanotechnology, Tel Aviv University, Tel Aviv 6997801, Israel
[5] The Center for Light Matter Interaction, Tel Aviv University, Tel Aviv 6997801, Israel

arXiv:2212.13487v1 [cond-mat.stat-mech] 27 Dec 2022

Estimating the dissipation, or the entropy production rate (EPR), can provide insights into the underlying mechanisms of nonequilibrium driven processes. Experimentally, however, only partial information can be accessed, and the ability to estimate the EPR varies depending on the available data. Here, we test different degrees of observed information stemming from coarse-grained time-series trajectory data, and apply several EPR estimators. Given increasing amount of information, we show a hierarchy of lower bounds on the total EPR. Further, we present a novel approach for utilizing waiting times in hidden states to provide a tighter lower bound on the total EPR.

The entropy production, or energy dissipation, is a fundamental physical quantity necessary to characterize the thermodynamics of nonequilibrium processes [1, 2]. In living systems, for example, the dissipation rate is closely related to the consumption rate of chemical fuel molecules, such as Adenosine triphosphate (ATP), by molecular motors [3]. The entropy production calculated along a single trajectory is a stochastic quantity that follows a set of mathematical relations, collectively known as the fluctuation theorems [4–10], which have been validated experimentally [11–13].

Estimating the total EPR from experimental data for a driven system is not always trivial, and can be challenging owing to the limited resolution and the huge number of degrees of freedom [2]. While calculating the EPR is straightforward given complete information about the nonequilibrium degrees of freedom, practically, only partial information is available. Such coarse-grained observation, where only some of the degrees of freedom are monitored or resolved, often cannot be treated with the Markovian approximation [14–17], and can only provide a lower bound on the total dissipation [18–21].

Partial information can stem from an observed subsystem, such that the rest of the system is hidden, or from coarse-graining some of the microstates into several meso-states [21–25]. The observed information may also be the transitions between states rather than the states themselves [26–28]. Therefore, different levels of coarse-graining can be considered based on the partial information available about the system.

There are several estimators for partial EPR that do not require any prior information about the system, such as the number of states or the underlying topology. The thermodynamic uncertainty relations (TUR), for example, provide a lower bound on the entropy production from the fluctuations of the transition fluxes or first passage times [29–40].

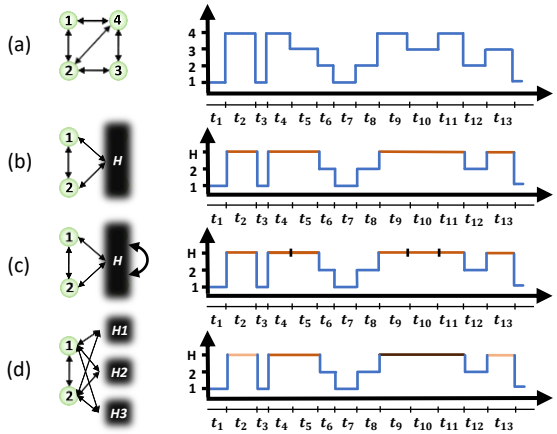
Another approach for inferring a lower bound on the total EPR is based on an optimization problem, searching over systems with known topology and the same observed statistics, preserving the first and second-order mass transfer rates [41], or the waiting time statistics [42], or both [43]. A similar approach was also demonstrated for discrete-time Markov chains, searching over the possible underlying hidden Markov models given the number of hidden states [44].

Building on the deep connection between the dissipation and the breaking of time-reversal symmetry [45], many estimators rely on the direct link between the EPR and the difficulty of distinguishing between forward and reverse processes, quantified by the relative entropy, or the Kullback–Leibler Divergence (KLD), between them [21, 46–51]. Calculating the KLD between probability distributions of forward and reverse trajectories for stationary data series can be done using different approaches [46–49, 52]. For example, the Plug-in method requires estimating the probabilities of sequences of data, discarding the information about transition times [48].

Applied to semi-Markov processes, the KLD breaks into two contributions, one of which captures irreversibility in the sequence of states, and the other captures irreversibility in waiting time distributions (WTD) [46]. For second-order semi-Markov processes, this KLD estimator can detect and quantify entropy production even in the absence of observable currents [46, 53, 54]. Machine-Learning (ML) tools have also been used for entropy production estimation by exploiting the irreversibility of data series [55–58]. The core idea is to optimize an objective function whose extremum is the KLD between the forward and reverse trajectories of sequences of states. For example, the recurrent neural network estimator for entropy production (RNEEP) estimates the EPR from coarse-grained data of partially observed systems, using a recurrent neural network to solve the optimization problem [55].

In this work, we focus on a continuous-time Markov chain (CTMC) model over a discrete set of states, in which a subset of the microstates are coarse-grained, or

DISTRIBUTION A: Distribution approved for public release.



Full Trajectory	State	1	4	1	4	3	2	1	2	4	3	4	2	3
	WT	t_1	t_2	t_3	t_4	t_5	t_6	t_7	t_8	t_9	t_{10}	t_{11}	t_{12}	t_{13}
Full-CG	State	1	H	1	H		2	1	2	H			2	H
	WT	t_1	t_2	t_3	t_4+t_5		t_6	t_7	t_8	$t_9+t_{10}+t_{11}$			t_{12}	t_{13}
Semi-CG	State	1	H	1	H	H	2	1	2	H	H	H	2	H
	WT	t_1	t_2	t_3	t_4	t_5	t_6	t_7	t_8	t_9	t_{10}	t_{11}	t_{12}	t_{13}
Transformed Semi-CG	State	1	H1	1	H2		2	1	2	H3			2	H1
	WT	t_1	t_2	t_3	t_4+t_5		t_6	t_7	t_8	$t_9+t_{10}+t_{11}$			t_{12}	t_{13}

FIG. 1. Illustration of the partial information frameworks for arbitrary 4-states system. (a) A fully-observed 4-states system. The trajectory (blue line) is described by the sequence of microstates and the corresponding waiting times (WT). (b) Full coarse graining (*full-CG*). States 3 and 4 cannot be resolved, and are lumped together to a single macrostate H (orange line) (c) Semi-coarse graining (*semi-CG*). States 3 and 4 cannot be resolved, but intra-transitions between the hidden microstates can be recorded, where consecutive visits in the hidden microstates (orange line with black markers) are recorded as sequence of H, with the corresponding WT of each hidden microstate between intra-transition events. (d) Transformed Semi-coarse graining (*Transformed semi-CG*). Each n consecutive visits to the hidden microstates in H are recorded as H_n (light orange, orange, and brown represent different sequence lengths) and the WT in H_n are the sum of the WT in consecutive visits in the hidden microstates 3 and 4.

"lumped", into a single macrostate. We consider different levels of observed statistics from different coarse-graining (CG) approaches, and infer the EPR from the observed data using the KLD estimator [46], the Plug-in estimator [48, 49], and the RNEEP estimator [55], when applicable. These estimators do not require prior knowledge of the systems, and only use the observed statistics to infer and quantify time-irreversibility. First, we use the sequence of observed microstates and coarse-grained macrostates, and the transitions between them. Then, we include information about transitions between the hidden microstates within the coarse-grained macrostates (intra-transitions). Finally, we reformulate the trajectory data of observed states and transitions, and intra-transitions within macrostates, by labeling the coarse-grained macrostates according to the number of times they are visited before jumping into an observed state. We apply the CG approaches to two model systems, namely, a 4-state (Fig. 1) system in which two of the states are coarse-grained into a single hidden state, and the discrete Flashing Ratchet (Fig. 2) with time-varying potential, whose values cannot be observed. We provide a unifying comparison between the estimators on the different CG schemes, and show how additional information is exploited for inferring tighter lower bounds on the total EPR.

We begin by explaining the different coarse-graining approaches, taking the 4-state model system as an example (Fig. 1a). In the first CG approach, termed *full-CG*, we lump together a subset of the microstates into a single observed state, giving rise to a second-order semi-Markov process (Fig. 1b), since the waiting time in the hidden state depends on the state visited before [46]. In this example, states 1 and 2 are observed, whereas states 3 and 4 can not be distinguished and are recorded as a single state, H. Here, the waiting time in H is the sum of the corresponding waiting times in the microstates 3 and 4 before jumping to one of the observed states.

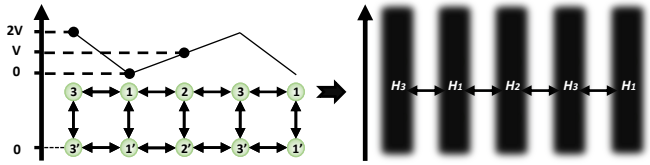


FIG. 2. Discrete flashing ratchet of 3 states with periodic boundaries, and a potential that can be switched on (i) and off (i') but is not accessible to the observer. State of the same position i, regardless of the potential, are coarse-grained into a single macrostate H_1, H_2, and H_3. In the *semi-CG* framework, intra-transitions $i \leftrightarrow i'$ are recorded.

In the second CG approach, termed *semi-CG*, we assume an observer can record intra-transitions within the hidden states (Fig. 1c). For example, a sequence of $1 \to 4 \to 3 \to 2$ is recorded as $1 \to H \to H \to 2$, with the corresponding waiting times, *i.e.*, the time spent in the first visit to H and the time spent in the second visit to H are recorded separately. In this case of observed intra-transitions within a coarse-grained state, the initial and final microstates are not known, as both are lumped together to the same macrostate. Still, the added information can be utilized for improving the lower bound on the total EPR.

DISTRIBUTION A: Distribution approved for public release.

The Plug-in and the RNEEP estimators rely on the sequence of states, and can be directly applied to the *semi-CG* trajectory. However, in order to apply the KLD estimator to the *semi-CG* data, we first need to reformulate the trajectory to a second-order semi-Markov process, and harness the information of the WTD. The transformation, depicted in Fig. 1d, consists of two steps. First, we look for all the consecutive sequences of the hidden state H, and record their length. Second, all sequences with the same length are considered a new state, *i.e.*, a sequence of n appearances of H is labeled H_n. The waiting time associated with H_n is now the sum of the individual waiting times in the n consecutive appearances of H. This new representation of the *semi-CG* observed data gives rise to a second-order semi-Markov process, from which we infer a tighter lower bound on the total EPR.

The Plug-in estimator, $\sigma_{\rm plug}$, was proposed for approximating the KLD rate between the forward and reverse sequences of discrete stationary time series, by counting sequences of data and calculating their probabilities [48, 49]. The approximated mth-order KLD between sequences of length m is:

$$D_m^x = \sum_{x_1,x_2,\ldots,x_n} p(x_{1\to m})\ln\left(\frac{p(x_{1\to m})}{p(x_{m\to 1})}\right) \tag{1}$$

where $p(x_{1\to m})$ and $p(x_{m\to 1})$ are the probabilities of a forward sequence $x_{1\to m}=(x_1,...,x_m)$ and the backward one $x_{m\to 1}=(x_m,...,x_1)$. These probabilities can be estimated from the number of appearances of each sequence in a long trajectory. Based on the approach in [48], the slope of D_m^x as a function of m,

$$\hat{d}_m^x = D_m^x - D_{m-1}^x \tag{2}$$

gives the entropy production per step in the limit of large m. However, for a non-Markov process that cannot be described by a semi-Markov process of any order, calculating $\hat{d}_m^x$ is challenging for large values of m. Therefore, the following ansatz [59] has been proposed:

$$\hat{d}_m^x \simeq \hat{d}_\infty^x - c\frac{\ln(m)}{m^\gamma} \tag{3}$$

where $\hat{d}_\infty^x$, c, and γ, are the fit parameters for $\hat{d}_m^x$ as a function of m. Our Plug-in estimator for the entropy production rate *per time*, is thus:

$$\sigma_{\rm plug} = \frac{1}{\tau}\hat{d}_\infty^x \tag{4}$$

where τ is the mean waiting time in each step. Note that this estimator can be directly used for both *semi-CG* and *full-CG* partial information framework without any modifications to the trajectory data.

The KLD estimator, $\sigma_{\rm KLD}$, derived by calculating the KLD between forward and reverse trajectories in semi-Markov processes, has two contributions [46]:

$$\sigma_{\rm KLD} = \sigma_{\rm aff} + \sigma_{\rm WTD} \tag{5}$$

where the affinity, $\sigma_{\rm aff}$, stems from observed currents, and the $\sigma_{\rm WTD}$ stems from time-asymmetries in WTD. In order to apply Eq. 5 to second-order semi-Markov processes, the observed states are reformulated as doublets, $[ij]$, where the first index is the previous state, and the second index is the current state [46]. The affinity contribution is:

$$\sigma_{\rm aff} = \frac{1}{\tau}\sum_{i,j,k} p_{(ijk)}\ln\left(\frac{p_{([ij]\to[jk])}}{p_{([kj]\to[ji])}}\right) \tag{6}$$

where $p_{(ijk)}$ is the probability to observe the sequence of state $i\to j\to k$, or $p_{(ijk)} = p_{([ij]\to[jk])}R_{[ij]}$, with $p_{([ij]\to[jk])}$ being the probability to jump to state k after jumping from i to j, and $R_{[ij]}$ being the fraction of visits to $[i,j]$. The affinity, $\sigma_{\rm aff}$, is governed by the relation between the forward and reverse transition probabilities.

The WTD contribution stems from the Kullback-Leibler divergence between WTD associated with forward ($i\to j\to k$) and backward ($k\to j\to i$) transitions:

$$\sigma_{\rm WTD} = \frac{1}{\tau}\sum_{i,j,k} p_{(ijk)} D\left[\psi(t|[ij]\to[jk])||\psi(t|[kj]\to[ji])\right] \tag{7}$$

where $\psi(t|[ij]\to[jk])$ is the WTD in state j given that the previous state was i and the following is k, τ is the average waiting time per state, and $D[u(x)||v(x)]$ is the Kullback-Leibler Divergence between two probability distributions, $u(x)$ and $v(x)$, defined as $D[u(x)||v(x)] = \sum_x u(x)\ln\left(u(x)/v(x)\right)$. See Supplemental Material (SM) [60] for details regarding WTD estimation. Note that for a fully observed system following Markovian dynamics, $\sigma_{\rm WTD}$ vanishes, and one cannot infer non-zero EPR without observable currents.

The RNEEP estimator, $\sigma_{\rm RNEEP}$, is formulated as an optimization problem [55], with a specific objective function to be minimized using stochastic gradient descent. The input of the problem is the set of all sequences of length m from a single long trajectory, and the solution is the coarse-grained entropy production rate per step along the input trajectory. Similar to the Plug-in estimator, the RNEEP uses the discrete sequence of states and does not exploit the WTD data, so estimating the full probability distributions of the waiting times is not required. Intuitively, this estimator should yield similar results to the Plug-in estimator, Eq. 4, and to $\sigma_{\rm aff}$, Eq. 6, as it uses the same information (see SM for further discussion [60]). The RNEEP can be directly applied to both *full-CG* and *semi-CG* frameworks, and it can be implemented by different machine learning models, such as recurrent or convolutional neural networks [55, 56]. Following the approach of [55], we use a recurrent neural network, whose input is a sequence of some length m, $x_t^m=(x_t,x_{t+1},...,x_{t+m-1})$, and its output is $h_\theta(x_t^m)$, where θ represents the learnable weights of the network. The output of the RNEEP is [55]:

$$\Delta S_\theta(x_t^m) \equiv h_\theta(x_t^m) - h_\theta(\tilde{x}_t^m) \tag{8}$$

DISTRIBUTION A: Distribution approved for public release.

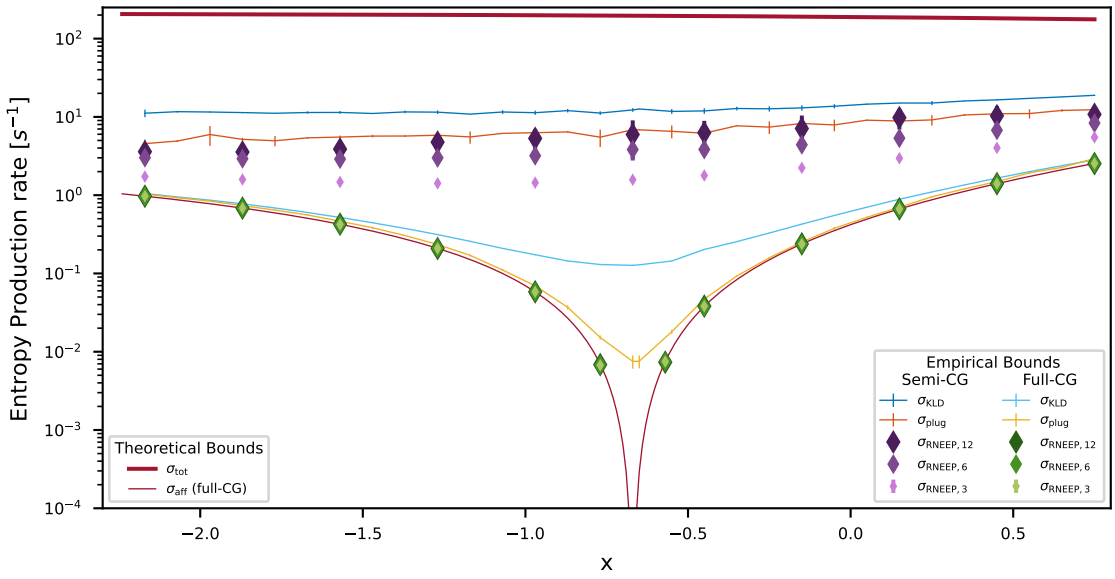


FIG. 3. Entropy production rates for the 4-state system. Total EPR, $\sigma_{\rm tot}$ (dark red), KLD estimator, $\sigma_{\rm KLD}$, for the *semi-CG* (dark blue) and *full-CG* (light blue) data, Plug-in estimator, $\sigma_{\rm plug}$, for the *semi-CG* (dark orange) and *full-CG* (light orange), RNEEP estimator, $\sigma_{{\rm RNEEP},m}$, for the *semi-CG* (light to dark purple for increasing sequence length m) and *full-CG* (light to dark green for increasing sequence length m) data, and the affinity contribution, $\sigma_{\rm aff}$, for the *full-CG* data (red). Rates: $\bar{\omega}_{12} = 2s^{-1}$, $\bar{\omega}_{21} = 3s^{-1}$, $\omega_{13} = 0s^{-1}$, $\omega_{14} = 1s^{-1}$, $\omega_{23} = 2s^{-1}$, $\omega_{24} = 35s^{-1}$, $\omega_{31} = 0s^{-1}$, $\omega_{32} = 50s^{-1}$, $\omega_{34} = 0.7s^{-1}$, $\omega_{41} = 8s^{-1}$, $\omega_{42} = 0.2s^{-1}$, $\omega_{43} = 75s^{-1}$.

where $\tilde{x}_t^m$ is the time-reversed sequence of x_t^m. The RNEEP estimator is the solution of the optimization problem of minimizing the following objective function over $\Delta S_\theta(x_t^m)$ for all possible sequences of length m:

$$\sigma_{{\rm RNEEP},m} = \frac{1}{\tau} \min_{\Delta S_\theta} {\rm E}_t {\rm E}_{(x_t^m)} \left[\Delta S_\theta(x_t^m) - e^{-\Delta S_\theta(x_t^m)} \right] \quad (9)$$

where ${\rm E}_t$ in the expectation over t, and ${\rm E}_{(x_t^m)}$ is the expectation over the observed sequences x_t^m. See SM [60] for a detailed explanation of the implementation of the estimators and the different numerical considerations.

We have evaluated the performance of the three EPR estimators on two coarse-grained systems, the 4-state system with 1 coarse-grained state, and the discrete flashing ratchet with the unobserved external potential. For each system, the two CG approaches, namely, the *full-CG* and *semi-CG*, were applied on trajectories of approximately $N = 10^7$ states, simulated using the Gillespie algorithm [61]. The code was implemented in PyTorch is available in [62].

The Plug-in estimator was fitted by gathering statistics of sequences of various lengths according to Eq. 3, as done in [48]. The RNEEP was calculated for different input sizes, where we have used the implementation of D.-K. Kim, *et. al.* [55] with some adjustments for our hardware, see [60]. The KLD estimator was applied without modifications on the *full-CG* data [46], whereas the trajectory reformulation was used only for calculating $\sigma_{\rm KLD}$ for the *semi-CG* statistics.

The results for the 4-states system (Fig. 1(a)) under the two CG schemes, *semi-CG* and *full-CG*, and the three estimators, RNEEP, Plug-in, and KLD, are presented in Fig. 3. The system has two observed states, 1, and 2, where the states 3 and 4 are coarse-grained into a single state H. The rates between the two observed microstates are tuned according to $\omega_{12} = \bar{\omega}_{12}e^{x}$ and $\omega_{21} = \bar{\omega}_{21}e^{-x}$ to mimic an external forcing, where the range of x was chosen to include the stalling force in which there is no observable current over the $1-2$ link [21].

As expected, The bounds on the total EPR obtained from estimators applied to the *semi-CG* statistics are better compared with the same estimators applied to the *full-CG* trajectories. In the *full-CG* case, $\sigma_{{\rm RNEEP},m}$ is similar to the affinity, $\sigma_{\rm aff}$, as both estimators use the same data. The Plug-in estimator, $\sigma_{\rm plug}$, which also uses the same data of the *full-CG* trajectory, provides similar results to $\sigma_{\rm aff}$ away from the stalling force. However, close to the stalling force, where $\sigma_{\rm aff}$ vanishes, $\sigma_{\rm plug}$ provides non-zero values that stem from the inherent bias of the method which assigns positive values to all the probabilities [49] (See [60]). The KLD estimator, $\sigma_{\rm KLD}$, provides the tightest lower bound for the *full-CG* data, as it is the only one that utilizes information of the irreversibility in WTD.

DISTRIBUTION A: Distribution approved for public release.

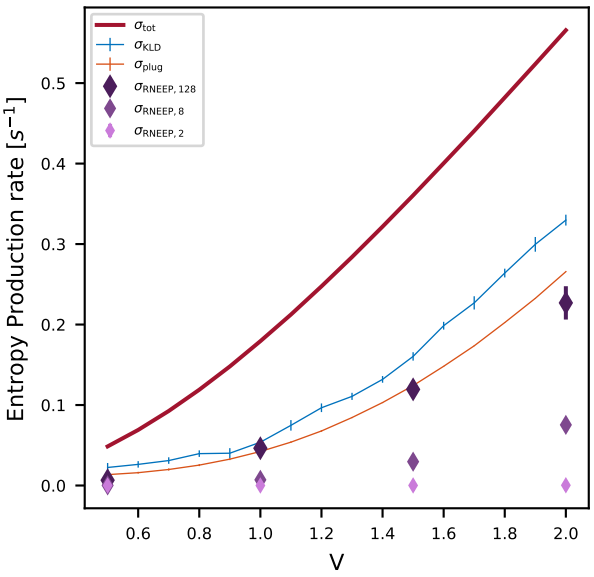


FIG. 4. Entropy production rates for the flashing ratchet. Total EPR, $\sigma_{\rm tot}$ (dark red) of the full trajectory, KLD estimator, $\sigma_{\rm KLD}$ (dark blue), Plug-in estimator, $\sigma_{\rm plug}$ (dark orange), and RNEEP estimator, $\sigma_{{\rm RNEEP},m}$ (light to dark purple for increasing sequence length m) for *semi-CG* data. The transition rates for $\forall i \neq j$ are: $\omega_{ii'} = \omega_{i'i} = \omega_{i'j'} = 1$, $\omega_{ij} = e^{(V_j - V_i)/2}$, where states i (i') are with turned-on (off) potential.

In the *semi-CG* case, the RNEEP estimator, $\sigma_{{\rm RNEEP},m}$, provides a tighter bound for increasing sequence lengths m, and it converges to $\sigma_{\rm plug}$ as in the *full-CG* case [60]. The KLD estimator $\sigma_{\rm KLD}$, provides the tightest lower bound on the total EPR compared to the other estimators tested, given the reformulation of the trajectory data according to the *Transformed semi-CG* scheme (Fig. 1(d)). The difference in $\sigma_{\rm KLD}$ between the *Transformed semi-CG* and the *full-CG* schemes reflects the additional information regarding irreversibility encoded in the intra-transitions between microstates in the hidden macrostate. Moreover, the irreversibility encoded in these intra-transitions in the *semi-CG* data is also reflected in the values of the 3 estimators that do not vary significantly near the stall force, in contrast to the estimators applied to the *full-CG* trajectories that strongly depend on the deviation from stalling conditions.

The results for the discrete flashing ratchet system [48, 49] under the *semi-CG* scheme and the three estimators, RNEEP, Plug-in, and KLD, are presented in Fig. 4. The system is of a Brownian particle moving along a periodic one-dimensional line, under the influence of a linear potential V that can be switched on and off at a constant rate. The particle is described by its position in the "on", i, or "off", i', states. Under CG, the information on the potential is not accessible, and both the on and off states are lumped into a single macrostate H_i. Here, we apply the 3 estimators to the non-Markovian *semi-CG* data, which includes the information of the intra-transition within the macrostates. Note that in [55], the RNEEP was compared to a semianalytical calculation of the KLD between trajectory distributions. However, it was shown that the Plug-in estimator yielded similar results to the semianalytical values for the *semi-CG* observed statistics [48]. Similar to the 4-state system results, the RNEEP estimator, $\sigma_{{\rm RNEEP},m}$, provides a tighter bound for increasing sequence lengths m. Moreover, the application of the KLD estimator to the *Transformed semi-CG* date yields the tightest lower bound on the total EPR, compared to the Plug-in [48, 49] and the RNEEP [55].

In summary, we have compared time-irreversibility-based EPR estimators for different coarse-graining schemes, focusing on KLD-based estimators, with (KLD) and without (Plug-in and RNEEP) WTD statistics, using two coarse-graining approaches. We have confirmed that the semi-coarse-graining framework, which includes intra-transitions data, yields tighter EPR bounds compared to the full-coarse-graining framework, as it exploits more information on time-irreversibility. In addition, we have proposed a novel approach for reformulating *semi-CG* trajectories, previously used for the Plug-in [48, 49] and RNEEP estimators [55], for applying the KLD estimator [46]. Using the *Transformed semi-CG* approach and the KLD estimator, we could distill time-irreversibility encoded in the intra-transitions within hidden microstates to achieve the tightest lower bound on the total EPR among the estimators we tested. Moreover, comparing the EPR bounds obtained from the *full-CG* and the *semi-CG* statistics provides a direct quantification of the time-irreversibility in the intra-transitions captured by each estimator. The proposed transformation and EPR estimators can be applied to other discrete-state continuous-time systems, to provide a lower bound on the total EPR, when only partial information is available.

G. Bisker acknowledges the Zuckerman STEM Leadership Program, and the Tel Aviv University Center for AI and Data Science (TAD). This work was supported by the ERC NanoNonEq 101039127, the Air Force Office of Scientific Research (AFOSR) under award number FA9550-20-1-0426, and by the Army Research Office (ARO) under Grant Number W911NF-21-1-0101. The views and conclusions contained in this document are those of the authors and should not be interpreted as representing the official policies, either expressed or implied, of the Army Research Office or the U.S. Government.

DISTRIBUTION A: Distribution approved for public release.

* bisker@tauex.tau.ac.il

[1] S. K. Manikandan, T. Ghosh, T. Mandal, A. Biswas, B. Sinha, and D. Mitra, Estimate of entropy generation rate can spatiotemporally resolve the active nature of cell flickering, arXiv:2205.12849 (2022).

[2] F. S. Gnesotto, F. Mura, J. Gladrow, and C. P. Broedersz, Broken detailed balance and non-equilibrium dynamics in living systems: a review, Reports on Progress in Physics **81**, 066601 (2018).

[3] J. M. Parrondo and B. Cisneros, Energetics of brownian motors: A review, Applied Physics A **75**, 179 (2002).

[4] S. Ciliberto, A. Imparato, A. Naert, and M. Tanase, Heat flux and entropy produced by thermal fluctuations, Phys. Rev. Lett. **110**, 180601 (2013).

[5] M. Esposito and C. Van den Broeck, Three detailed fluctuation theorems, Phys. Rev. Lett. **104**, 090601 (2010).

[6] U. Seifert, Stochastic thermodynamics, fluctuation theorems and molecular machines, Reports on Progress in Physics **75**, 126001 (2012).

[7] D. J. Evans and D. J. Searles, The fluctuation theorem, Advances in Physics **51**, 1529 (2002).

[8] E. Sevick, R. Prabhakar, S. R. Williams, and D. J. Searles, Fluctuation theorems, Annual Review of Physical Chemistry **59**, 603 (2008), pMID: 18393680.

[9] N. Shiraishi and T. Sagawa, Fluctuation theorem for partially masked nonequilibrium dynamics, Phys. Rev. E **91**, 012130 (2015).

[10] M. Polettini and M. Esposito, Effective fluctuation and response theory, Journal of Statistical Physics **176**, 94 (2019).

[11] F. Zamponi, Is it possible to experimentally verify the fluctuation relation? a review of theoretical motivations and numerical evidence, Journal of Statistical Mechanics: Theory and Experiment **2007**, P02008 (2007).

[12] G. M. Wang, E. M. Sevick, E. Mittag, D. J. Searles, and D. J. Evans, Experimental demonstration of violations of the second law of thermodynamics for small systems and short time scales, Phys. Rev. Lett. **89**, 050601 (2002).

[13] D. Collin, F. Ritort, C. Jarzynski, S. Smith, I. Tinôco, and C. Bustamante, Verification of the crooks fluctuation theorem and recovery of rna folding free energies, Nature **437**, 231 (2005).

[14] H. Wang and H. Qian, On detailed balance and reversibility of semi-markov processes and single-molecule enzyme kinetics, Journal of Mathematical Physics **48**, 013303 (2007).

[15] C. Maes, K. Netočný, and B. Wynants, Dynamical fluctuations for semi-markov processes, Journal of Physics A: Mathematical and Theoretical **42**, 365002 (2009).

[16] S. Rahav and C. Jarzynski, Fluctuation relations and coarse-graining, Journal of Statistical Mechanics: Theory and Experiment **2007**, P09012 (2007).

[17] D. Hartich and A. c. v. Godec, Emergent memory and kinetic hysteresis in strongly driven networks, Phys. Rev. X **11**, 041047 (2021).

[18] M. Esposito, Stochastic thermodynamics under coarse graining, Phys. Rev. E **85**, 041125 (2012).

[19] R. Kawai, J. M. R. Parrondo, and C. V. den Broeck, Dissipation: The phase-space perspective, Phys. Rev. Lett. **98**, 080602 (2007).

[20] J. Li, J. M. Horowitz, T. R. Gingrich, and N. Fakhri, Quantifying dissipation using fluctuating currents, Nature Communications **10**, 1666 (2019).

[21] G. Bisker, M. Polettini, T. R. Gingrich, and J. M. Horowitz, Hierarchical bounds on entropy production inferred from partial information, Journal of Statistical Mechanics: Theory and Experiment **2017**, 093210 (2017).

[22] D. Seiferth, P. Sollich, and S. Klumpp, Coarse graining of biochemical systems described by discrete stochastic dynamics, Phys. Rev. E **102**, 062149 (2020).

[23] P. Bilotto, L. Caprini, and A. Vulpiani, Excess and loss of entropy production for different levels of coarse graining, Phys. Rev. E **104**, 024140 (2021).

[24] A. Puglisi, S. Pigolotti, L. Rondoni, and A. Vulpiani, Entropy production and coarse graining in markov processes, Journal of Statistical Mechanics: Theory and Experiment **2010**, P05015 (2010).

[25] G. Teza and A. L. Stella, Exact coarse graining preserves entropy production out of equilibrium, Phys. Rev. Lett. **125**, 110601 (2020).

[26] P. E. Harunari, A. Dutta, M. Polettini, and É. Roldán, What to learn from few visible transitions' statistics?, arXiv:2203.07427 (2022).

[27] J. van der Meer, B. Ertel, and U. Seifert, Thermodynamic inference in partially accessible markov networks: A unifying perspective from transition-based waiting time distributions, Phys. Rev. X **12**, 031025 (2022).

[28] J. van der Meer, J. Degünther, and U. Seifert, Time-resolved statistics of snippets as general framework for model-free entropy estimators (2022), arXiv:2211.17032.

[29] N. Shiraishi, Optimal thermodynamic uncertainty relation in markov jump processes, Journal of Statistical Physics **185**, 1 (2021).

[30] J. M. Horowitz and T. R. Gingrich, Thermodynamic uncertainty relations constrain non-equilibrium fluctuations, Nature Physics **16**, 15 (2020).

[31] G. Falasco, M. Esposito, and J.-C. Delvenne, Unifying thermodynamic uncertainty relations, New Journal of Physics **22**, 053046 (2020).

[32] A. C. Barato and U. Seifert, Thermodynamic uncertainty relation for biomolecular processes, Physical review letters **114**, 158101 (2015).

[33] S. Otsubo, S. Ito, A. Dechant, and T. Sagawa, Estimating entropy production by machine learning of short-time fluctuating currents, Phys. Rev. E **101**, 062106 (2020).

[34] U. Seifert, From stochastic thermodynamics to thermodynamic inference, Annual Review of Condensed Matter Physics **10**, 171 (2019).

[35] T. V. Vu and Y. Hasegawa, Generalized uncertainty relations for semi-markov processes, Journal of Physics: Conference Series **1593**, 012006 (2020).

[36] B. Ertel, J. van der Meer, and U. Seifert, Operationally accessible uncertainty relations for thermodynamically consistent semi-markov processes, Phys. Rev. E **105**, 044113 (2022).

[37] T. Kamijima, S. Otsubo, Y. Ashida, and T. Sagawa, Higher-order efficiency bound and its application to nonlinear nanothermoelectrics, Phys. Rev. E **104**, 044115 (2021).

[38] N. Shiraishi, Inferring broken detailed balance in the absence of observable currents., J. Stat. Phys. **185**, 5 (2021).

[39] S. K Manikandan, S. Ghosh, A. Kundu, B. Das, V. Agrawal, D. Mitra, A. Banerjee, and S. Krishnamurthy, Quantitative analysis of non-equilibrium sys-

DISTRIBUTION A: Distribution approved for public release.

tems from short-time experimental data, Communications Physics **4** (2021).
[40] T. V. Vu and Y. Hasegawa, Generalized uncertainty relations for semi-markov processes, Journal of Physics: Conference Series **1593**, 012006 (2020).
[41] D. J. Skinner and J. Dunkel, Improved bounds on entropy production in living systems, Proceedings of the National Academy of Sciences **118**, e2024300118 (2021).
[42] D. J. Skinner and J. Dunkel, Estimating entropy production from waiting time distributions, Phys. Rev. Lett. **127**, 198101 (2021).
[43] E. Nitzan, A. Ghosal, and G. Bisker, Universal bounds on entropy production inferred from observed statistics (2022), arXiv:2212.01783.
[44] J. Ehrich, Tightest bound on hidden entropy production from partially observed dynamics, Journal of Statistical Mechanics: Theory and Experiment **2021**, 083214 (2021).
[45] J. M. Parrondo, C. Broeck, and R. Kawai, Entropy production and the arrow of time, New Journal of Physics **11** (2009).
[46] I. A. Mart´ınez, G. Bisker, J. M. Horowitz, and J. M. R. Parrondo, Inferring broken detailed balance in the absence of observable currents., Nat. Commun. **10**, 3542 (2019).
[47] Z. Rached, F. Alajaji, and L. Campbell, The kullback-leibler divergence rate between markov sources, IEEE Transactions on Information Theory **50**, 917 (2004).
[48] E. Roldán and J. M. R. Parrondo, Entropy production and kullback-leibler divergence between stationary trajectories of discrete systems, Phys. Rev. E **85**, 031129 (2012).
[49] E. Roldán and J. M. R. Parrondo, Estimating dissipation from single stationary trajectories, Phys. Rev. Lett. **105**, 150607 (2010).
[50] A. Ghosal and G. Bisker, Inferring entropy production rate from partially observed langevin dynamics under coarse-graining, Physical Chemistry Chemical Physics (2022).
[51] S. Ro, B. Guo, A. Shih, T. V. Phan, R. H. Austin, D. Levine, P. M. Chaikin, and S. Martiniani, Model-free measurement of local entropy production and extractable work in active matter, Phys. Rev. Lett. **129**, 220601 (2022).
[52] Q. Wang, S. R. Kulkarni, and S. Verdú, Divergence estimation of continuous distributions based on data-dependent partitions, IEEE Transactions on Information Theory **51**, 3064 (2005).
[53] G. Bisker, I. A. Martinez, J. M. Horowitz, and J. M. Parrondo, Comment on "inferring broken detailed balance in the absence of observable currents" (2022), arXiv:2202.02064.
[54] D. Hartich and A. Godec, Comment on "inferring broken detailed balance in the absence of observable currents" (2021), arXiv:2112.08978.
[55] D.-K. Kim, Y. Bae, S. Lee, and H. Jeong, Learning entropy production via neural networks, Phys. Rev. Lett. **125**, 140604 (2020).
[56] Y. Bae, D.-K. Kim, and H. Jeong, Inferring dissipation maps from videos using convolutional neural networks, Phys. Rev. Research **4**, 033094 (2022).
[57] S. Otsubo, S. Manikandan, and T. Sagawa, Estimate non-equilibrium trajectories., Commun. Phys. **5**, 11 (2022).
[58] S. Otsubo, S. K Manikandan, T. Sagawa, and S. Krishnamurthy, Estimating time-dependent entropy production from non-equilibrium trajectories, Communications Physics **5** (2022).
[59] T. Schürmann and P. Grassberger, Entropy estimation of symbol sequences, Chaos: An Interdisciplinary Journal of Nonlinear Science **6**, 414 (1996).
[60] See supplemental material at `https://www.overleaf.com/project/624a88871bc0a5357ca1be9e` for (1) waiting-time distributions estimation; (2) plug-in estimator implementation details; and (3) rneep convergence in 4-state system.
[61] D. T. Gillespie, Exact stochastic simulation of coupled chemical reactions, The Journal of Physical Chemistry **81**, 2340 (1977).
[62] https://github.com/urikm/utilizetimemeasurments.git.

DISTRIBUTION A: Distribution approved for public release.

arXiv:2212.13487v1 [cond-mat.stat-mech] 27 Dec 2022

Supplemental Material: Utilizing time-series measurements for entropy production estimation in partially observed systems

Uri Kapustin,[1] Aishani Ghosal,[2] and Gili Bisker[2,3,4,5,*]

[1] *School of Electrical Engineering, Faculty of Engineering, Tel Aviv University, Tel Aviv 6997801, Israel*

[2] *Department of Biomedical Engineering, Faculty of Engineering, Tel Aviv University, Tel Aviv 6997801, Israel*

[3] *The Center for Physics and Chemistry of Living Systems, Tel Aviv University, Tel Aviv 6997801, Israel*

[4] *The Center for Nanoscience and Nanotechnology, Tel Aviv University, Tel Aviv 6997801, Israel*

[5] *The Center for Light Matter Interaction, Tel Aviv University, Tel Aviv 6997801, Israel*

WAITING TIME DISTRIBUTIONS ESTIMATION

The KLD estimator, σ_{KLD}, has two contributions, namely, σ_{aff} and σ_{WTD}. While σ_{aff} can be directly calculated by counting second-order transitions for second-order semi-Markov processes, σ_{WTD} requires the estimation of continuous functions. In order to numerically evaluate continuous probability density functions, we use the Kernel Density Estimation (KDE) method [1]. In this approach, the estimated function depends on the bandwidth of the kernel, and the optimal bandwidth is correlated to the sample size. In our case, the sample size is the number of observed second-order jumps for each WTD, which can lead to a large variation between sample sizes for different transitions. We chose three different kernels, each for a different range of sample size, $2\times10^2-5\times10^3$, $5\times10^3-10^5$, and $>10^5$. Sample size of less than 2×10^2 was not considered due to the lack of statistics. The grid size of the KDE was also chosen empirically for optimized convergence to the WTD, considering the computational cost. The estimation of the WTD is better for longer trajectories, whereas short trajectories can result in an inaccurate estimation of the EPR due to insufficient statistics (Fig. S1). Moreover, the required trajectory length for a desired tolerance of the estimation depends on the system parameters [2].

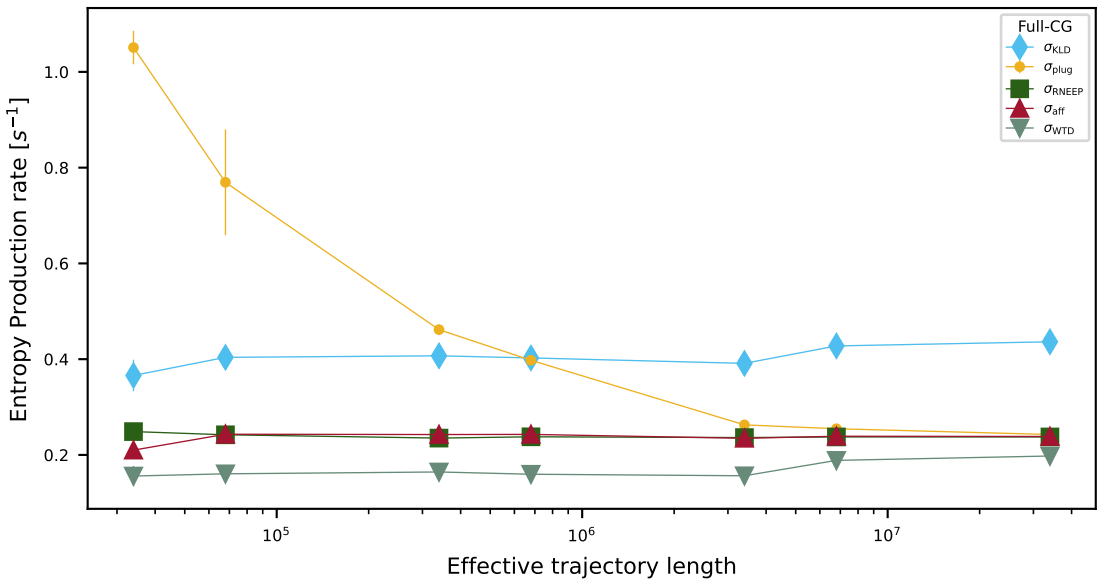


Fig. S1. Convergence of EPR estimators, σ_{KLD} (blue diamonds), σ_{plug} (light orange dots), σ_{RNEEP} (dark green squares), σ_{aff} (red triangles) and σ_{WTD} (gray triangles), as a function of effective trajectory length, calculated for the 4-states system and $x=-0.15$. The effective trajectory length is calculated after *full-CG*.

DISTRIBUTION A: Distribution approved for public release.

PLUG-IN ESTIMATOR IMPLEMENTATION DETAILS

The Plug-in estimator, σ_{plug}, is implemented according to [3]. Since its calculation includes ratios of probabilities of forward and reverse sequences, a small bias is added to the number of observations of each sequence to avoid probability values being zero. In contrast, for σ_{aff} estimation, unobserved second-order transitions are excluded from the calculation. This inherent difference in the calculations results in the deviation between the σ_{plug} and σ_{aff} values around the stalling force. The value of σ_{plug} as a function of the effective trajectory length can be seen in Fig. S1, demonstrating the need for sufficient statistics.

RNEEP CONVERGENCE IN 4-STATE SYSTEM

The RNEEP estimator, σ_{RNEEP}, is implemented according to [4], where each data point stems from 12 training trajectories run in parallel on 8 *Geforce RTX 2080 Ti* GPUs. The $\sigma_{\text{RNEEP},m}$ estimation gives a tighter bound on the total EPR for increasing sequence length, m, up to saturation for $m \approx 32$ (Fig. S2) for the 4-state system. In contrast, the flashing ratchet system requires longer sequences for convergence of $m \approx 64$ or longer.

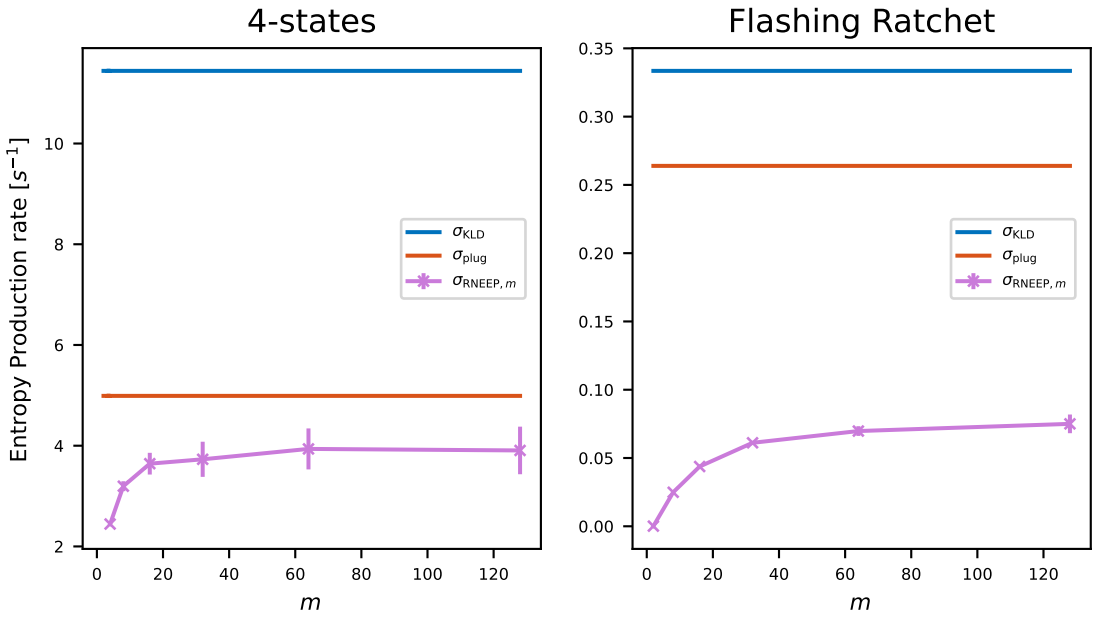


Fig. S2. Convergence of $\sigma_{\text{RNEEP},m}$ as a function of m (purple) for *semi-CG* data, compared to the values of the σ_{KLD} (blue diamo), and σ_{plug} (orange), which do not depend of m, for the 4-state system with $x = -2.17$ (left) and for the Discrete Flashing Ratchet with $V = 2$ (right).

* bisker@tauex.tau.ac.il

[1] E. Parzen, On Estimation of a Probability Density Function and Mode, The Annals of Mathematical Statistics **33**, 1065 (1962).
[2] I. A. Mart´ınez, G. Bisker, J. M. Horowitz, and J. M. R. Parrondo, Inferring broken detailed balance in the absence of observable currents., Nat. Commun. **10**, 3542 (2019).
[3] E. Roldán and J. M. R. Parrondo, Entropy production and kullback-leibler divergence between stationary trajectories of discrete systems, Phys. Rev. E **85**, 031129 (2012).
[4] D.-K. Kim, Y. Bae, S. Lee, and H. Jeong, Learning entropy production via neural networks, Phys. Rev. Lett. **125**, 140604 (2020).

DISTRIBUTION A: Distribution approved for public release.

Universal bounds on entropy production inferred from observed statistics

Eden Nitzan
School of Physics & Astronomy, Faculty of Exact Sciences, Tel Aviv University, Tel Aviv 6997801, Israel

Aishani Ghosal
Department of Biomedical Engineering, Tel Aviv University, Tel Aviv 6997801, Israel

Gili Bisker*
Department of Biomedical Engineering, Faculty of Engineering
The Center for Physics and Chemistry of Living Systems
The Center for Nanoscience and Nanotechnology
The Center for Light Matter Interaction
Tel Aviv University, Tel Aviv 6997801, Israel

(Dated: December 6, 2022)

Nonequilibrium processes break time-reversal symmetry and generate entropy. Living systems are driven out-of-equilibrium at the microscopic level of molecular motors that exploit chemical potential gradients to transduce free energy to mechanical work, while dissipating energy. The amount of energy dissipation, or the entropy production rate (EPR), sets thermodynamic constraints on cellular processes. Practically, calculating the total EPR in experimental systems is challenging due to the limited spatiotemporal resolution and the lack of complete information on every degree of freedom. Here, we propose a new inference approach for a tight lower bound on the total EPR given partial information, based on an optimization scheme that uses the observed transitions and waiting times statistics. We introduce hierarchical bounds relying on the first- and second-order transitions, and the moments of the observed waiting time distributions, and apply our approach to two generic systems of a hidden network and a molecular motor, with lumped states. Finally, we show that a lower bound on the total EPR can be obtained even when assuming a simpler network topology of the full system.

arXiv:2212.01783v1 [cond-mat.stat-mech] 4 Dec 2022

I. INTRODUCTION

Advances in experimental techniques over the last few decades have opened new possibilities for studying systems at the single-molecule level [1–3]. In parallel, new theoretical approaches of stochastic thermodynamics for studying the physics of nonequilibrium, small fluctuating systems have emerged [4–6]. These include the mathematical relations describing symmetry properties of the stochastic quantities like work [7–9] heat [9, 10], and entropy production [11, 12], leading to fundamental limits on physical systems like heat engines [13–15] refrigerators [16], and biological processes [17, 18].

Living systems operate far-from-equilibrium and constantly produce entropy. At the molecular level, the hydrolysis of fuel molecules, such as Adenosine triphosphate (ATP), powers nonequilibrium cellular processes, utilizing part of the liberated free energy for physical work, while the rest is dissipated [5]. The dissipation, or entropy production, is a signature of irreversible processes and can be used as a direct measure of the deviation from thermal equilibrium [19–22]. Therefore, the entropy production rate plays an important role in our understanding of the physics, and underlying mechanism, governing biological and chemical processes [13–15, 17, 18, 23].

Various studies have focused on estimating the mean entropy production rate using the thermodynamic uncertainty relations (TUR) using current fluctuations [24–29], fluctuations of first passage time [30, 31], kinetic uncertainty relation in terms of the activity [32], or unified thermodynamic and kinetic uncertainty relations [33]. Other approaches utilize waiting-time distributions [34, 35], machine learning [36–38], and single trajectory data [39–41]. Additional studies calculate higher moments of the full probability density function of the entropy production [42], use irreversible currents in stochastic dynamics described by a set of Langevin equations [43], or linear response theory [23].

Estimating the total EPR is only possible if we have knowledge regarding all of the degrees of freedom that are out-of-equilibrium [44]. However, due to practical limitations on the spatiotemporal resolution, not all of them can be experimentally accessible, and one can only obtain a lower bound on the total EPR for partially observed or coarse-grained systems [45].

The passive partial entropy production rate, $\sigma_{\rm pp}$, is an estimator for the EPR calculated from the transitions between two observed states, which bounds the total EPR [45–48]. This estimator, however, fails to provide a nonzero bound in case of vanishing current over the observed link, *i.e.*, at stalling conditions [45]. Other EPR estimators for partially observed systems based on inequality relations like the TUR [24–26, 32, 49] also fail to provide a non-trivial bound on the total EPR in the absence of net flux in the system.

* bisker@tauex.tau.ac.il

DISTRIBUTION A: Distribution approved for public release.

The Kullback-Leibler Divergence (KLD) estimator, σ_{KLD}, is based on the KLD, or the relative entropy, between the time-forward and the time-revered path probabilities [21, 50–55]. For semi-Markov processes, this estimator is a sum of two contributions. The first stems from transitions irreversibility or cycle affinities, σ_{aff}, whereas the second stems from broken time-reversal symmetry reflected in irreversibility in waiting time distributions (WTD), σ_{WTD} [56]. Using the KLD estimator, one can obtain a non-trivial lower bound on the total EPR for second-order semi-Markov processes even in the absence of the net current [35, 56–59]. Moreover, a lower bound on the total EPR can be obtained from the KLD between transition-based WTD [52, 57, 60].

Recently developed estimators solved an optimization problem to obtain a lower bound on the entropy production. For a discrete-time model, Ehrich proposed to search over the possible underlying systems that maintain the same observed statistics using knowledge on the number of hidden states [61]. For continuous-time models, Skinner and Dunkel minimized the EPR on a canonical form of the system that preserved the first- and second-order transition statistics to yield a lower bound on the total EPR, σ_2 [62]. The authors also formulated an optimization problem to infer the EPR in a system with two observed states using the waiting time statistics [34].

In this paper, we provide a tight bound on the total EPR by formulating an optimization problem based on the statistics of both transitions and waiting times. We use the first- and second-order statistics for the mass transition rates, and any chosen number of moments of the observed waiting time distributions. For a system with a known topology, we calculate the analytical expressions of the statistics as functions of the mass rates and the steady-state probabilities, which describe a possible underlying system and are used as variables in the optimization problem. These analytical expressions are then used to constrain the optimization variables to match the observed statistics. We show for a few continuous-time Markov chain systems that using the constraints of the mass rates and only the first moment of the WTD already provides close-to-total EPR value. Our approach outperforms other estimators, such as σ_{pp}, σ_{KLD}, σ_{aff}, and σ_2, in terms of the tightness of the lower bound. In the case of a complex model, where the formulation of the optimization problem might not be practical due to the number of constraints, or in case the full topology is not known, we show numerically that assuming a simpler underlying topology can provide a lower bound on the total EPR.

The paper is organized as follows. In section II, we describe our model system and the coarse-graining approach. The results are presented in section III: We discuss the estimator in subsection III A, apply it to different systems in subsection III B, demonstrate how the accuracy of the measured statistics affects the results of our estimator in subsection III C, and finally, we show the results of the optimization problem assuming a simpler underlying model in subsection III D. We conclude our findings in section IV.

II. MODEL

We assume a continuous time Markov chain over a finite and discrete set of states $i = \{1, 2, \ldots, N\}$. A trajectory is described by a sequence of states and their corresponding residence times before a transition to the next state occurs. Being a Markovian process, the jump probabilities depend only on the current state.

The transition rates w_{ij} from state i to j determine the time evolution of the probabilities for the system to be in each state, according to the Master equation $\frac{d}{dt}\boldsymbol{p}(t)^T = \boldsymbol{p}(t)^T\boldsymbol{W}$, where T is the transpose operator, and $\boldsymbol{W}$ is the rate matrix

$$[\boldsymbol{W}]_{ij} = \begin{cases} w_{ij} & j \neq i \\ -\lambda_i & j = i \end{cases} \tag{1}$$

$\boldsymbol{p}(t)$ is a column vector of the state probabilities at time t, with $\sum_i p_i(t) = 1$, and the diagonal entries are calculated according to $\lambda_i = \sum_{j\neq i} w_{ij}$ for probability conservation.

At the long-time limit, the system eventually reaches a steady state $\boldsymbol{\pi}$, where $\lim_{t\to\infty} p_i(t) = \pi_i$ such that $0 = \frac{d}{dt}\boldsymbol{\pi}^T = \boldsymbol{\pi}^T\boldsymbol{W}$ [63].

The waiting time at each state i is an exponential random variable with mean waiting time of $\tau_i = \lambda_i^{-1}$.

The mass rates n_{ij} are defined as follows:

$$n_{ij} = \begin{cases} \pi_i w_{ij} & j \neq i \\ 0 & j = i \end{cases} \tag{2}$$

The probabilities of jumping from state i to state j can be written in terms of the mass transition rates:

$$p_{ij} = \frac{w_{ij}}{\lambda_i} = \frac{n_{ij}}{\sum_{j'\neq i} n_{ij'}} \tag{3}$$

The steady-state total EPR can be calculated by multiplying the net currents and the mass rate ratios (affinities), summing over all the links[5, 6]:

$$\begin{aligned} \sigma_{\mathrm{tot}} &= \sum_{i,j} \pi_i w_{ij} \log\left(\frac{\pi_i w_{ij}}{\pi_j w_{ji}}\right) \\ &= \sum_{i,j} n_{ij} \log\left(\frac{n_{ij}}{n_{ji}}\right) \\ &= \sum_{i<j} (n_{ij} - n_{ji}) \log\left(\frac{n_{ij}}{n_{ji}}\right) \end{aligned} \tag{4}$$

Given a long trajectory of a total duration T, the steady-state probability π_i is the fraction of time spent in state i, and the mass rate n_{ij} is the number of transitions $i \to j$ divided by T.

DISTRIBUTION A: Distribution approved for public release.

according to the definition of the mass transition rates in Eq. 2, at the steady state, a mass conservation is satisfied at each state:

$$\forall_i : \sum_j n_{ij} = \sum_j n_{ji} \tag{5}$$

In many practical scenarios, some of the microstates cannot be distinguished, and the transitions between them cannot be observed. In such a case, a set of states $\{i_1, i_2, \ldots, i_{N_I}\}$ is observed as a single coarse-grained state I (Fig. 1(a)). The observed trajectory, therefore, includes only coarse-grained states and the combined residence time (Fig. 1(b)), and it is not necessarily a Markovian process [56]. Such a decimation procedure of lumping several states can give rise to semi-Markovian processes of any order depending on the topology of the network [62, 64–66]. In this case, the observed statistics of two or more consecutive transitions may give us additional information on the process.

III. RESULTS

A. Bounding the entropy production rate

Given a coarse-grained system with a model of the full underlying Markovian network topology, we can formulate an optimization problem for obtaining a tight bound on the total EPR. We consider a few observables: the coarse-grained steady-state probabilities, π_I, which is the probability to observe the system in the coarse-grained state I; the first-order mass transition rates, n_{IJ}, which is the rate of observing the transition $I \to J$; the second order mass transition rates, n_{IJK}, which is the rate of observing the transition $I \to J$ followed by the transition $J \to K$; and the conditional waiting time distributions $\psi_{IJK}(t)$, which is the distribution of waiting times in a coarse-grained state J before a transition to a coarse-grained state K occurs, conditioned on the previous transition being $I \to J$.

We search over the space of all possible underlying systems with the same topology as our hypothesized Markovian model that give rise to the same observed statistics, while minimizing the EPR. Trivially, the EPR of the coarse-grained system at hand is bounded from below by the EPR of the underlying Markovian system with the same observed statistics after coarse-graining, having the minimal value of entropy production.

1. *Analytical expressions of the observed statistics*

The observed statistics of the coarse-grained system can be expressed analytically in terms of the mass rates and steady-state probabilities of the model underlying system. From probability and mass conservation, $\pi_I = \sum_{i\in I} \pi_i$, and $n_{IJ} = \sum_{i\in I, j\in J} n_{ij}$, respectively. The mass conservation for the second-order transitions n_{IJK} must include all the paths starting at state $i \in I$, passing through a state in J, where any number of transitions might occur inside J, and jumping to state $k \in K$. To account for the transitions within J, we define the matrix $\boldsymbol{P}_{JJ}$ of the transition probabilities between states in J, $j_m, j_n \in J$:

$$[\boldsymbol{P}_{JJ}]_{mn} = \begin{cases} p_{j_m j_n} & m \neq n \\ 0 & m = n \end{cases} \tag{6}$$

Summing over the possible transitions from I, transitions within J, and transitions to K, we have (see Appendix A):

$$n_{IJK} = \sum_{i\in I, k\in K} \boldsymbol{n}_{iJ}^T [\mathbb{I} - \boldsymbol{P}_{JJ}]^{-1} \boldsymbol{p}_{Jk} \tag{7}$$

where $\mathbb{I}$ is the identity matrix of the size of $\boldsymbol{P}_{JJ}$, and $\boldsymbol{n}_{iJ}$ and $\boldsymbol{p}_{Jk}$ are column vectors of the mass transition rates from state $i \in I$ to any state $j \in J$, and jump probabilities from any state $j \in J$ to a state $k \in K$, respectively:

$$\boldsymbol{n}_{iJ}^T = [n_{ij_1}, n_{ij_2}, \cdots, n_{ij_{N_J}}] \tag{8}$$

and:

$$\boldsymbol{p}_{Jk}^T = [p_{j_1 k}, p_{j_2 k}, \cdots, p_{j_{N_J} k}] \tag{9}$$

The conditional waiting time distribution $\psi_{IJK}(t)$ can be calculated by the Laplace and inverse-Laplace transforms (full derivations can be found in Appendix B). We start from the Laplace transform of $\psi_{ij}(t) = w_{ij} e^{-\lambda_i t}$, the joint probability distribution of the transition $i \to j$ and the waiting time in the Markovian state i:

$$\tilde{\psi}_{ij}(s) = \mathcal{L}\{\psi_{ij}(t)\} = \int_0^\infty \psi_{ij}(t) e^{-ts} dt = \frac{w_{ij}}{s + \lambda_i} \tag{10}$$

Note that for any function $f(t)$, $\tilde{f}(s \to 0) = \int_0^\infty f(t) e^{-ts} dt|_{s\to 0} = \int_0^\infty f(t) dt$ is the normalization of $f(t)$. Here, $\psi_{ij}(t)$ is normalized to p_{ij}, *i.e.*, $p_{ij} = \int_0^\infty \psi_{ij}(t) dt$ (Eq. 3).

Now, we consider the simple case where the second-order transition through the coarse-grained state J starts and ends in specific Markovian states $i \in I$ and $k \in K$, respectively. The Laplace transform of the distribution of waiting times in J before a transition to k occur, given the previous transition was $i \to J$ is:

$$\tilde{\psi}_{iJk}(s) = \frac{\boldsymbol{p}_{iJ}^T}{\sum_{j\in J} p_{ij}} [\mathbb{I} - \tilde{\boldsymbol{\Psi}}_{JJ}(s)]^{-1} \tilde{\boldsymbol{\psi}}_{Jk}(s) \tag{11}$$

where

$$\tilde{\boldsymbol{\psi}}_{Jk}^T(s) = [\tilde{\psi}_{j_1 k}(s), \tilde{\psi}_{j_2 k}(s), \cdots, \tilde{\psi}_{j_{N_J} k}(s)] \tag{12}$$

DISTRIBUTION A: Distribution approved for public release.

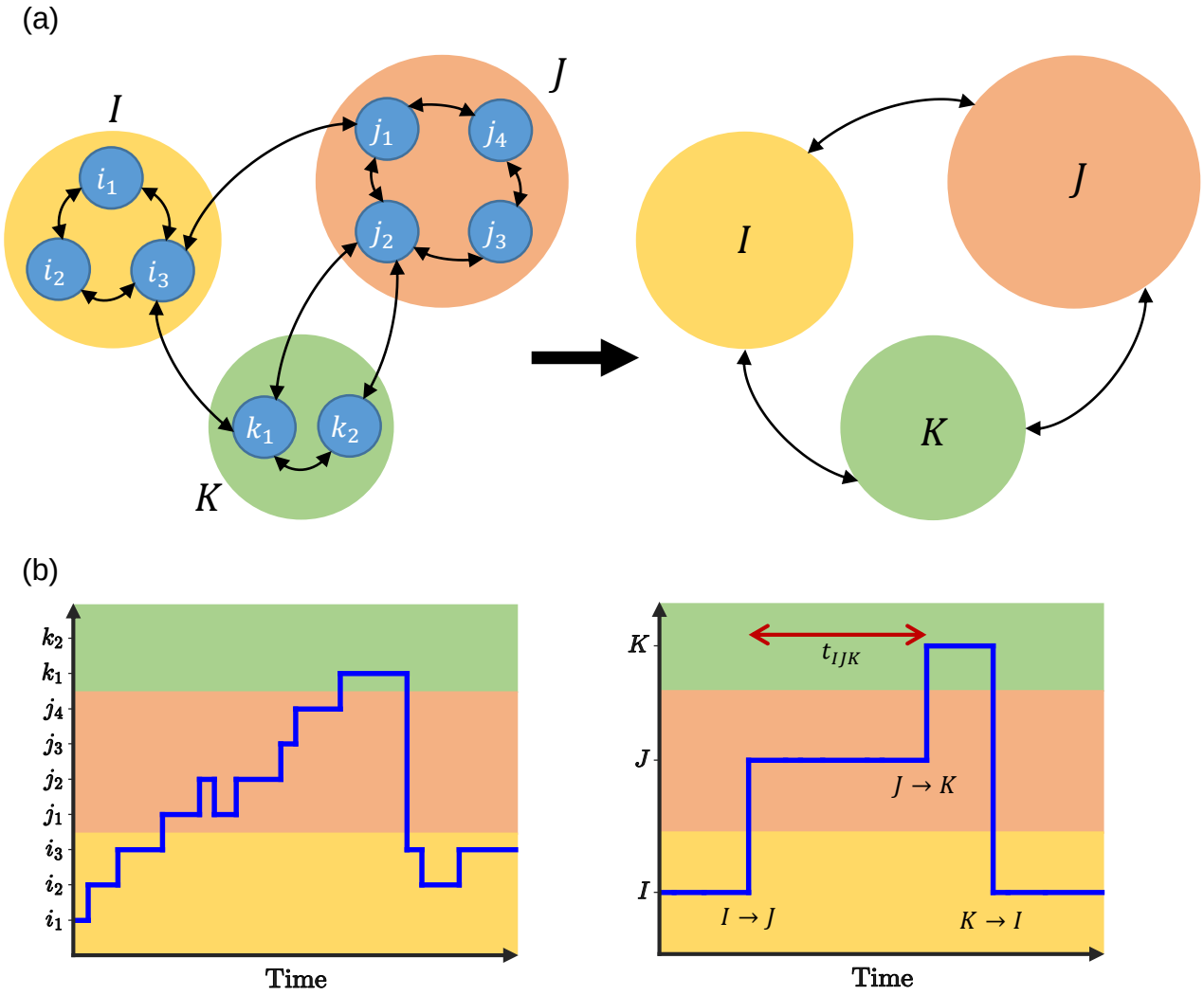


FIG. 1. Coarse graining. (a) The full Markovian system (left) and the coarse-grained system (right). (b) An example for a full trajectory (left) containing the actual states and the corresponding coarse-grained trajectory (right) containing only the observed states.

and $\tilde{\mathbf{\Psi}}_{JJ}(s)$ is a matrix of the Laplace transforms of every joint probability distribution of waiting times and transitions within J:

$$\tilde{\mathbf{\Psi}}_{JJ}(s) = \begin{cases} \tilde{\psi}_{j_m j_n}(s) & m \neq n \\ 0 & m = n \end{cases} \tag{13}$$

We denote $\tilde{\psi}_{iJK}(s) \equiv \sum_{k \in K} \tilde{\psi}_{iJk}(s)$. Then, the Laplace transform of the conditional waiting time distribution is:

$$\tilde{\psi}_{IJK}(s) = \sum_{i \in I} \frac{\pi_i}{\pi_I} \frac{\tilde{\psi}_{iJK}(s)}{\tilde{\psi}_{iJK}(s \to 0)} \tag{14}$$

Finally, we apply an inverse Laplace transform to obtain the conditional probability density:

$$\psi_{IJK}(t) = \mathcal{L}^{-1}\{\psi_{IJK}(s)\} \tag{15}$$

We further impose mass conservation at each of the Markovian states according to Eq. 5, to make sure the solution represents a valid Markovian system.

2. *Formalizing the optimization problem*

Let $\mathcal{S}$ be the real underlying Markovian system and let $\mathcal{R}$ be a general underlying system with the same topology as $\mathcal{S}$, i.e., the same states and possible transitions as $\mathcal{S}$, but $\mathcal{R}$ can have arbitrary mass rates and steady-state probabilities. Given the set of all systems $\mathcal{R}$ with the same steady-state probabilities $\pi_I^{\mathcal{R}} = \pi_I^{\mathcal{S}}$, same first-order mass transition rates $n_{IJ}^{\mathcal{R}} = n_{IJ}^{\mathcal{S}}$, same second-order mass transition rates $n_{IJK}^{\mathcal{R}} = n_{IJK}^{\mathcal{S}}$, and the same conditional waiting time distributions $\psi_{IJK}^{\mathcal{R}}(t) = \psi_{IJK}^{\mathcal{S}}(t)$, as the system $\mathcal{S}$, the following inequality holds for the EPR

of $\mathcal{S}$ and $\mathcal{R}$, $\sigma(\mathcal{S})$ and $\sigma(\mathcal{R})$, respectively:

$$\begin{aligned}\sigma_{\rm tot}(\mathcal{S}) \geq \min_{\mathcal{R}}\{\sigma_{\rm tot}(\mathcal{R})|\forall_{I,J,K}:\pi_I^{\mathcal{R}}=\pi_I^{\mathcal{S}}, n_{IJ}^{\mathcal{R}}=n_{IJ}^{\mathcal{S}},\\ n_{IJK}^{\mathcal{R}}=n_{IJK}^{\mathcal{S}},\\ \psi_{IJK}^{\mathcal{R}}(t)=\psi_{IJK}^{\mathcal{S}}(t)\}\equiv\sigma_{\rm opt}^{(\infty)}\end{aligned} \tag{16}$$

where $\sigma_{\rm opt}^{(\infty)}$ is the minimal EPR value of all the possible underlying systems $\mathcal{R}$. The inequality holds since the real system $\mathcal{S}$ belongs to the set of systems over which we minimize. The only variables of the optimization problem are n_{ij} and π_i, from which one can fully describe any of the possible underlying Markovian systems $\mathcal{R}$. All the constraints, π_I, n_{IJ}, n_{IJK}, and $\psi_{IJK}(t)$, as well as the EPR objective function, depend on these variables. Note that these variables are bounded by $0 \leq \pi_i \leq \pi_I$ and $0 \leq n_{ij} \leq n_{IJ}$.

In contrast to the constraints on the steady-state probabilities and the first- and second-order mass transition rate values, the constraint on the waiting-time distributions requires an equality of continuous functions $\psi_{IJK}(t)$, which one cannot fully reconstruct from trajectory data of finite duration. Moreover, solving the optimization problem using a constraint on a function with non-trivial dependency on the optimization problem variables is extremely challenging. Thus, we modify the optimization, and instead, use the moments of the waiting time distributions:

$$\begin{aligned}\sigma_{\rm opt}^{(n)}(\mathcal{S}) \equiv \min_{\mathcal{R}}\{\sigma_{\rm tot}(\mathcal{R})|\forall_{I,J,K}:\pi_I^{\mathcal{R}}=\pi_I^{\mathcal{S}}, n_{IJ}^{\mathcal{R}}=n_{IJ}^{\mathcal{S}},\\ n_{IJK}^{\mathcal{R}}=n_{IJK}^{\mathcal{S}},\\ \forall_{k\in\{1,2,\ldots,n\}}:\langle t_{IJK}^k\rangle^{\mathcal{R}}=\langle t_{IJK}^k\rangle^{\mathcal{S}}\}\end{aligned} \tag{17}$$

where $\langle t_{IJK}^k\rangle$ is the k-th moment of the conditional waiting time distribution $\psi_{IJK}(t)$. Using increasing number of moments, we can write the hierarchical bounds:

$$\forall_{n\in\mathbb{N}}:\sigma_{\rm tot}(\mathcal{S}) \geq \sigma_{\rm opt}^{(\infty)}(\mathcal{S}) \geq \sigma_{\rm opt}^{(n)}(\mathcal{S}) \geq \cdots \geq \sigma_{\rm opt}^{(1)}(\mathcal{S}) \tag{18}$$

We can easily get the analytical expressions for the moments $\langle t_{IJK}^k\rangle$ from the Laplace transform (see Appendix B):

$$\langle t_{IJK}^k\rangle = (-1)^k \frac{d^k\tilde{\psi}_{IJK}(s)}{ds^k}|_{s\to 0} \tag{19}$$

Now, for each moment, we have an expression that depends on the optimization problem variables in a simpler way, which in turn, simplifies the calculations. After calculating the values of the observables for the optimization problem, we solve it using a global search non-linear optimization algorithm [67].

B. Examples

1. 4-state system

We consider a fully-connected network of 4 states, with two observed states $\{1,2\}$ and two hidden states $\{3,4\}$, which are coarse-grained to state H (Fig. 2(a)), resulting in second-order semi-Markov dynamics [56]. The observed statistics of interest are the steady state probabilities π_1, π_2 and π_H, the first-order mass transition rates n_{1H}, n_{H1}, n_{2H}, and n_{H2}, the second-order mass transition rates n_{1H2} and n_{2H1} and the k-th moment of the conditional waiting time distributions $\langle t_{1H1}^k\rangle$, $\langle t_{1H2}^k\rangle$, $\langle t_{2H1}^k\rangle$ and $\langle t_{2H2}^k\rangle$. Notice we only used the second-order statistics through the coarse-grained state H, since states 1 and 2 are Markovian. Furthermore, we do not use n_{1H1} and n_{2H2} since they depend on the other mass transition rates: $n_{1H1} = n_{1H} - n_{1H2}$ and $n_{2H2} = n_{2H} - n_{2H1}$. The derivations of the analytical expressions of the second-order mass transition rates and the moments of the conditional waiting time moments, for this system, can be found in Appendix C.

We tune the transition rates over the observed link between states 1 and 2 according to $w_{12}(F) = w_{12}e^{-\beta FL}$ and $w_{21}(F) = w_{21}e^{\beta FL}$, where $\beta = T^{-1}$ is the inverse temperature (with $k_{\rm B} = 1$), and L is a characteristic length scale, to mimic external forcing. We compare the different EPR estimators on the system for several values for a driving force F over the observed link (Fig. 2(b)).

The passive partial EPR [45]:

$$\begin{aligned}\sigma_{\rm pp} &= (\pi_1 w_{12} - \pi_2 w_{21})\log\left(\frac{\pi_1 w_{12}}{\pi_2 w_{21}}\right)\\ &= (n_{12}-n_{21})\log\left(\frac{n_{12}}{n_{21}}\right)\end{aligned} \tag{20}$$

The KLD estimator is the sum of two contributions:

$$\begin{aligned}\sigma_{\rm KLD} &= \sigma_{\rm aff} + \sigma_{\rm WTD}\\ &= \frac{1}{\mathcal{T}}\sum_{I,J,K} p_{IJK}\log\left(\frac{p([IJ]\to[JK])}{p([KJ]\to[JI])}\right)\\ &+ \frac{1}{\mathcal{T}}\sum_{I,J,K} p_{IJK} D\left[\psi_{IJK}(t)||\psi_{KJI}(t)\right]\end{aligned} \tag{21}$$

where $p([IJ]\to[JK])$ is the probability to observe the transition $J \to K$ given the previous transition was $I \to J$, p_{IJK} is the probability to observe the second-order transition $I \to J \to K$, and $D[p||q]$ is the KLD between the probability distributions p and q. As was previously shown, the hierarchy between the EPR estimators is $\sigma_{\rm KLD} \geq \sigma_{\rm aff} \geq \sigma_{\rm pp}$ [45, 56].

The σ_2 estimator is also formulated as an optimization problem searching over a canonical form of the system with the same observed statistics, however, it only considers the first- and second-order mass transition rates [62]. Its place in the hierarchy between the EPR estimators varies for different systems. While σ_2 can be greater

DISTRIBUTION A: Distribution approved for public release.

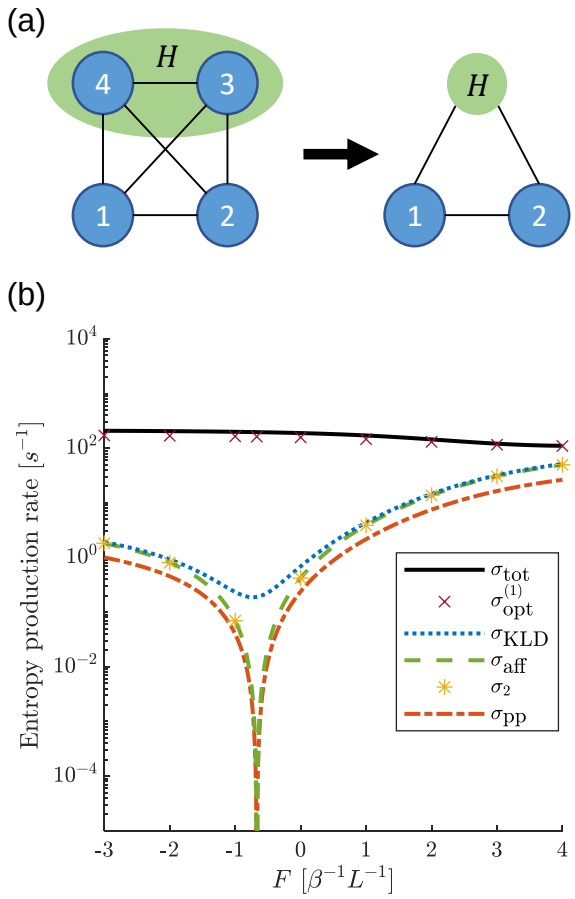


FIG. 2. 4-state system. (a) Illustration of the full 4-state system topology, including the coarse-graining of states 3 and 4 to state H. (b) Total EPR $\sigma_{\rm tot}$ (solid black line), our bound $\sigma^{(1)}_{\rm opt}$ (brown cross), KLD estimator $\sigma_{\rm KLD}$ (dotted blue line), affinity estimator $\sigma_{\rm aff}$ (dashed green line), two-step estimator σ_2 (yellow Asterisk), and the passive partial entropy production $\sigma_{\rm pp}$ (dashed-dotted orange line). The rates we used are $w_{12} = 3\ s^{-1}$, $w_{13} = 0\ s^{-1}$, $w_{14} = 8\ s^{-1}$, $w_{21} = 2\ s^{-1}$, $w_{23} = 50\ s^{-1}$, $w_{24} = 0.2\ s^{-1}$, $w_{31} = 0\ s^{-1}$, $w_{32} = 2\ s^{-1}$, $w_{34} = 75\ s^{-1}$, $w_{41} = 1\ s^{-1}$, $w_{42} = 35\ s^{-1}$, $w_{43} = 0.7\ s^{-1}$.

than $\sigma_{\rm KLD}$ in some cases [62], here, for the rate values we used, $\sigma_2 < \sigma_{\rm KLD}$. In fact, although the values of σ_2 and $\sigma_{\rm aff}$ appear to be similar (Fig. 2(b)), actually $\sigma_2 < \sigma_{\rm aff}$ for all of the values of F used.

At the stalling force, there is no current in the visible link and we get $\sigma_{\rm pp} = \sigma_{\rm aff} = \sigma_2 = 0$, which is the trivial bound. In contrast, $\sigma_{\rm KLD}$ and our estimator $\sigma^{(1)}_{\rm opt}$ give a non-trivial bound. Moreover, $\sigma^{(1)}_{\rm opt}$ surpasses $\sigma_{\rm KLD}$ significantly and yields a tight bound. For this system, using higher moments in order to calculate $\sigma^{(2)}_{\rm opt}$ did not make any improvement compared to $\sigma^{(1)}_{\rm opt}$.

2. *Molecular motor*

Here, we study a model of a molecular motor, illustrated in Fig. 3(a). The motor can physically move in space (upward or downward), $i \leftrightarrow i+1$, or change internal states (passive or active), $i \leftrightarrow i'$. An external source of chemical work $\Delta\mu$ drives the upward spatial jumps from the active state, and a mechanical force F acts against it and drives the downward transitions. We assume that an external observer cannot distinguish between the internal states of the motor, but rather can only record its physical position. The observed statistics are thus of a second-order Semi-Markov process [56].

Owing to the transnational symmetry in the model, we represent the molecule motor as a cyclic network of three coarse-grained states where each of them represents the physical location, lumping the active and passive internal states. We denote the steady-state probability of being in the passive and active states as π and π', respectively. Notice that the probability to be in each physical location in the 3-state cyclic system is the same, and that π and π' are the same for all of the physical locations, therefore, $\pi + \pi' = 1/3$.

We denote the upward and downward transitions from and to the passive state as u_1 and d_1, respectively, the upward and downward transitions from and to the active state as u_2 and d_2, respectively, and the transitions between the active and passive states at the same physical location as r (right) and l (left), respectively. The upward and downward coarse-grained transitions are labeled as U and D, respectively.

The observed statistics of interest are the first-order mass rates n_U, n_D, the second-order mass rates n_{UU}, n_{DD} and the k-th moment of the conditional waiting times $\langle t^k_{UU}\rangle$, $\langle t^k_{UD}\rangle$, $\langle t^k_{DU}\rangle$ and $\langle t^k_{DD}\rangle$. Note that we do not use n_{UD} and n_{DU}, since they depend on the other mass rates: $n_{UD} = n_U - n_{UU}$ and $n_{DU} = n_D - n_{DD}$. Owing to the symmetry of the cycle representation of the coarse-grained system, in which the steady-state probabilities are equally distributed, we only need the constraints on the upward and downward transitions. The derivations of the analytical expressions of the second-order mass transition rates and the moments of the conditional waiting time distributions, for this system, can be found in Appendix D.

The chemical affinity μ, arising from ATP hydrolysis for example, only affects the transitions u_2 and d_2, whereas the external force F affects all of the spatial transitions u_1, d_1, u_2 and d_2. The transition rates then obey local detailed balance: $w_{d1}/w_{u1} = e^{\beta FL}$ and $w_{d2}/w_{u2} = e^{\beta(FL-\mu)}$, where L is the length of a single spatial jump [56].

We compare the different EPR estimators for the molecular motor system for several values of μ and for each μ value, we tune the external forcing parameter F (Fig. 3(b)). Notice the passive partial EPR, $\sigma_{\rm pp}$, is not applicable for this system since all the original Markovian states are coarse-grained.

DISTRIBUTION A: Distribution approved for public release.

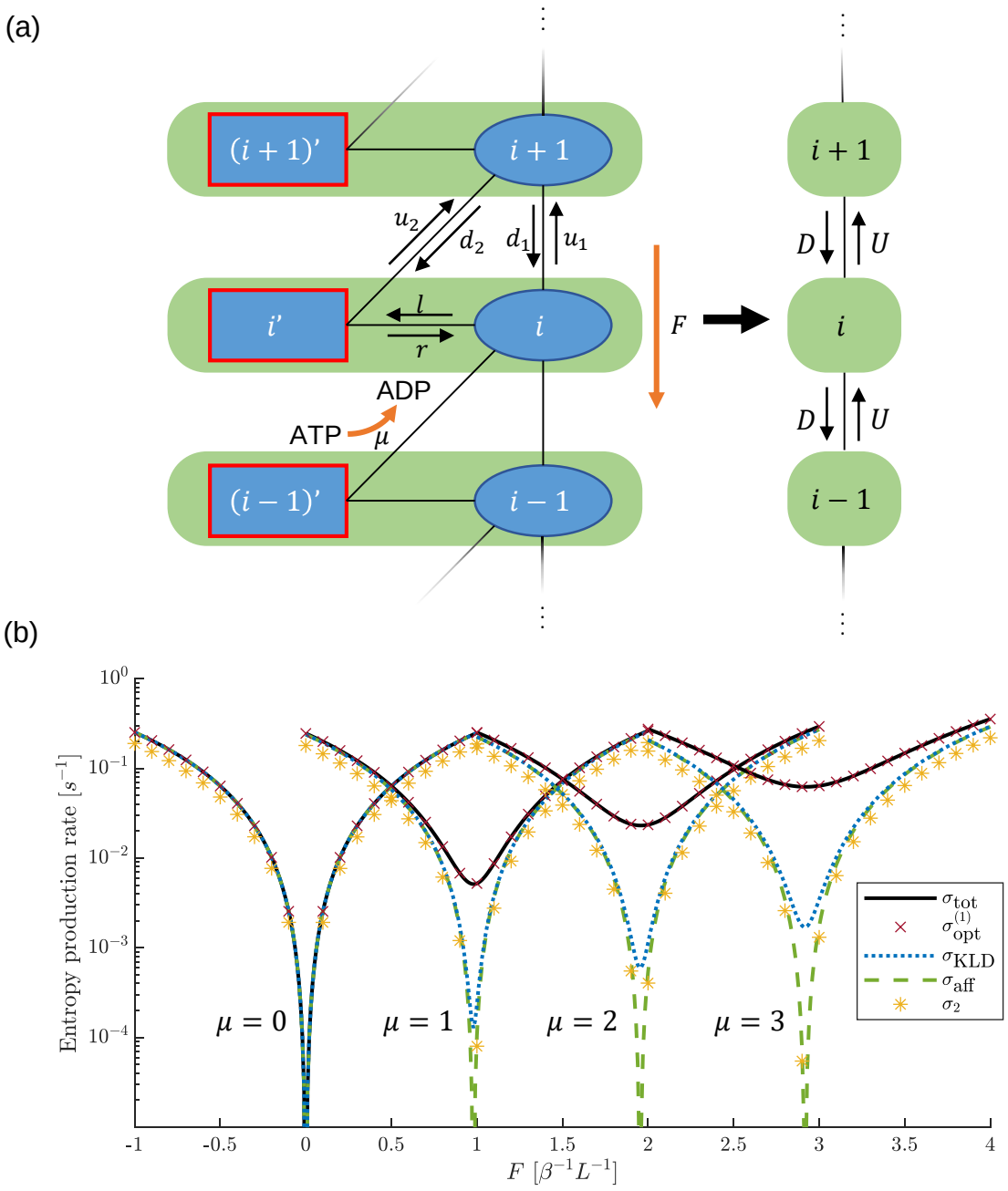


FIG. 3. Molecular motor. (a) Illustration of the full molecular motor system including the coarse-graining of the active (red boxed square) and passive (ellipse) states. (b) Total EPR $\sigma_{\rm tot}$ (solid black line), our bound $\sigma^{(1)}_{\rm opt}$ (brown cross), KLD estimator $\sigma_{\rm KLD}$ (dotted blue line), the affinity estimator $\sigma_{\rm aff}$ (dashed green line), and the two-step estimator σ_2 (yellow Asterisk). The rates we used are $w_r = w_l = w_{u2} = w_{d2} = 1\ s^{-1}$, $w_{u1} = w_{d1} = 0.01\ s^{-1}$.

The hierarchy of the different EPR estimators for the molecular motor, for the rate values we used, is $\sigma^{(1)}_{\rm opt} \geq \sigma_{\rm KLD} \geq \sigma_{\rm aff} \geq \sigma_2$. At the stalling force for each value of μ, where there is no visible current, we find $\sigma_{\rm aff} = \sigma_2 = 0$, which is the trivial bound. In contrast, similar to the 4-state system, $\sigma^{(1)}_{\rm opt}$ surpasses $\sigma_{\rm KLD}$ significantly and yields a tight bound.

C. Importance of data accuracy

One of the hyper parameters defining the optimization problem is the constraint tolerance, which indicates the acceptable numerical error of the solution. If ϵ is the absolute error of the trajectory statistics with respect to the true analytical ones, then the constraint tolerance must be equal to or greater than ϵ. Otherwise, the optimiza-

DISTRIBUTION A: Distribution approved for public release.

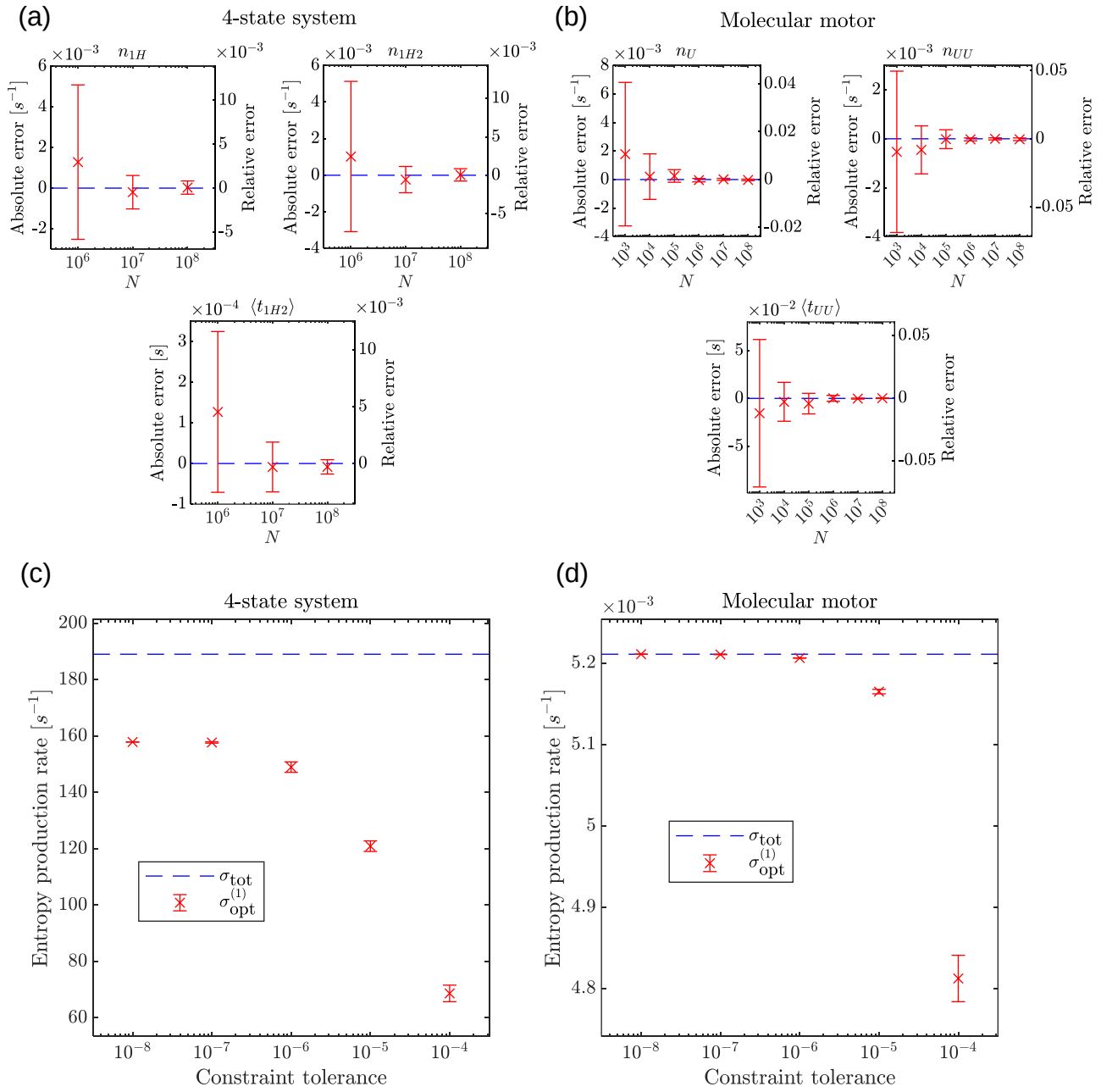


FIG. 4. Importance of data accuracy. (a) The error of some statistics of the 4-state system for different values of the trajectory length N. The absolute and relative errors are on the left and right axes, respectively. (b) The error of some statistics of the molecular motor system for different values of the trajectory length N. The absolute and relative errors are on the left and right axes, respectively. (c) The error of $\sigma^{(1)}_{\rm opt}$ results for the 4-state system for different constraint tolerance values, using the analytical statistics values. (d) The error of $\sigma^{(1)}_{\rm opt}$ results for the molecular motor system for different constraint tolerance values, using the analytical statistics values. Error bars stand for the standard deviation of 10 different realizations.

tion problem might not converge or give an overestimate in the worst-case scenario.

In Fig. 4, we plot the absolute (and relative) error of a few statistics values calculated from several trajectories as function of the trajectory length N, for both systems discussed in the previous sections. Moreover, using the analytical values of the statistics for maximum accuracy, we plot the results of our estimator $\sigma^{(1)}_{\rm opt}$ as function of the constraint tolerance.

As expected, longer trajectory data result in a more accurate estimation of the observed statistics used for our optimization problem for both systems, as evident

DISTRIBUTION A: Distribution approved for public release.

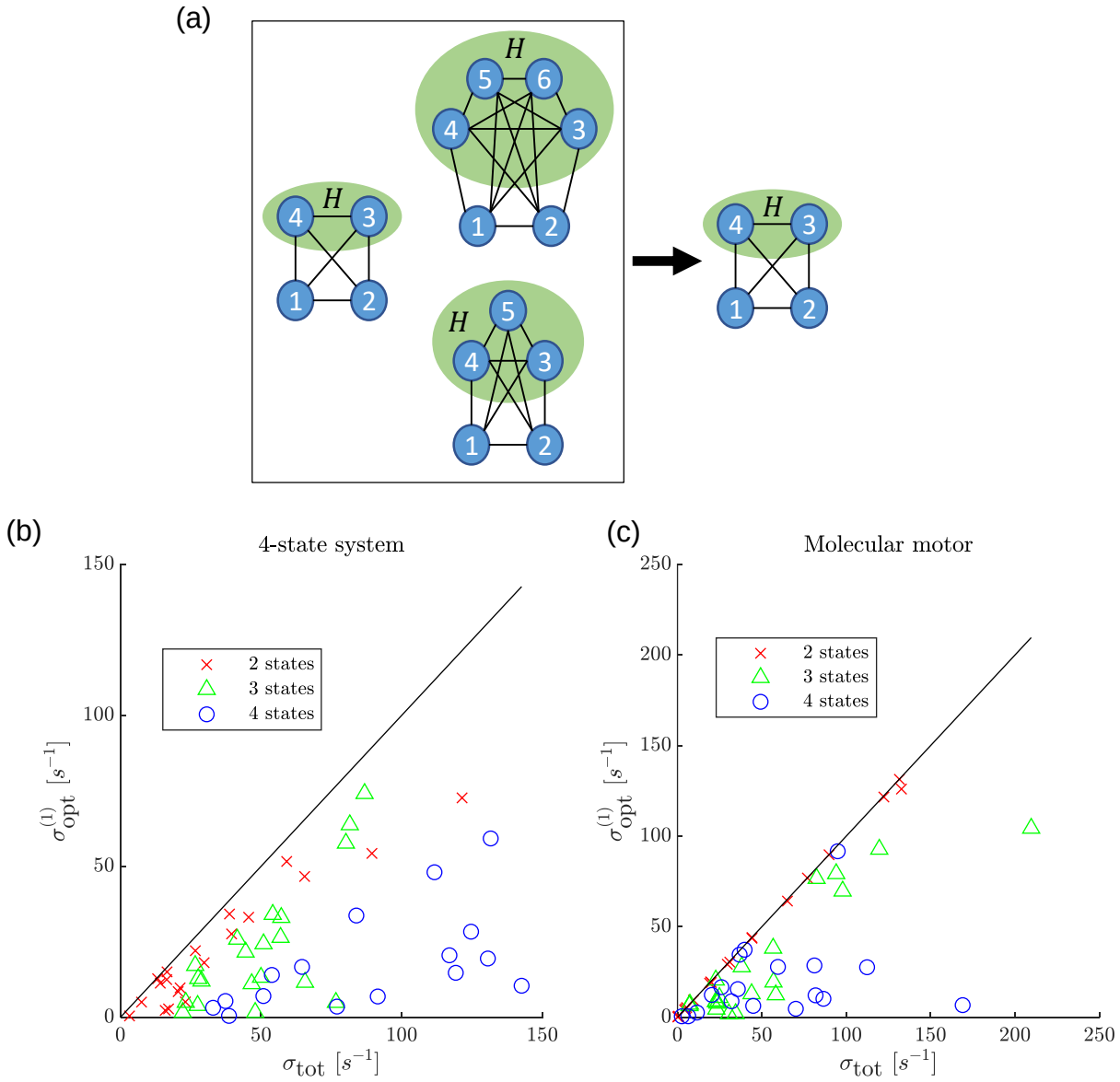


FIG. 5. Optimizing using a simple model. (a) Illustration of solving the optimization problem for a simple model with 2 hidden states (right), whereas the real system has more hidden states (left). (b) The results of $\sigma_{\rm opt}^{(1)}$ assuming the simple 4-state model (2 hidden states), when the real system has 2 (red cross), 3 (green triangle) or 4 (blue circle) hidden states. (c) The results of $\sigma_{\rm opt}^{(1)}$ assuming the simple molecular motor model (2 hidden states), when the real system has 2 (red cross), 3 (green triangles) or 4 (blue circle) hidden states. For both systems, the results are presented for random generated transition rates (for each case) with statistics calculated from trajectories of length $N = 10^8$ using a constraint tolerance of 10^{-5}.

from the values of n_{1H}, n_{1H2} and $\langle t_{1H2}\rangle$ for the 4-state system (Fig. 4(a)), and from the values of n_U, n_{UU}, and $\langle t_{UU}\rangle$ for the molecular motor (Fig. 4(b)). For smaller errors, we can use a smaller constraint tolerance.

For both systems, smaller constraint tolerance leads to a better estimator as the value of the lower bound on the EPR approaches the true analytical value (Fig. 4(c) and (d)), demonstrating the importance of an accurate estimation of the observables.

D. Optimizing a simple model

Although our approach can be generalized to any number of hidden states, the analytical expressions for the observables become complicated, and the number of variables increases for a more complex coarse-grained topology. In turn, solving the optimization problem would require longer computation times. In order to test the performance of our estimator, we solved the optimization problem for a larger number of hidden states in a fully-

DISTRIBUTION A: Distribution approved for public release.

connected network of 4, 5, and 6 states with only 2 observed states, assuming only 2 states are coarse-grained (Fig. 5(a)). Similarly, we tested the performance of our estimator for the case of the molecular motor with 2, 3, and 4 internal states at each physical position, assuming there are only 2. While generally, the estimator gives a more accurate result for the case of the 2 hidden state, which matches the assumption, it still provides a lower bound on the total EPR with comparable accuracy for a larger number of hidden states in the two systems (Fig. 5(b) and (c)).

IV. CONCLUSION

We present a new estimator for the entropy production rate, which gives a tight bound by formulating an optimization problem using both transitions and waiting times statistics. Our estimator can be applied to any system with known topology and it significantly surpasses previous estimators, as demonstrated for the two studied systems, the fully-connected hidden network, and the molecular motor. The variables for the optimization problem can be inferred from the observed statistics, where longer trajectories result in more accurate estimation and enable a smaller constraint tolerance value. Finally, for both systems, our approach can provide a lower bound on the total EPR for more complex systems, assuming a simpler underlying topology of the hidden states. Although we numerically showed that searching over all the systems with a simpler topology of the hidden part and the same observed statistics as the true system gave a lower bound on the total EPR for the two systems we studied, it remains an open problem to show this approach is universal. It would be interesting for future work to determine whether removing states from the hidden sub-network can only decrease the entropy production, given the observed statistics are conserved.

In summary, our approach is based on an optimization problem formulated using the observed statistics of a partially accessible system and provides a tight lower bound on the total EPR. The estimator can be used as a benchmark for comparing the performance of other estimators that rely on coarse-grained or partial information about the system.

ACKNOWLEDGMENTS

G. Bisker acknowledges the Zuckerman STEM Leadership Program, and the Tel Aviv University Center for AI and Data Science (TAD). This work was supported by the ERC NanoNonEq 101039127, the Air Force Office of Scientific Research (AFOSR) under award number FA9550-20-1-0426, and by the Army Research Office (ARO) under Grant Number W911NF-21-1-0101. The views and conclusions contained in this document are those of the authors and should not be interpreted as representing the official policies, either expressed or implied, of the Army Research Office or the U.S. Government.

Appendix A: Second-order mass rates

In order to find the second-order mass transition rates for two consecutive transitions between coarse-grained states, n_{IJK}, we need to take into account every possible original state $i \in I$, every possible path within the coarse grained state J, and every possible transition from a state in J to every possible final state $k \in K$. Let us start by considering a specific initial Markovian state $i \in I$ and a specific final Markovian state $k \in K$ and calculate the mass transition rate n_{iJk}:

$$\begin{aligned} n_{iJk} &= \sum_{N=0}^{\infty} \sum_{j_0,\ldots,j_N \in J} n_{ij_0} p_{j_0 j_1} p_{j_1 j_2} \cdots p_{j_{N-1} j_N} p_{j_N k} \\ &= \sum_{N=0}^{\infty} \sum_{j',j'' \in J} n_{ij'} \left[\boldsymbol{P}_{JJ}^{N}\right]_{j'j''} p_{j''k} \\ &= \sum_{j',j'' \in J} n_{ij'} \left(\sum_{N=0}^{\infty} \left[\boldsymbol{P}_{JJ}^{N}\right]_{j'j''} \right) p_{j''k} \\ &= \sum_{j',j'' \in J} n_{ij'} \left[\mathbb{I} - \boldsymbol{P}_{JJ}\right]^{-1}_{j'j''} p_{j''k} \\ &= \boldsymbol{n}_{iJ}^{T} \left[\mathbb{I} - \boldsymbol{P}_{JJ}\right]^{-1} \boldsymbol{p}_{Jk} \end{aligned} \tag{A1}$$

The two summations are for all the possible lengths N of trajectories within J, and all the optional paths with the given length $\{j_0, j_1, \cdots, j_N\}$ in J. From mass conservation, we can now obtain the expression for n_{IJK} by summing over all the optional original $i \in I$ and final $k \in K$ states:

$$n_{IJK} = \sum_{i \in I} \sum_{k \in K} n_{iJk} \tag{A2}$$

Appendix B: Conditional waiting time moments

The waiting time at each Markovian state i is an exponentially distributed random variable $\psi_i(t)$ with mean waiting time $\tau_i = \lambda_i^{-1}$:

$$\psi_i(t) = \lambda_i e^{-\lambda_i t} \tag{B1}$$

For the calculations, we used the joint distribution of the waiting time and the transition $i \to j$:

$$\psi_{ij}(t) = w_{ij} e^{-\lambda_i t} \tag{B2}$$

Notice that $\psi_{ij}(t)$ is not normalized to 1 as $\int_0^\infty \psi_{ij}(t)dt = p_{ij}$.

DISTRIBUTION A: Distribution approved for public release.

The probability to observe a trajectory $\gamma_N : i_0 \to i_1 \to \cdots \to i_N$ with a total duration of T is:

$$\begin{aligned} &p(\gamma_N, T) = \\ &= \int_{\sum_{i=0}^{N-1} t_i = T} \psi_{i_0 i_1}(t_0)\psi_{i_1 i_2}(t_1)\cdots\psi_{i_{N-1} i_N}(t_{N-1}) \\ &\qquad dt_0 dt_1 \cdots dt_{N-1} \end{aligned} \tag{B3}$$

Since this is a convolution, we can perform a Laplace transform to get a simpler formula of multiplications of Laplace transforms of Markovian joint distributions of waiting times and transitions:

$$\tilde{p}(\gamma_N, s) = \tilde{\psi}_{i_0 i_1}(s)\tilde{\psi}_{i_1 i_2}(s)\cdots\tilde{\psi}_{i_{N-1} i_N}(s) \tag{B4}$$

where

$$\begin{aligned} \tilde{\psi}_{ij}(s) &= \int_0^\infty \psi_{ij}(t)e^{-st}dt = \int_0^\infty w_{ij}e^{-\lambda_i t}e^{-st}dt \\ &= w_{ij}\int_0^\infty e^{-(s+\lambda_i)t}dt = w_{ij}\left[-\frac{e^{-(s+\lambda_i)t}}{s+\lambda_i}\right]_0^\infty \\ &= \frac{w_{ij}}{s+\lambda_i} \end{aligned} \tag{B5}$$

In order to calculate the moments of the conditional waiting time distribution $\psi_{IJK}(t)$ for the coarse-grained state J conditioned on an initial state in I and a final state in K, our strategy is to calculate its Laplace transform $\tilde{\psi}_{IJK}(s)$. We start by calculating $\tilde{\psi}_{iJk}(s)$ which is the Laplace transform of the waiting distribution in coarse-grained state J, before jumping to a specific Markovian state $k \in K$, given it came from a specific Markovian state $i \in I$. Since we want the waiting time in J, we sum over all of the paths with any length N inside J with a final transition to $k \in K$, $j_0 \to j_1 \to \cdots \to j_N \to k$, weighed by the probability to jump from $i \in I$ to the first state $j_0 \in J$:

$$\begin{aligned} &\tilde{\psi}_{iJk}(s) = \\ &= \sum_{N=0}^\infty \sum_{j_0,\ldots,j_N \in J} \frac{p_{ij_0}}{\sum_{j\in J} p_{ij}} \tilde{p}(j_0 \to j_1 \to \cdots \to j_N \to k, s) \\ &= \sum_{N=0}^\infty \sum_{j_0,\ldots,j_N \in J} \frac{p_{ij_0}}{\sum_{j\in J} p_{ij}} \tilde{\psi}_{j_0 j_1}(s)\cdots\tilde{\psi}_{j_{N-1} j_N}(s)\tilde{\psi}_{j_N k}(s) \\ &= \sum_{N=0}^\infty \sum_{j',j'' \in J} \frac{p_{ij'}}{\sum_{j\in J} p_{ij}} \left[\tilde{\boldsymbol{\Psi}}_{JJ}(s)^N\right]_{j',j''} \tilde{\psi}_{j'' k}(s) \\ &= \sum_{j',j'' \in J} \frac{p_{ij'}}{\sum_{j\in J} p_{ij}} \sum_{N=0}^\infty \left[\tilde{\boldsymbol{\Psi}}_{JJ}(s)^N\right]_{j',j''} \tilde{\psi}_{j'' k}(s) \\ &= \sum_{j',j'' \in J} \frac{p_{ij'}}{\sum_{j\in J} p_{ij}} \left[\mathbb{I} - \tilde{\boldsymbol{\Psi}}_{JJ}(s)\right]^{-1}_{j',j''} \tilde{\psi}_{j'' k}(s) \\ &= \frac{\boldsymbol{p}_{iJ}^T}{\sum_{j\in J} p_{ij}} \left[\mathbb{I} - \tilde{\boldsymbol{\Psi}}_{JJ}(s)\right]^{-1} \tilde{\boldsymbol{\psi}}_{Jk}(s) \end{aligned} \tag{B6}$$

where $\tilde{\boldsymbol{\Psi}}_{JJ}(s)$ is a matrix of size $N_J \times N_J$, and N_J is the number of Markovian states inside J:

$$\left[\tilde{\boldsymbol{\Psi}}_{JJ}(s)\right]_{j_1,j_2} = \begin{cases} \tilde{\Psi}_{j_1 j_2}(s) & j_1 \neq j_2 \\ 0 & j_1 = j_2 \end{cases} \tag{B7}$$

As mentioned in the main text we denote $\tilde{\psi}_{iJK}(s) \equiv \sum_{k\in K} \tilde{\psi}_{iJk}(s)$. Notice that $\tilde{\psi}_{iJK}(s)$ is not normalized to 1 and it needs to be divided by $\tilde{\psi}_{iJK}(s \to 0)$, which is exactly the probability to jump from J to K, given the transition to J was from i.

$$\tilde{\psi}_{iJK}^{Normalized}(s) = \frac{\tilde{\psi}_{iJK}(s)}{\tilde{\psi}_{iJK}(s \to 0)} \tag{B8}$$

This results from the fact that we used $\psi_{ij}(t)$, which is normalized to p_{ij}.

In order to get $\tilde{\psi}_{IJK}(s)$, we sum $\tilde{\psi}_{iJK}^{Normalized}(s)$ over all of the Markovian states $i \in I$, weighed by the corresponding probability π_i/π_I of being in state i, given the system is in the coarse-grained state I:

$$\tilde{\psi}_{IJK}(s) = \sum_{i\in I} \frac{\pi_i}{\pi_I} \tilde{\psi}_{iJK}^{Normalized}(s) \tag{B9}$$

For a general probability density function $f(t) : [0,\infty] \to [0,1]$ the Laplace transform is:

$$\tilde{f}(s) = \int_0^\infty f(t)e^{-st}dt \tag{B10}$$

and its k-th derivative by s is:

$$\frac{d^k \tilde{f}(s)}{ds^k} = (-1)^k \int_0^\infty t^k f(t)e^{-st}dt \tag{B11}$$

DISTRIBUTION A: Distribution approved for public release.

Taking the limit $s \to 0$:

$$\begin{aligned}\frac{d^k \tilde{f}(s)}{ds^k}|_{s\to 0} &= (-1)^k \int_0^\infty t^k f(t) dt \\ &= (-1)^k \langle t^k \rangle\end{aligned} \tag{B12}$$

we find the k-th moment of the probability density function $f(t)$:

$$\langle t^k \rangle = (-1)^k \frac{d^k \tilde{f}(s)}{ds^k}|_{s\to 0} \tag{B13}$$

Therefore, the k-th moment $\langle t^k_{IJK} \rangle$ of the conditional waiting time distribution $\psi_{IJK}(t)$ is:

$$\langle t^k_{IJK} \rangle = (-1)^k \frac{d^k \tilde{\psi}_{IJK}(s)}{ds^k}|_{s\to 0} \tag{B14}$$

Appendix C: Analytical expressions for the 4-state system

The variables to consider for this system are the mass transition rates n_{ij} and the steady-state probabilities π_i for $i, j \in \{1, 2, 3, 4\}$, meaning a total of 16 variables. Note that π_1, π_2, n_{12} and n_{21} are fully observed. Therefore, we are left with 12 variables. With the following linear constraints, we can immediately reduce the problem to 6 variables.

1. Linear constraints

We impose probability conservation, mass transition rate conservation in the hidden Markovian states, and mass transition rate conservation between an observed Markovian state and the hidden coarse-grained state.

a. Probabilities

From conservation of the steady-state probability of the Markovian states within the coarse-grained hidden state:

$$\pi_H = \pi_3 + \pi_4 \tag{C1}$$

b. Mass conservation at any Markovian state

We write the mass conservation for one of the hidden states (3 or 4), which for this system, is enough to guaranty the mass conservation for the other hidden state:

$$n_{13} + n_{23} + n_{43} = n_{31} + n_{32} + n_{34} \tag{C2}$$

c. First-order mass rates

Here, we require the mass rate conservation of transitions in and out of the hidden state, providing 4 constraint equations:

$$\begin{aligned}\forall_{i\in\{1,2\}} &: n_{iH} = n_{i3} + n_{i4} \\ \forall_{i\in\{1,2\}} &: n_{Hi} = n_{3i} + n_{4i}\end{aligned} \tag{C3}$$

2. Non-linear constraints

The second-order mass transition rates and the conditional waiting times moments can be expressed only as a non-linear function of the optimization problem variables. Here, we show the full derivations of these relations.

a. Second-order mass rates

For this system, as mentioned in the text, we are interested in n_{1H2} and n_{2H1}, where the first and the last states are the observed Markovian states. From equation Eq. A1:

$$n_{iHj} = \boldsymbol{n}_{iH}^T \left[\mathbb{I} - \boldsymbol{P}_{HH}\right]^{-1} \boldsymbol{p}_{Hj} \tag{C4}$$

Where

$$\boldsymbol{P}_{HH} = \begin{bmatrix} 0 & p_{34} \\ p_{43} & 0 \end{bmatrix} \tag{C5}$$

and

$$\left[\mathbb{I} - \boldsymbol{P}_{HH}\right]^{-1} = \frac{1}{1 - p_{34}p_{43}} \begin{bmatrix} 1 & p_{34} \\ p_{43} & 1 \end{bmatrix} \tag{C6}$$

Plugging into Eq. C4, we have:

$$\begin{aligned} n_{iHj} &= \boldsymbol{n}_{iH}^T \left[\mathbb{I} - \boldsymbol{P}_{HH}\right]^{-1} \boldsymbol{p}_{Hj} \\ &= \begin{bmatrix} n_{i3} & n_{i4} \end{bmatrix} \left(\frac{1}{1 - p_{34}p_{43}} \begin{bmatrix} 1 & p_{34} \\ p_{43} & 1 \end{bmatrix} \right) \begin{bmatrix} p_{3j} \\ p_{4j} \end{bmatrix} \\ &= \frac{1}{1 - p_{34}p_{43}} \begin{bmatrix} n_{i3} & n_{i4} \end{bmatrix} \begin{bmatrix} p_{3j} + p_{34}p_{4j} \\ p_{4j} + p_{43}p_{3j} \end{bmatrix} \\ &= \frac{n_{i3}(p_{3j} + p_{34}p_{4j}) + n_{i4}(p_{4j} + p_{43}p_{3j})}{1 - p_{34}p_{43}} \end{aligned} \tag{C7}$$

Remember we can express p_{ij} in terms of the mass transition rates (Eq. 3).

b. Conditional waiting time moments

We calculate the conditional waiting times moments $\langle t^k_{iHj} \rangle$ for $i, j \in \{1, 2\}$, in terms of the problem variables. Based on Eq. B14, we need to calculate $\tilde{\psi}^{Normalized}_{iHj}(s)$.

DISTRIBUTION A: Distribution approved for public release.

From Eq. B6:

$$\tilde{\psi}_{iHj}(s) = \frac{\boldsymbol{p}_{iH}^T}{\sum_{h\in\{3,4\}} p_{ih}} \left[\mathbb{I} - \tilde{\boldsymbol{\Psi}}_{HH}(s)\right]^{-1} \tilde{\boldsymbol{\psi}}_{Hj}(s) \quad \text{(C8)}$$

Now, we can calculate $\tilde{\boldsymbol{\psi}}_{Hj}(s)$ from Eq. 12 and Eq. B5:

$$\tilde{\boldsymbol{\psi}}_{Hj}(s) = \begin{bmatrix}\tilde{\psi}_{3j}(s)\\ \tilde{\psi}_{4j}(s)\end{bmatrix} = \begin{bmatrix}\frac{w_{3j}}{s+\lambda_3}\\ \frac{w_{4j}}{s+\lambda_4}\end{bmatrix} \quad \text{(C9)}$$

Given that (Eq. B7 and Eq. B5):

$$\begin{aligned}\tilde{\boldsymbol{\Psi}}_{HH}(s) &= \begin{bmatrix}0 & \tilde{\psi}_{34}(s)\\ \tilde{\psi}_{43}(s) & 0\end{bmatrix}\\ &= \begin{bmatrix}0 & \frac{w_{34}}{s+\lambda_3}\\ \frac{w_{43}}{s+\lambda_4} & 0\end{bmatrix}\end{aligned} \quad \text{(C10)}$$

We can plug into Eq. C8:

$$\begin{aligned}&\tilde{\psi}_{iHj}(s) =\\ &= \frac{\boldsymbol{p}_{iH}^T}{\sum_{h\in\{3,4\}} p_{ih}} \left[\mathbb{I} - \tilde{\boldsymbol{\Psi}}_{HH}(s)\right]^{-1} \tilde{\boldsymbol{\psi}}_{Hj}(s)\\ &= \frac{1}{p_{i3}+p_{i4}} \begin{bmatrix}p_{i3} & p_{i4}\end{bmatrix}\\ &\quad \left(\left(1 - \frac{w_{34}w_{43}}{(s+\lambda_3)(s+\lambda_4)}\right)^{-1} \begin{bmatrix}1 & \frac{w_{34}}{s+\lambda_3}\\ \frac{w_{43}}{s+\lambda_4} & 1\end{bmatrix}\right)\\ &\quad \begin{bmatrix}\frac{w_{3j}}{s+\lambda_3}\\ \frac{w_{4j}}{s+\lambda_4}\end{bmatrix}\\ &= \frac{1}{p_{i3}+p_{i4}} \left(1 - \frac{w_{34}w_{43}}{(s+\lambda_3)(s+\lambda_4)}\right)^{-1}\\ &\quad \begin{bmatrix}p_{i3} & p_{i4}\end{bmatrix} \begin{bmatrix}\frac{w_{3j}}{s+\lambda_3} + \frac{w_{34}}{s+\lambda_3}\frac{w_{4j}}{s+\lambda_4}\\ \frac{w_{4j}}{s+\lambda_4} + \frac{w_{43}}{s+\lambda_4}\frac{w_{3j}}{s+\lambda_3}\end{bmatrix}\\ &= \left(1 - \frac{w_{34}w_{43}}{(s+\lambda_3)(s+\lambda_4)}\right)^{-1}\\ &\quad \left[\frac{p_{i3}}{p_{i3}+p_{i4}}\left(\frac{w_{3j}}{s+\lambda_3} + \frac{w_{34}}{s+\lambda_3}\frac{w_{4j}}{s+\lambda_4}\right)\right.\\ &\quad \left.+\frac{p_{i4}}{p_{i3}+p_{i4}}\left(\frac{w_{4j}}{s+\lambda_4} + \frac{w_{43}}{s+\lambda_4}\frac{w_{3j}}{s+\lambda_3}\right)\right]\end{aligned} \quad \text{(C11)}$$

Since the states i and j are Markovian, we just need to normalize this expression in order to get the desired result:

$$\begin{aligned}&\tilde{\psi}_{iHj}(s\to 0) =\\ &= \left(1 - \frac{w_{34}w_{43}}{\lambda_3\lambda_4}\right)^{-1}\\ &\quad \left[\frac{p_{i3}}{p_{i3}+p_{i4}}\left(\frac{w_{3j}}{\lambda_3} + \frac{w_{34}}{\lambda_3}\frac{w_{4j}}{\lambda_4}\right)\right.\\ &\quad \left.+\frac{p_{i4}}{p_{i3}+p_{i4}}\left(\frac{w_{4j}}{\lambda_4} + \frac{w_{43}}{\lambda_4}\frac{w_{3j}}{\lambda_3}\right)\right]\\ &= \frac{p_{i3}\left(p_{3j}+p_{34}p_{4j}\right) + p_{i4}\left(p_{4j}+p_{43}p_{3j}\right)}{\left(p_{i3}+p_{i4}\right)\left(1-p_{34}p_{43}\right)}\end{aligned} \quad \text{(C12)}$$

Therefore:

$$\tilde{\psi}_{iHj}^{Normalized}(s) = \frac{\tilde{\psi}_{iHj}(s)}{\tilde{\psi}_{iHj}(s\to 0)} \quad \text{(C13)}$$

Finally, we get the moments from Eq. B14.

In order to get the expressions of the derivatives, we used the package Sympy in Python.

Appendix D: Analytical expressions for the molecular motor system

The variables to consider for the molecular motor system are the mass transition rates n_{u1}, n_{u2}, n_{d1}, n_{d2}, n_l, n_r and the steady-state probabilities π and π', meaning a total of 8 variables. With the following linear constraints, we can immediately reduce the problem to 4 variables.

1. Linear constraints

As in the 4-state system, we impose probability conservation, mass transition rate conservation in the Markovian states, and mass transition rate conservation for the observed transitions U and D.

a. Probabilities

From conservation of the steady-state probability of the Markovian states within the coarse-grained states:

$$\pi + \pi' = \frac{1}{3} \quad \text{(D1)}$$

b. Mass conservation at any Markovian state

We write the mass conservation for one of the hidden states (active or passive), which for this system, is enough to guaranty the mass conservation for the other hidden state:

$$n_r + n_{u2} = n_l + n_{d2} \quad \text{(D2)}$$

DISTRIBUTION A: Distribution approved for public release.

c. First-order mass rates

Here, we require the mass rate conservation of transitions in and out of the coarse-grained state, providing 2 constraint equations:

$$\begin{aligned} n_U &= n_{u1} + n_{u2} \\ n_D &= n_{d1} + n_{d2} \end{aligned} \tag{D3}$$

2. Non-linear constraints

Since we have 2 hidden states as in the 4-state system, the results from Appendix C can be used here.

a. Second-order mass rates

We use the results for the 4-state system in Eq. C7, together with Eq. A2. For n_{UU}, we need to sum over all the mass that goes up from the passive or active state, and then up again only to the passive state:

$$\begin{aligned} n_{UU} &= \frac{n_{u1}(p_{u1} + p_l p_{u2})}{1 - p_l p_r} + \frac{n_{u2}(p_{u1} + p_l p_{u2})}{1 - p_l p_r} \\ &= \frac{(n_{u1} + n_{u2})(p_{u1} + p_l p_{u2})}{1 - p_l p_r} \end{aligned} \tag{D4}$$

For n_{DD}, we need to sum over all the mass that goes down only from the passive state, and then down again to the passive or active state:

$$\begin{aligned} n_{DD} &= \frac{n_{d1} p_{d1} + n_{d2} p_r p_{d1}}{1 - p_l p_r} + \frac{n_{d1} p_{d2} + n_{d2} p_r p_{d2}}{1 - p_l p_r} \\ &= \frac{(n_{d1} + n_{d2} p_r)(p_{d1} + p_{d2})}{1 - p_l p_r} \end{aligned} \tag{D5}$$

b. Conditional waiting time moments

We account for all of the transitions through a coarse-grained state i, and specify in the following calculations the Markovian state before jumping to i, and the following Markovian state, after state i, where i' (i) denoted an active (passive) state. For example, $(i-1) \to (i+1)$ represent two consecutive transitions, $(i-1) \to i \to (i+1)$.

Note that a transition upward is only to a passive state, so the previous state (being passive or active) in the first transition does not affect the waiting time. Furthermore, a transition downward is only from a passive state.

From Eq. B9:

$$\begin{aligned} \tilde{\psi}_{UU}(s) &= \frac{\pi}{\pi + \pi'} \frac{\tilde{\psi}_{(i-1)\to(i+1)}(s)}{\tilde{\psi}_{(i-1)\to(i+1)}(s \to 0)} \\ &+ \frac{\pi'}{\pi + \pi'} \frac{\tilde{\psi}_{(i-1)'\to(i+1)}(s)}{\tilde{\psi}_{(i-1)'\to(i+1)}(s \to 0)} \\ &= \frac{\tilde{\psi}_{(i-1)\to(i+1)}(s)}{\tilde{\psi}_{(i-1)\to(i+1)}(s \to 0)} \end{aligned} \tag{D6a}$$

and similarly:

$$\begin{aligned} &\tilde{\psi}_{UD}(s) = \\ &= \frac{\pi}{\pi + \pi'} \frac{\left(\tilde{\psi}_{(i-1)\to(i-1)} + \tilde{\psi}_{(i-1)\to(i-1)'}\right)(s)}{\left(\tilde{\psi}_{(i-1)\to(i-1)} + \tilde{\psi}_{(i-1)\to(i-1)'}\right)(s \to 0)} \\ &+ \frac{\pi'}{\pi + \pi'} \frac{\left(\tilde{\psi}_{(i-1)'\to(i-1)} + \tilde{\psi}_{(i-1)'\to(i-1)'}\right)(s)}{\left(\tilde{\psi}_{(i-1)'\to(i-1)} + \tilde{\psi}_{(i-1)'\to(i-1)'}\right)(s \to 0)} \\ &= \frac{\left(\tilde{\psi}_{(i-1)\to(i-1)} + \tilde{\psi}_{(i-1)\to(i-1)'}\right)(s)}{\left(\tilde{\psi}_{(i-1)\to(i-1)} + \tilde{\psi}_{(i-1)\to(i-1)'}\right)(s \to 0)} \end{aligned} \tag{D6b}$$

Moreover:

$$\tilde{\psi}_{DU}(s) = \frac{\tilde{\psi}_{(i+1)\to(i+1)}(s)}{\tilde{\psi}_{(i+1)\to(i+1)}(s \to 0)} \tag{D6c}$$

and:

$$\tilde{\psi}_{DD}(s) = \frac{\left(\tilde{\psi}_{(i+1)\to(i-1)} + \tilde{\psi}_{(i+1)\to(i-1)'}\right)(s)}{\left(\tilde{\psi}_{(i+1)\to(i-1)} + \tilde{\psi}_{(i+1)\to(i-1)'}\right)(s \to 0)} \tag{D6d}$$

Now we calculate all the terms in the numerators, using Eq. C11 from the 4-state system results:

$$\begin{aligned} \tilde{\psi}_{(i-1)\to(i+1)}(s) = &\left(1 - \frac{w_l w_r}{(s+\lambda)(s+\lambda')}\right)^{-1} \\ &\left(\frac{w_{u1}}{s+\lambda} + \frac{w_l}{s+\lambda}\frac{w_{u2}}{s+\lambda'}\right) \end{aligned} \tag{D7a}$$

$$\begin{aligned} &\left(\tilde{\psi}_{(i-1)\to(i-1)} + \tilde{\psi}_{(i-1)\to(i-1)'}\right)(s) = \\ &= \left(1 - \frac{w_l w_r}{(s+\lambda)(s+\lambda')}\right)^{-1} \left(\frac{w_{d1}}{s+\lambda} + \frac{w_{d2}}{s+\lambda}\right) \\ &= \left(1 - \frac{w_l w_r}{(s+\lambda)(s+\lambda')}\right)^{-1} \frac{w_{d1} + w_{d2}}{s+\lambda} \end{aligned} \tag{D7b}$$

$$\begin{aligned} &\tilde{\psi}_{(i+1)\to(i+1)}(s) = \\ &= \left(1 - \frac{w_l w_r}{(s+\lambda)(s+\lambda')}\right)^{-1} \\ &\left[\frac{p_{d1}}{p_{d1}+p_{d2}}\frac{w_{u1}}{s+\lambda} + \frac{p_{d2}}{p_{d1}+p_{d2}}\frac{w_r}{s+\lambda'}\frac{w_{u1}}{s+\lambda}\right] \\ &= \left(1 - \frac{w_l w_r}{(s+\lambda)(s+\lambda')}\right)^{-1} \\ &\frac{1}{p_{d1}+p_{d2}}\frac{w_{u1}}{s+\lambda}\left[p_{d1} + \frac{p_{d2} w_r}{s+\lambda'}\right] \end{aligned} \tag{D7c}$$

$$
\begin{aligned}
&\left(\tilde{\psi}_{(i+1)\to(i-1)} + \tilde{\psi}_{(i+1)\to(i-1)'}\right)(s) = \\
&= \left(1 - \frac{w_l w_r}{(s+\lambda)(s+\lambda')}\right)^{-1} \\
&\left[\frac{p_{d1}}{p_{d1}+p_{d2}}\frac{w_{d1}}{s+\lambda} + \frac{p_{d2}}{p_{d1}+p_{d2}}\frac{w_r}{s+\lambda'}\frac{w_{d1}}{s+\lambda}\right. \\
&\left.+\frac{p_{d1}}{p_{d1}+p_{d2}}\frac{w_{d2}}{s+\lambda} + \frac{p_{d2}}{p_{d1}+p_{d2}}\frac{w_r}{s+\lambda'}\frac{w_{d2}}{s+\lambda}\right] \\
&= \left(1 - \frac{w_l w_r}{(s+\lambda)(s+\lambda')}\right)^{-1} \\
&\left[\frac{p_{d1}}{p_{d1}+p_{d2}}\frac{w_{d1}+w_{d2}}{s+\lambda} + \frac{p_{d2}}{p_{d1}+p_{d2}}\frac{w_r}{s+\lambda'}\frac{w_{d1}+w_{d2}}{s+\lambda}\right] \\
&= \left(1 - \frac{w_l w_r}{(s+\lambda)(s+\lambda')}\right)^{-1} \\
&\frac{1}{p_{d1}+p_{d2}}\frac{w_{d1}+w_{d2}}{s+\lambda}\left[p_{d1} + \frac{p_{d2}w_r}{s+\lambda'}\right]
\end{aligned}
\tag{D7d}
$$

All of the denominators from Eq. D6 can be calculated by setting $s \to 0$ in Eq. D7. Finally, we get the moments from equation Eq. B14.

In order to get the expressions of the derivatives, we used the package Sympy in Python.

DISTRIBUTION A: Distribution approved for public release.

[1] C. J. Bustamante, Y. R. Chemla, S. Liu, and M. D. Wang, Nature Reviews Methods Primers **1**, 1 (2021).
[2] C. D. Kinz-Thompson, K. K. Ray, and R. L. Gonzalez Jr, Annual Review of Biophysics **50**, 191 (2021).
[3] C. Bustamante, L. Alexander, K. Maciuba, and C. M. Kaiser, Annual review of biochemistry **89**, 443 (2020).
[4] C. Bustamante, Quarterly reviews of biophysics **38**, 291 (2005).
[5] U. Seifert, Reports on progress in physics **75**, 126001 (2012).
[6] C. Van den Broeck and M. Esposito, Physica A: Statistical Mechanics and its Applications **418**, 6 (2015).
[7] R. Van Zon and E. Cohen, Physical Review E **67**, 046102 (2003).
[8] F. Douarche, S. Joubaud, N. B. Garnier, A. Petrosyan, and S. Ciliberto, Physical review letters **97**, 140603 (2006).
[9] S. Sabhapandit, Physical Review E **85**, 021108 (2012).
[10] P. Visco, Journal of Statistical Mechanics: Theory and Experiment **2006**, P06006 (2006).
[11] G. Wang, E. M. Sevick, E. Mittag, D. J. Searles, and D. J. Evans, Physical Review Letters **89**, 050601 (2002).
[12] S. Ciliberto, A. Imparato, A. Naert, and M. Tanase, Physical review letters **110**, 180601 (2013).
[13] I. A. Martínez, É. Roldán, L. Dinis, D. Petrov, J. M. Parrondo, and R. A. Rica, Nature physics **12**, 67 (2016).
[14] C. Van den Broeck, N. Kumar, and K. Lindenberg, Physical review letters **108**, 210602 (2012).
[15] G. Verley, M. Esposito, T. Willaert, and C. Van den Broeck, Nature communications **5**, 1 (2014).
[16] S. Mohanta, S. Saryal, and B. K. Agarwalla, Physical Review E **105**, 034127 (2022).
[17] S. Bo, M. Del Giudice, and A. Celani, Journal of Statistical Mechanics: Theory and Experiment **2015**, P01014 (2015).
[18] N. P. Saadat, T. Nies, Y. Rousset, and O. Ebenhöh, Entropy **22**, 277 (2020).
[19] J. Li, J. M. Horowitz, T. R. Gingrich, and N. Fakhri, Nature communications **10**, 1 (2019).
[20] É. Fodor, C. Nardini, M. E. Cates, J. Tailleur, P. Visco, and F. Van Wijland, Physical review letters **117**, 038103 (2016).
[21] C. Maes and K. Netočnỳ, Journal of statistical physics **110**, 269 (2003).
[22] J. M. Parrondo, C. Van den Broeck, and R. Kawai, New Journal of Physics **11**, 073008 (2009).
[23] P. Pietzonka, A. C. Barato, and U. Seifert, Journal of Statistical Mechanics: Theory and Experiment **2016**, 124004 (2016).
[24] N. Shiraishi, Journal of Statistical Physics **185**, 1 (2021).
[25] J. M. Horowitz and T. R. Gingrich, Nature Physics **16**, 15 (2020).
[26] T. R. Gingrich, J. M. Horowitz, N. Perunov, and J. L. England, Physical review letters **116**, 120601 (2016).
[27] A. C. Barato and U. Seifert, Physical review letters **114**, 158101 (2015).
[28] S. K. Manikandan, S. Ghosh, A. Kundu, B. Das, V. Agrawal, D. Mitra, A. Banerjee, and S. Krishnamurthy, Communications Physics **4**, 1 (2021).
[29] S. K. Manikandan, D. Gupta, and S. Krishnamurthy, Physical review letters **124**, 120603 (2020).
[30] T. R. Gingrich and J. M. Horowitz, Phys. Rev. Lett. **119**, 170601 (2017).
[31] A. Pal, S. Reuveni, and S. Rahav, Phys. Rev. Research **3**, L032034 (2021).
[32] I. Di Terlizzi and M. Baiesi, Journal of Physics A: Mathematical and Theoretical **52**, 02LT03 (2018).
[33] V. T. Vo, T. V. Vu, and Y. Hasegawa, Journal of Physics A: Mathematical and Theoretical **55**, 405004 (2022).
[34] D. J. Skinner and J. Dunkel, Physical review letters **127**, 198101 (2021).
[35] A. Ghosal and G. Bisker, Phys. Chem. Chem. Phys. **24**, 24021 (2022).
[36] S. Otsubo, S. Ito, A. Dechant, and T. Sagawa, Physical Review E **101**, 062106 (2020).
[37] D.-K. Kim, Y. Bae, S. Lee, and H. Jeong, Physical Review Letters **125**, 140604 (2020).
[38] Y. Bae, D.-K. Kim, and H. Jeong, Physical Review Research **4**, 033094 (2022).
[39] É. Roldán and J. M. Parrondo, Physical review letters **105**, 150607 (2010).
[40] S. Otsubo, S. K. Manikandan, T. Sagawa, and S. Krishnamurthy, Communications Physics **5**, 1 (2022).
[41] B. Lander, J. Mehl, V. Blickle, C. Bechinger, and U. Seifert, Physical Review E **86**, 030401 (2012).
[42] P. Padmanabha, D. M. Busiello, A. Maritan, and D. Gupta, arXiv preprint arXiv:2207.12091 (2022).
[43] A. Dechant and S.-i. Sasa, Physical Review E **97**, 062101 (2018).
[44] R. Kawai, J. M. R. Parrondo, and C. V. den Broeck, Phys. Rev. Lett. **98**, 080602 (2007).
[45] G. Bisker, M. Polettini, T. R. Gingrich, and J. M. Horowitz, Journal of Statistical Mechanics: Theory and Experiment **2017**, 093210 (2017).
[46] N. Shiraishi, S. Ito, K. Kawaguchi, and T. Sagawa, New Journal of Physics **17**, 045012 (2015).
[47] N. Shiraishi and T. Sagawa, Physical Review E **91**, 012130 (2015).
[48] M. Polettini and M. Esposito, Physical review letters **119**, 240601 (2017).
[49] V. T. Vo, T. Van Vu, and Y. Hasegawa, arXiv preprint arXiv:2203.11501 (2022).
[50] R. Kawai, J. M. Parrondo, and C. Van den Broeck, Physical review letters **98**, 080602 (2007).
[51] C. Maes, Journal of statistical physics **95**, 367 (1999).
[52] É. Roldán, J. Barral, P. Martin, J. M. Parrondo, and F. Jülicher, New Journal of Physics **23**, 083013 (2021).
[53] J. Horowitz and C. Jarzynski, Physical Review E **79**, 021106 (2009).
[54] B. Gaveau, L. Granger, M. Moreau, and L. Schulman, Physical Review E **89**, 032107 (2014).
[55] B. Gaveau, L. Granger, M. Moreau, and L. S. Schulman, Entropy **16**, 3173 (2014).
[56] I. A. Martínez, G. Bisker, J. M. Horowitz, and J. M. Parrondo, Nature communications **10**, 1 (2019).
[57] J. van der Meer, B. Ertel, and U. Seifert, Phys. Rev. X **12**, 031025 (2022).
[58] D. Hartich and A. Godec, arXiv preprint arXiv:2112.08978 (2021).
[59] G. Bisker, I. A. Martinez, J. M. Horowitz, and J. M.

DISTRIBUTION A: Distribution approved for public release.

Parrondo, arXiv preprint arXiv:2202.02064 (2022).
[60] J. van der Meer, J. Degünther, and U. Seifert, arXiv preprint arXiv:2211.17032 (2022).
[61] J. Ehrich, Journal of Statistical Mechanics: Theory and Experiment **2021**, 083214 (2021).
[62] D. J. Skinner and J. Dunkel, Proceedings of the National Academy of Sciences **118**, e2024300118 (2021).
[63] J. Schnakenberg, Reviews of Modern physics **48**, 571 (1976).
[64] C. Maes, K. Netočnỳ, and B. Wynants, Journal of Physics A: Mathematical and Theoretical **42**, 365002 (2009).
[65] J. Zhang and T. Zhou, Proceedings of the National Academy of Sciences **116**, 23542 (2019).
[66] D. Hartich and A. Godec, arXiv preprint arXiv:2111.14734 (2021).
[67] Z. Ugray, L. Lasdon, J. Plummer, F. Glover, J. Kelly, and R. Martí, INFORMS Journal on computing **19**, 328 (2007).

DISTRIBUTION A: Distribution approved for public release.